

Zeitschrift: IABSE publications = Mémoires AIPC = IVBH Abhandlungen
Band: 35 (1975)

Teilband: IABSE Publications = Mémoires AIPC = IVBH Abhandlungen

Nutzungsbedingungen

Die ETH-Bibliothek ist die Anbieterin der digitalisierten Zeitschriften auf E-Periodica. Sie besitzt keine Urheberrechte an den Zeitschriften und ist nicht verantwortlich für deren Inhalte. Die Rechte liegen in der Regel bei den Herausgebern beziehungsweise den externen Rechteinhabern. Das Veröffentlichen von Bildern in Print- und Online-Publikationen sowie auf Social Media-Kanälen oder Webseiten ist nur mit vorheriger Genehmigung der Rechteinhaber erlaubt. [Mehr erfahren](#)

Conditions d'utilisation

L'ETH Library est le fournisseur des revues numérisées. Elle ne détient aucun droit d'auteur sur les revues et n'est pas responsable de leur contenu. En règle générale, les droits sont détenus par les éditeurs ou les détenteurs de droits externes. La reproduction d'images dans des publications imprimées ou en ligne ainsi que sur des canaux de médias sociaux ou des sites web n'est autorisée qu'avec l'accord préalable des détenteurs des droits. [En savoir plus](#)

Terms of use

The ETH Library is the provider of the digitised journals. It does not own any copyrights to the journals and is not responsible for their content. The rights usually lie with the publishers or the external rights holders. Publishing images in print and online publications, as well as on social media channels or websites, is only permitted with the prior consent of the rights holders. [Find out more](#)

Download PDF: 25.08.2025

ETH-Bibliothek Zürich, E-Periodica, <https://www.e-periodica.ch>

ASSOCIATION INTERNATIONALE DES PONTS ET CHARPENTES
INTERNATIONALE VEREINIGUNG FÜR BRÜCKENBAU UND HOCHBAU
INTERNATIONAL ASSOCIATION FOR BRIDGE AND STRUCTURAL
ENGINEERING

MÉMOIRES ABHANDLUNGEN PUBLICATIONS

35-I

1975

PUBLIÉS PAR LE SECRÉTARIAT GÉNÉRAL À ZÜRICH
HERAUSGEGEBEN VOM GENERALSEKRETARIAT IN ZÜRICH
PUBLISHED BY THE GENERAL SECRETARIAT IN ZÜRICH

Editeur - Verleger - Publisher

*Association Internationale des Ponts et Charpentes
Ecole Polytechnique Fédérale de Zurich*

*Internationale Vereinigung für Brückenbau und Hochbau
Eidgenössische Technische Hochschule Zürich*

*International Association for Bridge and Structural Engineering
Swiss Federal Institute of Technology, Zurich*

Printed in Switzerland

ISBN 3 85748 004 1

Préface

Par les «Mémoires» qu'elle publie, l'AIPC s'honore d'offrir aux ingénieurs du monde entier, agissant dans des milieux divers au profit des structures, une tribune de valeur reconnue. Chaque contribution n'a pas la même valeur sur le plan pratique, mais toutes contribuent à améliorer l'état de la science et la connaissance du comportement des ouvrages. Je n'hésite pas à répéter ici le vœu émis de voir les auteurs apporter des conclusions pratiques afin que toute étude théorique, souvent difficile à comprendre pour le praticien de tous les jours, trouve son point d'accrochage dans la vie. Ces conclusions contribueraient à accroître l'intérêt pour nos «Mémoires» et par là augmenteraient leur audience.

Je remercie et félicite tous les auteurs pour l'intérêt témoigné et la qualité des travaux.

Zurich, avril 1975.

Le Président de l'AIPC:

Prof. MAURICE COSANDEY

Président de l'Ecole Polytechnique Fédérale de Lausanne

Les Secrétaires Généraux:

Dr. sc. techn. HANS VON GUNTEN

Professeur à l'Ecole Polytechnique
Fédérale de Zurich

Dr. sc. techn. PIERRE DUBAS

Professeur à l'Ecole Polytechnique
Fédérale de Zurich

JÖRG SCHNEIDER

Professeur à l'Ecole Polytechnique Fédérale de Zurich

Vorwort

Mit ihren «Abhandlungen» betrachtet es die IVBH als Ehrenpflicht, den in den verschiedensten Sparten der Baukunst tätigen Ingenieuren der ganzen Welt ein Forum von allseitig anerkanntem Niveau zu bieten. Nicht jeder Beitrag besitzt denselben Wert in praktischer Hinsicht, doch tragen alle Aufsätze dazu bei, den wissenschaftlichen Stand und unsere Kenntnisse über das Verhalten von Bauwerken zu vertiefen. Ich zögere nicht, meinen früher geäußerten Wunsch zu wiederholen, das heisst praktische Schlussfolgerungen zu ziehen. Dadurch soll jede theoretische, für den Praktiker des Alltags häufig schwer verständliche Untersuchung ihren Ansatzpunkt im Leben finden. Diese Schlussfolgerungen würden dazu beitragen, das Interesse an unseren «Abhandlungen» zu erhöhen und ihnen dadurch vermehrt Gehör zu verschaffen.

Ich beglückwünsche alle Autoren und danke ihnen für das bewiesene Interesse und für die Qualität ihrer Arbeiten.

Zürich, April 1975.

Der Präsident der IVBH:

Prof. MAURICE COSANDEY

Präsident der Eidgenössischen Technischen Hochschule Lausanne

Die Generalsekretäre:

Dr. sc. techn. HANS VON GUNTEN

Professor an der Eidgenössischen
Technischen Hochschule Zürich

Dr. sc. techn. PIERRE DUBAS

Professor an der Eidgenössischen
Technischen Hochschule Zürich

JÖRG SCHNEIDER

Professor an der Eidgenössischen Technischen Hochschule Zürich

Preface

By their “Publications” the IABSE consider it an honour to offer to the engineers all around the world and working in the most different branches of building, a tribune of recognized standard. Not each of the published papers has the same value on the practical field but they all contribute to improve the scientific standing and our knowledge on the behaviour of structures. I don’t hesitate to repeat hereby the formerly expressed desire adressed to the authors for drawing practical conclusions. Thereby any theoretical study often rather difficult understandable by the pratician should meet its point of application in realty. These conclusions would contribute to increase the interest on our “Publications” and to obtain sustained hearing.

I thank and congratulate the authors for their interest and for the quality of their work.

Zurich, April 1975.

The President of IABSE:

Prof. MAURICE COSANDEY

President of the Swiss Federal Institute of Technology, Lausanne

The General Secretaries:

Dr. sc. techn. HANS VON GUNTEN

Professor at the Swiss Federal Institute
of Technology, Zurich

Dr. sc. techn. PIERRE DUBAS

Professor at the Swiss Federal Institute
of Technology, Zurich

JÖRG SCHNEIDER

Professor at the Swiss Federal Institute of Technology, Zurich

Leere Seite
Blank page
Page vide

Table des matières - Inhaltsverzeichnis - Table of Contents

P. ALBRECHT, J.W. FISHER	English	1
Analyse technique de l'accroissement de fissures aux raidisseurs transversaux Technische Berechnung des Anwachsens von Rissen an Querversteifungen An Engineering Analysis of Crack Growth at Transverse Stiffeners		
W.F. CHEN, M.T. SHORAKA	English	23
Méthode tangente de raidissement pour la flexion biaxiale de colonnes en béton armé Tangent Steifigkeitsmethode zur biaxialen Biegung von Stahlbetonstützen Tangent Stiffness Method for Biaxial Bending of Reinforced Concrete Columns		
D.L. DEAN, R.R. AVENT	English	45
Analyse de tabliers métalliques renforcés par entretoises longitudinales et transversales Berechnung von Brückenfahrbahnen aus Metallplatten mit Längs- und Querverstrebungen Analysis of Metal Plate-Stringer-Diaphragm Bridge Decks		
A. HRENNIKOFF, K.M. AGRAWAL	English	65
Eléments en forme trapézoïdale chargés dans leur plan In ihrer Ebene belastete trapezoidale Stabelemente Trapezoidal Bar Cells in Plane Stress		
R.P. JOHNSON, J.J. CLIMENHAGA	English	89
Résistance à la fatigue de plaques composites en béton armé pour tabliers de ponts Ermüdungsfestigkeit von Stahlbeton-Verbundplatten für Brückenfahrbahnen Fatigue Strength of Form-Reinforced Composite Slabs for Bridge Decks		
A. KHOUDAY, J. PROULX	Français	103
Réaction dynamique des structures soumises aux charges mobiles Dynamisches Verhalten durch bewegliche Lasten beanspruchter Bauwerke Dynamic Response of Structures to Moving Loads		
S. KLIMINSKI	Français	115
Structures en poutres-caissons reliées par des dalles Kastenträger-Brücken mit untereinander verbundenen Platten Structures of Box Girders Joint Together by Slabs		

VIII

T. VAN LANGENDONCK	English	149
--------------------------	---------	-----

Charges critiques de constructions en cadres
 Kritische Lasten von Rahmentragwerken
 Critical Loads of Building Frames

A.S. MAWENYA	English	159
--------------------	---------	-----

Analyse de plaques minces, épaisses et sandwich par la méthode des bandes finies
 Berechnung dünner, dicker und Sandwichplatten mittels der finiten Streifenmethode
 The Analysis of Thin, Thick and Sandwich Plates by the Finite Strip Method

A.T. RACTLIFFE	English	169
----------------------	---------	-----

Une analyse hybride des lignes de rupture moyennant la méthode des éléments finis
 Eine hybride Bruchlinien-Analyse mittels der finiten Elementenmethode
 Hybrid Yield-Line Finite Element Analysis

K.C. ROCKEY, H.R. EVANS	English	185
-------------------------------	---------	-----

La méthode de section nodale pour l'analyse de poutres en caisson
 Die nodale Querschnittsmethode zur Berechnung von Kastenträgern
 The Nodal Section Method for the Analysis of Box Girders

A.C. WALKER, N.W. MURRAY	English	217
--------------------------------	---------	-----

Un mécanisme de rupture plastique pour plaques comprimées
 Ein plastischer Bruchmechanismus für gedrückte Platten
 A Plastic Collapse Mechanism for Compressed Plates

V.A. YERLICI	English	237
--------------------	---------	-----

Epaisseur minimale de réservoirs en béton armé de section circulaire
 Mindestwandstärke kreisförmiger Stahlbetontanks
 Minimum Wall Thickness of Circular Concrete Tanks

ERRATUM		247
---------------	--	-----

An Engineering Analysis of Crack Growth at Transverse Stiffeners

Une analyse technique de l'accroissement de fissures aux raidisseurs transversaux

Eine technische Berechnung der Ausbreitung von Rissen an Querversteifungen

P. ALBRECHT

Asst. Prof. of Civil Engr., University of Maryland;
former Research Asst., Fritz Engineering Lab.,
Lehigh University

J.W. FISHER

Prof. of Civil Engr., Assoc. Director, Fritz
Engr. Laboratory, Lehigh University, Bethlehem,
Pa.

Introduction

In this paper the fatigue behavior of welded beams and girders with transverse stiffeners is described.

Further, it is shown that for purposes of design, the constant amplitude fatigue life of stiffener details often encountered in highway bridge construction can be predicted using fracture mechanics concepts of crack propagation. To accomplish this, the stress intensity factor is estimated and the analysis is performed assuming that the portion of the life expended during initiation is negligible when compared with the number of cycles required to propagate the crack. Such an assumption appears to be justified for details having a high notch effect, and which are susceptible to initial flaws built-in during the fabrication process.

In general, initiation and growth of fatigue cracks are most likely to occur in areas subjected to a high tensile stress range and where initial flaws exist. The higher the stress range and the larger the initial flaw, the faster fatigue cracks will propagate. Both conditions exist along the toe of the fillet welds connecting the stiffeners to the web or flanges.

The initial flaw condition is given by discontinuities at the weld toe, such as weld cracking, slag inclusions and undercut [3, 5]. Imperfections of this nature are common to all welding processes. They cannot be avoided, although their sizes and frequency of occurrence may be controlled by good welding techniques.

Secondly, the critical tensile stress range which drives the crack is brought about by a combination of two effects. One is the geometrical stress concentration produced by the weld geometry and the stiffener which magnify the stresses due to the applied loads. Further, a residual tensile stress field is generated by the welding process. The net effect of having residual tensile stresses and the stresses due to the applied load is a tension-tension stress range at the weld toe, even in cases of nominal stress reversal. In fact, fatigue cracks were also observed at weld toes sub-

jected to a nominal compression-compression stress cycle. These cracks, however, arrested as they outgrew the residual tension field and did not impair the load carrying capability of the beam.

Experimental Investigation

The experimental investigation consisted of testing thirty 14-inch (168 mm) deep beams and twenty-two 38-inch (965 mm) deep girders. All specimens had stiffeners welded to the web, as well as stiffeners welded to the web and flanges. The stiffeners were located in a region of moment gradient as shown in Fig. 1.

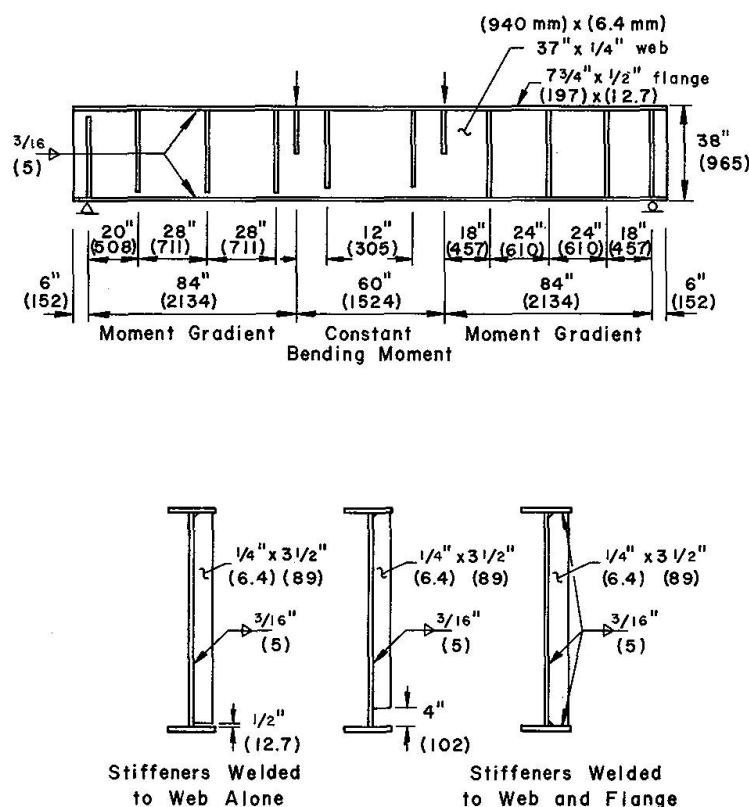


Fig. 1. Details of Test Girders.

To permit the statistical evaluation of the significance of several stress and geometrical variables, the specimens were arranged into factorial experiments. The experimental data including an analysis of the test variables were presented in Refs. 1 and 2. It was found that the bending stress range is the dominant variable which defines the fatigue strength of full depth transverse stiffener details. Other variables such as maximum stress, specimen size, yield strength, and type of stiffener (welded to the web alone or to the web and flanges), are not significant for purposes of design of stiffened bridge members.

Crack Initiation and Growth

Fatigue cracks at the stiffeners, whether welded to the web alone or welded to the web and flanges, had one major feature in common: the cracks initiated and grew from surface flaws at the toe of non-load carrying fillet welds. Also, the plane of the crack remained at all stages perpendicular to the direction of the principal stress.

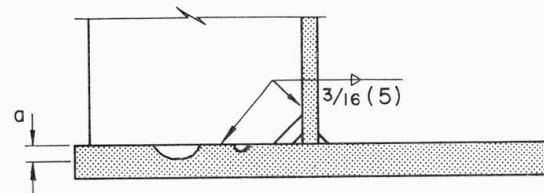
Stiffeners Welded to the Web and Flanges

A typical fatigue crack causing failure at a stiffener welded to the web and the flanges is shown in Fig. 2. Crack growth was characterized by the two stages illustrated in Fig. 3. During the first stage, one or more cracks initiated along the toe of the fillet weld connecting the stiffener to the tension flange, and propagated in a semi-elliptical shape as shown in Fig. 4. When the small cracks grew larger they joined and eventually assumed the shape of a larger semi-elliptical crack as illustrated in Fig. 5. By the time the leading edge reached the extreme fiber of the tension flange, the crack width had spread over most of the weld length. After breaking through the extreme fiber, it grew in the second stage as a through crack across the tension flange and up into the web. Visual observation of several specimens indicated that approximately 96% of the number of cycles to failure

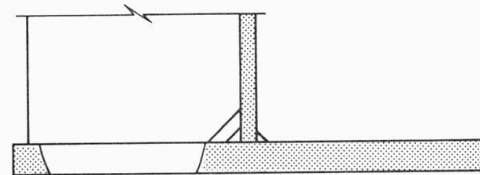


Fig. 2. Typical Failure at Stiffeners Welded to Web and Flange.

Stage 1: Part - Through Crack



Stage 2: Through Crack



Specimen SGB 312

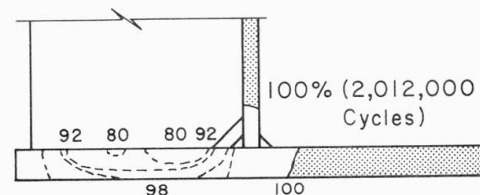


Fig. 3. Stages of Crack Growth at Stiffener-to-Flange Connection.



Fig. 4. 0.028-inch Deep Crack at the Toe of the Stiffener-to-Tension Flange Weld.

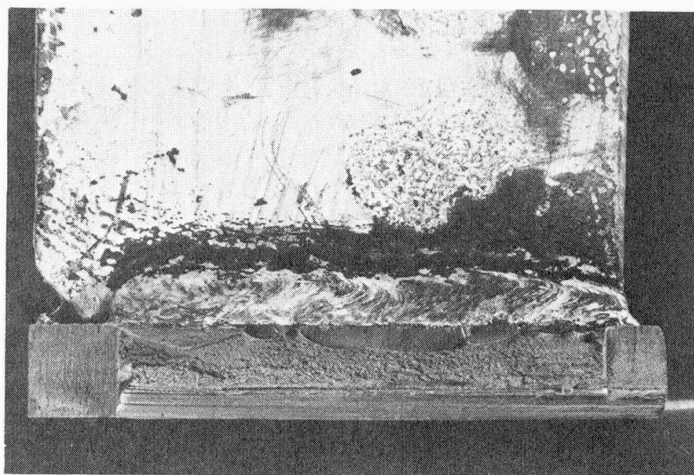


Fig. 5. Multiple Fatigue Crack Growth at the Toe of Stiffener-to-Tension Flange Weld.

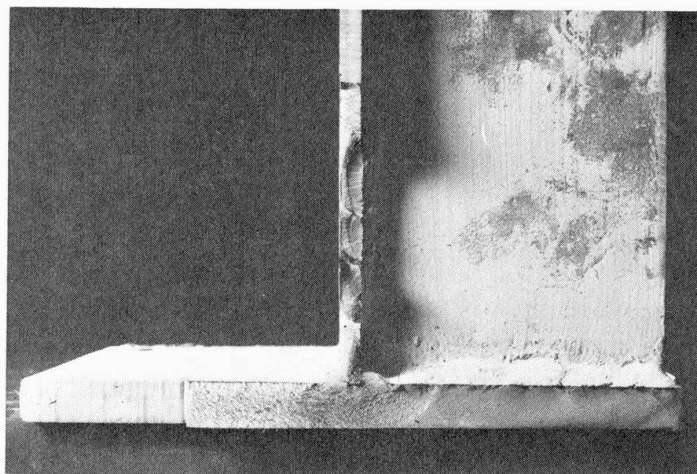


Fig. 6. Typical Fatigue Crack Surface at Failure.

were consumed growing the crack through the thickness of the flange. The remaining 4% of the life was spent in Stage 2 of growth. Figure 3 illustrates the extent of crack growth observed on the surface of the flange plate at different numbers of applied cycles. The contour and depth of the leading edge of the part-through at 80% and 92% of the final life are shown qualitatively.

Figure 6 shows a fatigue crack surface at failure. The crack is seen to have initiated at the stiffener-to-flange weld. As it eventually advanced up into the web, it joined with several semi-elliptical cracks growing from the toe of the stiffener-to-web weld.

Stiffeners Welded to the Web Alone

The cracks causing failure at the stiffeners welded to the web alone initiated at one or more points along the toe of the stiffener-to-web weld. They propagated in a direction perpendicular to the principal tensile stress.

The overall appearance of the crack seemed to indicate two growth patterns, one diagonally off the end of the stiffener-to-web weld, the other following the weld toe before branching off diagonally into the web as illustrated in Fig. 7. The fatigue crack surfaces were exposed by saw cutting most of the net section and prying the remaining ligaments open. This fractographic examination revealed the reasons for the two observed patterns. Cracks initiating at the end of the weld (at one point), grew in all stages along a plane perpendicular to the changing direction of the principal stress as illustrated in Fig. 8. Cracks following the weld toe had multiple initiation points from which individual cracks grew in separate planes, each one perpendicular to the direction of the principal stress at that point. As the individual cracks overlapped they broke through and joined each other, forming a longer crack with an irregular contour along the weld toe as illustrated in Fig. 9b. This phenomena gave the appearance of a crack growing along the toe of the weld,



Fig. 7. Typical Failure at Web Stiffeners.

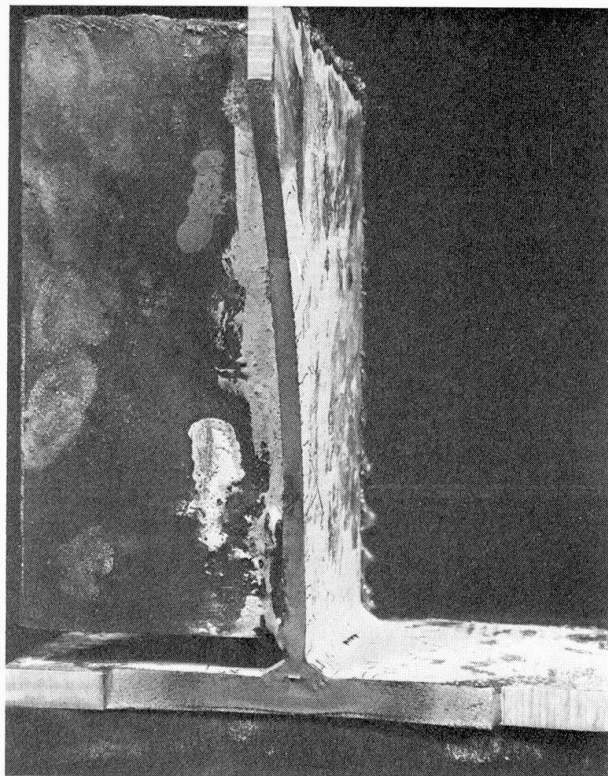


Fig. 8. Typical Fatigue Crack Surface at Web Stiffener at Failure.

before branching off diagonally. Once this pattern had developed it was sustained by the stress concentration effect of the weld which created a more severe path for propagation along the toe than in the web away from the weld toe.

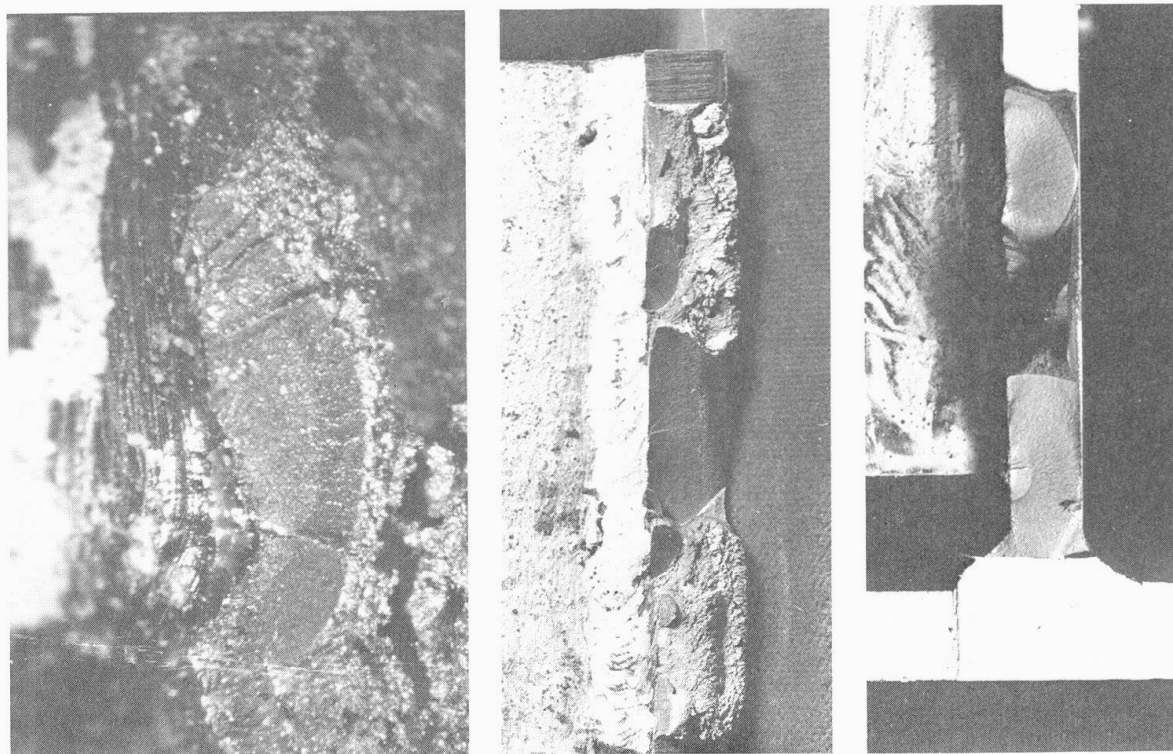
Typically, the crack advanced through the three stages of growth as depicted by Fig. 10. In the first stage, one or more semielliptical cracks were driven through the thickness of the web plate, as shown in Fig. 9. Each one retained the approximate shape of a semiellipse as long as it did not join and interact with adjacent cracks.

Once the crack front had penetrated the web plate, the crack changed into a two-ended through crack. This transition after web plate penetration into Stage 2 occurred within a short number of cycles. Figures 9c shows one part-through crack at the beginning of the transition and one at the end.

In the third stage, after the lower front of the two-ended crack had broken through the extreme fiber of the tension flange, it grew as a three-ended crack (see Figs. 8 and 10) across the flange and extended further up into the web. Eventually, the ever decreasing net section of the flange yielded, and the test was terminated before the flange fractured. No "brittle" fracture was observed in any of the specimens.

Of the total number of cycles to failure at web stiffeners, 80% were consumed growing the crack through the thickness of the web plate during Stage 1. The second and third stages amounted to 16% and 4% respectively as indicated schematically in Fig. 10.

Figure 9 shows small ellipses inside the fatigue crack surface. They correspond to the crack size at the time the beam had failed at stiffeners welded to the web and flange and reflect the oxidation of the crack area.



(a) 0.035-inch Deep Crack.

(b) Multiple Fatigue Cracks.

(c) Multiple Fatigue Cracks through the Web.

Fig. 9. Fatigue Crack Growth at the Toe of Stiffener-to-Web Weld.

Mathematical Model for Crack Propagation

The fatigue life of a detail is defined by the sum of the number of cycles required for crack initiation and the number of cycles required for crack propagation to failure. Available information indicates that the fatigue life prediction of welded details can be based on crack propagation alone [1, 4, 5]. In this study fatigue life was estimated by considering crack propagation alone and any initiation phase was ignored.

SIGNES et al. [3] showed that fatigue cracks initiate at the toes of fillet welds from mechanical defects constituting a sharp notch with a typical root radius of 0.0001 inch (0.0025 mm) or less when the applied stress was perpendicular to the weld toe. These crack-like defects exist in welds made with all conventional welding processes. They are equivalent to an initial crack, which propagates under repeated loading. WATKINSON et al. [5] reported directly comparable fatigue lives for welded joints in an as-welded condition and welded joints with an additional machined

notch with a depth of 0.005 inch (0.127 mm) and 0.0005 inch (0.013 mm) root radius. Since the added notch did not lead to a further reduction in fatigue strength, it was assumed that the sharp weld defects constituted an equally severe initial crack condition and that fatigue life prediction of welded joints can be based on crack propagation alone.

Stage 1: Part-Through Crack in Web

Stage 2: Two-Ended Through Crack in Web

Stage 3: Three-Ended Crack

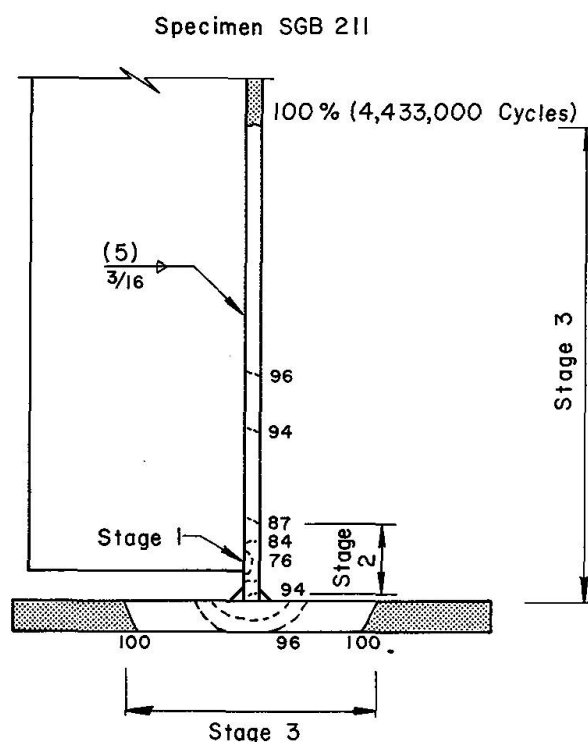


Fig. 10. Stages of Crack Growth at Web Stiffeners.

Analysis of Crack Propagation

The fracture mechanics approach to crack propagation appears to be the most rational method currently available for predicting the fatigue life. It has been used to provide an explanation of the fatigue crack growth of a number of welded steel details.

The empirical differential equation of crack growth proposed by Paris [6] has the form:

$$\frac{da}{dN} = C (\Delta K)^n \quad (1)$$

and relates measured rates of crack growth (da/dN) to ΔK , the range of the stress-intensity factor K proposed by IRWIN [7]. C and n are constants. Equation 1 can be integrated to obtain the number of cycles N required to propagate a crack

from an initial size a_i to a final size a_f . For stress ranges of constant amplitude and assuming that C and n remain constant within the span of ΔK values which are of major importance, the integration yields:

$$N = \frac{1}{C} \int_{a_i}^{a_f} \frac{1}{(\Delta K)^n} da = \frac{\sigma_r^{-n}}{C} \int_{a_i}^{a_f} \left(\frac{da}{(\Delta K/\sigma_r)^n} \right) \quad (2)$$

As was noted in Ref. 8, Eq. 2 suggests that the relationship between the Life N and the applied stress range σ_r is exponential and can be expressed as:

$$N = G \sigma_r^{-n} \quad (3)$$

where

$$G = \frac{1}{C} \int_{a_i}^{a_f} \frac{da}{(\Delta K/\sigma_r)^n} \quad (4)$$

Since ΔK , the range of the stress intensity factor, is directly proportional to the applied stress range σ_r , G is independent of σ_r . The results of an extensive statistical analysis of fatigue data collected from over 500 full size beam specimens [1] [8] bears out the validity of the above conclusions for purposes of fatigue design of structural details built from steels commonly used in highway bridge construction. Indeed, of all models investigated, the linear regression equation

$$\log N = B_1 - B_2 \log \sigma_r \quad (5)$$

provided the best fit to the experimental data. From Eqs. 3 and 5 it is also apparent that B_2 and n are the same.

The solution of Eq. 2 requires a knowledge of the constants C and n , and an adequate approximation for the stress intensity factor for the crack at the detail being examined.

Crack Growth Rates

The coefficient C and the exponent n in Eq. 1 are constants which define the rate of crack growth for a given value of ΔK . They are determined empirically from tests of precracked "fracture mechanics" specimens for which an analytical expression for the stress intensity factor, ΔK , is known. From measurements of crack size, the increases in size corresponding to increments of cyclic loading are related to the range of the stress-intensity factor, ΔK .

Several investigators have reported growth rates for structural steels [9, 10, 11, 12]. BARSOM [9] found that the growth rates in four ferrite-pearlite steels fell into a band.

He suggested that the slope of the logarithmically transformed data decreased slightly as the yield strength increased. The slope varied from 3.3 to 2.8 for steels with yield strengths between 36 (25) and 69 ksi (48 kN/mm²). Data have also been reported by CROOKER and LANGE [11]. A relatively large scatterband was indicated for carbon and low-alloy determined the growth rates for four different weld metals. Three of the weld metals had yield strengths equal to about 67 ksi (46 kN/mm²) and the fourth to 90 ksi (62 kN/mm²).

Most of the test data on crack growth is for ΔK values above 10 ksi $\sqrt{\text{in.}}$ (11 MPa $\sqrt{\text{m.}}$). Only a limited amount of data is available below that level. PARIS [10] reported on very slow growth and suggested a threshold value at $\Delta K = 5$ ksi $\sqrt{\text{in.}}$ (5.5 MPa $\sqrt{\text{m.}}$).

From a study of experimental results published in the literature, HARRISON [13] concluded that fatigue cracks will not propagate in mild steel if $\Delta K < 3.3$ ksi $\sqrt{\text{in.}}$ (3.6 MPa $\sqrt{\text{m.}}$). The level of the threshold was observed to be also a function of the mean stress [10], the threshold being lower the higher the mean stress. Hence, a low threshold value can be expected for fatigue crack growth from weld toes where the applied stresses are magnified by the discontinuities of the weld geometry and where high residual tensile stresses are known to exist.

The coefficients of the crack growth equation were also established by HIRT and FISHER [14] using the equivalence between the crack growth equation and the stress range-cyclic life relationship for plain welded beams. A penny-shaped crack was assumed to describe the disc-like cracks that grew in the flange-to-web weldment of beams. This yielded values of $n \simeq 3$ and $C \simeq 2 \times 10^{-10}$ where C has the units implied by Eq. 1 assuming ΔK in units of ksi $\sqrt{\text{in.}}$ and da/dN in units of inches. ($C \cong 3.8 \times 10^{-9}$ when ΔK in MPa $\sqrt{\text{m.}}$ and da/dN in millimeters).

In this study it was assumed that C and n remained constant for all values of ΔK . The relationship found by HIRT and FISHER was rounded and used. The crack growth rate was taken as

$$\frac{da}{dN} = 2 \times 10^{-10} \Delta K^3 \quad (6)$$

for all details. The relationship developed from beam test is in good agreement with the crack growth data from fracture mechanics specimens. The beam tests had indicated that crack initiation took place at values of ΔK between 3 (3.3) and 5 ksi $\sqrt{\text{in.}}$ (5.5 MPa $\sqrt{\text{m.}}$). This was at or below the threshold level suggested by PARIS [10].

Stress-Intensity Factors for Part-Through Cracks at Fillet Weld Toes

With an appropriate expression for the stress-intensity factor K at the toe of a non-load carrying fillet weld, the propagation of a crack through the thickness of the web or flange can be predicted. As noted in the discussion of crack growth at stiffener details, 80% of the total number of cycles to failure for web stiffeners were consumed by crack propagation of a flaw through the thickness of the web and 96% for stiffeners welded to the flange. Hence, an analysis of this stage of fatigue crack growth represents essentially a study of the fatigue life of beams with stiffeners.

It was observed that cracks at both types of stiffeners initiated from discontinuities at the weld toe and propagated as a semi-elliptical crack through the thickness of the web or the flange plate during most of the specimen's life.

The average change in shape of crack size was found empirically. After the beam had failed at the critical stiffener the planes through the weld toes of the other less critical stiffeners were exposed. Subsequent examination of the surfaces, both visually and with a $50\times$ microscope, revealed the presence of part-through cracks at specific stages of growth in a large number of specimens [2]. The measured crack sizes are plotted in Fig. 11, together with the exponential relationship.

$$b = 1.088a^{0.946} \quad (7)$$

describing the average change in size, where b and a are the two semi-axes of the semi-elliptical crack. This variation of b with a was considered in the analysis of fatigue crack propagation. Equation 7 is seen to approach the circular crack ($a/b = 1$) with increasing crack size.

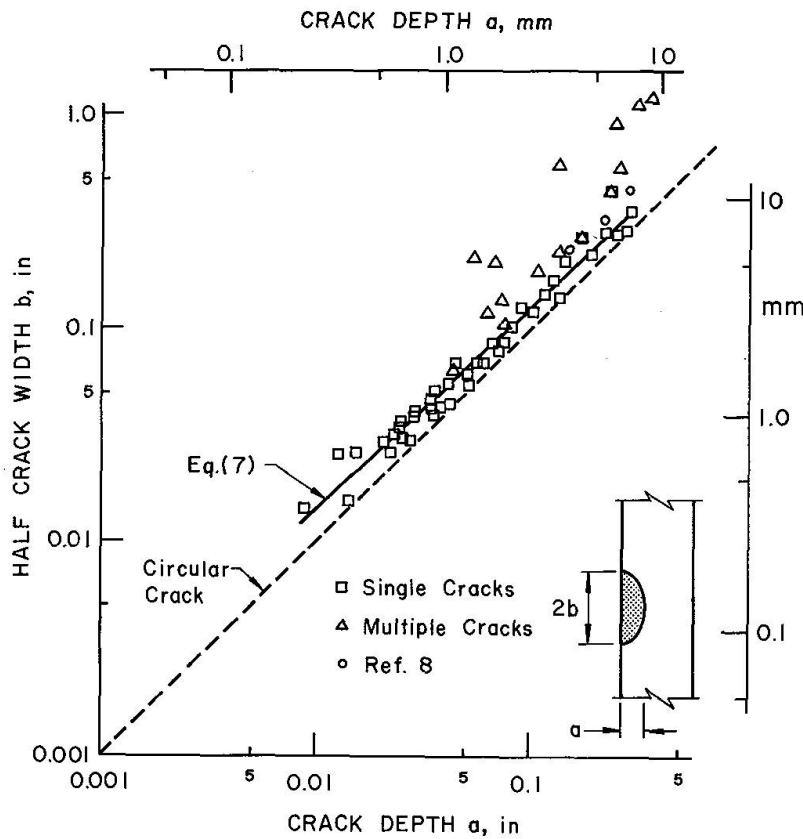


Fig. 11. Size of Part-Through Cracks at Fillet Weld Toes.

Part-through cracks which initiated at more than one point are also plotted in Fig. 11 as open triangles. They were not included in the regression of b on a . Three part-through cracks observed at the end of longitudinally welded cover plates [8] are shown as circles and fall near the mean regression line.

The stress-intensity factor for a part-through crack developed by IRWIN [16] can be used with the secant correction [17] for a free surface representing the side of

the plate opposite from the crack opening to describe the condition illustrated in Fig. 12a. This results in

$$K = \frac{1 + 0.12(1 - a/b)}{\Phi_o} \sigma \sqrt{\pi a} \sqrt{\sec \frac{\pi a}{2t}} \quad (8)$$

where Φ_o is an elliptical integral which depends on the minor to major axis ratio, a/b , of the crack.

Equation 8 cannot be directly applied to part-through cracks at the toe of non-load carrying fillet welds connecting stiffeners to the flange and the web, unless the stress concentration effect of the weld is considered. If the part-through crack is removed from the uniformly stressed flat plate shown in Fig. 12a, then the stress field, σ , will remain constant throughout the plate. This is not the case for the detail shown in Fig. 12b which represents a plate strip of either the web or the flange with a portion of the stiffener welded on.

In the absence of a crack, the weld geometry acts as a stress raiser, magnifying the nominal stress at the weld toe by the stress concentration factor K_T . The stress concentration effect decays rapidly with increasing distance from the weld toe.

In order to apply the stress intensity factor given by Eq. 8 to the detail shown in Fig. 12b requires an additional geometry correction function accounting for the stress magnification effect of the weld. FRANK used a finite element and compliance analysis to evaluate the stress-intensity factor for tunnel-shaped cracks at

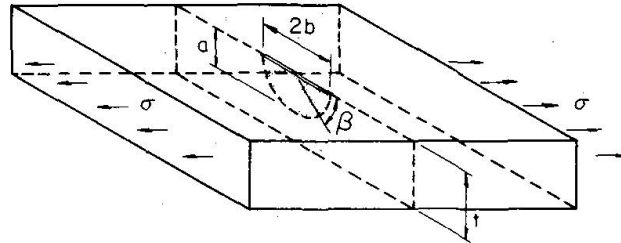


Fig. 12a. Part-through Crack in a Flat Plate.

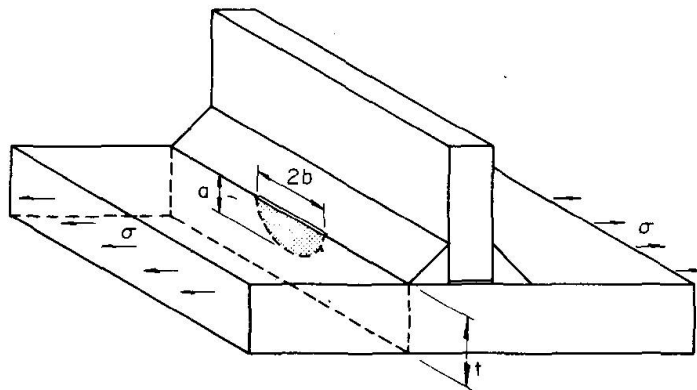


Fig. 12b. Part-through Crack at the Toe of a Non-load Carrying Fillet Weld.

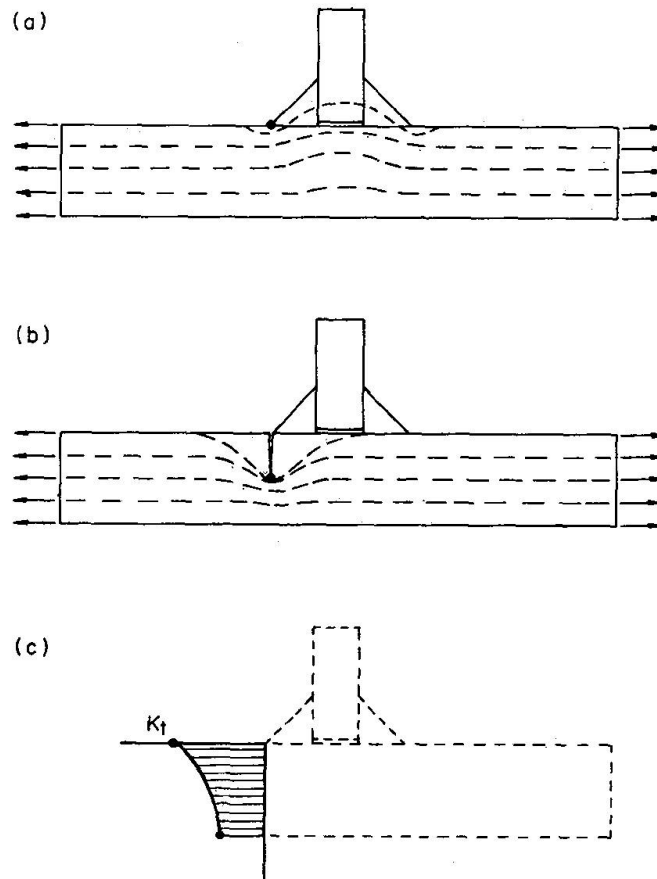


Fig. 13. Correction Function for the Applied Stress Field.

the weld toe of cruciform joints [4]. On the basis of this analysis he developed a correction function for the weld geometry which was equal to the stress concentration factor, K_T for vanishing crack size and which decreased as the crack propagates into the plate (see Eq. 9). Others have assumed a constant value of K_T for the correction function of a similar detail but did not make an allowance for the decay with increasing distance from the weld [19].

The idea of utilizing the theoretical stress concentration factor, K_T , to arrive at an estimate of the stress intensity factor, K , is not a new one. It is well known, for example, that K for a small crack emanating from a much larger circular hole in a sheet [18] is approximately equal to the value of K for a free surface crack multiplied by the stress concentration factor for the circular hole. As the crack deepens it runs out of the area effected by the stress concentration, and the K calculation can be based upon a crack length larger than the actual crack size only by the diameter of the hole.

A similar approach was taken in this study. The solution suggested in Ref. 4 is the only known approximation for the stress-intensity factor K at fillet weld toes. There are obvious differences in the stiffener details evaluated in this study and the welded cruciforms examined by Frank. In the cruciform joint a half tunnel crack was assumed at the weld toe together with a plate stress condition. Symmetry was also considered with plates attached to both surfaces. At the stiffener

details semi-elliptical cracks were observed. In addition, the stiffener was only attached to one side of the web or flange plate.

Two solutions were used to describe the stress-intensity factor at the fillet weld toes on the web or flange. One modified the solution obtained for a tunnel crack to reflect the semi-elliptical surface cracks. The decay polynomial obtained by Frank was assumed to describe the weld geometry effect and its decay with increasing crack depth. This yielded

$$K_T\left(\frac{a}{t}\right) = K_T \left[1 - 3.215 \frac{a}{t} + 7.897 \left(\frac{a}{t}\right)^2 - 9.288 \left(\frac{a}{t}\right)^3 + 4.086 \left(\frac{a}{t}\right)^4 \right] \quad (9)$$

A second decay characteristic was also examined [2]. This assumed the geometry correction function to decrease parabolically from a maximum of K_T with an infinitesimal crack, to no effect at a depth equal to the weld size. The relationship was assumed and had the following form:

for $0 < a \leq w$:

$$K_T\left(\frac{a}{t}\right) = K_T - 2(K_T - 1) \frac{a}{w} + (K_T - 1) \left(\frac{a}{w}\right)^2 \quad (10)$$

and for $a \geq w$: $K_T\left(\frac{a}{t}\right) = 1.0$

where w is the weld size.

The stress intensity factor for part-through cracks at fillet weld toes is then given by:

$$K = \frac{1 + 0.12 \left(1 - \frac{a}{b}\right)}{\Phi_o} K_T\left(\frac{a}{t}\right) \sigma \sqrt{\pi a} \sqrt{\sec \frac{\pi a}{2t}} \quad (11)$$

where $K_T\left(\frac{a}{t}\right)$ is a magnification factor which accounts for the stress raising effect of the fillet weld; a is the crack depth, and t is the thickness of the plate in which the crack is growing.

Equation 9 describes the correction function for the weld geometry in terms of the ratio a/t ; it is independent of the weld size, w except for its effect on K_T . The decay characteristic given by Eq. 10 is written in terms of the ratio a/w , crack size to weld size, in an attempt to better account for variation in geometries, such as may occur when stiffeners are connected to flanges by fillet welds where the difference between t and w is substantial.

Both decay characteristics are useful when evaluating crack propagation at welded structural details where crack growth occurs at the weld termination. Equation 9 and 10 are compared in Fig. 14 for a girder with a $\frac{1}{2}$ inch (12.7 mm) flange and a stiffener attached with $\frac{1}{4}$ inch (5 mm) fillet welds.

Equations 9 and 10 provide about the same estimate of stress concentration factor in the region of critical crack size. Equation 10 provides simplicity in estimating K and appears to be applicable to a wider range of plate thickness.

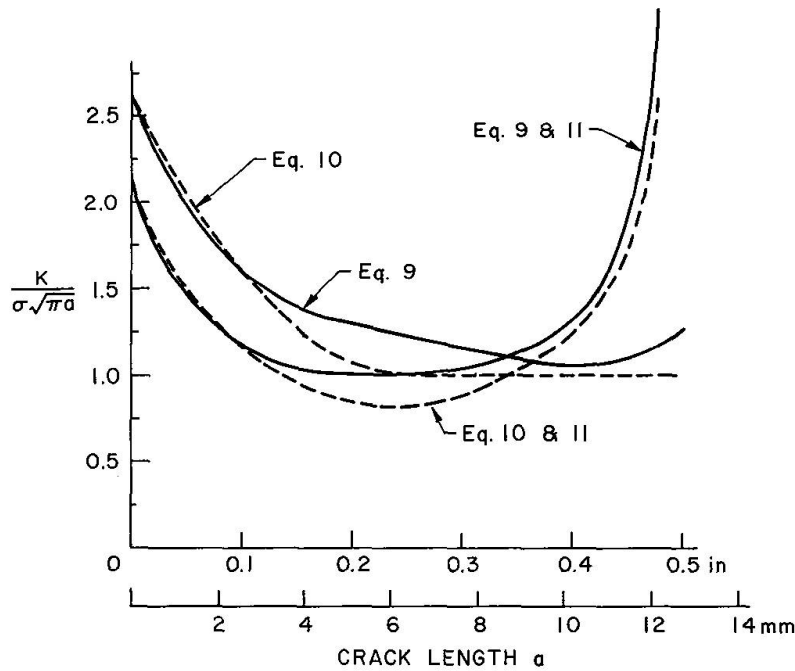


Fig. 14. Change in Stress Intensity Factor at Fillet Weld Toe with Crack Size.

Analysis of Crack Growth at Stiffeners

Equations 2, 6 and 11 were used to evaluate the crack propagation through the web and flange of the stiffener details. Since all cracks were observed to grow perpendicular to the principal stress, only Mode I crack growth was considered as there was no evidence of other modes of crack growth. Before carrying out the analysis, the theoretical stress concentration factor K_T at the fillet weld toe was determined using a finite element solution. The results are tabulated in Table 1. The weld and stiffener geometry were found to have only a local concentration effect on the stress field.

The nominal stress range at stiffeners welded to the web alone was taken as the principal stress range at the end of the stiffener-to-web weld. The nominal bending stress range at the stiffener-to-flange weld was used for stiffeners welded to the web and flange.

A family of curves depicting the relationship between initial crack sizes and fatigue life for the stress range levels of this study were constructed. These curves are plotted in Figs. 15, 16 and 17 for the two types of stiffeners. The final crack sizes correspond to the values of plate thickness listed in Table 1. The points on the curves correspond to the observed fatigue lives of beams with stiffeners which experienced crack propagation through the web or flange thickness at the weld toe. For stiffeners welded to the web alone this corresponded to about 80% of the total life. For stiffeners welded to flange and web the failure life was used.

Table 1. Data for Analysis of Propagation of Part-Through Cracks

Specimen	Plate Thickness in. (mm)	Stiffener Thickness in. (mm)	Weld Size in. (mm)	Stress Concentration Factor K_T	Stress Range at Detail			
					ksi (kN/mm ²)			
					in. (mm)	in. (mm)	in. (mm)	in. (mm)
<i>Stiffeners Welded to Web</i>								
Beam	9/32(7.1)	9/32(7.1)	1/4(6.4)	2.20	14.8(10.2)	19.8(13.7)	24.7(17.0)	29.7(20.5)
Girder	1/4(6.4)	1/4(6.4)	1/4(6.4)	2.12	16.1(11.1)	21.5(14.8)	26.9(18.6)	
<i>Stiffeners Welded to Flange</i>								
Beam	3/8(9.5)	9/32(7.1)	1/4(6.4)	2.42	14.4(9.4)	19.2(13.3)	23.9(16.5)	28.7(19.8)
Girder	1/2(12.7)	1/4(6.4)	1/4(6.4)	2.64	13.8(9.5)	18.4(12.7)	22.9(15.8)	

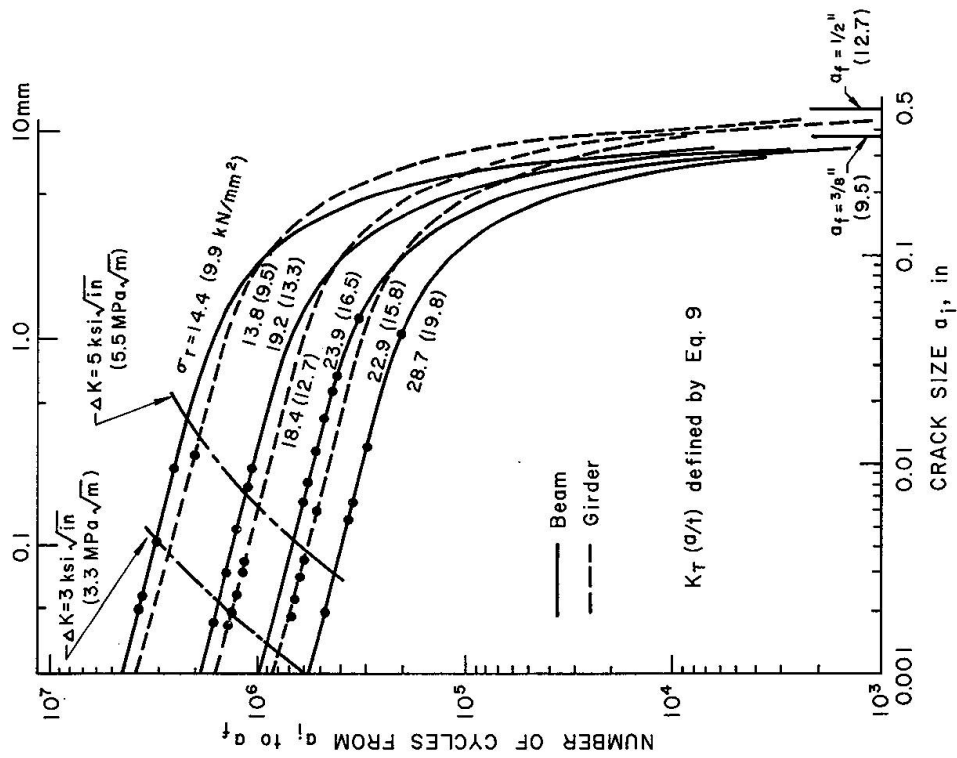


Fig. 15. Propagation of a Part-Through Crack at Stiffeners Attached to the Web Alone.

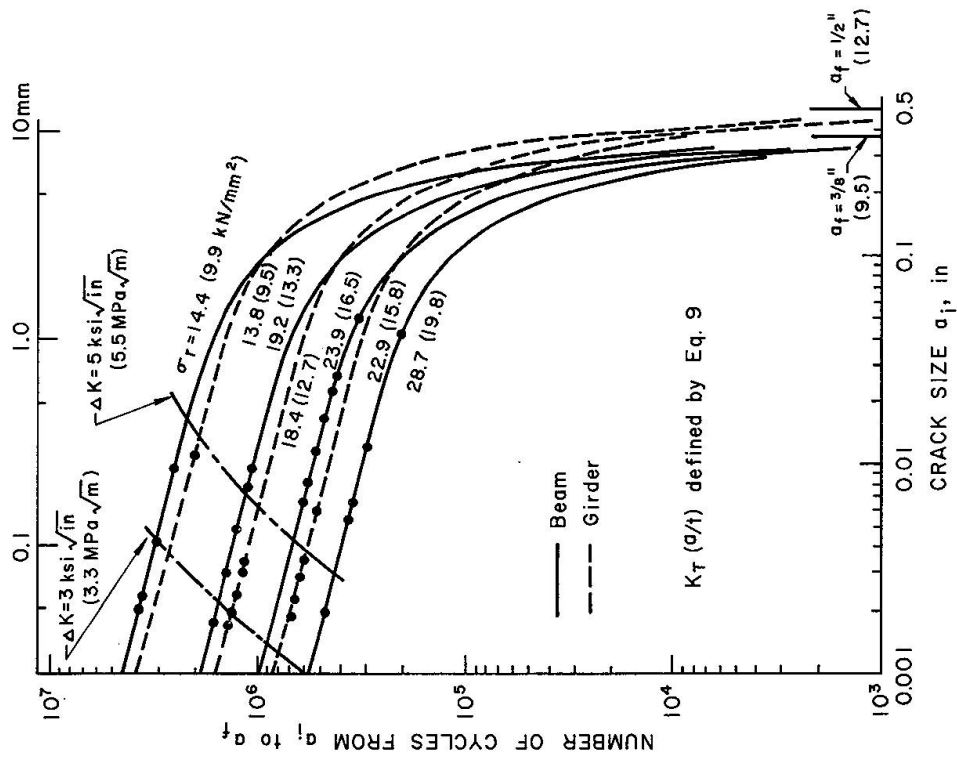


Fig. 16. Propagation of a Part-Through Crack at the Stiffener-to-Flange Connection Using Eq. 9.

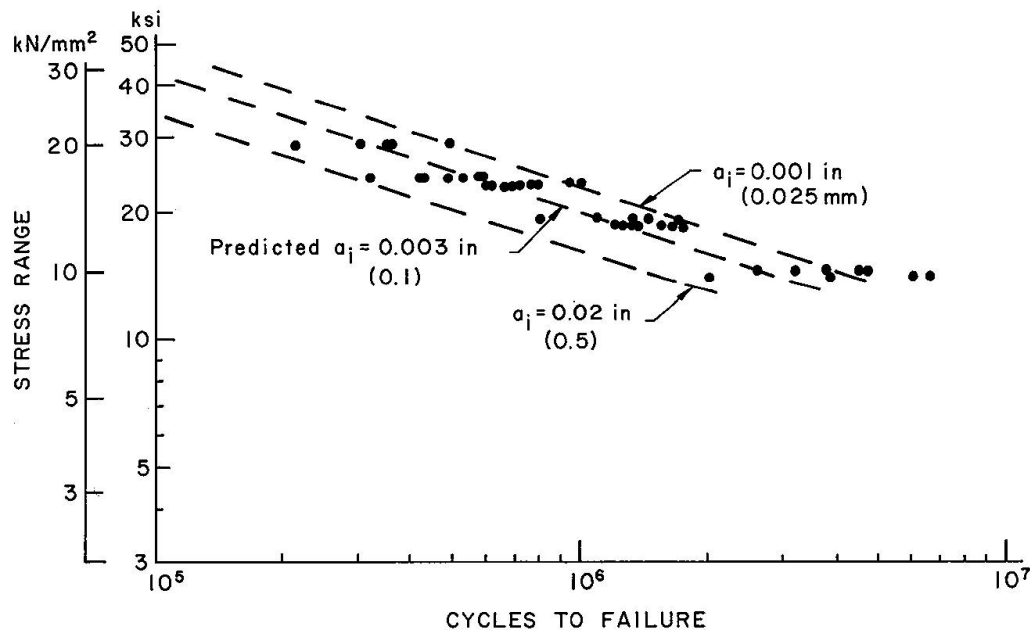


Fig. 18. Comparison of Predicted Fatigue Life with Test Data for Stiffeners Welded to Web and Flange.

data. Only test data at the 13.8 ksi (9.5 kN/mm²) stress range level exceeded the predicted life. As can be seen in Figs. 16 and 17, specimens with average or below average initial crack sizes may be at or below the fatigue crack growth threshold. The probability of this happening increases with a decreasing stress range.

The results obtained from the analysis indicate that the proposed mathematical model for propagation of a part-through crack at the weld toe of stiffeners is in good agreement with the observed fatigue behavior.

Conclusions and Application

Fracture mechanics was used to analyze the fatigue behavior of transverse stiffeners welded to the web alone or to the web and flanges. The analysis considered crack propagation of a crack through the thickness of the web and the flange. This showed that 80% of the total number of cycles to failure at web stiffeners and 96% at web-flange stiffeners were consumed during this stage of growth.

The main conclusions are:

1. The fatigue cracks initiated from weld discontinuities at the fillet weld toes. They retained the approximate shape of a semi-ellipse as they propagated through the plate thickness.
2. The stress-intensity factor for a part-through crack in a flat plate can be used in conjunction with a correction function accounting for the stress concentration effect of the weld geometry to describe the stress condition at the leading edge of the crack.

3. Integration of the differential equation of crack growth revealed that the mean fatigue life corresponded to an equivalent initial crack depth of about 0.003 in. (0.1 mm).
4. The scatter in the test data can be associated with the variation of the initial crack sizes.
5. At the lowest stress range, to which the test specimens were subjected, and an equivalent mean initial crack size $a_i = 0.003$ in. (0.1 mm), crack growth appeared to occur slightly below the threshold levels reported in the literature.
6. 98% of the number of cycles required to propagate the part-through crack across the plate thickness elapsed as the leading edge of the crack advanced to a depth of 0.75 t.

Application: Since most of the details fatigue life was consumed growing a part-through crack, the study emphasizes the need for properly designing a structure to assure adequate performance without premature failure. There is little likelihood of detecting part-through cracks before failure or in fabricating smaller discontinuities. The paper shows that design for a proper stress range level and adequately assessing the loading of structures are the most realistic and reliable means of assuring the desired service life.

The method also provides a means to evaluate the formation and propagation of cracks in other types of welded built-up structures.

Notation

a	crack size, minor half-axis for semi elliptical crack.
a_f	final crack size.
a_i	initial crack size.
B_1, B_2	regression coefficients.
b	major half-axis for semi-elliptical crack.
C	coefficient in crack growth equation.
da/dN	rate of crack growth, inch/cycle.
G	constant in regression equation ($= 10^{B_1}$).
K	stress-intensity factor.
K_T	theoretical stress concentration factor.
N	number of applied stress cycles.
n	exponent in crack growth equation.
t	plate thickness.
Φ_o	complete elliptical integral of the second kind.
ΔK	stress-intensity factor range.
σ	stress.
σ_r	stress range.

Acknowledgments

The research reported herein was performed under the National Cooperative Highway Research Project 12-7 at Fritz Engineering Laboratory, Department of Civil Engineering, Lehigh University, Bethlehem, Pennsylvania.

The opinions and findings expressed or implied in this paper are those of the writers. They are not necessarily those of the Highway Research Board, the National Academy of Science, the Bureau of Public Roads, the American Association of State Highway Officials, nor of the individual states participating in the National Cooperative Highway Research Program.

References

1. FISHER, J.W., ALBRECHT, P., YEN, B.T., KLINGERMAN, D.J., and MCNAMEE, B.M.: Effect of Weldments on the Fatigue Strength of Steel Beams with Transverse Stiffeners and Attachments. NCHRP Report, No. 147, Highway Research Board, National Academy of Sciences — National Research Council, Washington, D.C., 1974.
2. ALBRECHT, P.: Fatigue Strength of Welded Beams with Stiffeners. Ph. Dissertation, Lehigh University, Bethlehem, Pennsylvania, July 1972.
3. SIGNES, E.G., BAKER, R.G., HARRISON, J.D., and BURDEKIN, F.M.: Factors Affecting the Fatigue Strength of Welded High-Strength Steels. *British Welding Journal*, February 1967.
4. FRANK, K.H.: The Fatigue Strength of Fillet Welded Connections. Ph. D. Dissertation, Lehigh University, Bethlehem, Pennsylvania, 1971.
5. WATKINSON, F., BODGER, P.H., and HARRISON, J.D.: The Fatigue Strength of Welded Joints in High-Strength Steels and Methods for its Improvement. *Proceedings, Fatigue of Welded Structures Conference, the Welding Institute, Brighton, England, July 1970.*
6. PARIS, P.D., GOMEZ, M.P., and ANDERSON, W.E.: A Rational Analytical Theory of Fatigue. *The Trend in Engineering*, University of Washington, Vol. 13, No. 1, January 1961.
7. IRWIN, G.R.: Analysis of Stresses and Strains Near the End of a Crack Traversing a Plate. *Transactions, ASME, Series E*, Vol. 24, No. 3, September 1957.
8. FISHER, J.W., FRANK, K.H., HIRT, M.A., and MCNAMEE, B.M.: Effect of Weldments on the Fatigue Strength of Steel Beams. NCHRP Report No. 102, Highway Research Board, National Academy of Sciences — National Research Council, Washington, D.C., 1970.
9. BARSOM, J.M.: Fatigue-Crack Propagation in Steel of Various Yield Strengths, U.S. Steel Corp., Applied Research Laboratory, Monroeville, Pennsylvania, 1971.
10. PARIS, P.C.: Testing for Very Slow Growth of Fatigue Cracks. *Closed Loop*, MTS System Corp., Vol. 2, No. 5, 1970.
11. CROOKER, T.W., and LANGE, E.A.: How Yield Strength and Fracture Toughness Considerations can Influence Fatigue Design Procedures for Structural Steel. *Welding Research Supplement*, Vol. 49, No. 10, October 1970.
12. MADDOX, S.J.: Fatigue Crack Propagation in Weld Metal and Heat Affected Zone Material. *Members' Report No. E/29/69*, The Welding Institute, England, December 1969.
13. HARRISON, J.D.: An Analysis of Data of Non-Propagating Fatigue Cracks on a Fracture Mechanics Basis, *British Welding Journal*, Vol. 2, No. 3, March 1970.
14. HIRT, M.A., and FISHER, J.W.: Fatigue Crack Growth in Welded Beams. To be published in the *Journal of Engineering Fracture Mechanics*.
15. FRANK, K.H., and FISHER, J.W.: The Fatigue Strength of Welded Coverplated Beams. Fritz Engineering Laboratory Report No. 334.1, Lehigh University, Bethlehem, Pennsylvania, March 1969.
16. IRWIN, G.R.: Crack Extension Force for a Part-Through Crack in a Plate. *Transactions, ASME, Series E*. Vol. 29, December 1962.

17. IRWIN, G.R., LIEBOWITZ, H., and PARIS, P.D.: A Mystery of Fracture Mechanics. Engineering Fracture Mechanics, Vol. 1, 1968.
18. PARIS, P.D., and SIH, G.C.: Stress Analysis of Cracks. ASTM Special Technical Publication, No. 381, 1970.
19. MADDOX, S.J.: Calculating the Fatigue Strength of a Welded Joint Using Fracture Mechanics. Metal Construction, Vol. 2, No. 8, August 1970.

Summary

The fatigue behavior of welded beams with transverse stiffeners was determined experimentally by carrying out 52 tests on 350 mm and 970 mm deep beams. Initiation of fatigue cracks from defects at weld toes and their propagation through characteristic stages of growth to failure of the beams are described. Fracture mechanics concepts are applied to the stage of growth as a part-through crack during which most of the fatigue life is spent, in order to relate the observed life to the crack size.

Résumé

La résistance à la fatigue des poutrelles d'acier de 350 mm et 970 mm de hauteur pourvues de raidisseurs soudés a été déterminée à l'aide de 52 essais. L'article montre que les fissures commencent le long des soudures et se propagent en plusieurs stages caractéristiques. En utilisant les méthodes d'analyse de la mécanique de rupture, on établit la relation entre le nombre de charges appliquées et les dimensions de la fissure pendant le premier stage, qui est le plus important.

Zusammenfassung

Die Ermüdungsfestigkeit geschweisster Stahlbalken mit Querversteifungen wurde experimentell anhand von 52 Versuchen an Balken von 350×970 mm bestimmt. Der Artikel zeigt, dass die Risse entlang den Schweißstellen beginnen und sich auf mehrere charakteristische Stadien ausbreiten. Unter Verwertung der Berechnungsmethode über die Mechanik des Bruchvorganges wird die Beziehung zwischen der Zahl der angewandten Lasten und den Abmessungen des Risses während der ersten Phase, welche die wichtigste ist, aufgestellt.

Tangent Stiffness Method for Biaxial Bending of Reinforced Concrete Columns

Méthode tangente de raidissement pour la flexion biaxiale de colonnes en béton armé

Tangent Steifigkeitsmethode zur biaxialen Biegung von Stahlbetonstützen

W.F. CHEN

Assoc. Prof., Dept. of Civil Engrg., Lehigh
University, Bethlehem, Pa.

M.T. SHORAKA

Grad. Student, Dept. of Civil Engrg., Lehigh
University, Bethlehem, Pa.; Formerly Engineer,
Nava Construction Co., Teheran, Iran

Introduction

Moment-curvature-thrust relationships are of prime importance in the analysis of reinforced concrete columns. For a biaxially loaded columns, the appropriate loadings are bending moments M_x and M_y and axial force P . The corresponding deformations are bending curvatures ϕ_x and ϕ_y and axial strain ϵ_o at corner 0. The positive directions of force and deformation vectors are shown in Fig. 1a. For convenience in further discussion, the following vectors of force and deformation are defined;

$$\{F\} = \begin{Bmatrix} M_x \\ M_y \\ P \end{Bmatrix} \quad \{D\} = \begin{Bmatrix} \phi_x \\ \phi_y \\ \epsilon_o \end{Bmatrix} \quad (1)$$

Herein a study is made of the relationship of the force vector $\{F\}$ with the deformation vector $\{D\}$ for a reinforced concrete column segment in biaxial bending.

The non-linear stress-strain relationship in compression as well as the low strength in tension of concrete complicate the analysis of structures using such a material. Hence it is useful to establish an analytical relationship of the force deformation equation in terms of the infinitesimal changes $\{\delta F\}$ and $\{\delta D\}$. This leads to an assumed linear relationship between these vectors.

$$\{\delta F\} = [Q] \{\delta D\} \quad (2)$$

The matrix $[Q]$ is defined as the tangent stiffness matrix as it represents the tangent of the force-deformation curve as well as the stiffness of the cross section.

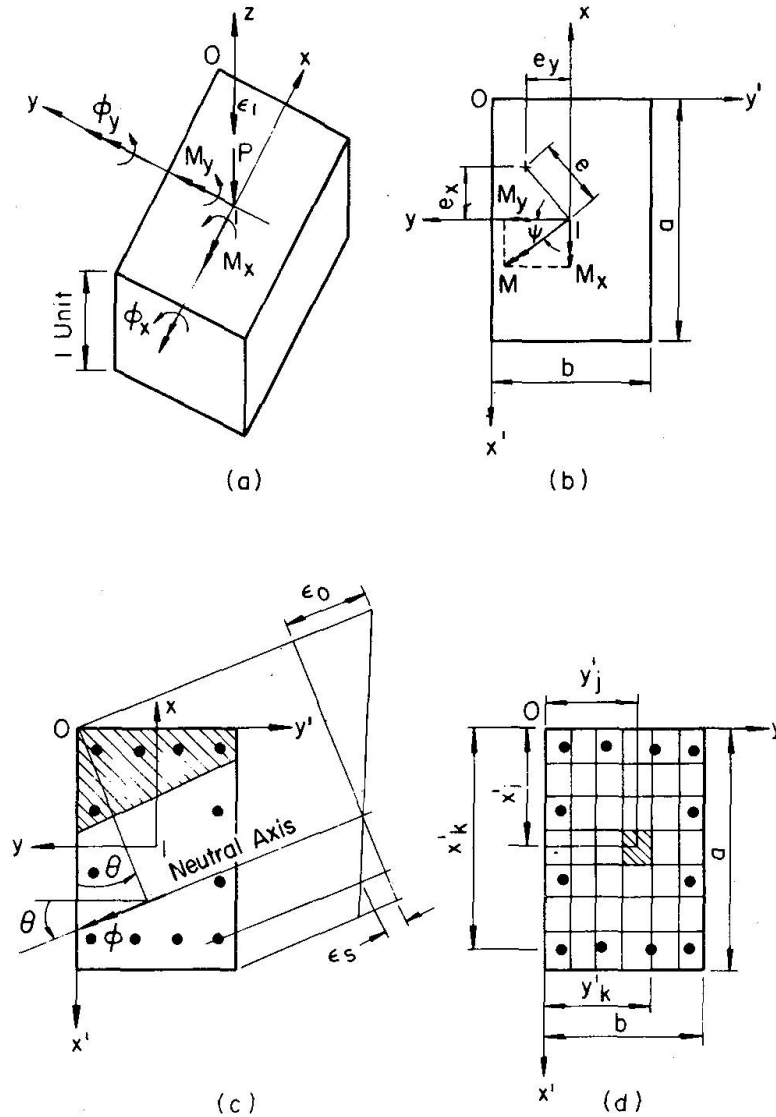


Fig. 1. Moment, Curvature and Strain in Cross Section and Partitioning of Cross Section.

Once this linear relationship is established, it is easy to answer the following three questions:

1. For a given path of force $\{F\}$, the corresponding path of deformation $\{D\}$ can be obtained by step-by-step calculations using Eq. 2, in the form

$$\{\delta D\} = [Q]^{-1} \{\delta F\} \quad (3)$$

and by applying the tangent stiffness method developed in Ref. [1] (Fig. 1 b) for numerical solutions.

2. For a given path of deformation $\{D\}$, the corresponding path of force $\{F\}$ can be obtained by direct step-by-step application of this linear relation, Eq. 2 (Fig. 1 c).
3. This incremental equation (Eq. 2) can also handle any mixed path of force and deformation. For example, the column may be first loaded axially to some

value; and then, holding the axial force P constant, the bending curvatures ϕ_x and ϕ_y may be increased proportionally in magnitude from zero. The corresponding bending moments M_x , M_y and the axial strain ϵ_o can then be obtained by simply subdividing the stiffness matrix $[Q]$ into submatrices. Thus,

$$\begin{Bmatrix} \delta M_x \\ \delta M_y \\ \delta P \end{Bmatrix} = \begin{bmatrix} Q_{11} & Q_{12} & Q_{13} \\ Q_{21} & Q_{22} & Q_{23} \\ Q_{31} & Q_{32} & Q_{33} \end{bmatrix} \begin{Bmatrix} \delta \phi_x \\ \delta \phi_y \\ \delta \epsilon_o \end{Bmatrix} \quad (4)$$

Since $\{\delta P\} = 0$, and $\delta \phi_x$ and $\delta \phi_y$ are known,

$$\delta \epsilon_o = \frac{-1}{Q_{33}} \{Q_{31} \ Q_{32}\} \begin{Bmatrix} \delta \phi_x \\ \delta \phi_y \end{Bmatrix} \quad (5)$$

and

$$\begin{Bmatrix} \delta M_x \\ \delta M_y \end{Bmatrix} = \begin{bmatrix} Q_{11} & Q_{12} & Q_{13} \\ Q_{21} & Q_{22} & Q_{23} \end{bmatrix} \begin{Bmatrix} \delta \phi_x \\ \delta \phi_y \\ \delta \epsilon_o \end{Bmatrix} \quad (6)$$

A somewhat similar solution for this particular mixed path of force and deformations has recently been reported by WARNER [2]. Based upon the equations formulated, a computer program has been developed to provide various numerical results. The elements of the tangent stiffness matrix were evaluated numerically by dividing the concrete section into finite elements and by considering each steel bar as an element (Fig. 1d).

Assumptions

The procedure is based on the following assumptions.

1. Concrete has no tensile strength, Fig. 2a, and in the usual notation

$$\bar{f}_c = \frac{f_c}{k_1 f_c} = 0 \text{ when } \bar{\epsilon}_c = \frac{\epsilon_c}{\epsilon'_c} \leq 0 \quad (7)$$

2. The stress-strain relationship for concrete in compression is nonlinear and is of the form as shown in Fig. 2a

$$\bar{f}_c = \gamma_1 \bar{\epsilon}_c + (3 - 2\gamma_1) \bar{\epsilon}_c^2 + (\gamma_1 - 2) \bar{\epsilon}_c^3 \text{ when } 0 \leq \bar{\epsilon}_c \leq 1 \quad (8a)$$

$$\bar{f}_c = 1 - \frac{1 - 2\bar{\epsilon}_c + \bar{\epsilon}_c^2}{1 - 2\gamma_2 + \gamma_2^2} \text{ when } 1 \leq \bar{\epsilon}_c \leq \gamma_2 \quad (8b)$$

$$\bar{f}_c = 0 \text{ when } \bar{\epsilon}_c \geq \gamma_2 \quad (8c)$$

where

$$\gamma_1 = \frac{E_c \epsilon'_c}{k_1 f_c} \quad (8d)$$

and γ_2 represents the point of intersection of the stress-strain curve with the strain axis.

3. The stress-strain relationship for steel is elastic perfectly plastic in both tension and compression (Fig. 2b), and in the usual notation

$$\bar{f}_s = \frac{f_s}{f_y} = -1 \quad \text{when } \bar{\epsilon}_s = \frac{\epsilon_s}{\epsilon_y} < -1 \quad (9a)$$

$$\bar{f}_s = \bar{\epsilon}_s \quad \text{when } -1 \leq \bar{\epsilon}_s \leq 1 \quad (9b)$$

$$\bar{f}_s = 1 \quad \text{when } \bar{\epsilon}_s > 1 \quad (9c)$$

4. The effects of creep and shrinkage of the concrete are disregarded.

5. Plane sections remain plane before and after bending.

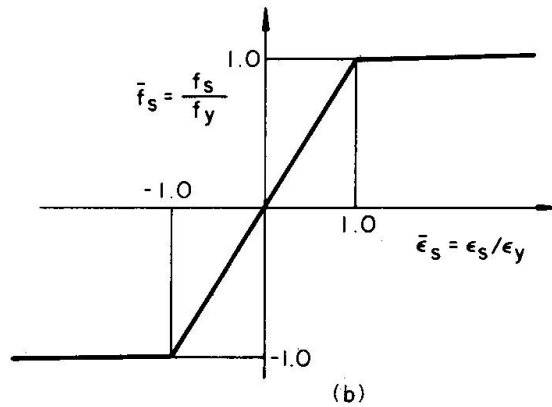
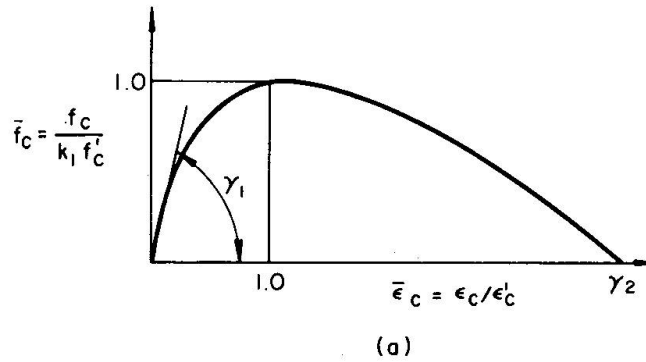


Fig. 2. Stress-Strain Relations.

Formulation of the Basic Equation

Consider the partially yielded cross section shown in Fig. 1c. Equilibrium is satisfied when the internal forces equal the external forces. In x - y coordinate system,

$$M_x = \int \sigma y dA \quad (10a)$$

$$M_y = \int \sigma x dA \quad (10b)$$

$$P = \int \sigma dA \quad (10c)$$

in $x'-y'$ coordinate system,

$$M_{x'} = - \int \sigma y' dA \quad (11a)$$

$$M_{y'} = - \int \sigma x' dA \quad (11b)$$

$$P = \int \sigma dA \quad (11c)$$

In order to evaluate the internal actions, the concrete area is divided by horizontal and vertical lines into a total of N_c small rectangular elements, ΔA_c (Fig. 1d). The total steel area is assumed to be distributed in N_s elements, all of equal area ΔA_s . The relation between ΔA_s and ΔA_c is

$$\Delta A_s = p' \Delta A_c \quad (12)$$

where

$$p' = \frac{N_c}{N_s} p, \quad p = \frac{A_s}{ab} \quad (13)$$

and Eq. 11 may be rewritten in the form (Fig. 1d)

$$M_{x'} = - \left\{ \sum_{i=1}^{N_a} \sum_{j=1}^{N_b} y'_j (f_c)_{ij} + p' \sum_{k=1}^{N_s} y'_k (f_s)_k - p' \sum_{k=1}^{N_s} y'_k (f_c)_k \right\} \Delta A_c \quad (14)$$

$$M_{y'} = - \left\{ \sum_{i=1}^{N_a} \sum_{j=1}^{N_b} x'_i (f_c)_{ij} + p' \sum_{k=1}^{N_s} x'_k (f_s)_k - p' \sum_{k=1}^{N_s} x'_k (f_c)_k \right\} \Delta A_c \quad (14b)$$

$$P = \left\{ \sum_{i=1}^{N_a} \sum_{j=1}^{N_b} (f_c)_{ij} + p' \sum_{k=1}^{N_s} (f_s)_k - p' \sum_{k=1}^{N_s} (f_c)_k \right\} \Delta A_c \quad (14c)$$

where N_a and N_b are the numbers of rows and columns of elemental concrete areas respectively, and N_s is the number of bars.

The incremental forms of the equilibrium equations are

$$\delta M_{x'} = - \left\{ \sum_{i=1}^{N_a} \sum_{j=1}^{N_b} y'_j (\delta f_c)_{ij} + p' \sum_{k=1}^{N_s} y'_k (\delta f_s)_k - p' \sum_{k=1}^{N_s} y'_k (\delta f_c)_k \right\} \Delta A_c \quad (15a)$$

$$\delta M_{y'} = - \left\{ \sum_{i=1}^{N_a} \sum_{j=1}^{N_b} x'_i (\delta f_c)_{ij} + p' \sum_{k=1}^{N_s} x'_k (\delta f_s)_k - p' \sum_{k=1}^{N_s} x'_k (\delta f_c)_k \right\} \Delta A_c \quad (15b)$$

$$\delta P = \left\{ \sum_{i=1}^{N_a} \sum_{j=1}^{N_b} (\delta f_c)_{ij} + p' \sum_{k=1}^{N_s} (\delta f_s)_k - p' \sum_{k=1}^{N_s} (\delta f_c)_k \right\} \Delta A_c \quad (15c)$$

The incremental changes of stress and strain in concrete are related by

$$\delta f_c = G_c \delta \epsilon_c \quad (16)$$

where

$$G_c = 0, \text{ when } \epsilon_c \leq 0 \quad (17a)$$

$$G_c = \frac{k_1 f'_c}{\epsilon'_c} \gamma_1 + 2 \frac{k_1 f'_c}{\epsilon'^2_c} (3 - 2\gamma_1) \epsilon_c + 3 \frac{k_1 f'_c}{\epsilon'^3_c} (\gamma_1 - 2) \epsilon_c^2 \quad (17b)$$

when

$$0 < \varepsilon_c \leq \varepsilon'_c$$

and

$$G_c = 2 \frac{k_1 f'_c}{\varepsilon'_c (1 - 2\gamma_2 + \gamma_2^2)} - 2 \frac{k_1 f'_c}{\varepsilon'^2_c (1 - 2\gamma_2 + \gamma_2^2)} \varepsilon_c \quad (17c)$$

when

$$\varepsilon'_c < \varepsilon_c \leq \varepsilon'_c \gamma_2$$

and

$$G_c = 0, \text{ when } \varepsilon_c > \varepsilon'_c \gamma_2 \quad (17d)$$

The incremental changes in stress and strain of steel are related by

$$\delta f_s = G_s \delta \varepsilon_s \quad (18)$$

where

$$G_s = 0, \text{ when } \varepsilon_s < -\varepsilon_y \quad (19a)$$

and

$$G_s = \frac{f_y}{\varepsilon_y} = E_s, \text{ when } -\varepsilon_y \leq \varepsilon_s \leq \varepsilon_y \quad (19b)$$

and

$$G_s = 0, \text{ when } \varepsilon_s > \varepsilon_y \quad (19c)$$

Substituting δf_c and δf_s from equations 16 and 18 into equation 15, we have,

$$\begin{aligned} \delta M_{x'} = & - \left\{ \sum_{i=1}^{N_a} \sum_{j=1}^{N_b} y'_j (G_c)_{ij} (\delta \varepsilon_c)_{ij} + p' \sum_{k=1}^{N_s} y'_k (G_s)_k (\delta \varepsilon_s)_k - \right. \\ & \left. p' \sum_{k=1}^{N_s} y'_k (G_c)_k (\delta \varepsilon_c)_k \right\} \Delta A_c \end{aligned} \quad (20a)$$

$$\begin{aligned} \delta M_{y'} = & - \left\{ \sum_{i=1}^{N_a} \sum_{j=1}^{N_b} x'_i (G_c)_{ij} (\delta \varepsilon_c)_{ij} + p' \sum_{k=1}^{N_s} x'_k (G_s)_k (\delta \varepsilon_s)_k - \right. \\ & \left. p' \sum_{k=1}^{N_s} x'_k (G_c)_k (\delta \varepsilon_c)_k \right\} \Delta A_c \end{aligned} \quad (20b)$$

$$\delta P = \left\{ \sum_{i=1}^{N_a} \sum_{j=1}^{N_b} (G_c)_{ij} (\delta \varepsilon_c)_{ij} + p' \sum_{k=1}^{N_s} (G_s)_k (\delta \varepsilon_s)_k - p' \sum_{k=1}^{N_s} (G_c)_k (\delta \varepsilon_c)_k \right\} \Delta A_c \quad (20c)$$

The strain ε at any point in the cross section with respect to $x'y'$ coordinate can be expressed in a linear form as

$$\varepsilon = -y' \varphi_{x'} - x' \varphi_{y'} + \varepsilon_o \quad (21)$$

where ε_o is the strain at the corner 0 (Fig. 1). The incremental change of the strain is

$$\delta \varepsilon = -y' \delta \varphi_{x'} - x' \delta \varphi_{y'} + \delta \varepsilon_o \quad (22)$$

or (Fig. 1 d)

$$(\delta \varepsilon_c)_{ij} = -y'_j \delta \varphi_{x'} - x'_i \delta \varphi_{y'} + \delta \varepsilon_o \quad (23a)$$

$$(\delta \varepsilon_s)_k = (\delta \varepsilon_c)_k = -y'_k \delta \varphi_{x'} - x'_k \delta \varphi_{y'} + \delta \varepsilon_o \quad (23b)$$

where $\delta\epsilon_o$ is the strain increment at the corner 0 of the cross section. Combinations of equations 20 and 23 gives a set of simultaneous linear equations which can be written in the matrix form as

$$\begin{Bmatrix} \delta M_{x'} \\ \delta M_{y'} \\ \delta P \end{Bmatrix} = \begin{bmatrix} Q_{11} & Q_{12} & Q_{13} \\ Q_{21} & Q_{22} & Q_{23} \\ Q_{31} & Q_{32} & Q_{33} \end{bmatrix} \begin{Bmatrix} \delta\phi_{x'} \\ \delta\phi_{y'} \\ \delta\epsilon_o \end{Bmatrix} \quad (24)$$

where Q_{ij} is defined as

$$Q_{11} = \left\{ \sum_{i=1}^{N_a} \sum_{j=1}^{N_b} (y'_j)^2 (G_c)_{ij} + p' \sum_{k=1}^{N_s} (y'_k)^2 (G_s)_k - p' \sum_{k=1}^{N_s} (y'_k)^2 (G_c)_k \right\} \Delta A_c \quad (25a)$$

$$Q_{22} = \left\{ \sum_{i=1}^{N_a} \sum_{j=1}^{N_b} (x'_i)^2 (G_c)_{ij} + p' \sum_{k=1}^{N_s} (x'_k)^2 (G_s)_k - p' \sum_{k=1}^{N_s} (x'_k)^2 (G_c)_k \right\} \Delta A_c \quad (25b)$$

$$Q_{33} = \left\{ \sum_{i=1}^{N_a} \sum_{j=1}^{N_b} (G_c)_{ij} + p' \sum_{k=1}^{N_s} (G_s)_k - p' \sum_{k=1}^{N_s} (G_c)_k \right\} \Delta A_c \quad (25c)$$

$$Q_{12} = Q_{21} = \left\{ \sum_{i=1}^{N_a} \sum_{j=1}^{N_b} x'_i y'_j (G_c)_{ij} + p' \sum_{k=1}^{N_s} x'_k y'_k (G_s)_k - p' \sum_{k=1}^{N_s} x'_k y'_k (G_c)_k \right\} \Delta A_c \quad (25d)$$

$$Q_{13} = Q_{31} = - \left\{ \sum_{i=1}^{N_a} \sum_{j=1}^{N_b} y'_j (G_c)_{ij} + p' \sum_{k=1}^{N_s} y'_k (G_s)_k - p' \sum_{k=1}^{N_s} y'_k (G_c)_k \right\} \Delta A_c \quad (25e)$$

$$Q_{23} = Q_{32} = - \left\{ \sum_{i=1}^{N_a} \sum_{j=1}^{N_b} x'_i (G_c)_{ij} + p' \sum_{k=1}^{N_s} x'_k (G_s)_k - p' \sum_{k=1}^{N_s} x'_k (G_c)_k \right\} \Delta A_c \quad (25f)$$

Equation 24 can be rewritten as

$$\{\delta F\} = [Q] \{\delta D\} \quad (26)$$

The symmetric matrix $[Q]$, whose elements are given by Equation 25 is known as the tangent stiffness matrix as it represents the tangent of the force-deformation curve as well as the stiffness of the cross section.

Numerical Studies

Based upon the equations formulated, a computer program using the tangent stiffness technique [1] was developed to provide numerical results. The numerical work was performed on a high speed digital computer (CDC 6400). The specific case of a square section with the following input values was treated as a standard concrete column cross section:

$$a = 24 \text{ in, } b = 24 \text{ in, } N_a = 10, N_b = 10$$

$$N_s = 12, p = \frac{A_s}{ab} = 0.0325, k_1 f'_c = 4.2 \text{ ksi}$$

$$k_1 = 0.85, f_s = 60.0 \text{ ksi, } \epsilon'_c = 0.002$$

$$E_s = 29,000,000 \text{ psi, } E_c = 57,600 \sqrt{f'_c} \text{ (for normal weight concrete)}$$

$$\gamma_2 = 4, \gamma_1 = \text{computed from Eq. 8d.}$$

The elements of the tangent stiffness matrix of the cross section were evaluated numerically by dividing the cross section into finite elements N_c (Fig. 1d). The value of N_c was varied from 100 (10×10) to 400 (20×20) for the square section. The increase in accuracy obtained by using the finer grids was only 0.1%. A partitioning of the concrete cross section into 100 elements and the steel areas into 12 elements distributed uniformly around the sides of the section are used herein. A somewhat similar partitioning was also suggested in Ref. 2.

The strain and stress in each element were computed as the average value at its centroid. All force and deformation vectors are nondimensionalized as,

Force vector

$$\left\{ \frac{P}{f'_c ab} \quad \frac{M_x}{f'_c ab^2} \quad \frac{M_y}{f'_c a^2 b} \right\}$$

Deformation vector

$$\left\{ \frac{\phi_x}{\left(\frac{\epsilon'_c}{a}\right)} \quad \frac{\phi_y}{\left(\frac{\epsilon'_c}{b}\right)} \quad \frac{\epsilon_o}{\epsilon'_c} \right\}$$

The allowable error in $P/f'_c a b$ was 0.002.

The resultant moment on the section may be represented by the two components M_x and M_y or by a vector M of magnitude $\sqrt{M_x^2 + M_y^2}$ and inclined at the angle $\Psi = \tan^{-1}(M_x/M_y)$ to the y axis (see Fig. 1b). The resultant curvature ϕ of magnitude $\sqrt{\phi_x^2 + \phi_y^2}$ and inclined at the angle $\theta = \tan^{-1}(\phi_x/\phi_y)$ to the y axis (Fig. 1c) is nondimensionalized as $\phi/(\epsilon'_c/b)$.

Example – Given Path of Loading

The moment-curvature curves plotted in Fig. 3, 4, 6, 7, and 8 are for M_x vs. ϕ_x for various values of M_y . The column section is first loaded axially up to some value and then bent by M_y to some other value while keeping P constant and finally bent by M_x to failure while keeping P and M_y constant. The curves have been terminated when the strain ratio ϵ_o/ϵ'_c reaches the value 3.0. To indicate the magnitude of the strains in the cross section, two other lines of constant $\epsilon_o/\epsilon'_c =$ recommended by ACI [3] and 2.0 have been plotted across the main curves (dotted lines in the figures).

It is of interest to note that the values of the maximum moment $M_x/f'_c ab^2$ lie between the values of $\epsilon_o/\epsilon'_c = 2.0$ to 3.0 and generally very close to the constant line $\epsilon_o/\epsilon'_c = 3.0$. The maximum values of the moment are indicated by the small circles in Figures 3 to 8. These moment curvature curves indicate that the maximum strength of short columns in biaxial bending and compression are not unduly sensitive to the variations in the assumed concrete ultimate strain which is often chosen in the range between 0.003 and 0.004.

The moment curvature curves shown in Fig. 3 are considered to be the standard cases. The important factors influencing the behavior of the curves are the magnitude of compression force P , concrete quality $k_1 f'_c$, steel quality f_y , and percentage of

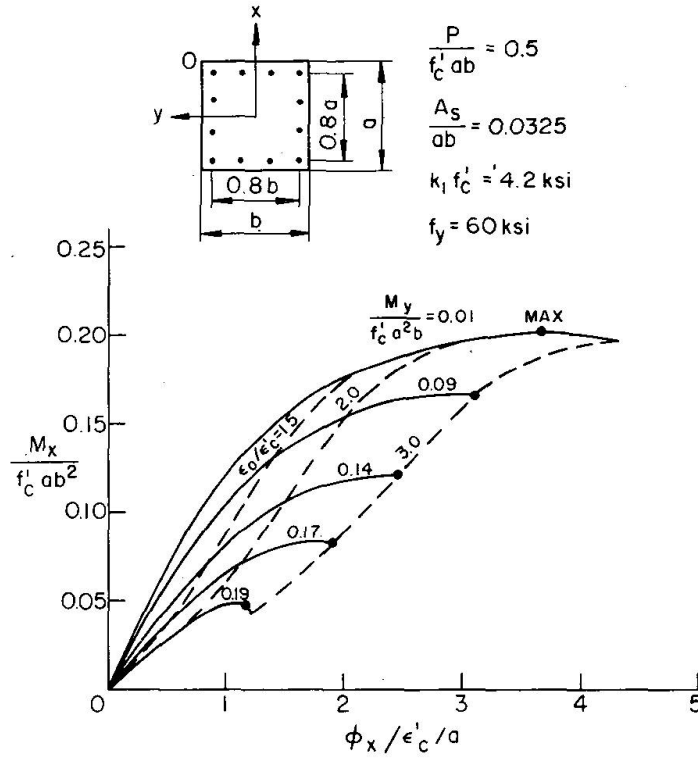


Fig. 3. Moment-Curvature Relations: Standard Case.

reinforcement A_s/ab . The variations of these factors with respect to the standard case are given in Figs. 4, 6, 7, and 8.

The influence of axial compression force on the moment curvature curves is shown in Fig. 4. The unloading of the moment, M_x , with respect to an increase in curvature ϕ_x is not seen for the curves $P = 0.1 f'_c ab$ within the range $\epsilon_o/\epsilon'_c = 3.0$ but is rather rapid for the curves with $P = 1.0 f'_c ab$. It is also observed, that when $P = 1.0 f'_c ab$ and the bending moment $M_y \geq 0.05 f'_c a^2 b$, there is a very rapid unloading for both moment M_x and curvature ϕ_x . The curvature ϕ_y or the resultant curvature ϕ is, of course, not unloaded with respect to a decrease in moment M_x , as shown in Fig. 5.

The influence of concrete quality $k_1 f'_c$ and steel quality f_y on the moment curvature curves is shown in Figs. 6 and 7. The results are calculated for concrete with $k_1 f'_c = 3.0 \text{ ksi}$ and 5.0 ksi (Fig. 6) and for steel with $f_y = 40 \text{ ksi}$ and 80 ksi (Fig. 7) respectively. As can be seen, an increase in material qualities significantly increases the stiffness and strength of a biaxially loaded cross section.

Figure 8 shows the influence of the percentage reinforcement A_s/ab on the moment curvature relationships. It is evident from the figure that the percentage steel reinforcement has an appreciable effect on the behavior of a biaxially loaded cross section.

The maximum points of the moment curvature curves as shown by the small circles in Figs. 3 to 8 represent the maximum strength of the biaxially loaded cross section. The maximum loads obtained in this way for the standard cross section (Fig. 3) with three values of strain ratio, $\epsilon_o/\epsilon'_c = 1.5, 2.0$ and 3.0 are represented by the interaction curves in Figs. 9 to 13. The small circles in these figures indicate

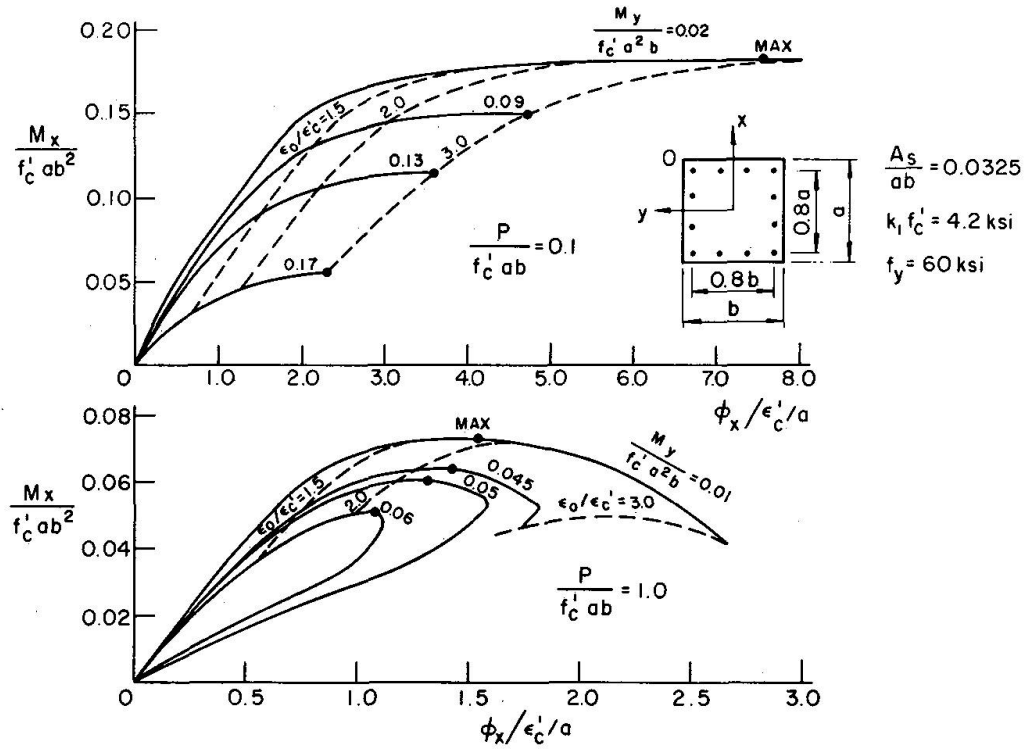


Fig. 4. Moment-Curvature Relations: Axial Compression Force Effect.

the regions where the maximum load is controlled either by the maximum concrete strain or by the overall stress distribution of the cross section. The important factors influencing the maximum carrying capacity of a biaxially loaded short column are the axial compression force, P , the concrete quality, $k_1 f'_c$, steel quality, f_y , and percentage of reinforcement A_s/ab , as shown in Figs. 9 to 13, respectively. Since the interaction curves are nondimensionalized, they can be directly used in analysis and design computations.

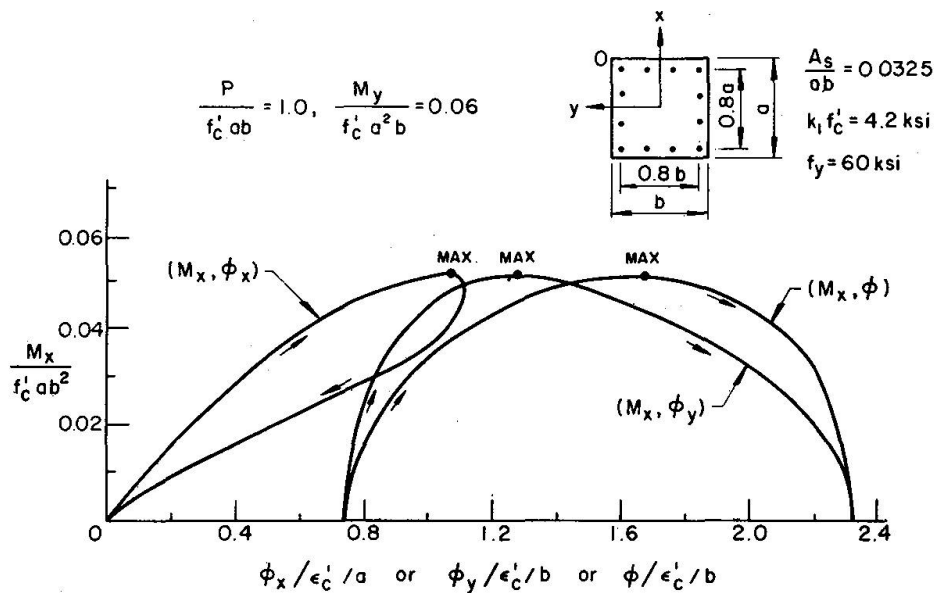


Fig. 5. Moment-Curvature Relations: Complete Unloading.

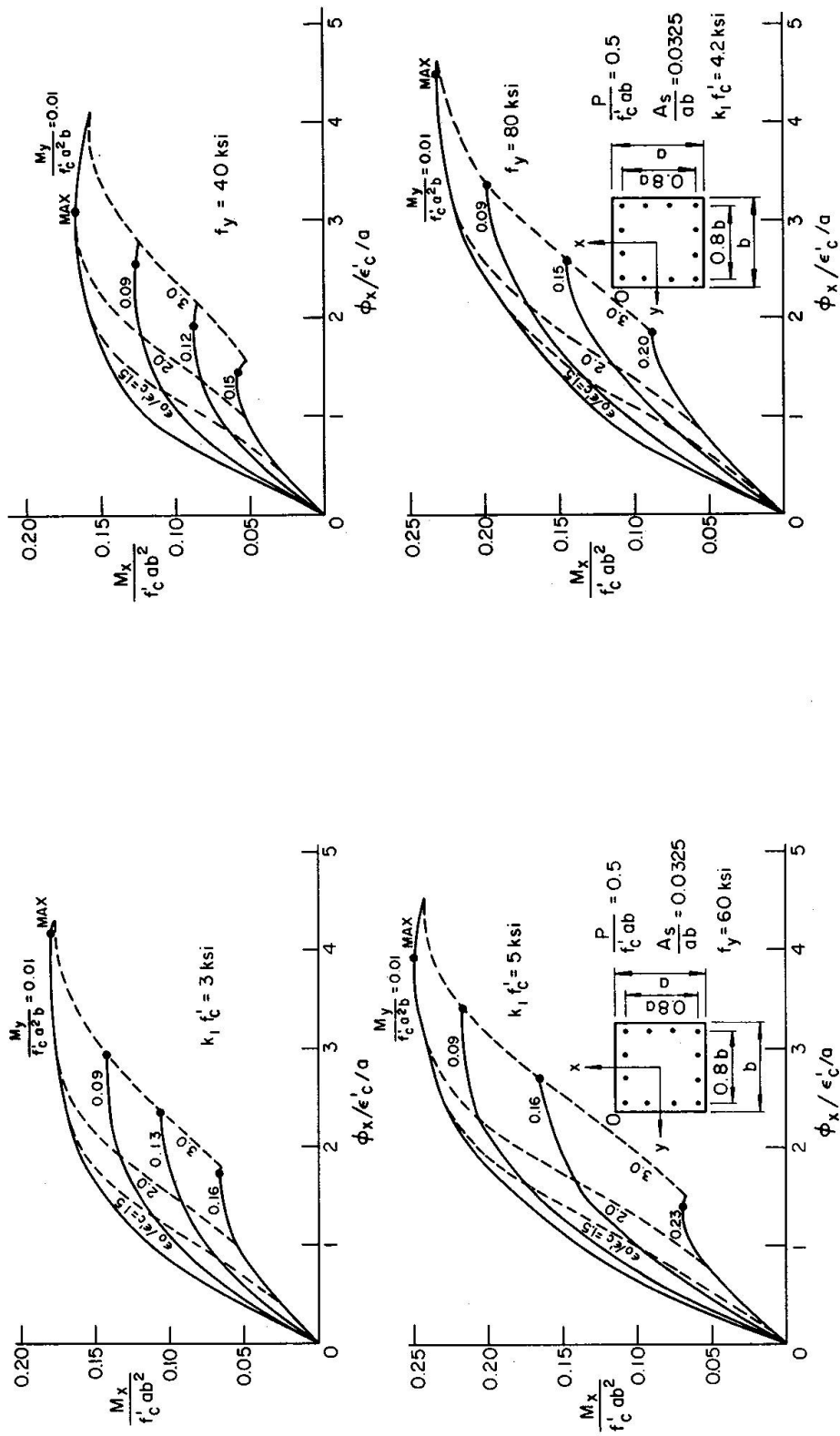


Fig. 6. Moment-Curvature Relations: Concrete Quality Effect.

Fig. 7. Moment-Curvature Relations: Steel Quality Effect.

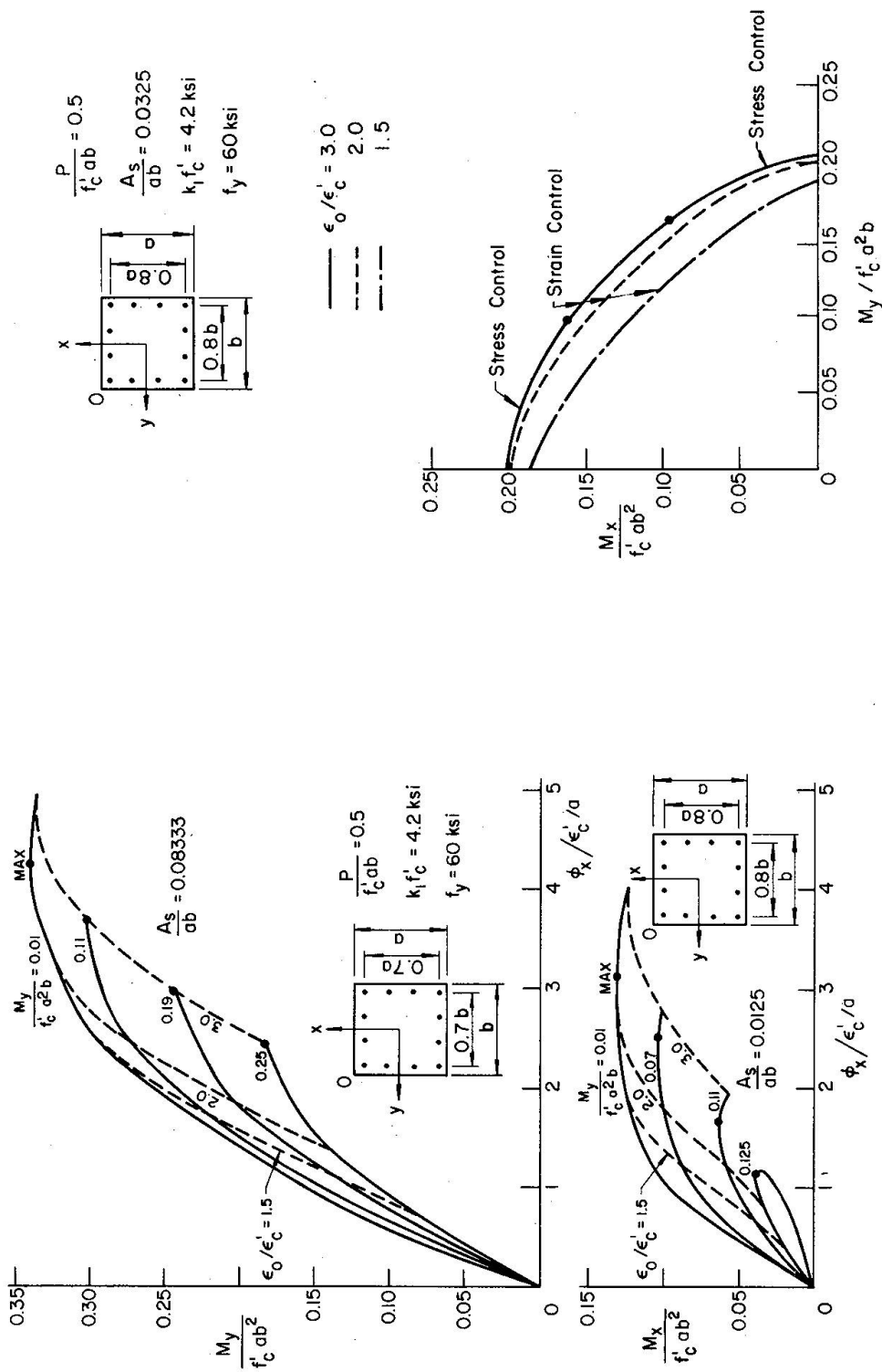


Fig. 8. Moment-Curvature Relations: Percentage of Reinforcement Effect.

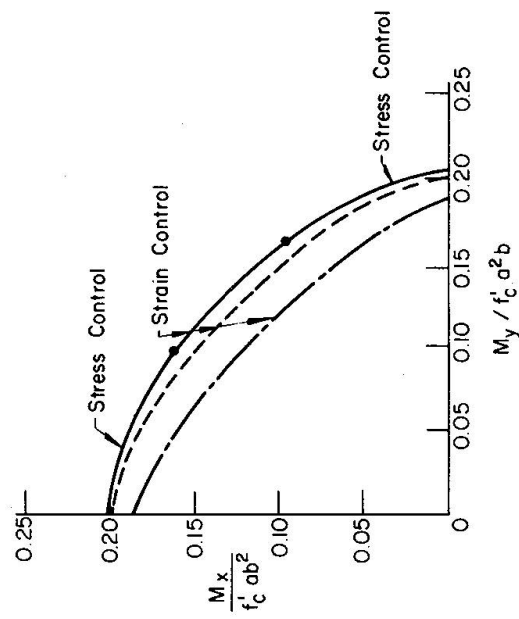


Fig. 9. Interaction Curves: Standard Case.

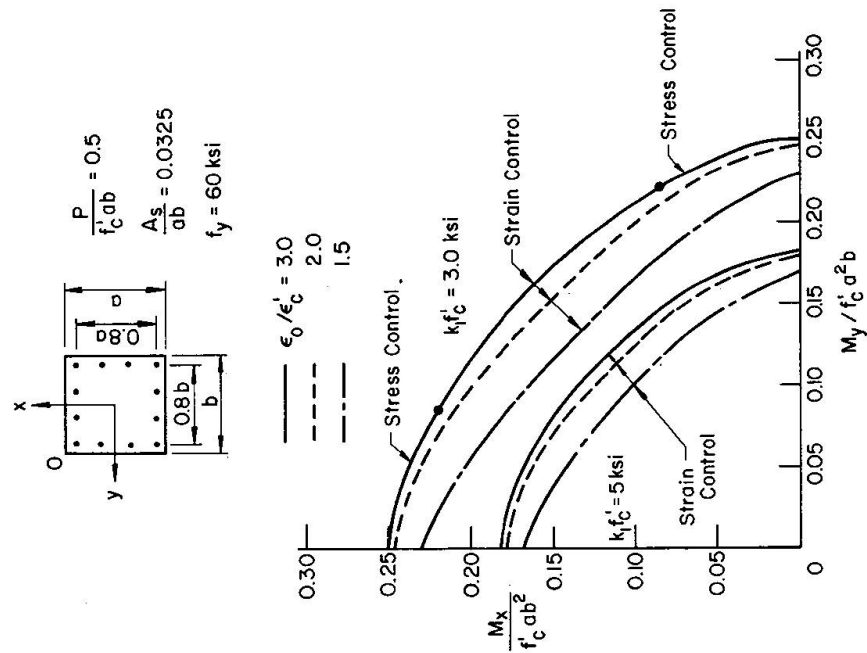


Fig. 11. Interaction Curves: Concrete Quality Effect.

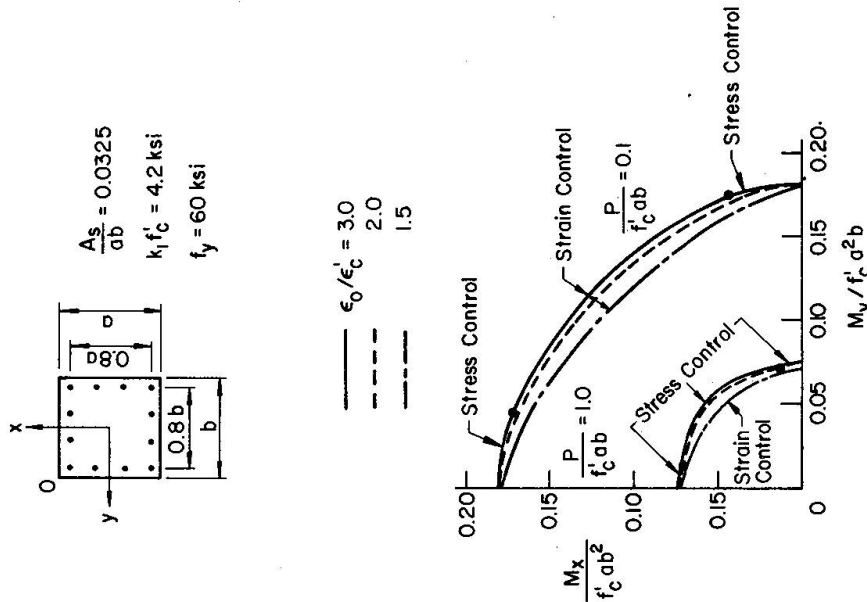


Fig. 10. Interaction Curves: Axial Compression Force Effect.

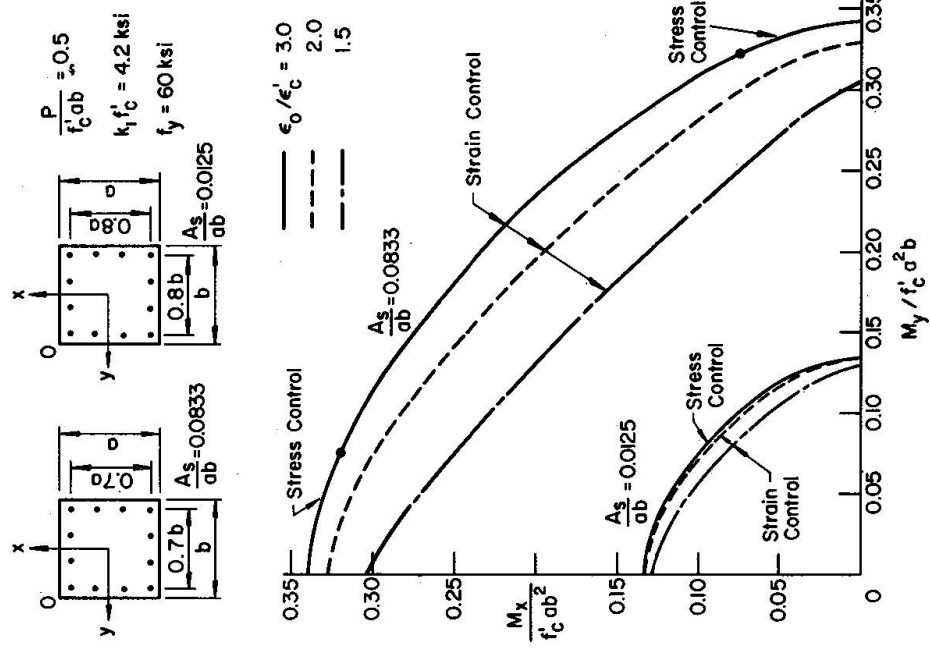


Fig. 13. Interaction Curves: Percentage of Reinforcement Effect.

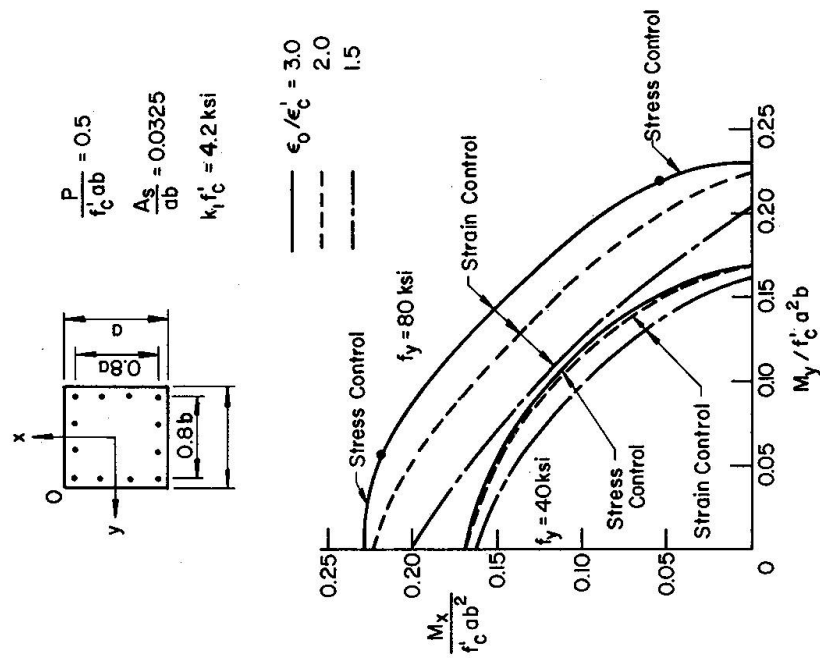


Fig. 12. Interaction Curves: Steel Quality Effect.

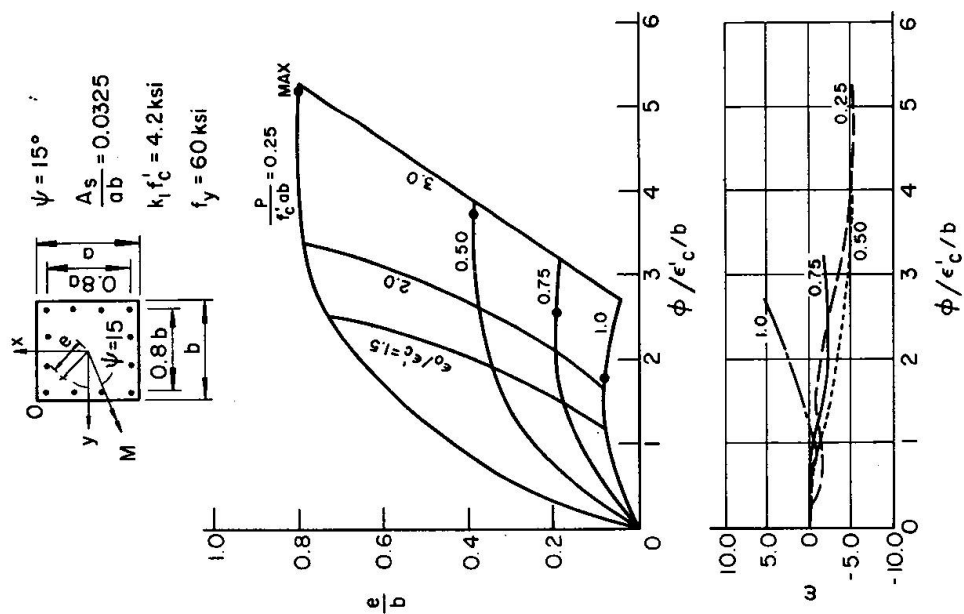


Fig. 14. Moment-Curvature Relations: $\theta = 15^\circ$.
($\omega = \Psi - \theta$)

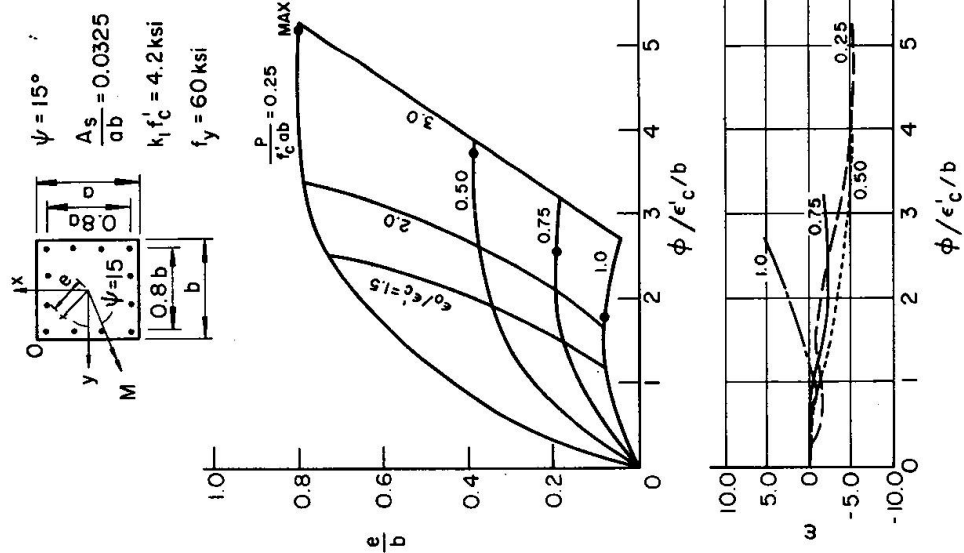


Fig. 15. Moment-Curvature Relations: $\Psi = 15^\circ$.
($\omega = \Psi - \theta$)

Example — Given Mixed Path of Loading and Deformation

The moment-curvature curves plotted in Fig. 14 are for e/b vs. ϕ for a given set of values of $\theta = \tan^{-1} (\phi_x/\phi_y) = 15^\circ$ and $P/P_u = 0.2, 0.4, 0.6$ and 0.8 . In the figure, the column section is first loaded axially to some value; and then the axial force P is held constant while the bending curvatures ϕ_x and ϕ_y (or $\phi = \sqrt{\phi_x^2 + \phi_y^2}$) are increased proportionally in magnitude from zero. The corresponding bending moments M_x and M_y (or $e = M/P = \sqrt{M_x^2 + M_y^2}/P$) and axial strain ϵ_o at the corner 0 (Fig. 14) can be obtained by the Eqs. 5 and 6 using the iterative procedure reported in Ref. 2. These moment curvature curves were compared with those obtained previously by Warner and an excellent agreement was found in all cases [2].

The maximum difference between the angles θ and Ψ , i.e. between the directions of the resultant curvature ϕ and resultant moment vectors, $\omega = \Psi - \theta$, is also shown in Fig. 14. It can be seen that the moment and curvature vectors nearly coincide in direction throughout the entire range of loading. The maximum difference between the two vectors is of the order of ten degrees.

It is also of interest to note that a similar conclusion is also true for the case of other loading paths. For example, in Fig. 15, the section is first loaded axially to some constant value and then the axial force P is held constant while the bending moments M_x and M_y are increased proportionally in magnitude; i.e. $\Psi = \tan^{-1} (M_x/M_y)$. The corresponding bending curvatures ϕ_x and ϕ_y and axial strain ϵ_o can be obtained by Eq. 3 using the iterative procedure reported in Ref. 1. The maximum difference between the angles θ and Ψ is again only of the order of ten degrees.

Simple Interaction Equations

The general form of the interaction curves shown in Figs. 9-13 may be approximated by a non-dimensional interaction equation [4]:

$$\left(\frac{M_x}{M_{xo}} \right)^\alpha + \left(\frac{M_y}{M_{yo}} \right)^\alpha = 1.0 \quad (27)$$

where M_{xo} and M_{yo} represent the load carrying capacities of a particular column under compression and uniaxial bending moment about x and y axes, respectively. Thus, for a given compression P , M_{xo} and M_{yo} are the values given on the $M_y = 0$ and $M_x = 0$ axes shown in Figs. 9-13. The value α is the exponent depending on column dimensions, amount and distribution of steel reinforcement, stress-strain characteristics of steel and concrete, and magnitude of axial compression. For a given compression and a given column characteristic, the value of α is a numerical constant.

The interaction surface corresponding to the column section given in Figs. 9 and 10 is shown in Fig. 16a. The interaction curves given previously in Figs. 9 and 10 for the particular case of strain ratio $\epsilon_o/\epsilon'_c = 1.5$ are now non-dimensionalized by the values M_{xo} and M_{yo} and plotted in Fig. 16b. These curves corresponding to constant values of $P/f'_c ab = 0.1, 0.5$ and 1.0 which may be thought of as "load contours".

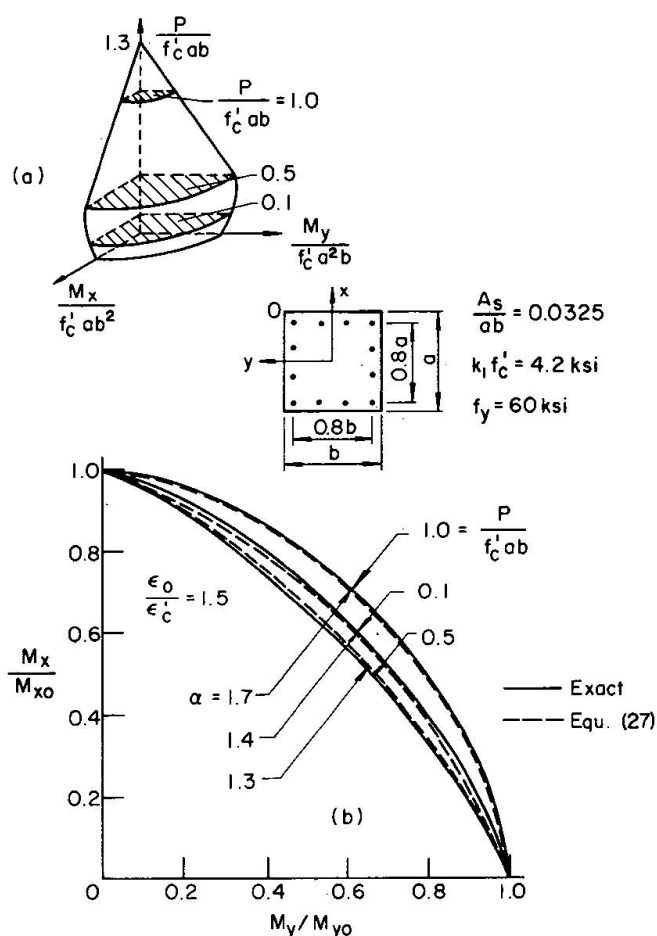


Fig. 16. Comparison of Interaction Curves.

Using Eq. 27, values of α are calculated for this column. The calculated values of α are found, varying from 1.3 to 1.4 for $P/f'_c ab = 0.1$ and 0.5 but jumping to 1.7 for $P/f'_c ab = 1.0$. The comparison between the actual curves computed directly on the basis of stress-strain relations and the theoretical curves obtained from Eq. 27 is also shown in Fig. 16b and good agreement is observed. The values of α for columns with a wide range of variation in values of f'_c , f_y and A_s/ab are tabulated in Table 1 for the particular case of strain ratio $\epsilon_o/\epsilon'_c = 1.5$ (recom-

Table 1. Computed Values of α in Eq. 27

$\frac{P}{f'_c ab}$	$k_1 f'_c$	f_y	$\frac{A_s}{ab}$	α	Note
0.5	4.2	60	0.0325	1.3	
0.1	4.2	60	0.0325	1.4	
1.0	4.2	60	0.0325	1.7	
0.5	3	60	0.0325	1.3	$\frac{\epsilon_o}{\epsilon'_c} = 1.5$ for all cases.
0.5	5	60	0.0325	1.4	
0.5	4.2	40	0.0325	1.4	
0.5	4.2	80	0.0325	1.2	
0.5	4.2	60	0.0125	1.4	
0.5	4.2	60	0.0833	1.1	

mended by ACI). In general, the values of α in the range 1.1 to 1.4 are seen to give a good approximation for all the cases investigated in the low and moderate axial compression range, but large variation in values of α is observed for columns with high axial compression.

Notations

a	depth of section.
b	width of section.
$\{D\}$	$\{\varphi_x \varphi_y \varepsilon_o\}$ = deformation vector.
E_c	modulus of elasticity of concrete.
E_s	modulus of elasticity of steel.
e	$\frac{M}{P}$ = (Fig. 1 b).
$\{F\}$	$\{M_x M_y P\}$ = force vector.
f_c	concrete stress.
f'_c	specified cylinder compression strength of concrete.
$\frac{f_c}{f'_c}$	f_c/f'_c .
f_s	steel stress.
$\frac{f_s}{f_y}$	f_s/f_y .
f_y	specified yield strength of reinforcement.
G_c	$\frac{\delta f_c}{\delta \varepsilon_c}$.
G_s	$\frac{\delta f_s}{\delta \varepsilon_s}$.
k_1	ratio of strength of concrete in member to specified cylinder compression strength.
M	$\sqrt{M_x^2 + M_y^2}$;
$M_x, M_{x'}$	moment with respect to x and x' axes respectively.
M_{xo}, M_{yo}	maximum moment capacity with respect to x and y axes respectively.
$M_y, M_{y'}$	moment with respect to y and y' axes respectively.
N_a	number of rows of elemental concrete areas.
N_b	number of columns of elemental concrete areas.
N_c	$N_a N_b$ = total number of elemental concrete areas.
N_s	number of reinforcement elemental areas.
P	compression force in section.
P_u	failure load of section for zero eccentricity.
p	A_s/ab .
p'	$\frac{N_c}{N_s} p$.
α	defined in Eq. 27.
γ_1	$\frac{E_c \varepsilon'_c}{k_1 f'_c}$.
γ_2	the point of intersection of the stress-strain curve with strain axis (Fig. 2a).
ε	strain.
ε_c	concrete strain.

ϵ'_c	concrete strain when concrete stress is $k_1 f'_c$.
$\bar{\epsilon}_c$	$\frac{\epsilon_c}{\epsilon'_c}$.
ϵ_o	strain at corner 0.
ϵ_s	steel strain.
ϵ_y	steel yield strain.
$\bar{\epsilon}_s$	$\frac{\epsilon_s}{\epsilon_y}$.
θ	inclination of the curvature vector to the y axis.
σ	stress.
ϕ	$\sqrt{\phi_x^2 + \phi_y^2}$.
$\phi_x, \phi_{x'}$	curvature with respect to x and x' axes respectively.
$\phi_y, \phi_{y'}$	curvature with respect to y and y' axes respectively.
Ψ	inclination of moment vector to the y axis. And
ω	$\Psi - \theta$.

Acknowledgments

The research reported here was supported by the National Science Foundation under Grant GK-35886 to Lehigh University.

Key Words

Moments; Biaxial bending; Columns; Plasticity; Reinforced Concrete; Curvature; Computers; Structural Engineering.

Abstract

Analytical formulations and procedures are developed for computing moment-thrust-curvature relations for reinforced concrete column sections in biaxial bending. The cross section is partitioned by a rectangular grid into a large number of small elemental areas of steel and concrete. The moment-thrust-curvature relations are obtained by step-by-step application of the analytically developed linear force-deformation equation using the tangent stiffness iterative procedure. The method is found to be extremely powerful and efficient for computer solution.

Numerical results are obtained for two types of loading paths: (a) given path of loading; and (b) given mixed path of loading and deformation. Results are presented in the form of moment-curvature-thrust curves and interaction curves relating axial compression and biaxial bending moments. The important factors influencing the behavior of these curves are discussed such as strength of materials, percentage of reinforcement and the magnitude of compression force. Simple analytical expressions to approximate the interaction curves of square sections are obtained.

Objective consequences with respect to the security and economy

The elastic-plastic behavior of an isolated, reinforced concrete column subjected to an axial load, and two bending moments acting in two perpendicular directions, is an important technical problem with frequent engineering applications. The obvious example is a corner column in a space building frame. Because the behavior of a space structure is characterized by the behavior of each of its individual members, it is of fundamental importance in the analysis and design of a three-dimensional space structure that we develop basic knowledge of the response of each individual member to forces acting at its ends and/or to loads acting on it.

Solutions that describe the elastic-plastic in-plane (two-dimensional) behavior of columns and beam-columns comprise the most highly developed aspect of column research in recent years. Applications to practical analysis and design for building frames are quite common, and the basic techniques are given in several texts and codes.

Despite this progress in obtaining solutions for in-plane behavior of columns, their extensions to three-dimensional space situations are just beginning, although some solutions have been obtained. The mathematics of such columns is quite involved, even for the special case of relatively short columns for which the effect of lateral deflections on the magnitudes of bending moments is negligible. For the most part, analysis and design of such columns have in the past been directed toward the study of ultimate strength of reinforced concrete short columns. For the case of long columns, the present design procedure of biaxially loaded columns does not differ from uniaxially loaded columns. The 1971 ACI Building Code, for example, recommends to calculate the moment magnifier separately and apply to the moment about each axis independently. The long columns are then designed according to the given axial compressive load and the magnified biaxial moments.

Although this procedure has been used extensively in design computations, it does not give accurate indications of the true load carrying capacity of a biaxially loaded column. To determine the ultimate strength of such a column, it is necessary to perform an elastic plastic stability analysis that considers the entire range of loading up to ultimate load. In order to perform such an analysis, we must have the knowledge of elastic-plastic behavior of a section under combined axial force, and biaxial bending moments. This is described in the present paper.

In this paper, an elastic-plastic analysis of a reinforced concrete segment under combined axial force, and biaxial bending has been obtained. The segment can be loaded with various combinations of loading path. For example, the section can be loaded first under a constant axial load P , and bending moment M_x , and then P , and M_x held constant while the section is loaded to its fully plastic state by the bending moment M_y . Computer programs have been used to replace the tedious calculations and series of plots which would have to be made to obtain the corresponding generalized strains of the segments at various stages of loading. With the knowledge of this elastic-plastic behavior of a segment under combined axial force, and biaxial bending, this fundamental result has been applied successfully to obtain elastic-plastic long column solutions. Several design criteria for reinforced

concrete columns subjected to compression combined with biaxial bending are developed and reported elsewhere (IABSE Symposium on Design and Safety of Reinforced Concrete Compression Members, Quebec, 1974).

References

1. SANTATHADAPORN, S., and CHEN, W.F.: Tangent Stiffness Method for Biaxial Bending. J. of the Structural Division, ASCE, Vol. 98, No. ST1, January 1972, pp. 153-163.
2. WARNER, R.F.: Biaxial Moment Thrust Curvature Relation. J. of the Structural Division, ASCE, Vol. 95, No. ST5, May 1969, pp. 923-940.
3. ACI Committee 318-71: Building Code Requirements for Reinforced Concrete (ACI 318-71). American Concrete Institute, Detroit, 1971.
4. BRESLER, B.: Design Criteria for Reinforced Columns under Axial Load and Biaxial Bending. J. of the American Concrete Institute, v. 32, No. 5, November 1960.

Summary

An analytical formulation of the force-deformation equations in terms of the increments has been developed which enables one to obtain the complete moment curvature relationships of a short reinforced concrete column, subjected to axial load and biaxial bending moments, at all load levels. The method is found to be extremely powerful and efficient for computer solution.

The computer program based on this formulation can be integrated into the long column analysis or into overall structural analysis programs, and is probably very useful and essential in such a study.

Résumé

On développe une formulation analytique des équations force/déformation en termes de l'accroissement permettant d'obtenir les relations complètes de moment/courbure d'une courte colonne en béton armé soumise à une charge axiale et à des moments de flexion biaxiaux pour tous les degrés de charges. La méthode est extrêmement efficace pour la solution par ordinateur. Le programme d'ordinateur basé sur cette formulation peut être intégré dans l'analyse de colonnes longues ou dans tous les programmes d'analyse structurale et s'avérera probablement très utile.

Zusammenfassung

Es wird eine rechnerische Formulierung der Kraft/Deformations-Gleichungen in Termen des Zuwachses entwickelt, die es gestattet, die vollständige Moment/Krümmungsbeziehung einer kurzen Stahlbetonstütze unter Einfluss axialer Belastungsstufen zu erfassen. Die Methode erwies sich als äusserst wirksam und

brauchbar für eine Lösung mittels Computer. Das auf der Formulierung beruhende Computerprogramm lässt sich entweder auf die Berechnung für lange Stützen oder auf alle baulichen Rechenprogramme anwenden und erweist sich voraussichtlich als ebenso nützlich wie wesentlich.

Analysis of Metal Plate-Stringer-Diaphragm Bridge Decks

Analyse de tabliers métalliques renforcés par entretoises longitudinales et transversales

Berechnung von Brückenfahrbahnen aus Metallplatten mit Längs- und Querverstreibungen

D.L. DEAN

Professor of Civil Engineering, North Carolina
State University, Raleigh, North Carolina U.S.A.

R.R. AVENT

Assistant Professor, Civil Engineering, Georgia
Institute of Technology Atlanta, Georgia U.S.A.

Introduction

The object of this paper is the derivation of formulas for the analysis of deck systems constructed of thin plates reinforced and composite with a set of equally spaced longitudinal stringers which are braced by a set of equally spaced transverse diaphragms (see Fig. 1). The formulas will be applicable for the design of cellular decks-systems with both top and bottom plates — as well as orthotropic decks-systems with a top plate only. Specifically, the formulas are for the exact elastic analysis of those systems that 1) are proportioned and detailed so that all

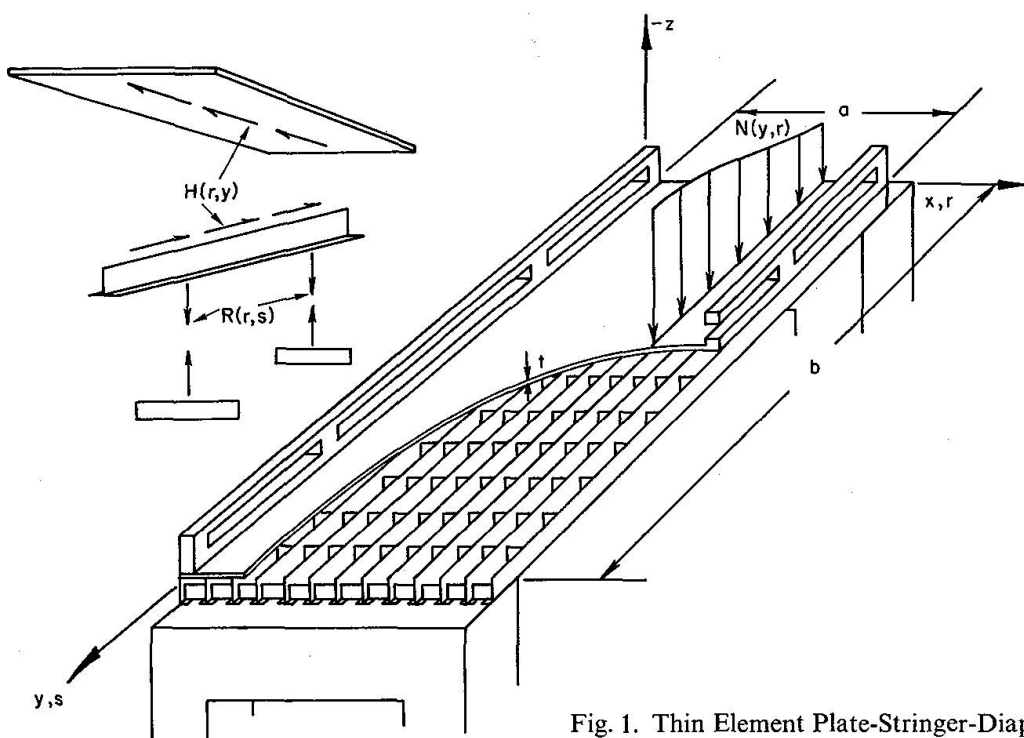


Fig. 1. Thin Element Plate-Stringer-Diaphragm Deck.

components have negligible out-of-plane stiffness and 2) are simply supported at the ends. Thus, the linear superposition of several solutions is required to analyze decks that are continuous over intermediate supports.

The thin element plate-stringer-diaphragm deck in either cellular or orthotropic form is one of the most efficient load carrying systems employed by designers today and the literature includes many references to recommended methods of analysis. However, none of the existing methods are rationally based even though some are rather complex and require voluminous computations. The present methods of analysis fall into three categories, 1) use of totally empirical design formulas to compute an "effective flange width" and the distribution of loads between the resulting "T" beam stringers (8); 2) use of a "smearing out" technique to replace the mixed discrete-continuous system by an "equivalent" (usually orthotropic) continuum (5, 9) and 3) use of a discrete or latticed system to approximate the real system through a finite difference or finite element approach (1, 7).

The "equivalent continuum" method is attractive in that a single continuum solution can be used for preliminary design studies of a variety of discrete-continuous deck systems; however, the steps of selecting the substitute continuum and interpreting the results for the real system lack rational bases and introduce significant errors for coarse lattices and those closely stiffened decks with relatively stiff ribs. Also, the solution for the approximate continuous model is often more difficult and less elegant than the solution for the exact discrete-continuous model.

Of the various substitute lattice approaches the finite element method is currently the most popular and canned programs are available for office use; however, their use for numerous alternate designs is quite expensive due to the voluminous computations and the extensive input data required for each case. Furthermore the state of the art of error analysis for this method is not sufficiently well developed to insure against errors which are orders of magnitude larger than predicted. One example of such a situation is the case of a deck with stiff ribs and a flexible plate so that the higher harmonics contribute significantly to the deflection field. In such a case it is extremely difficult to get a meaningful stress analysis via a finite element approach.

The concept of deriving exact formulas for the elastic analysis of reinforced bridge decks is not entirely new as both the micro discrete field approach (i.e. use of difference equation models) (2) and the macro discrete field approach (i.e. use of summation equation models) (3, 4) have been used for the rational analysis of ribbed plates or decks composite with supporting stringers. This paper extends the use of the macro approach to thin plates supported by both stringers and diaphragms and thus covers the more general concept of an orthotropic deck.

It is proposed that the exact elastic analysis presented herein be used for final design review. (While the formulas may be considered complex for manual computations, they can be conveniently employed through the use of a small computer or one of the several programmable electronic desk calculators that have recently come on the market). A secondary goal is to make available a standard analysis for use in studying existing and proposed approximate formulas in order to establish range of applicability, magnitude of errors, etc. This should obviate the unsatisfactory practice of making judgements based upon comparison of one empirical method with another empirical method.

The major results are numerically illustrated through use of the formulas for the analysis of realistic structures. One bridge is also analyzed by a finite element method for comparative purposes.

Mathematical Model

A macro discrete field approach (3) is used to find the in-plane interactive forces, $H(r, y)$, between the stringers and the plate and the out-of-plane interactive forces, $R(r, s)$, between the stringers and the diaphragms (see Fig. 1). The macro approach is dictated by the fact that an analysis of the entire top plate is tractable for a general loading due to the simple end support conditions at $y = 0$ and b . A rational micro discrete field approach, on the other hand, is not possible as it requires the general boundary solution for a typical rectangular plate element, between two successive stringers and diaphragms, which is unavailable.

The solutions for continuous and discrete deflection or force fields are found in terms of infinite and finite sinusoidal series, respectively. For example the unknown horizontal interactive forces between the top of the stringers and the plate is expressed as follows:

$$H(r, y) = \sum_{j=1}^{\infty} \sum_{k=1}^{m-1} H_{kj} \sin \frac{k\pi r}{m} \cos \bar{\alpha}_j y \quad (1)$$

$$H_{kj} = \frac{4}{mb} \sum_{r=1}^{m-1} \int_0^b H(r, y) \sin \frac{k\pi r}{m} \cos \bar{\alpha}_j y dy \quad (2)$$

in which $\bar{\alpha}_j = \frac{j\pi}{b}$ and $r = 1, (1), m - 1$.

The continuous plate deflections can be found in terms of the unknown stringer plate interactive forces as follows:

$$u(x, y) = u^h(x, y) + \sum_{\alpha=1}^{m-1} \int_0^b H(\alpha, \eta) K^{uy}(x, y, \frac{a}{m} \alpha, \eta) d\eta \quad (3)$$

$$v(x, y) = v^h(x, y) + \sum_{\alpha=1}^{m-1} \int_0^b H(\alpha, \eta) K^{vy}(x, y, \frac{a}{m} \alpha, \eta) d\eta \quad (4)$$

in which K^{uy} and K^{vy} are the kernel functions for u and v respectively due to a unit impulse load in the y direction on the plate with simple edge supports (see Eqs. A-2-5) and u^h and v^h are the homogeneous solutions due to the side boundary displacements $v^h(\frac{a}{m}, y)$ (see Eqs. A-8-13).

Substitution of Eqs. A-2, A-3, A-8, and A-9 and use of the relation given in Eq. 2, gives the following series for the continuous plate displacements in terms of the boundary displacement coefficients \bar{V}_{ij} and the interactive force coefficients H_{kj} :

$$u(x, y) = \sum_{j=1}^{\infty} \sum_{i=0}^{\infty} \left(\frac{4}{a} \phi_i^* \bar{V}_{ij} \bar{A}_{ij}^* + \frac{m}{a} H_{ij} \bar{A}_{ij}^* \right) \cos \alpha_i x \sin \bar{\alpha}_j y \quad (5)$$

$$v(x, y) = \sum_{j=1}^{\infty} \sum_{i=1}^{\infty} \left(\frac{4}{a} \bar{V}_{ij} \bar{B}_{ij}^* + \frac{m}{a} H_{ij} B_{ij}^* \right) \sin \alpha_i x \cos \bar{\alpha}_j y \quad (6)$$

in which H_{ij} is sine wise cyclic, having a period of $2m$, with respect to the first index and the coefficients \bar{A}_{ij} , \bar{B}_{ij} , \bar{A}_{ij} and \bar{B}_{ij} are given by Eqs. A-4, A-5, A-12 and A-7 respectively. The stringer line displacements $v(r, y)$ can be expressed as a mixed finite-infinite series thru use of Eq. A-17 with the following results:

$$v(r, y) = \sum_{j=1}^{\infty} \sum_{k=1}^{m-1} \left[\frac{4}{m} \bar{V}_{kj} \bar{B}_{kj} + H_{kj} B_{kj} \right] \sin \frac{k\pi r}{m} \cos \bar{\alpha}_j y \quad (7)$$

in which B_{kj} and \bar{B}_{kj} are given by Eqs. A-23, and A-24 respectively.

The stringer and diaphragm deflections depend upon the out-of-plane plate loads, $N(r, y)$, which are applied along the stringer lines, and the out-of-plane stringer-diaphragm interactive node forces, $R(r, s)$, as well as the in-plane plate-stringer interactive forces $H(r, y)$. The series expression for these additional quantities are:

$$N(r, y) = \sum_{j=1}^{\infty} \sum_{k=1}^{m-1} N_{kj} \sin \frac{k\pi r}{m} \sin \bar{\alpha}_j y \quad (8)$$

$$N_{kj} = \frac{4}{mb} \sum_{r=1}^{m-1} \int_0^b N(r, y) \sin \frac{k\pi r}{m} \sin \bar{\alpha}_j y dy \quad (9)$$

$$R(r, s) = \sum_{l=1}^{n-1} \sum_{k=1}^{m-1} R_{kl} \sin \frac{k\pi r}{m} \sin \frac{l\pi s}{n} \quad (10)$$

$$R_{kl} = \frac{4}{mn} \sum_{s=1}^{n-1} \sum_{r=1}^{m-1} R(r, s) \sin \frac{k\pi r}{m} \sin \frac{l\pi s}{n} \quad (11)$$

The series for the in-plane and out-of-plane displacements at the tops of the interior stringers can now be written as follows:

$$v(r, y) = \sum_{j=1}^{\infty} \sum_{k=1}^{m-1} \left[\bar{D}_j^* N_{kj} - \bar{B}_j^* H_{kj} - \frac{n}{b} \bar{D}_j^* R_{kj} \right] \sin \frac{k\pi r}{m} \cos \bar{\alpha}_j y \quad (12)$$

$$w(r, y) = \sum_{j=1}^{\infty} \sum_{k=1}^{m-1} \left[\bar{A}_j^* N_{kj} - \bar{D}_j^* H_{kj} - \frac{n}{b} \bar{A}_j^* R_{kj} \right] \sin \frac{k\pi r}{m} \sin \bar{\alpha}_j y \quad (13)$$

in which $r = 1, (1), m-1, 0 \leq y \leq b$, \bar{A}_j^* , \bar{B}_j^* and \bar{D}_j^* are given by Eq. A-27 and R_{kj} is sinewise cyclic on j with a period of $2n$ i.e. $R_{kl} = R_{k, 2Jn+l} = -R_{k, 2Jn-l}$ for integer values of J .

The double finite series for the out-of-plane stringer node deflections is found by use of Eq. A-17 as follows:

$$w(r, s) = \sum_{l=1}^{n-1} \sum_{k=1}^{m-1} \left[W_{kl}^N - W_{kl}^H - A_l R_{kl} \right] \sin \frac{k\pi r}{m} \sin \frac{l\pi s}{n} \quad (14)$$

in which $r = 1, (1), m-1, s = 0, (1), n$, A_l is given by Eq. A-29

$$W_{kl}^N = \sum_{J=-\infty}^{+\infty} \bar{A}_{2Jn+l}^* N_{k,2Jn+l} \simeq \bar{A}_l^* N_{kl} \quad (15a, b)$$

$$W_{kl}^H = \sum_{J=-\infty}^{+\infty} \bar{D}_{2Jn+l}^* H_{k,2Jn+l} \simeq \bar{D}_l^* H_{kl} \quad (16a, b)$$

The out-of-plane node deflections of the diaphragms depend upon the out-of-plane side boundary deflections as well as the stringer-diaphragm interactive forces.

$$w_a^{(0)}(y) = \sum_{j=1}^{\infty} (W_j^s \pm W_j^{a/s}) \sin \bar{\alpha}_j y \quad (17)$$

$$w(r, s) = \sum_{l=1}^{n-1} \sum_{k=1}^{m-1} [C_k \bar{W}_{kl}^f + A_k^d R_{kl}] \sin \frac{k\pi r}{m} \sin \frac{l\pi s}{n} \quad (18)$$

in which $r = 1, (1), m-1, s = 0, (1), n$, A_k^d is the discrete kernel function coefficient for a typical diaphragm, similar to Eq. A-29 for stringers, i.e.

$$A_k^d = \frac{1}{12B^d} \left(\frac{a}{m}\right)^3 \frac{3 - \sigma_k}{(\sigma_k)^2}; \quad \sigma_k = 1 - \cos \frac{k\pi}{m} \quad (19a, b)$$

and B^d equals the flexural rigidity of the diaphragm.

$$\bar{W}_{kl}^f = \sum_{J=-\infty}^{+\infty} \bar{W}_{k,2Jn+l} \quad (20a)$$

$$\bar{W}_{kj} = \begin{cases} W_j^s & \text{for } k \text{ odd} \\ W_j^{a/s} & \text{for } k \text{ even} \end{cases} \quad (20b)$$

$$1 = \sum_{k=1,3,\dots}^{m-1} C_k \sin \frac{k\pi r}{m}; \quad 1 - 2\frac{r}{m} = \sum_{k=2,4,\dots}^{m-1} C_k \sin \frac{k\pi r}{m} \quad (21a, b)$$

$$C_k = \frac{2}{m} \cot \frac{k\pi}{2m} \quad (21c)$$

The relations developed thus far are sufficient for the analysis of a deck system or orthotropic panel with known side boundary displacements, e.g. $\bar{V}_{kj} = \bar{W}_{kj} = 0$; however for the typical bridge deck one usually has to determine the side boundary displacements so as to establish compatibility with the boundary stringers, which have physical properties denoted by B^b , e^b and ρ^b and may be loaded as follows:

$$N_m^{(0)}(y) = \sum_{j=1}^{\infty} (P_j^s \pm P_j^{a/s}) \sin \bar{\alpha}_j y \quad (22)$$

The compatibility of boundary stringer and deck boundary displacements can be established by expressing the boundary stringer displacements in terms of their

applied loads plus the loads transferred to them by deck action. For example, consider the stringer at $r = 0$

$$v(0, y) = \int_0^b [P^t(0, \eta) K_b^{vz}(y, \eta) + T^t(0, \eta) K_b^{vy}(y, \eta)] d\eta \quad (23)$$

$$w(0, y) = \int_0^b [P^t(0, \eta) K_b^{wz}(y, \eta) + T^t(0, \eta) K_b^{wy}(y, \eta)] d\eta \quad (24)$$

in which the coefficients of K_b^{vz} , K_b^{vy} , K_b^{wz} , and K_b^{wy} are as given by Eq. A-27 except that all the interior stringer descriptors, B , e , and ρ , are replaced by boundary stringer descriptors, B^b , e^b and ρ^b to get \bar{A}_j^b , \bar{B}_j^b and \bar{D}_j^b . The quantities $P^t(0, \eta)$ and $T^t(0, \eta)$ represent total out-of-plane or transverse and in-plane or longitudinal load components applied to the boundary stringer from all effects. That is,

$$P^t(0, y) = N(0, y) + \sum_{\alpha=1}^{m-1} \sum_{\beta=1}^{n-1} R(\alpha, \beta) (1 - \frac{\alpha}{m}) \delta(y - \frac{\beta}{n}) \quad (25)$$

$$T^t(0, y) = n_{xy}^h(0, y) + \sum_{\alpha=1}^{m-1} \int_0^b H(\alpha, \eta) K^{Ty}(0, y, \frac{\alpha}{m}, \eta) d\eta \quad (26)$$

or carrying out the indicated operations

$$P^t(0, y) = \sum_{j=1}^{\infty} [(P_j^s + P_j^{a/s}) + \frac{mn}{4b} \sum_{k=1}^{m-1} C_k R_{kj}] \sin \bar{\alpha}_j y \quad (27)$$

$$T^t(0, y) = \sum_{j=1}^{\infty} [(\bar{T}_j^s V_j^s + \bar{T}_j^{a/s} V_j^{a/s}) + \sum_{k=1}^{m-1} \bar{B}_{kj} H_{kj}] \cos \bar{\alpha}_j y \quad (28)$$

in which \bar{T}_j^s and $\bar{T}_j^{a/s}$ are given by Eq. A-15 and \bar{B}_{kj} is given by Eq. A-24c.

All the necessary relations are now available to complete the mathematical model needed to solve for H_{kj} , R_{kl} , V_j^s (or $V_j^{a/s}$) and W_j^s (or $W_j^{a/s}$) as follows: 1) compatibility of in-plane stringer line displacements between the plate and the stringer tops is obtained by equating Eqs. 7 and 12; 2) compatibility of out-of-plane node displacements between the stringers and the diaphragms is obtained by equating Eqs. 14 and 18; 3) compatibility of in-plane boundary displacements is obtained by substituting Eqs. 27 and 28 into Eq. 23; and 4) compatibility of out-of-plane boundary displacements is obtained by substituting Eqs. 27 and 28 into Eq. 24. The resulting model (shown for symmetric component of boundary displacements) is:

$$(B_{kj} + \bar{B}_j^*) H_{kj} + \frac{n}{b} \bar{D}_j^* R_{kj} + \frac{4}{m} \bar{B}_{kj} V_j^s = \bar{D}_j^* N_{kj} \quad (29)$$

$$\sum_j \bar{D}_{2Jn+l}^* H_{k, 2Jn+l} + (A_k^d + A_l) R_{kl} + C_k \sum_j W_{2Jn+l}^s = \sum_j \bar{A}_{2Jn+l}^* N_{k, 2Jn+l} \quad (30)$$

$$\sum_k [\bar{B}_j^* \bar{B}_{kj} H_{kj} + \frac{mn}{4b} \bar{D}_j^* C_k R_{kj}] + [\bar{B}_j^* \bar{T}_j^s - 1] V_j^s = -\bar{D}_j^* P_j^s \quad (31)$$

$$\sum_k [\bar{D}_j^* \bar{B}_{kj} H_{kj} + \frac{mn}{4b} \bar{A}_j^* C_k R_{kj}] + \bar{D}_j^* \bar{T}_j^s V_j^s - W_j^s = -\bar{A}_j^* P_j^s \quad (32)$$

in which $J = -\infty, (1), +\infty$ with convergence about $J = 0$ and $k = 1, (2), m-1$. To solve for antisymmetric boundary displacements replace all s quantities by the analogous a/s quantities and use $k = 2, (2), m-1$. It is apparent that this model cannot be dealt with as a set of algebraic equations due to inconformability — i.e. Eq. 29 is for kj indexed quantities, Eq. 30 is for kl indexed quantities and Eqs. 31 and 32 are for j indexed quantities — and the fact that some terms are sums; however, as will be shown in subsequent sections, the simultaneous equations can be solved by successive elimination of unknowns.

Solution for Simple Side Supports

For the case of a panel or deck with known side boundary deflections, V_j^s (and/or $V_j^{a/s}$) and W_j^s (and/or $W_j^{a/s}$), Eqs. 31 and 32 are not needed and one can solve Eqs. 29 and 30 for H_{kj} and R_{kl} in terms of N_{kj} , V_j^s and W_j^s by using Eq. 29 to eliminate H_{kj} from Eq. 30 which is then solved for R_{kl} . For example, consider the title case of simple side supports, i.e. $V_j^s = V_j^{a/s} = W_j^s = W_j^{a/s} = 0$, such as an orthotropic or sandwich panel with relatively rigid supports along all four edges. The exact solution is:

$$H_{kj} = \frac{D_j^*(N_{kj} - \frac{n}{b} R_{kj})}{B_{kj} + \bar{B}_j^*} \quad (33)$$

$$R_{kl} = \frac{W_{kl}^N - A_{kl}^N}{A_l + A_k^d - \frac{n}{b} \bar{A}_{kl}^R} \quad (34)$$

in which \bar{B}_j^* and D_j^* are given by Eq. A-27; A_l and A_k^d are given by Eqs. A-29 and 20; B_{kj} is given by Eq. A-24; W_{kl}^N is given by Eq. 15; R_{kj} is sinewise cyclic on j with a period of $2n$; and the two special terms A_{kl}^N and \bar{A}_{kl}^R are:

$$A_{kl}^N = \sum_{J=-\infty}^{+\infty} \frac{(D_{2Jn+l}^*)^2 N_{k, 2Jn+l}}{B_{k, 2Jn+l} + \bar{B}_{2Jn+l}^*} \simeq \frac{(D_l^*)^2 N_{kl}}{B_{kl} + \bar{B}_l^*} \quad (35a, b)$$

$$\bar{A}_{kl}^R = \sum_{J=-\infty}^{+\infty} \frac{(D_{2Jn+l}^*)^2}{B_{k, 2Jn+l} + \bar{B}_{2Jn+l}^*} \simeq \frac{(D_l^*)^2}{B_{kl} + \bar{B}_l^*} \quad (36a, b)$$

It should be noted that for the simply supported panel each “k” (first index) load harmonic yields a single “k” solution harmonic but the effect of a j (second index) loading harmonic is different due to action of the diaphragms; i.e. each “j” loading harmonic yields 1) a single finite series “l” solution harmonic, whose relation to “j” is through $l = j - 2Jn$ or $2Jn - j$ ($l < n$) and 2) an infinite set of “j” solution harmonics related to j through $j' = 2Jn \pm j$.

An accurate approximate solution for H_{kj} and R_{kl} , which contains only algebraic terms, can be written by consistently truncating all the transformation series after the first term. (e.g. use $J = 0$ only so that Eqs. 35b and 36b are used instead of 35a and 26a). The accuracy of such a rational approximation increases as the

numbers of stringers, $m - 1$, and diaphragms, $n - 1$, increases. The result of this simplification of Eqs. 33 and 34 is:

$$H_{kj} \simeq \frac{\left(\frac{e}{\alpha_j}\right) (N_{kj} - \frac{n}{b} R_{kj})}{e^2 + \bar{\rho}_{kj}^2} \quad (37)$$

$$R_{kl} \simeq \frac{\frac{b}{n} N_{kl}}{1 + \psi_{kl} \left[\frac{e^2 + \bar{\rho}_{kl}^2}{\bar{\rho}_{kl}^2} \right]} \quad (38)$$

$$\bar{\rho}_{kj}^2 = \rho^2 + \left(\frac{mb}{aK}\right) \left(\frac{ja}{kb}\right)^2 \frac{\frac{2}{1-\mu} + \left(\frac{ja}{kb}\right)^2}{\left[1 + \left(\frac{ja}{kb}\right)^2\right]^2} \quad (39)$$

$$\psi_{kl} = \left(\frac{la}{kb}\right)^4 \left(\frac{mbB}{naB^d}\right) \quad (40)$$

These approximate formulas for H_{kj} and R_{kl} can be evaluated manually in less than 10 minutes.

Numerical Example 1

In order to illustrate the numerical use of the above solutions for a simply supported thin element plate-stringer-diaphragm system, consider a panel (similar to Fig. 1 except simply supported, on the sides as well as the ends) with physical data as follows:

$a = 144$ in.; $b = 72$ in., $m = 12$, $n = 4$, $t = .125$, $\mu = .3$, $E = 29,000$ ksi, $B = \frac{5}{3} E$ kip/in.², $e = 2.0$ in., $\rho^2 = \frac{4}{3}$ in.²; and $B^d = \frac{40}{3} E$ kip. in.². The out-of-plane stringer line load is harmonic; i.e. $N_{11} = .01$ kip/in. All other $N_{kj} = 0$ or $N(r, y) = (.01) \sin \frac{\pi r}{m} \sin \frac{\pi y}{b}$. Some of the intermediate results are: $\bar{A}_1^* = 5.7080$ in.²/kip, $\bar{B}_1^* = .05796$ in.²/kip, $\bar{D}_1^* = .49812$ in.²/kip (Eq. A-27); $W_{11}^N = .05708$ in. (Eq. 15a); $A_1 = .3173$ in./kip (Eq. A-29) or $A_1 \simeq .3171$ in./kip (Eq. A-28b); $A_1^d = .95134$ in./kip (Eq. 19); $K = 3983.5$ kip/in. (Eq. A-1); $\bar{B}_{1,1}^* = .14466$ in.³/kip (Eq. A-5); $B_{1,1} = .012770$ in.²/kip (Eq. A-23c) or $B_{1,1} \simeq .01205$ in.²/kip (Eq. A-23b); $A_{11}^N = .03508$ in. (Eq. 35a); $\bar{A}_{11}^R = 3.5096$ in.²/kip (Eq. 36a) or $\bar{A}_{11}^R \simeq 3.5081$ in.²/kip (Eq. 36b); $R_{11} = .0204897$ kip. Other $R_{kl} = 0$ (Eq. 34) or $R_{11} \simeq .0202$ kip (Eq. 38); and $H_{11} = .062410$ kip/in., $H_{1,7} = .000851$ kip/in., $H_{1,9} = -.000590$ kip/in., $H_{1,15} = .000268$ kip/in. and $H_{1,17} = -.000219$ kip/in. (Eq. 33) or $H_{11} \simeq .06316$ kip/in. (Eq. 37). These intermediate results were used in the deflection field equations with the following results (inch units): The out-of-plane node deflections (Eq. 19 with $\bar{W}_{kl}^f = 0$) are

$$w(r, s) = (.019493) \sin \frac{\pi r}{m} \sin \frac{\pi y}{b}.$$

The out-of-plane stringer line deflections (Eq. 13) are

$$w(r, y) = (.019495) \sin \frac{\pi r}{m} \left[\sin \frac{\pi y}{b} + .000075 \sin \frac{7\pi y}{b} - .000030 \sin \frac{9\pi y}{b} + .000004 \sin \frac{15\pi y}{b} - .000003 \sin \frac{17\pi y}{b} + \dots \right]$$

The in-plane stringer line deflections (Eq. 12 or Eq. 7) with $\bar{V}_{kj} = 0$ are:

$$v(r, y) = (7.9695 \times 10^{-4}) \sin \frac{\pi r}{m} \left[\cos \frac{\pi y}{b} + .00081 \cos \frac{7\pi y}{b} - .00045 \cos \frac{9\pi y}{b} + .00012 \cos \frac{15\pi y}{b} - .00009 \cos \frac{17\pi y}{b} + \dots \right]$$

and the continuous in-plane plate deflections (Eq. 6 with $\bar{V}_{ij} = 0$) are:

$$v(x, y) = (7.5238 \times 10^{-4}) \sin \frac{\pi x}{a} \left[\cos \frac{\pi y}{b} + .00025 \cos \frac{7\pi y}{b} + .00011 \cos \frac{9\pi y}{b} + \dots \right] - (.1463 \times 10^{-4}) \sin \frac{23\pi x}{a} \cos \frac{\pi y}{b} + (.12408 \times 10^{-4}) \sin \frac{25\pi x}{a} \cos \frac{\pi y}{b} + \dots$$

Note that convergence is rapid even for this case of a relatively small number of diaphragms, $n = 4$.

Analysis of Cellular Decks

As mentioned in the introduction, formulas for the exact elastic analysis of an orthotropic deck can also be used for the analysis of cellular decks that are symmetric about the middle plane, i.e. the top and bottom plates have equal thicknesses. All that is required is to modify the input data for an orthotropic deck so as to produce a condition of anti-symmetry with respect to the middle plane as follows: 1) use only the antisymmetric component of the top and bottom stringer line loads (the symmetric component only squeezes the stringers and can be ignored); 2) use one half the actual flexural rigidity of the stringers B and B^b , and diaphragms, B^d ; and 3) use radius of gyration, ρ and ρ^b equal to zero (or if stringer representation is flexural rigidity and cross sectional area use an area approaching infinity).

Numerical Example 2

In order to briefly illustrate modification of data for the analysis of a cellular panel, consider the investigation of a cellular design alternative to example 1 using the same amount of material; i.e., same stringers and diaphragms but two 1/16 in. plates instead of a single 1/8 in. plate. For this case, the input data are $a = 144$ in., $b = 72$ in., $m = 12$, $n = 4$, $t = .0625$ in., $\mu = .3$, $E = 29000$ ksi., $B = \frac{5}{6} E$ kip/in.², $e = 2.0$ in., $\rho^2 = 0$, $B^d = \frac{20}{3} E$ kip/in.² and $N_{11} = .005$ kip/in. (other $N_{kj} = 0$). The calculations are too similar to those for Example 1 to warrant showing detailed results, but a design comparison can be made by showing the out-of-plane node deflections as follows:

$$w(r, s) = (.01205) \sin \frac{\pi r}{m} \sin \frac{\pi s}{n}$$

That is, the cellular construction gives a 62% stiffer panel with the same amount of material.

Solution for Flexible Side Supports

The most general case considered in this paper is that of an orthotropic deck with flexible side supports. The two identical boundary stringers are of an arbitrary size and shape with arbitrary loads. The analysis allows for possibility that the boundary stringers are also composite with the deck plate, but detailing for non-composite action can be dealt with by setting the boundary stringer eccentricity, e^b , equal to zero. For this general case, one must solve Eqs. 29-32 for H_{kj} , R_{kl} , V_j^s (or $V_j^{a/s}$) and W_j^s (or $W_j^{a/s}$) in terms of the load coefficients N_{kj} and P_j^s (or $P_j^{a/s}$). This exact elastic model can be formally reduced to a single equation with one unknown by successive elimination as was done with the two equation model for the simple side support case; however, the results for the four equation model are unwieldy and many of the coefficients are sums of obscure physical significance. (Even in the simpler case of simultaneous algebraic equations, it is seldom practical to derive an explicit formula solution for a model with more than three equations). For this model, convergence of the series summed on J is very rapid and indications are that computers, or programmable calculators will normally be used to get numerical results; thus, an alternate procedure is recommended as follows:

1. Truncate the series on H_{kj} and W_j^s in Eq. 30 after one term (i.e. use $J = 0$ only) and solve Eqs. 29 and 30 simultaneously for H_{kl} and R_{kl} ($l < n$) in terms of N_{kl} , V_l^s (or $V_l^{a/s}$) and W_l^s (or $W_l^{a/s}$).
2. Substitute the results of step 1 into Eqs. 31 and 32 solve the resulting algebraic equation for V_l^s (or $V_l^{a/s}$) and W_l^s (or $W_l^{a/s}$).
3. Substitute results of step 2 into the results of step 1 to find H_{kl} and R_{kl} .
4. Use the cyclic properties of R_{kj} (e.g. $R_{kl} = R_{k, 2n+l} = R_{k, l-2n}$) to solve Eqs. 29 and 31 for the higher harmonics of H_{kj} and V_j^s ($j > n$) and then substitute into Eq. 32 to find the higher harmonics of W_j^s . (That is, first use Eq. 29 to eliminate H_{kj} from Eq. 31 and solve for V_j^s (or $V_j^{a/s}$). Then find H_{kj} from Eq. 29 and, in turn, W_j^s from Eq. 32).
5. If unusual accuracy is required, retain additional terms in the summations of H_{kj} and W_j^s in Eq. 30 ($J = -2$ to $+2$ is sufficient), solve for improved results for R_{kl} and repeat step 4. (In most cases, the results obtained in step 4 on the initial cycle are sufficiently accurate so that step 5 can be omitted).

This completes the algorithm for the general case of flexible side supports. Note that the effects of the side boundary deflections invalidate the one-to-one relation between the "k" loading and solution harmonics that existed for the case of simple side supports. For example, a single "k odd" loading harmonic will normally cause a deflection field with series coefficients containing all possible k odd harmonics. The relation between the "j" (second index) loading and solution harmonics is as described in the section on simple side supports.

Numerical Example 3

In order to illustrate numerical use of the general bridge deck formulas under loading conditions which place a severe test on the convergence of the solution series, consider a bridge with the following physical parameters and loading:

$a = 360$ in., $b = 720$ in.; $m = 12$; $n = 4$; $t = .375$ in.; $\mu = .29$; $E = 29000$ ksi; $B = B^b = 10.2681 \times 10^6$ kip in.²; $e = e^b = 14.4286$ in., $\rho = \rho^b = 5.807$ in. and $B^d = 8.41 \times 10^6$ kip in.². The loading consists of two symmetrically placed 20 kip concentrated loads, i.e. $N(r, y) = 20(\delta_r^5 + \delta_r^7) \delta(y - \frac{b}{2})$ or $N_{kj} = \frac{8P}{mb} (-1)^{\frac{k-1}{2}} (-1)^{\frac{j-1}{2}} \cos \frac{k\pi}{m} (k \text{ and } j \text{ odd only})$ and $P_j^s = P_j^{as} = 0$. The combination of a relatively small number of stringers and diaphragms and loads of infinite intensity tend to show a harmonic analysis in a poor light due to slow convergence; however, as the results below indicate, even for this case the convergence is quite good, yielding practical results after only a small numbers of terms.

Some of the intermediate results are:

$K = 11,873$ kip/in. (Eq. A-1); $\bar{A}_1^* = 268.68$ in.²/kip, $\bar{B}_1^* = 1.2374$ in.²/kip and $\bar{D}_1^* = 16.915$ in.²/kip (Eq. A-27); $B_{11} = 0.07295$ in.²/kip (Eq. A-23); $W_{11}^N = 4.8088$ in. (Eq. 15); $A_1 = 1.494$ in./kip, (Eq. A-29) $\bar{A}_1^d = .6834$ in./kip. (Eq. 19); $\bar{B}_{11} = 2.2456$ (Eq. A-24); and $\bar{T}_1^s = -26.179$ ksi (Eq. A-15). $V_1^s = .01530$ in., $W_1^s = .2818$ in. (step 2 of algorithm p. 52); $H_{11} = .1705$ kip/in., $R_{11} = .7203$ kip (step 3 of algorithm p. 52); $V_7^s = -1.123 \times 10^{-5}$ in., $H_{17} = -.02362$ kip/in., $W_7^s = -5.213 \times 10^{-5}$ in., (step 4 of algorithm p. 52); $R_{11} = .7195$ kip (step 5 of algorithm p. 52 which confirms that recycling is unnecessary).

The deflection fields are as follows:

$$v(r, y) = [23.97 \cos \frac{\pi y}{b} - 1.318 \cos \frac{3\pi y}{b} + .2976 \cos \frac{5\pi y}{b} + \dots] 10^{-3} \sin \frac{\pi r}{m} + [5.774 \cos \frac{\pi y}{b} + .7076 \cos \frac{3\pi y}{b} - .1253 \cos \frac{5\pi y}{b} + \dots] 10^{-3} \sin \frac{3\pi r}{m} + [3.261 \cos \frac{\pi y}{b} + .01996 \cos \frac{3\pi y}{b} - .00567 \cos \frac{5\pi y}{b} + \dots] 10^{-3} \sin \frac{5\pi r}{m} + \dots$$

$$w(r, y) = [848.0 \sin \frac{\pi y}{b} - 14.20 \sin \frac{3\pi y}{b} + 1.876 \sin \frac{5\pi y}{b} + \dots] 10^{-3} \sin \frac{\pi r}{m} + [92.89 \sin \frac{\pi y}{b} + 7.133 \sin \frac{3\pi y}{b} - .8491 \sin \frac{5\pi y}{b} + \dots] 10^{-3} \sin \frac{3\pi r}{m} + [62.07 \sin \frac{\pi y}{b} - .1742 \sin \frac{3\pi y}{b} + .01886 \sin \frac{5\pi y}{b} + \dots] 10^{-3} \sin \frac{5\pi r}{m} + \dots$$

The membrane stress resultant field, n_y , (from Eq. A-1) is

$$n_y(x, y) = -K \{ [.0944 \sin \frac{\pi y}{b} - .01433 \sin \frac{3\pi y}{b} + .005499 \sin \frac{5\pi y}{b} + \dots] 10^{-3} \sin \frac{\pi x}{a} + [.02460 \sin \frac{\pi y}{b} + .003893 \sin \frac{3\pi y}{b} - .002209 \sin \frac{5\pi y}{b} + \dots] 10^{-3} \sin \frac{3\pi x}{a} + [.01533 \sin \frac{\pi y}{b} + .00067 \sin \frac{3\pi y}{b} - .000239 \sin \frac{5\pi y}{b} + \dots] 10^{-3} \sin \frac{5\pi x}{a} + \dots$$

The membrane stress resultant, n_y , at the center of the deck ($x = \frac{a}{2}$, $y = \frac{b}{2}$) is $n_y = 1.293$ kips/in. The finite element analysis described in the next section yields a stress $n_y = 1.179$, 1.192 or 1.419 kips/in. depending upon type of element utilized.

Comparison with Alternative Approaches

For comparative purposes the bridge system analyzed for Example 3 was also analyzed by use of a more comprehensive theoretical model and by use of discretized or finite element model.

The more comprehensive theoretical model was one which included the out-of-plane stiffness or flexural actions of the deck plate as well as its inplane stiffness. The composite membrane-flexural model treated $N(r, y)$ as an unknown out-of-plane interactive force between the stringers and the plate and rationally accounted for the effects of deck loads applied between stringers. The computations were

thus complicated considerably but gave essentially the same deflection field, for example the maximum difference for $w(r, y)$ was 2.3% which confirmed the authors' hypothesis that the composite membrane model (Eqs. 29-32) is sufficiently sophisticated to analyze metal deck bridges of orthotropic design.

There was also some question as to the need for a rational theoretical analysis in view of the availability of various open form finite element programs which can be modified to approximately model such decks. A space frame program (for the stringers, diaphragms and pseudo stud members of length e to model composite action) was combined with a finite element plane stress program (using elements whose width equaled the stringer spacing and length equaled $\frac{1}{3}$ the diaphragm spacing) to analyze the deck as an "equivalent" framework. Even though double symmetry was utilized, this relatively coarse network required two orders of magnitude more computing time than did the formula approach (which incidently was written to give research accuracy rather than computational efficiency) and, of more significance, required nearly three orders of magnitude more input information (only one card is needed to read in data for the theoretical approach). The finite element results were in error by up to 10% for deflections and the plate stress distributions bore little resemblance to the exact results. The need for rationally based formulas appeared to be confirmed.

Conclusions

Formulas were introduced which provide the designer with an exact elastic analysis of thin element bridge decks consisting of a set of evenly spaced stringers that are composite with a rectangular plate and are braced by a set of evenly spaced diaphragms. The system is simply supported at the ends with simple or flexible side supports. The loading consists of an arbitrary distribution of stringer line loads. The solution is readily modified to analyze cellular decks or, through superposition, decks with intermediate supports.

The formulas are simple enough for manual use if the loading can be adequately represented by one or two sinusoidal harmonics but in most cases the designer will probably prefer to use a small programmable calculator or a computer. Additional work using these exact formulas seems indicated to modify and determine applicable range for the various empirical formulas presently in use and possibly to point the way toward a more accurate finite element analysis.

Acknowledgments

This paper is based on research carried out as part of the Highway Research Program at North Carolina State University at Raleigh in co-operation with the North Carolina State Highway Commission and the United States Department of Transportation, Bureau of Public Roads. Computer services for this presentation including comparative finite element studies, were provided by the Georgia Institute of Technology.

Reference Formules

Membrane Analysis. — Certain formulas from the classical plane stress elasticity solution for a rectangular plate subjected to in-plane loads and boundary displacements (see Fig. A-1) are needed to account for composite action between the plate and stringers.

The membrane stress resultants, in terms of in-plane displacements, are:

$$\begin{bmatrix} n_x(x, y) \\ n_{xy}(x, y) \\ n_y(x, y) \end{bmatrix} = K \begin{bmatrix} D_x & \mu D_y \\ \frac{1-\mu}{2} D_y & \frac{1-\mu}{2} D_x \\ \mu D_x & D_y \end{bmatrix} \begin{bmatrix} u(x, y) \\ v(x, y) \end{bmatrix} \quad (\text{A-1})$$

in which D denotes differentiation with respect to the indicated variable, μ equals poissons ratio and $K = Et/(1 - \mu^2)$.

The kernel function solutions for the u and v displacements due to a unit concentrated load in y direction are:

$$K^{uy}(x, y, \xi, \eta) = \frac{4}{ab} \sum_{j=1}^{\infty} \sum_{i=1}^{\infty} \bar{A}_{ij}^* \sin \alpha_i \xi \cos \bar{\alpha}_j \eta \cos \alpha_i x \sin \bar{\alpha}_j y \quad (\text{A-2})$$

$$K^{vy}(x, y, \xi, \eta) = \frac{4}{ab} \sum_{j=0}^{\infty} \sum_{i=1}^{\infty} \bar{\phi}_j^* \bar{B}_{ij}^* \sin \alpha_i \xi \cos \bar{\alpha}_j \eta \sin \alpha_i x \cos \bar{\alpha}_j y \quad (\text{A-3})$$

in which $\alpha_i = \frac{i\pi}{a}$, $\bar{\alpha}_j = \frac{j\pi}{b}$, $\bar{\phi}_j^* = 1 - \frac{1}{2} \delta_j^0$.

$$\bar{A}_{ij}^* = \left(\frac{-1}{K} \right) \frac{(1 + \mu) \alpha_i \bar{\alpha}_j}{(1 - \mu) (\alpha_i^2 + \bar{\alpha}_j^2)^2} \quad (\text{A-4})$$

$$\bar{B}_{ij}^* = \frac{1}{K} \frac{2 \alpha_i^2 + (1 - \mu) \bar{\alpha}_j^2}{(1 - \mu) (\alpha_i^2 + \bar{\alpha}_j^2)^2} \quad (\text{A-5})$$

It should be noted that the displacement kernel functions K^{uy} and K^{vy} are for a plate that is simply supported along all four edges i.e. $u(x, \frac{0}{b}) = n_y(x, \frac{0}{b}) = 0$ and $v(\frac{0}{a}, y) = n_x(\frac{0}{a}, y) = 0$.

The in-plane membrane shear, n_{xy} , due to the above impulse loading is:

$$K^{Ty}(x, y, \xi, \eta) = \frac{4}{ab} \sum_{j=0}^{\infty} \sum_{i=1}^{\infty} \bar{\phi}_j^* \bar{B}_{ij}^* \sin \alpha_i \xi \cos \alpha_j \eta \cos \alpha_i x \cos \bar{\alpha}_j y \quad (\text{A-6})$$

$$\bar{B}_{ij}^* = \frac{\alpha_i (\alpha_i^2 - \mu \bar{\alpha}_j^2)}{(\alpha_i^2 + \bar{\alpha}_j^2)^2} \quad (\text{A-7})$$

The homogeneous membrane solutions due to known boundary displacements are:

$$v^h(\frac{0}{a}, y) = \sum_{j=1}^{\infty} (V_j^s \pm V_j^{a/s}) \cos \bar{\alpha}_j y \quad (\text{A-8})$$

$$v^h(x, y) = \frac{4}{a} \sum_{j=1}^{\infty} \sum_{i=1}^{\infty} \bar{V}_{ij} \bar{B}_{ij}^* \sin \alpha_i x \cos \bar{\alpha}_j y \quad 0 < x < a \quad (\text{A-9})$$

$$\bar{V}_{ij} = \begin{cases} V_j^s & \text{for } i \text{ odd} \\ V_j^{a/s} & \text{for } i \text{ even} \end{cases}$$

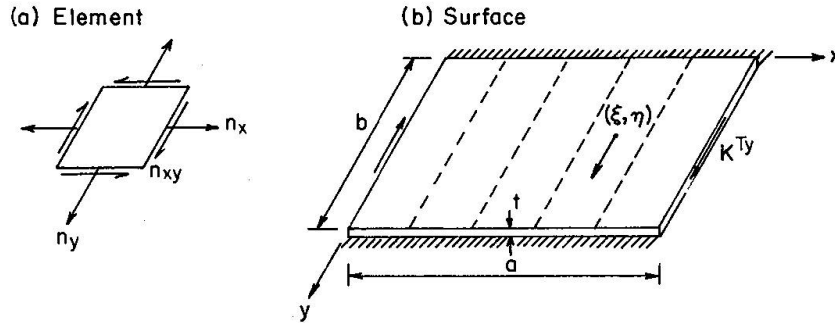


Fig. A-1. Membrane deck action.

$$u^h(x, y) = \frac{4}{a} \sum_{j=1}^{\infty} \sum_{i=0}^{\infty} \phi_i \bar{V}_{ij} \bar{A}_{ij}^* \cos \alpha_i x \sin \bar{\alpha}_j y \quad (\text{A-11})$$

$$\bar{A}_{ij}^* = \frac{\bar{\alpha}_j(\bar{\alpha}_j^2 - \mu \alpha_i^2)}{(\alpha_i^2 + \bar{\alpha}_j^2)^2} \quad (\text{A-12})$$

Many applications require use of the following more rapidly converging mixed formulas for v^h

$$v^h(x, y) = \sum_{j=1}^{\infty} [V_j^s + V_j^{a/s} (1 - 2\frac{x}{a}) + \frac{4}{a} \sum_{i=1}^{\infty} \bar{V}_{ij} (\bar{B}_{ij}^* - \frac{1}{\alpha_i}) \sin \alpha_i x] \cos \bar{\alpha}_j y \quad 0 \leq x \leq a \quad (\text{A-13})$$

The boundary membrane shears due to known boundary displacements are:

$$n_{xy}^h(0, y) = \sum_{j=1}^{\infty} [V_j^s \bar{T}_j^s \pm V_j^{a/s} \bar{T}_j^{a/s}] \cos \bar{\alpha}_j y \quad (\text{A-14})$$

$$\left[\frac{\bar{T}_j^s}{\bar{T}_j^{a/s}} \right] = -\frac{K}{2} (1 - \mu^2) \bar{\alpha}_j \left[\frac{\sinh a \bar{\alpha}_j \pm a \bar{\alpha}_j}{\cosh a \bar{\alpha}_j \pm 1} \right] \quad (\text{A-15})$$

Series Transformation. — For a macro discrete field analysis, one typically needs to express a discrete function as a finite sinusoidal series when the function is given as a infinite sinusoidal series evaluated at evenly spaced intervals of the independent variable. Thus it is required to transform a special infinite series into a finite series; i.e.

$$f(x) \Big|_{x=\frac{a}{m}r} = \sum_{i=1}^{\infty} \bar{A}_i^* \sin \frac{ir}{m} = \sum_{k=1}^{m-1} A_k \sin \frac{k\pi r}{m} \quad (\text{A-16 a, b})$$

The formula for the finite series coefficients, A_k , in terms of the infinite series coefficients \bar{A}_i^* (see Ref. 3) is:

$$A_k = \sum_{I=-\infty}^{+\infty} \bar{A}_{2Im+k}^* \quad (\text{A-17})$$

These transformation series are often available in closed form; for example see Ref. (6).

Another typical problem is that of expressing a discrete load function, for example a set of evenly spaced concentrated loads, as a continuous function in the form of an infinite sinusoidal series. Consider the following functional form

$$\bar{P}(x) = \sum_{\alpha=1}^{m-1} P(\alpha) \delta(x - \frac{a}{m}\alpha) \quad (\text{A-18})$$

in which the discrete load function, P , is available as a finite series, i.e.

$$P(\alpha) = \sum_{k=1}^{m-1} P_k \sin \frac{k\pi\alpha}{m} \quad (\text{A-19})$$

$$P_k = \frac{2}{m} \sum_{\alpha=1}^{m-1} P(\alpha) \sin \frac{k\pi\alpha}{m} \quad (\text{A-20})$$

Substituting the infinite series for the Dirac delta function in Eq. A-18 and making use of Eq. A-20 gives the following infinite series for the set of concentrated loads.

$$\bar{P}(x) = \sum_{i=1}^{\infty} \frac{m}{b} P_i \sin \alpha_i x \quad (\text{A-21})$$

in which P_i is sine wise cyclic with a period of $2m$ for values of the index outside the normal finite series range of 0 thru m ; i.e.,

$$P_k = P_{2Im+k} = -P_{2Im-k} = P_{k-2Im} \quad (\text{A-22 a, b, c})$$

for all integer values of I .

Stringer Line Quantities. — In order to satisfy displacement compatibility between a membrane and a set of composite stringers it is necessary to transform certain of the double infinite series in the continuous membrane analysis to mixed finite-infinite series for quantities evaluated only along stringer lines. Some of the required transformations are as follows:

$$B_{kj} = \frac{m}{a} \sum_{I=-\infty}^{+\infty} \bar{B}_{2Im+k, j}^* \simeq \frac{m}{a} \bar{B}_{kj}^* \\ B_{kj} = \left(\frac{a}{K} \right) \frac{1}{4m(1-\mu) \bar{D}_{kj}} \left[\frac{3-\mu}{\bar{\lambda}_j} \sinh \bar{\lambda}_j + \frac{1+\mu}{\bar{D}_{kj}} (1 - \cosh \bar{\lambda}_j \cos \frac{k\pi}{m}) \right] \quad (\text{A-23 a, b, c})$$

$$\bar{B}_{kj} = \frac{m}{a} \sum_{I=-\infty}^{+\infty} \bar{B}_{2Im+k,j}^* \simeq \frac{m}{a} \bar{B}_{kj}^*$$

$$\bar{B}_{kj} = \frac{\sin \frac{k\pi}{m}}{4\bar{D}_{kj}} \left[2 - \frac{(1+\mu) \bar{\lambda}_j \sinh \bar{\lambda}_j}{\bar{D}_{kj}} \right] \quad (\text{A-24 a, b, c})$$

$$\text{in which } \bar{\lambda}_j = \frac{a}{m} \bar{\alpha}_j, \bar{D}_{kj} = \cosh \bar{\lambda}_j - \cos \frac{k\pi}{m} \quad (\text{A-25 a, b})$$

Stringer Analysis. — For the analysis of a deck in which the top surface is composite with the stringers, a set of beam kernel functions (often termed a Green's tensor) is required to give the longitudinal and transverse displacement fields at the top of the stringer due to independent unit impulse longitudinal and transverse loads, that is, for $N(y) = \delta(y-\eta)$ the w and v displacements are K^{wz} and K^{vz} respectively while for $F(y) = \delta(y-\eta)$ the w and v displacements are K^{wy} and K^{vy} respectively (see Fig. A-2). The required kernel functions are

$$\begin{bmatrix} K^{wz}(y, \eta) & K^{wy}(y, \eta) \\ K^{vz}(y, \eta) & K^{vy}(y, \eta) \end{bmatrix} = \frac{2}{b} \sum_{j=1}^{\infty} \begin{bmatrix} \bar{A}_j^* \sin \bar{\alpha}_j \eta \sin \bar{\alpha}_j y & \bar{D}_j^* \cos \bar{\alpha}_j \eta \sin \bar{\alpha}_j y \\ \bar{D}_j^* \sin \bar{\alpha}_j \eta \cos \bar{\alpha}_j y & \bar{B}_j^* \cos \bar{\alpha}_j \eta \cos \bar{\alpha}_j y \end{bmatrix} \quad (\text{A-26})$$

in which

$$\bar{A}_j^* = \frac{1}{B\bar{\alpha}_j^4}; \bar{D}_j^* = \frac{e}{B\bar{\alpha}_j^3}; \bar{B}_j^* = \frac{\rho^2 + e^2}{B\bar{\alpha}_j^2} \quad (\text{A-27 a, b, c})$$

B equals the flexural rigidity of the stringer, e equals the eccentricity of the longitudinal loads with respect to the stringer centroid and ρ equals the radius of gyration with respect to the cross sectional axis parallel to the deck surface. (Note that the term with \bar{B}_0^* is omitted due to the fact that $F(y)$ will be self equilibrating).

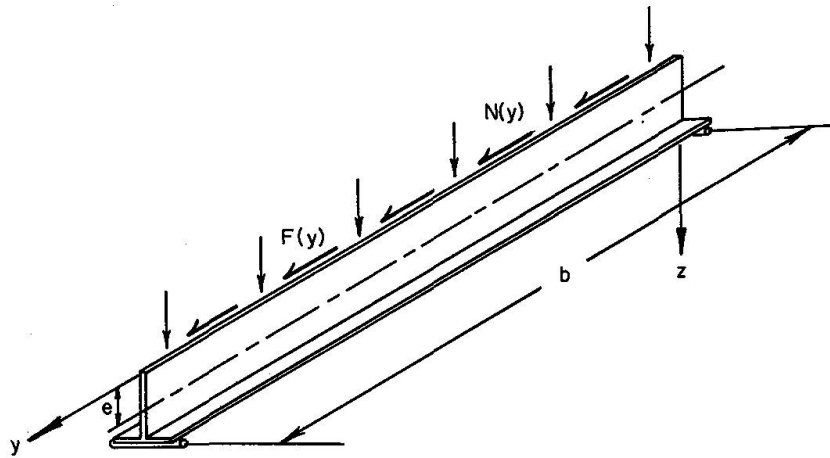


Fig. A-2. Stringer forces

In order to evaluate stringer node deflections due to a discrete loading (e.g. at the stringer-diaphragm intersections) one requires the coefficients of a discrete kernel function series A_l as follows:

$$A_l = \frac{n}{b} \sum_{j=-\infty}^{+\infty} \bar{A}_{2jn+l}^* \simeq \frac{n}{b} \bar{A}_l^* \quad (\text{A-28 a, b})$$

$$A_l = \frac{1}{12B} \left(\frac{b}{n}\right)^3 \frac{3 - \bar{\alpha}_l}{(\bar{\alpha}_l)^2}; \quad \bar{\alpha}_l = 1 - \cos \frac{l\pi}{n} \quad (\text{A-29 a, b})$$

Notation

The following symbols are used in this paper:

\bar{A}_i^*, \bar{A}_k^*	coefficients of infinite and finite series.
$\bar{A}_j^*, \bar{B}_j^*, \bar{D}_j^*$	coefficients of stringer kernel functions.
$\bar{A}_{ij}^*, \bar{B}_{ij}^*$	coefficients of infinite kernel function series.
$\bar{A}_{ij}, \bar{B}_{ij}$	
a, b	plate dimensions.
B	flexural rigidity of stringer.
B_{kj}, \bar{B}_{kj}	coefficients of discrete kernel function series.
\bar{D}_x, \bar{D}_y	differential operators.
\bar{D}_{kj}	series parameter (Eq. A-25).
E	Young's modulus.
e	eccentricity of membrane forces.
$H(r, y), H_{kj}$	membrane – stringer interactive force and series coefficients.
i, j	indices for infinite series.
K	membrane plate stiffness.
K^{uy}, K^{vy}, K^{Ty}	membrane kernel functions.
k, l	indices for finite series.
m, n	limits of finite series indices.
$N(r, y), N_{kj}$	applied stringer load and series coefficients.
N_x, N_{xy}, N_y	membrane stress resultants.
$P(x), P(\alpha)$	continuous and discrete load functions.
$P_j^s, P_j^{a/s}$	coefficients of boundary stringer load series.
$R(r, s), R_{kl}$	stringer-diaphragm interactive forces and series coefficients.
$\bar{T}_j^s, \bar{T}_j^{a/s}$	coefficients of boundary shear.
t	plate thickness.
u, v	membrane displacements.
$V_j^s, V_j^{a/s}, \bar{V}_{ij}$	coefficients of boundary displacements.
$w(r, y)$	out-of-plane stringer displacements.
x, y	continuous coordinates.
$\alpha_i, \bar{\alpha}_j$	$\frac{i\pi}{a}, \frac{j\pi}{b}$ respectively.
$\delta_j^o, \delta(x - \eta)$	Kronecker and Dirac delta functions.
$\bar{\lambda}_j$	series parameter (Eq. A-25).

μ	Poisson's ratio.
ξ, η	impulse load coordinates.
ρ	radius of gyration of stringer.
ϕ_j^*	weighting function.

Practical implications

The thin element or metal plate-stringer-diaphragm bridge deck in either cellular or orthotropic form is one of the most efficient load carrying systems employed by designers today and the literature includes many references to recommended methods of analysis. However, none of the existing methods are rationally based even though some are rather complex and require voluminous computations.

New formulas are presented herein for the exact elastic analysis of plate-stringer-diaphragm bridge deck systems that 1) are proportioned and detailed so that all components have negligible out-of-plane stiffness and 2) are simply supported at the ends. The formulas are unrestricted as to range of parameters in the structural class; that is, they apply equally well to decks with small edge beams with diaphragms serving as transverse load distributors and to decks with primary support by the edge girders with diaphragms serving as floor beams. Minor modification of the formulas permits their use for symmetrical sandwich decks and for decks continuous over intermediate supports.

It is proposed that these exact formulas be used for final design review. They are in the form of double sinusoidal series and can be programmed for use of desk top or miniature computers or simplified for manual calculations through truncation of the series. The formulas can also serve as a standard analysis for use in studying existing and proposed approximate formulas in order to establish range of applicability, magnitude of errors, etc. This should obviate the unsatisfactory practice of making judgements based upon comparison of one empirical method with another empirical method.

Existing alternatives to the proposed method are: 1) use of code sanctioned empirical formulas to compute an "effective flange width" for the stringers and to compute distribution of loads between the resulting "T" beams; 2) use of a "smearing out" technique to replace the mixed discrete-continuous system by an "equivalent" (usually orthotropic) continuum and 3) use of a discrete or latticed system to approximate the real system through a finite difference or finite element approach. The "equivalent continuum" method lacks rational bases for selecting the substitute continuum and for applying the results to the real system. The errors introduced are significant for coarse lattices and for decks with stiff ribs. The finite element version of the substitute lattice approach is superior to the substitute continuum approach but lacks well-developed error analyses. Also, its use for numerous alternate designs is quite expensive due to the voluminous computations and the extensive input data required for each case. For example, the relatively coarse finite element network used to check one of the numerical examples required two orders of magnitude more computing time than did the formula approach and nearly three orders of magnitude more input information.

It is hoped that this introduction of a rational analysis for orthotropic bridge decks will encourage expanded use by designers of this attractive system, especially in those countries where they are not presently in popular use.

References

1. CHEUNG, Y.K., KING, I.P., and ZIENKIEWICZ, O.C.: Slab Bridges With Arbitrary Shape and Support Conditions: A General Method of Analysis Based on Finite Elements. The Institute of Civil Engineering, London, Vol. 40, May 1968, pp. 9–36.
2. DEAN, D.L., and OMID'VARAN, C.: Analysis of Ribbed Plates. *Journal of the Structural Division*, ASCE, Vol. 95, No. ST3, March 1969, pp. 411–440.
3. DEAN, D.L., and GANGARAO: Macro Approach to Discrete Field Analysis, *Journal of the Engineering Mechanics Division*, ASCE, Vol. 96, No. EM4, August 1970, pp. 377–394.
4. DEAN, D.L., and ABDEL-MALEK, R.A.: Rational Analysis of Orthotropic Bridge Decks. *International Journal of Mechanical Sciences*, Pergamon Press, Vol. 16, 1974, pp. 173–192.
5. Design Manual for Orthotropic Steel Plate Deck Bridges: AISC, New York, 1961.
6. JOLLEY, L.B.W.: Summation of Series. Dover Publications, Inc., New York, 1961.
7. POWELL, G.H., and OGDEN, D.W.: Analysis of Orthotropic Steel Plate Bridge Decks. *Journal of the Structural Division*, ASCE, Vol. 95, No. ST5, May 1969, pp. 909–922.
8. Standard Specifications for Highway Bridges: The American Association of State Highway Officials, 10th Edition, 1969, Washington, D.C., pp. 28–31.
9. TRIOTSKY, M.S.: Orthotropic Bridges Theory and Design. James, F. Lincoln Arc Welding Foundation, Cleveland, Ohio, August 1967, pp. 53–213.

Summary

Formulas are introduced which provide the designer with an exact elastic analysis of thin element bridge decks consisting of a set of evenly spaced stringers that are composite with a rectangular plate and are braced by a set of evenly spaced diaphragms. The system is simply supported at the ends with simple or flexible side supports. The loading consists of an arbitrary distribution of stringer line loads. The solution is readily modified to analyze cellular decks or, through superposition, decks with intermediate supports.

Résumé

On introduit des formules fournissant au projeteur une analyse élastique exacte d'éléments minces de tabliers composés d'un groupe de poutres longitudinales réparties à distances égales et jointes avec une plaque rectangulaire et renforcées par des diaphragmes répartis à distances égales. Le système est simplement supporté aux extrémités par des supports latéraux simples ou flexibles. La charge agit par une distribution arbitraire de charges linéaires. La solution est légèrement modifiée pour l'analyse des tabliers cellulaires ou, par superposition de tabliers avec supports intermédiaires.

Zusammenfassung

Es werden Formeln eingeführt, die dem Projektbearbeiter eine genaue elastische Analyse dünner Fahrbahnelemente liefern, welche aus einem Satz in gleichem Abstand verteilter Längsträger bestehen, die mit einer Rechteckplatte verbunden und durch eine Anzahl in gleichem Abstand verteilter Diaphragmen versteift sind. Das System wird an den Enden durch einfache oder flexible seitliche Auflager gestützt. Die Belastung besteht aus einer beliebig verteilten Längsträger-Linienlast. Die Lösung lässt sich leicht modifizieren, je nachdem es sich um zellenförmige Fahrbahnen oder, durch Übereinanderlagern, um Fahrbahnen mit zwischenliegenden Auflagern handelt.

Trapezoidal Bar Cells in Plane Stress

Éléments en forme trapézoïdale chargés dans leur plan

In ihrer Ebene belastete trapezoidale Stabelemente

A. HRENNIKOFF Sc.D.

Research Professor Emeritus of Civil Engineering
University of British Columbia, Vancouver, B.C.
Canada

K.M. AGRAWAL Ph.D.

Research Officer, B.C. Research, Vancouver,
B.C. Canada

General

In solution of plane stress problems by the finite element method trapezoidal cells have advantage over cells of other shapes when the geometry of the plates under investigation may be conveniently described in polar coordinates. In general two quite distinct kinds of cells (elements) are possible, the bar or framework cells and the no-bar cells. The cell proposed here is of the bar type, and it has the shape of an isosceles trapezoid endowed with certain distinctive features contributing to precision. The present study includes the description of the cell and the derivation of its stiffness matrix in explicit form. This is followed by description of results of application of the theory to examples.

Bar Cells

The bar cells used in plane stress problems are made of certain combinations of elastic bars endowed with extensional stiffnesses assuring the same deformability of the model as of the prototype in conditions of any arbitrary uniform stress. The requirement of this equivalence of deformations may be most conveniently satisfied, if the cell is made to deform identically with the plate in the following three separate strain conditions: uniform normal strain ϵ_x , uniform normal strain ϵ_y , and uniform shearing strain γ_{xy} . The deformations of the cell are judged by the displacements of its corners [2].

The extensional bar stiffnesses EA , found from these relations, on the assumption of the modulus of elasticity E being the same as in the plate, depend on the geometry of the cell and the value of the Poisson's ratio μ of the material of the plate.

In most cases some bar areas become negative within certain ranges of μ and proportions of the cell, and this at times results in lowering of precision. A bar

area may sometimes also become zero. This in effect removes the bar from the cell, making the model in some cases non-rigid and unusable for analysis. The undesirable bar arrangement of this kind may be avoided by the use of additional bars and other special measures.

With the necessary cell geometry decided upon and the bar areas known, the stiffness matrix of the cell is determined.

In analysis of bar stresses in the cell the equations of equilibrium are written for an undeformed structure, on the assumption that the deformations of the bars do not affect appreciably the geometry of the model. Instability of particular bars or groups of bars need not be contemplated.

In the model of the plate the cells of the chosen pattern join each other at the main corners, outlining the shape of the cell. These joints may be considered as hinges, although such articulation is not essential, since the bars are devoid of flexural stiffness. Secondary junctions between the bars belonging to one cell only, are also possible. These joints lie sometimes outside the outline of the particular cell, as will be illustrated presently.

Trapezoidal Bar Cells

The shape of an isosceles trapezoid modelled by the cell is shown in Fig. 1. It is described by the ratios k and k_1 of the two bases and the height of the cell. The thickness of the plate is t .

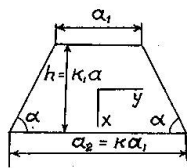


Fig. 1

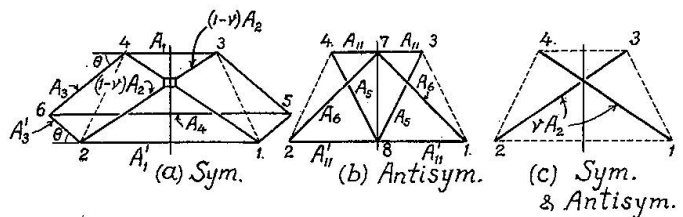


Fig. 2

$$k = \frac{a_2}{a_1} \text{ and } k_1 = \frac{h}{a_1} \quad (1)$$

The bar framework of the cell is presented in Figs. 2a, b and c, depicting a single cell. It consists of several bars, whose cross-section areas are designated by the letters A with different number indices. The areas of the top and bottom bars A_1 and A_1' in Fig. 2a are assumed equal, and so are the areas of the bars A_{11} and A_{11}' in Fig. 2b. The sloping bars A_3 and A_3' are inclined at the same angle θ to the horizontal, and are also equal in areas. The area of the horizontal bar A_4 , joining the points 5 and 6, is assumed for simplicity infinite. The bars A_{11} go over the bar A_1 and have common joints 3 and 4 with it, but their intermediate joint 7 is separate from the bar A_1 . The bottom bars A_{11}' and A_1' are in a similar situation.

The pairs of nodes 2-3 and 1-4 are joined by two sets of bars, the solid bars in Fig. 2c and the ones in Fig. 2a, attached to each other in a special way at the intersection, by means of a hinged rectangle of infinitesimal size. When the cell is under the action of a loading symmetrical about the vertical axis, the diagonals

2-3 and 1-4 are stressed equally, and the rectangle is fully capable of transmitting their stresses through it, as if it were absent. On the other hand, antisymmetrical loading of the cell would tend to make the stresses in the diagonals equal and opposite in sign; the rectangle would not permit this, and the diagonals would be inactive. In arriving at these conclusions it is necessary to view the cell geometry as undeformed by stress. The area of the solid diagonal bar is assumed vA_2 , and of the hinged part $(1-v)A_2$, where v is a fractional coefficient. Thus, the effective area of the diagonal is A_2 under the symmetric loading, and vA_2 under the antisymmetric.

The nodes 1, 2, 3 and 4 are the external joints, at which the cell connects to its neighbours, and where it is acted upon by the external loads. The joints 5 and 6, where the bars A_3 , A'_3 and A_4 meet, are parts of the internal mechanism of the cell, unattached to the other cells. With the angles θ as shown, the nodes 5 and 6 protrude into the areas of the neighbouring cells; however, the action of these bars is considered unaffected by such interpenetration.

Simple static analysis shows, that the bars A_3 , A'_3 and A_4 are inactive, when the loads are antisymmetric about the vertical axis of symmetry of the cell. At the same time the inclined bars A_5 and A_6 in Fig. 2b are inactive when the loads are symmetrical about the same axis. In case of symmetrical loading the bars A_{11} and A'_{11} become combined with A_1 and A'_1 respectively, and work together with them. The inclined bars vA_2 (Fig. 2c) and the horizontal bars A_{11} and A'_{11} are the only ones which work both under the symmetrical and the antisymmetrical loads.

The cell possesses two free parameters, to be assigned by special considerations, as explained later, the fractional coefficient v of the diagonal bars and the angle θ of inclination of the side bars A_3 and A'_3 . This angle may exceed 90° .

The number of bars in the cell is more than sufficient for its rigidity, even when the values of the parameters k , k_1 and θ combine to make some of the bar areas zero, in other words, cause these bars to disappear.

The uniform strain conditions in the plate ϵ_x , ϵ_y and γ_{xy} , which the cell must imitate, are illustrated in Figs. 3a, b and c, with the deformations of the cell indicated by dotted lines. The corner forces X and Y , stated in Fig. 3, are found by transferring the stresses, acting on the edges of the cell, to the corners on the sides of each edge, the transfer being carried out in accordance with statics. In each of the three conditions these corner forces are equal at all corners. It may be observed, that the stress conditions represented in Figs. 3a and b are symmetrical, and the one in Fig. 3c antisymmetrical about the vertical axis x .

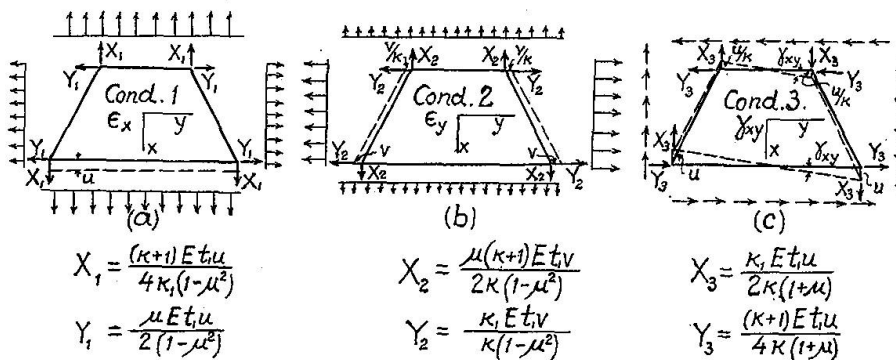


Fig. 3

Determination of the Bar Areas

The cell of Fig. 2 is subjected to the strain Condition 1, uniform strain in x direction, Fig. 3a. The four corners develop the forces X_1 and Y_1 , as shown. The antisymmetrical bars A_5 and A_6 of Fig. 2b remain idle. The stresses in the bars A_3 and A'_3 are equal, in view of equality of their angles of inclination to horizontal. The stresses F_2 and F_3 in the bars A_2 and A_3 may be expressed in terms of the geometry of the cell, the elongation u and the areas of the bars. Equating the sums of the x and y components of F_2 and F_3 to the nodal forces X_1 and Y_1 in Fig. 3a, the areas A_2 and A_3 are found as follows

$$A_2 = \frac{[(k+1) + 2\mu k_1 \tan \theta] [4k_1^2 + (k+1)^2]^{3/2}}{16k_1^2 (1-\mu^2) 2k_1 + (k+1) \tan \theta} a_1 t. \quad (2)$$

$$A_3 = \frac{[(k+1)^2 - 4\mu k_1^2]}{4(1-\mu^2) [2k_1 \cos \theta + (k+1) \sin \theta] \sin^2 \theta} a_1 t. \quad (3)$$

The cell is now strained horizontally in accordance with the Condition 2 in Fig. 3b. The bars $(A_1 + A_{11})$ and $(A'_1 + A'_{11})$ are stressed equally in view of equality of their areas and proportionality of elongations to their lengths. The bars of Fig. 2b, other than A_{11} and A'_{11} again develop no stress. Following a procedure similar to the one just outlined, the equation $\sum Y = 0$ at one of the corners of the cell leads to determination of the stress F_1 in the top and bottom horizontal bars and to the expression for the sum of the areas $(A_1 + A_{11})$.

$$(A_1 + A_{11}) = \frac{(k+1) [4\mu k_1^2 - (k+1)^2] + 2k_1 \tan \theta [4k_1^2 - \mu(k+1)^2]}{16k_1^2 (1-\mu^2) \tan \theta} a_1 t \quad (4)$$

It may be pointed out that the equation $\sum X = 0$ can give no new information, being satisfied automatically by Betti's reciprocal theorem, irrespective of the areas of bars.

The shear Condition 3 (Fig. 3c) causes stresses in the antisymmetric system of bars of Fig. 2b with participation of the diagonals vA_2 . The ratio of components of corner forces in Condition 3 is

$$\frac{X_3}{Y_3} = \frac{2k_1}{k+1} \quad (5)$$

This indicates, that the resultants of X_3 and Y_3 at all corners act in the directions of the diagonals.

For purposes becoming clear later, it is desirable to subdivide the corner forces X_3 and Y_3 into parts carried by the diagonals vA_2 and the antisymmetrical bar system of Fig. 2b. These parts, expressed in terms of a new fractional parameter η , are presented in Figs. 4a and b. By equating the stress in the diagonal in Fig. 4b to its expression in terms of the elongation of the bar vA_2 , the parameter η is found related to v by the equation

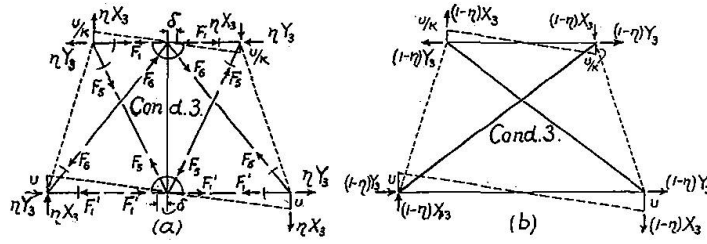


Fig. 4

$$(1 - \eta) = \nu \frac{(k + 1) [(k + 1) + 2\mu k_1 \tan \theta]}{k_1 (1 - \mu) [2k_1 + (k + 1) \tan \theta]} \quad (6)$$

The antisymmetrically loaded structure of Fig. 4a is statically determinate, and the stresses in all its bars, equal and opposite in sign on the opposite sides of the axis of symmetry, are expressible in terms of the corner forces. Thus the stresses in the horizontal members are

$$\left. \begin{aligned} F_1 &= \frac{k}{2k_1} X_3 = \frac{k}{k + 1} \eta Y_3 \\ F'_1 &= \frac{1}{2k_1} X_3 = \frac{1}{k + 1} \eta Y_3 \end{aligned} \right\} \quad (7)$$

The areas of these bars could be found in terms of the displacement u and the geometry of the cell, but this is not needed for determination of the terms of the stiffness matrix.

The bar systems pictured in Figs. 4a and b provide two independent alternative routes for the corner forces X_3 and Y_3 to travel through the cell. For this reason the parameter η must be viewed at this stage as an arbitrary number of a magnitude anywhere between zero and unity.

Terms of the Stiffness Matrix

Condition u_1

If the bar areas in the cell are known, the nodal forces in it, produced by unit displacements of any of the nodes, such as $u_1 = 1$, may be found using the equations of structural theory. This however is a laborious procedure, and in many cases it is possible to arrive at the same results more easily by a judicial combination of several elementary strain conditions with knowledge of only a few bar areas, and even without them. In the present case of the trapezoidal bar cell the method of combination of elementary conditions also leads to a significant refinement of the cell, resulting in improvement of precision. The combination producing the Condition $u_1 = 1$, is presented in Fig. 5.

The three component conditions are the basic Conditions 1 and 3, and a non-basic flexural Condition 4, in which the nodes move in x direction. The corner

displacements in these three conditions add up to zero, except for the corner 1, where their sum equals u_1 . The corner forces in Fig. 5, on comparison with those in Fig. 3, are one half as great for the Condition 1 and one quarter as great for the Condition 3.

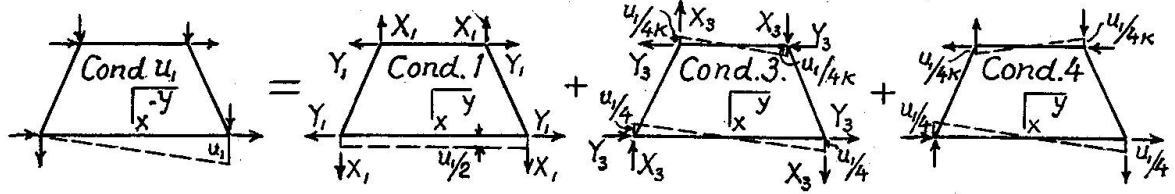


Fig. 5

The Condition 4, as the Condition 3, is antisymmetrical, and its corner forces may be deduced from comparison of its corner displacements with those in Condition 3. For this purpose Condition 4 is broken up into two parts, shown in Figs. 6a and b, corresponding to separate actions of the diagonals and the antisymmetric bar system.

As follows from comparison of corner displacements, the diagonal bars in Fig. 6b deform less than in Fig. 4b in the ratio $\frac{k-1}{k+1}$, and so the components of their stresses must stand in the same ratio.

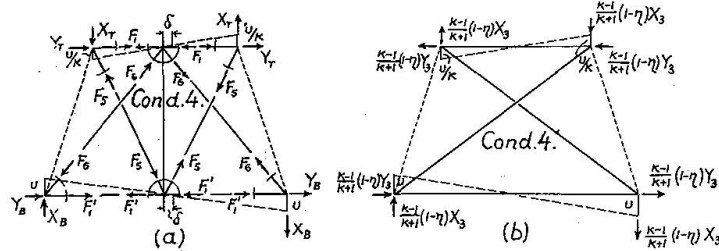


Fig. 6

$$\text{Thus, } X = \frac{k-1}{k+1}(1-\eta)X_3 \text{ and } Y = \frac{k-1}{k+1}(1-\eta)Y_3 \quad (8)$$

The corner displacements of the antisymmetrical bar system in Fig. 6a equal those in Fig. 4a, and so must do the horizontal displacements of the junctions of the horizontal and the inclined bars, in order to preserve the equilibrium between the horizontal and the inclined members. For this reason all bar stresses in Fig. 6a are numerically equal to those in Fig. 4a, although their signs, as indicated by arrows in both figures, are in some members different.

The corner forces in Fig. 6a may now be expressed by comparison with Fig. 4a, making use of Eqs. (7).

$$\left. \begin{aligned} X_B &= X_T = \eta X_3 \\ Y_B &= \eta Y_3 - 2F'_1 = \frac{k-1}{k+1} \eta Y_3 \\ Y_T &= \eta Y_3 - 2F_1 = -\frac{k-1}{k+1} \eta Y_3 \end{aligned} \right\} \quad (9)$$

Combining these with the ones in Fig. 6b, the total corner forces in the Condition 4 (see Fig. 7) are:

$$\left. \begin{aligned} X_{4B} &= \frac{k-1}{k+1} X_3 + \frac{2}{k+1} \eta X_3 \\ X_{4T} &= \frac{k-1}{k+1} X_3 - \frac{2k}{k+1} \eta X_3 \\ Y_{4B} &= Y_{4T} = \frac{k-1}{k+1} Y_3 \end{aligned} \right\} \quad (10)$$

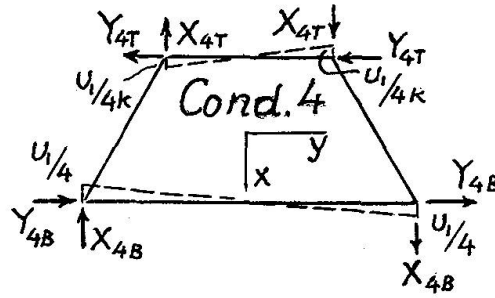


Fig. 7

The members of the first column of the stiffness matrix of the cell, i.e. the corner forces corresponding to Condition $u_1 = 1$, are found by adding up the values of the three component cases in Fig. 5, and are stated in Table 1.

Condition v_1

This condition may likewise be obtained by addition of the three component conditions, the basic Conditions 2 and 3, and the non-basic flexural Condition 5, in which the strains occur in y direction (Fig. 8).

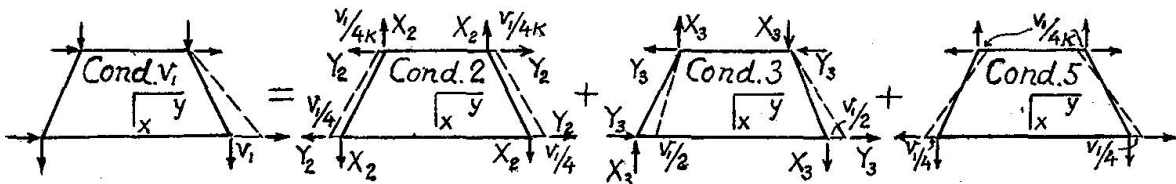
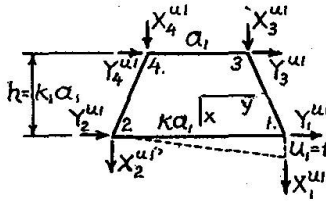


Fig. 8

Table 1. Trapezoidal Bar Cell



$$X_1^{u1} = \left[\frac{(k+1)^2 + 2k_1^2(1-\mu) + 2\frac{\eta}{k}k_1^2(1-\mu)}{8(k+1)k_1(1-\mu^2)} \right] Et$$

$$X_2^{u1} = \left[\frac{(k+1)^2 - 2k_1^2(1-\mu) - 2\frac{\eta}{k}k_1^2(1-\mu)}{8(k+1)k_1(1-\mu^2)} \right] Et$$

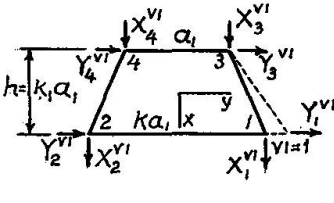
$$X_3^{u1} = \left[\frac{-(k+1)^2 + 2k_1^2(1-\mu) - 2\eta k_1^2(1-\mu)}{8(k+1)k_1(1-\mu^2)} \right] Et$$

$$X_4^{u1} = \left[\frac{-(k+1)^2 - 2k_1^2(1-\mu) + 2\eta k_1^2(1-\mu)}{8(k+1)k_1(1-\mu^2)} \right] Et$$

$$Y_1^{u1} = -Y_4^{u1} = \frac{Et}{8(1-\mu)}$$

$$Y_2^{u1} = -Y_3^{u1} = \frac{1-3\mu}{8(1-\mu^2)} Et$$

Table 2. Trapezoidal Bar Cell



$$Y_1^{v1} = \frac{8k_1^2 + (k+1)^2(1-\mu) + 16\frac{A_1 + A_{11}}{kat}k_1(1-\mu^2)}{16(k+1)k_1(1-\mu^2)} Et$$

$$Y_2^{v1} = \frac{-8k_1^2 + (k+1)^2(1-\mu) - 16\frac{A_1 + A_{11}}{kat}k_1(1-\mu^2)}{16(k+1)k_1(1-\mu^2)} Et$$

$$Y_3^{v1} = \frac{8k_1^2 - (k+1)^2(1-\mu) - 16\frac{A_1 + A_{11}}{at}k_1(1-\mu^2)}{16(k+1)k_1(1-\mu^2)} Et$$

$$Y_4^{v1} = \frac{-8k_1^2 - (k+1)^2(1-\mu) + 16\frac{A_1 + A_{11}}{at}k_1(1-\mu^2)}{16(k+1)k_1(1-\mu^2)} Et$$

$$X_1^{v1} = -X_4^{v1} = \frac{Et}{8(1-\mu)}$$

$$X_3^{v1} = -X_2^{v1} = \frac{(1-3\mu)}{8(1-\mu^2)} Et$$

The nodal forces of the flexural Condition 5 may be correlated with those of Condition 2 by observing the displacements of the joints and the action of the bars forming the cell (Fig. 9). Since both Conditions 2 and 5 are symmetrical about the vertical axis, the bars A_5 and A_6 are inactive.

The horizontal movements of the nodes 1 and 2 are both outward and equal to $\frac{v_1}{4}$, while the displacements of the upper nodes $\frac{v_1}{4k}$ are outward in Condition 2 and inward in Condition 5.

The nodal forces in both conditions are contributed by the inclined bars A_2 , A_3 and A_3' , and the double horizontal bars $(A_1 + A_{11})$ and $(A_1' + A_{11}')$. The stresses in the inclined bars, and the nodal forces resulting from them, stand in the ratio of the algebraic sums of their nodal displacements, i.e. in the ratio $\frac{k-1}{k+1}$.

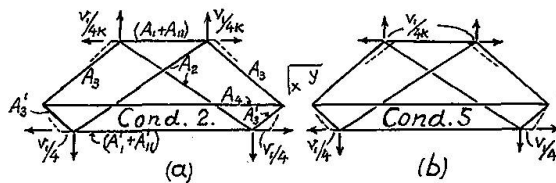


Fig. 9

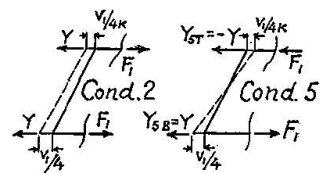


Fig. 10

The stresses F_1 are numerically equal in all horizontal bars in both conditions 2 and 5. In the first of these, F_1 are tensile, and in the second — tensile at the bottom and compressive at the top, as indicated in Fig. 10. Their contributions, Y_{5B} at the bottom, and Y_{5T} at the top, to the horizontal nodal forces may be expressed as follows:

$$Y_{5B} = F_1 = \frac{k-1}{k+1} F_1 + \frac{2}{k+1} F_1$$

and $Y_{5T} = -F_1 = \frac{k-1}{k+1} F_1 - \frac{2k}{k+1} F_1.$

The first parts of these expressions may be combined with the contributions of the other bars, and the total nodal forces in Condition 5 may be expressed through their counterparts in Condition 2 and the stresses F_1 as follows:

$$X_5 = \frac{k-1}{k+1} X_2$$

$$Y_5 (\text{bot. joints}) = \frac{k-1}{k+1} Y_2 + \frac{2}{k+1} F_1 \quad (11)$$

$$Y_5 (\text{top joints}) = \frac{k-1}{k+1} Y_2 - \frac{2k}{k+1} F_1$$

The corner forces X_2 and Y_2 of these expressions are given in Fig. 8. The forces F_1 are:

$$F_1 = \frac{(A_1 + A_{11}) E v_1}{2ka_1} \quad (12)$$

The terms of the second column of stiffness matrix, corresponding to the Condition $v_1 = 1$, are stated in Table 2.

Other Terms of the Stiffness Matrix

The matrix terms, produced by the displacements of the node 3, are found by procedures similar to the ones described, and those corresponding to the displacements of the nodes 2 and 4, by applying the principles of symmetry to the terms already found.

Refinement of the Stiffness Matrix

The desired stiffness matrix should be applicable to isosceles trapezoids of all kinds, including rectangles, whose coefficient $k = 1$.

While the matrix of Tables 1 and 2 describes stresses and strains in uniform strain conditions perfectly, its descriptions of non-uniform conditions naturally is

only approximate. Furthermore, the arrangement of framework in a rectangular cell, viewed as a special case of a trapezoid, is different in x and y directions, and so it may be expected, that the results of analyses of model made of such cells, would depend on orientation of rectangles, with some unfavourable effect on precision, which is likely to extend to cells with values of k distinct from unity. Experience confirms correctness of this supposition.

Fortunately however, the existence of free parameters θ and ν or η makes possible a refinement of the stiffness matrix with favourable effect on precision. The idea is to assign to θ and ν such values, that the limiting case of a trapezoid with $k = 1$ will have the same elastic properties in the directions of both axes.

The terms X_1^{u1} and Y_1^{v1} of the stiffness matrix in Tables 1 and 2 involve quantities η and $(A_1 + A_{11})$. These are present only in the last members of the numerators of their expressions. Replace these members by different expressions involving a new parameter ω . This version of the stiffness matrix is assembled in Table 3. The parameter ω in it is related to η and $(A_1 + A_{11})$ by the expressions

$$\omega = \frac{\eta k_1^2 (1 - \mu)}{2} = \frac{2(A_1 + A_{11})(1 - \mu^2)}{k_1 a_1 t} \quad (13)$$

On substitution of $k = 1$ in Table 3 the terms X_1^{u1} and Y_1^{v1} (see Fig. 11) become

$$\left. \begin{aligned} X_1^{u1} &= \frac{2 + k_1^2 (1 - \mu) + 2\omega}{8k_1 (1 - \mu^2)} \\ Y_1^{v1} &= \frac{2k_1^2 + 1 - \mu + 2k_1^2 \omega}{8k_1 (1 - \mu^2)} \end{aligned} \right\} \quad (14)$$

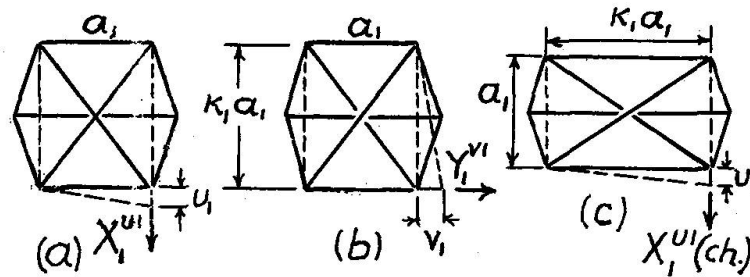
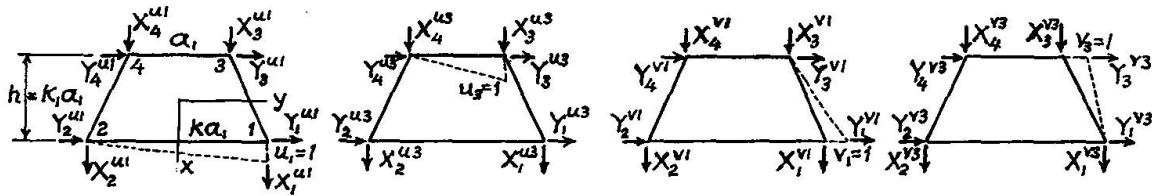


Fig. 11

It may be pointed out, that introduction of the new parameter ω is legitimate. This is simply equivalent to attributing some particular values to the quantity η and the angle θ . ω as η must be positive.

Change now the bar arrangement from Fig. 11 a to Fig. 11 c. The new expression for X_1^{u1} is obtainable from the old by replacing k_1 with $\frac{1}{k_1}$. This makes X_1^{u1} (changed) identical with Y_1^{v1} in Eq. (14). Similarly, Y_1^{v1} (changed) is found the same as X_1^{u1} . It may be observed, that the members with ω satisfying Eq. (13), fit all terms of the stiffness matrix, and not just X_1^{u1} and Y_1^{v1} .

Table 3. Trapezoidal Bar Cell



$$X_1^{u1} = \frac{(k+1)^2 + 2k_1^2(1-\mu) + \frac{4\omega}{k}}{8k_1(k+1)(1-\mu^2)} Et$$

$$X_2^{u1} = \frac{(k+1)^2 + 2k_1^2(1-\mu) + \frac{4\omega}{k}}{8k_1(k+1)(1-\mu^2)} Et$$

$$X_3^{u1} = \frac{-(k+1)^2 + 2k_1^2(1-\mu) - 4\omega}{8k_1(k+1)(1-\mu^2)} Et$$

$$X_4^{u1} = \frac{-(k+1)^2 - 2k_1^2(1-\mu) + 4\omega}{8k_1(k+1)(1-\mu^2)} Et$$

$$X_1^{u3} = \frac{-(k+1)^2 + 2k_1^2(1-\mu) - 4\omega}{8k_1(k+1)(1-\mu^2)} Et$$

$$X_2^{u3} = \frac{-(k+1)^2 - 2k_1^2(1-\mu) + 4\omega}{8k_1(k+1)(1-\mu^2)} Et$$

$$X_3^{u3} = \frac{(k+1)^2 + 2k_1^2(1-\mu) + 4k\omega}{8k_1(k+1)(1-\mu^2)} Et$$

$$X_4^{u3} = \frac{(k+1)^2 - 2k_1^2(1-\mu) - 4k\omega}{8k_1(k+1)(1-\mu^2)} Et$$

$$X_1^{v1} = \frac{1}{8(1-\mu)} Et$$

$$X_2^{v1} = -\frac{1-3\mu}{8(1-\mu^2)} Et$$

$$X_3^{v1} = \frac{1-3\mu}{8(1-\mu^2)} Et$$

$$X_4^{v1} = -\frac{1}{8(1-\mu)} Et$$

$$X_1^{v3} = -\frac{1-3\mu}{8(1-\mu^2)} Et$$

$$X_2^{v3} = \frac{1}{8(1-\mu)} Et$$

$$X_3^{v3} = -\frac{1}{8(1-\mu)} Et$$

$$X_4^{v3} = \frac{1-3\mu}{8(1-\mu^2)} Et$$

$$Y_1^{u1} = \frac{1}{8(1-\mu)} Et$$

$$Y_2^{u1} = \frac{1-3\mu}{8(1-\mu^2)} Et$$

$$Y_3^{u1} = -\frac{1-3\mu}{8(1-\mu^2)} Et$$

$$Y_4^{u1} = -\frac{1}{8(1-\mu)} Et$$

$$Y_1^{u3} = \frac{1-3\mu}{8(1-\mu^2)} Et$$

$$Y_2^{u3} = \frac{1}{8(1-\mu)} Et$$

$$Y_3^{u3} = -\frac{1}{8(1-\mu)} Et$$

$$Y_4^{u3} = -\frac{1-3\mu}{8(1-\mu^2)} Et$$

$$Y_1^{v1} = \frac{8k_1^2 k + k(k+1)^2(1-\mu) + 8k_1^2 \omega}{16k(k+1)k_1(1-\mu^2)} Et$$

$$Y_2^{v1} = \frac{-8k_1^2 k + k(k+1)^2(1-\mu) - 8k_1^2 \omega}{16k(k+1)k_1(1-\mu^2)} Et$$

$$Y_3^{v1} = \frac{8k_1^2 - (k+1)^2(1-\mu) - 8k_1^2 \omega}{16(k+1)k_1(1-\mu^2)} Et$$

$$Y_4^{v1} = \frac{-8k_1^2 - (k+1)^2(1-\mu) + 8k_1^2 \omega}{16(k+1)k_1(1-\mu^2)} Et$$

$$Y_1^{v3} = \frac{8k_1^2 - (k+1)^2(1-\mu) - 8k_1^2 \omega}{16(k+1)k_1(1-\mu^2)} Et$$

$$Y_2^{v3} = \frac{-8k_1^2 - (k+1)^2(1-\mu) + 8k_1^2 \omega}{16(k+1)k_1(1-\mu^2)} Et$$

$$Y_3^{v3} = \frac{8k_1^2 + (k+1)^2(1-\mu) + 8k_1^2 \omega}{16(k+1)k_1(1-\mu^2)} Et$$

$$Y_4^{v3} = \frac{-8k_1^2 + (k+1)^2(1-\mu) - 8k_1^2 \omega}{16(k+1)k_1(1-\mu^2)} Et$$

The Value of ω

The question of what values of ω should be preferably assigned to the cells composing the model may be answered by resorting to the energy principles.

Suppose, that by using some particular values of this parameter the nodal displacements of all cells in the model, under the action of given loads, have been determined. Consider one of these cells by itself, and apply to it the three uniform strain conditions in appropriate amounts, so that the nodes 2, 3 and 4 are placed in their relative positions conforming to the distortion of the model, while the node 1 still remains short of its proper place. The cell so deformed is held in this state by appropriate nodal forces, none of which is a function of the parameter ω . To make the node 1 move the remaining distances u_o and v_o (Fig. 12), it is necessary to apply to it additional forces

$$\begin{aligned} X &= X_1^{u1} u_o + X_1^{v1} v_o \\ Y &= Y_1^{v1} v_o + Y_1^{u1} u_o \end{aligned} \quad (15)$$

while restraining the other nodes from further movements.

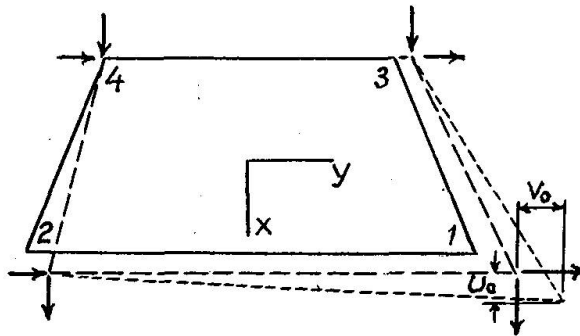


Fig. 12

The forces represented by the first terms in the expressions for X and Y always act in the directions of u_o and v_o , irrespective of the signs of these displacements, thus making positive contributions to the energy of deformation of the cell. The contributions of the second terms to the energy of deformation may be positive or negative, but their effect is minor.

Re-assemble now all cells of the model. The energy of its deformation U is composed of the energies of individual cells. Assume, that ω is decreased, while all nodes are left in the same locations. For this they must be restrained, because the assembly is no more in equilibrium. A smaller ω makes the terms X_1^{u1} and Y_1^{v1} , and with them the energy of deformation U , smaller, while the potential energy of the loads V is the same as before, because the nodes have not moved. This makes the total energy of the system T smaller than before.

Now remove slowly the nodal restraints and allow the model to find its new state of equilibrium. By the Rayleigh-Ritz principle the energies U and V change in such a way, that their sum T decreases. A smaller ω thus has resulted in a smaller T of the deformed structure.

The same reasoning is equally valid in application to models constructed of other types of cells, both bar and no-bar. Cells with smaller values of X_1^{u1} and Y_1^{v1} would possess a smaller total energy T of the model than cells of the same shape and size, but with bigger X_1^{u1} and Y_1^{v1} terms.

A question still remains, which of the two sets of terms X_1^{u1} , Y_1^{v1} , or more generally, what kind of cell, is better for precision of results. This question presents itself, as the cells are subdivided into smaller units, with zero size being the limit, when the model becomes in effect the actual plate prototype.

The numerical progress of energy T on subdivision of cells has been examined closely on models composed of rectangular cells [4]. The value of T on reduction of the size of cells in such models was found to increase or to decrease, at times non-monotonically, with the direction of change depending mostly on the stiffness matrix terms of the cells used. Since rectangle is a special case of trapezoid, one may expect, that with trapezoidal cells the convergence of the total energy should also proceed up or down numerically depending on the particulars of the problem, including the type of cells with their parameters k and k_1 , and the geometry of the structure and its loading. These relationships will be demonstrated below on examples.

A few explanatory words about the parameter ω are in order. This parameter should be positive, but not zero. If $\omega = 0$, the antisymmetrical bar system of the cell is eliminated. This feature is not objectionable in itself, but it makes the nodal forces, brought about by unit movements of the nodes 1 and 3, equal at respective corners, which is unreasonable. If $\omega = 0$, a rectangular cell becomes non-rigid.

It is necessary to point out, that negative bar areas, making their appearance in certain geometrical configurations of cells, and leading in some framework systems to reduced precision, need not be feared in case of cells under consideration, because they all become absorbed in a single positive parameter ω .

While solution of a cell model resulting in a better energy T is superior to the ones characterized by less satisfactory values of T , this does not necessarily signify superiority of precision of displacements everywhere in the model. For its equilibrium structure seeks condition of the least total energy. This roughly corresponds to least weighted errors in deflections of the points of application of loads in the directions of the loads. Deflections normal to the loads, as well as the ones of the unloaded nodes, are not reflected in the value of T .

Examples

The application of the theory presented here is illustrated on displacement analysis of a thin plate of thickness t in the shape of a 90° sector of hollow circle (Fig. 13), acted upon by a radial load, applied on one radial edge, while the other edge is supported on rollers, allowing its points to move only radially. An exact solution of this problem is available [5].

In the examples solved here the inner radius is assumed to be one third of the outer radius R . The Poisson's ratio $\mu = 0.2$. The boundary conditions allow the

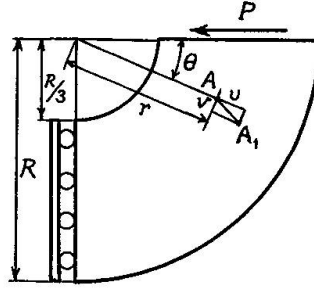


Fig. 13

plate to undergo an arbitrary vertical movement; this in the theoretical solution is assigned a certain definite value. The expressions for the radial and tangential displacements, u and v respectively, are given by Eqs. (16) and (17), in which r and θ signify the polar coordinate of the point.

$$u = \left\{ \left[-3.34882 (1 - \mu) 1n \frac{r}{R} + 1.50697 (1 - 3\mu) \frac{r^2}{R^2} - 0.16744 (1 + \mu) \frac{R^2}{r^2} \right] \sin \theta - 10.5206 \cos \theta + 6.69764 \theta \cos \theta \right\} \frac{P}{Et} \quad (16)$$

$$v = \left\{ 10.5206 \sin \theta - \left[3.34882 \left((1 + \mu) + (1 - \mu) 1n \frac{r}{R} \right) + 1.50697 (5 + \mu) \frac{r^2}{R^2} - 0.16744 (1 + \mu) \frac{R^2}{r^2} \right] \cos \theta - 6.69764 \theta \sin \theta \right\} \frac{P}{Et} \quad (17)$$

The tangential stress by means of which the load P is applied to the edge $\theta = 0$, is given by the equation

$$\tau_{r\theta} = \left[\frac{3.34882}{r} - \frac{3.01394 r}{R^2} - \frac{0.33488 R^2}{r^3} \right] \frac{P}{t}. \quad (18)$$

The finite element models used in solution of this problem are formed by subdividing the plate into trapezoids by radial and circumferential lines. To trace the improvement of precision with reduction of mesh size three models are used. The coarsest one of 15 cells has 3 cells in radial direction and 5 in tangential (Fig. 14). Two other models possess 60 and 240 cells, i.e., two and four times as many cells in each direction as the first model.

To reduce the number of significant variables and by that to simplify the problem of identifying the more precise types of elements, the elements are made geometrically similar in all circumferential rows. Elements so proportioned have the same parameters k and k_1 , and the same stiffness matrices in spite of difference in sizes, as they grow larger away from the centre.

Geometry of the cells and the model may be easily determined by elementary means.

The parameter k , which is also the magnification factor between two radially adjacent cells is $k = \sqrt[n]{3}$, where n is the number of circumferential rows, i.e., 3, 6 and 12 in the three models employed.

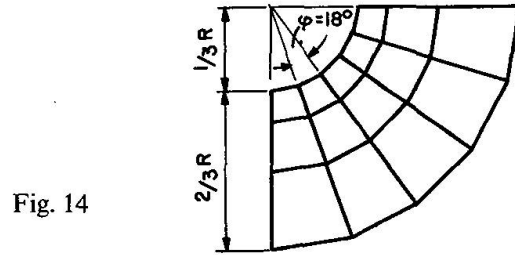


Fig. 14

The parameter $k_1 = \frac{k-1}{2 \tan \frac{1}{2}\phi}$, where ϕ is the central angle subtended by each cell and equal to 18° , 9° and $4^\circ 30'$. The small base of the smallest trapezoid $a = \frac{2}{3} R \sin \frac{1}{2}\phi$.

The numerical values of these quantities are assembled in Table 4.

Table 4. Value of Significant Quantities of Cells in Models Used

Quantity	Model	5 × 3 Cells	10 × 6 Cells	20 × 12 Cells
a_1		0.104290	0.052306	0.026173
k		1.44225	1.200936	1.09587
k_1		1.39613	1.28052	1.22003

The shearing stress $\tau_{r\theta}$ (Eq. 18) on the edge $\theta = 0^\circ$ is non-uniform; this raises question of how to assign proper fractions of the active load P to the nodes on this edge. Fig. 15 shows three consecutive edge nodes A , B , C and their distances from the centre of the sector. It is felt, that a load element dP , situated

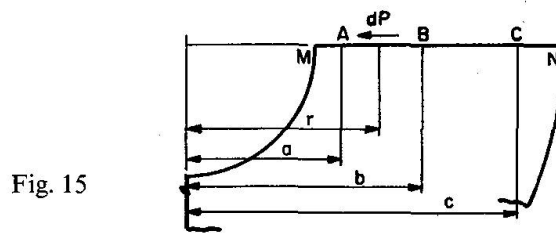


Fig. 15

between the nodes A and B should contribute only to these two nodes, and that its contribution at the node nearer it should be greater than at the more distant one. From these considerations nodal concentrations at B have been determined by "the Law of Proximity", mathematically identical with the law of the lever. This was done separately for the contributions coming from the inner panel AB and the outer panel BC . The extreme nodes M and N have their contributions coming only from one side.

The computed values of the nodal loads in the three models used, numbered from the inside, are stated in Table 5.

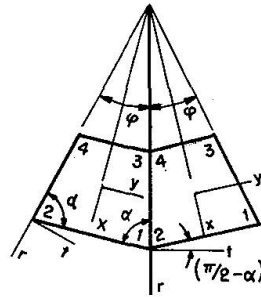
Table 5. Nodal Loads in Models Used. Numbered from Inside the Sector

Model 5 × 3 Cells	Model 10 × 6 Cells	Model 20 × 12 Cells	
$P_0 = 0.086925 P$	$P_0 = 0.025530 P$	$P_0 = 0.006930 P$	$P_7 = 0.119020 P$
$P_1 = 0.398441 P$	$P_1 = 0.135140 P$	$P_1 = 0.039011 P$	$P_8 = 0.109722 P$
$P_2 = 0.411183 P$	$P_2 = 0.215155 P$	$P_2 = 0.070124 P$	$P_9 = 0.093734 P$
$P_3 = 0.103452 P$	$P_3 = 0.241144 P$	$P_3 = 0.093426 P$	$P_{10} = 0.070608 P$
	$P_4 = 0.216664 P$	$P_4 = 0.109595 P$	$P_{11} = 0.039518 P$
	$P_5 = 0.138483 P$	$P_5 = 0.119015 P$	$P_{12} = 0.007220 P$
	$P_6 = 0.027883 P$	$P_6 = 0.122073 P$	

Finite Element Solution

In view of circular shape of the model the x and y axes of the adjacent cells at the common nodes do not coincide (Fig. 16). Convenience of computer programming calls for the use of nodal displacements in the radial and tangential directions r and t , common to the neighbouring cells.

Fig. 16



The stiffness matrix of the cell in model coordinates $[K_o]$ is found from the one in cell coordinates $[K]$ by the equation

$$[K_o] = [L] [K] [L]^T \quad (19)$$

in which $[L]$ is the transformation matrix for the vectors of nodal displacements or forces, from the cell to the model coordinates, and $[L]^T$ is its transpose. Derivation of explicit expressions for the terms of $[K_o]$ is laborious and must be left to computer.

To make nodal displacements in the model solution consistent with the theoretical values, one of its nodes on the edge $\theta = \frac{1}{2}\pi$ must be given the exact value of u in Eq. (16). This calls for an additional step in the solution of the model. As the node in question, in this case the inner node on the edge $\theta = \frac{1}{2}\pi$, is being moved radially to its intended location, the three adjacent nodes, one on the same edge, and two on the neighbouring radial line, are kept at rest. This requires application to these nodes of the load vector equal to the product of proper terms of stiffness matrix and the displacement of the moved node. Following this, the moved node is kept at rest, and the reverse of the load vector at the three neighbouring nodes is added on to the active load system in solving the model for the displacement of the nodes.

Results

Calculation of displacements of the cell nodes in the sector plate is carried out with both, the bar cells described in this work, and the no-bar cells of the same trapezoidal shape [3], using the energy type stiffness matrix.

The action of the plate under consideration is substantially that of a sharply curved short cantilever beam, fixed at one end. Most of movement occurs in radial direction at the loaded free end, and it gets gradually smaller on recession from it. There is also some tangential movement resulting from normal stresses in lengthwise direction, tension on the outside and compression on the inside of the sector.

The bar cells of all three models are endowed with the values of the parameter ω equal to 0.001, 0.02, 0.2, 0.4. No-bar cells are also used.

In Table 6 the nodal displacements, or rather their coefficients c before $\frac{P}{Et}$, determined by the finite element method, are compared with the exact values, given by Eqs. (16) and (17). Quality of each solution is described by the greatest at all nodes value of error in c , separately in radial and tangential displacements. In the same table are also stated the percentages of the total number of nodes, at which the percentage error is no more than 2% in the coarse model, and 1% in the two other models.

To correlate the quality of the obtained displacement values with the total energies T of the deformed models, the values of the latter are stated in the table and also presented graphically in Fig. 17.

Since the true values of u given by Eq. (16) on the radial line $\theta = 0^\circ$, over which the load P is distributed, are all the same and are equal to $10.5206 \frac{P}{Et}$, the actual total energy of the sector is $T = -\frac{1}{2} (10.5206) \frac{P^2}{Et} = -5.2603 \frac{P^2}{Et}$. This may be compared with the values of T in the models.

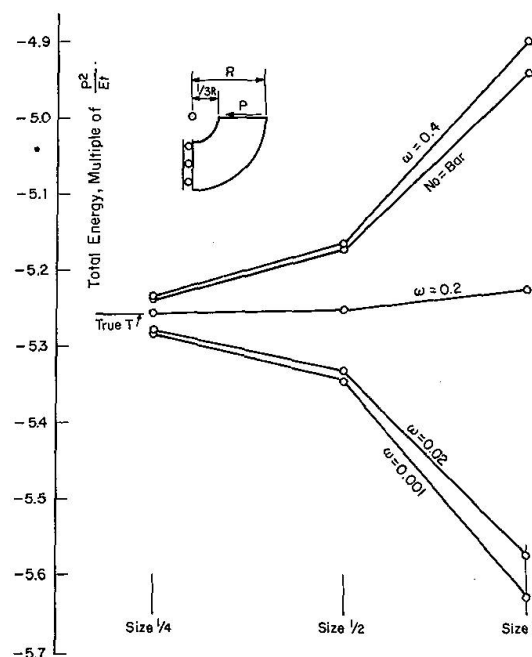


Fig. 17

Table 7. Models of 90° Sector Plate, $\mu = 0.2$.
Comparative Precision of Displacements in Pairs of Models
% of More Precise Displacements in Pairs of Models.

	#1. 15 Cell Model.					#2. 60 Cell Model.					#3. 240 Cell Model.				
	$\omega = 0.001$	$\omega = 0.02$	$\omega = 0.2$	$\omega = 0.4$	No-Bar	$\omega = 0.001$	$\omega = 0.02$	$\omega = 0.2$	$\omega = 0.4$	No-Bar	$\omega = 0.001$	$\omega = 0.02$	$\omega = 0.2$	$\omega = 0.4$	No-Bar
Radial Displacements			65%		35%			83%		17%			74%		26%
		26%	74%				37%	63%				24%	76%		
	9%	91%				20%	80%				24%	76%			
			91%	9%				87%	13%				84%	16%	
				9%	91%				8%	92%				18%	82%
Tangential Displacements			80%		20%			67%		33%			94%		6%
		25%	75%				23%	77%				8%	92%		
	15%	85%				13%	87%				33%	67%			
			95%	5%				87%	13%				93%	7%	
				55%	45%				53%	47%				57%	43%

In Table 7 several pairs of solutions, such as the ones with the bar cells involving $\omega = 0.001$ and $\omega = 0.02$, are compared on the basis of percentages of nodes, at which the displacements in one solution are better than in the other, and vice versa, irrespective of how great the differences are numerically.

Examination of results in Tables 6 and 7 leads to the following conclusions.

1. The total energies T in all models are quite close to the exact value in the sector $-5.2603 \frac{P^2}{Et}$. In the models having cells with $\omega = 0.001$ and 0.02 , they are numerically greater than the true T (i.e. algebraically smaller), and in the other three types of cells — numerically smaller. In the cells with $\omega = 0.2$ the value of T comes very close to the true one. As the 15 cells in the coarse models are subdivided into 60 and 240 cells, their energies T change monotonically towards the true value.
2. Precision of nodal displacements in the bar cell models with $\omega = 0.2$, whose T values are the closest to the exact, is by far the best, as judged by most of the criteria in Tables 6 and 7. This applies equally well to the coarse and the fine cell models.
3. Displacement precision of all models in all ways of description improves substantially, as the number of cells increases.
4. Results with models of $\omega = 0.02$ and the no-bar cells come next in precision to those with $\omega = 0.2$. In some ways of measurement the former are better, and in the others — the latter. Farther behind them are the models with cells of $\omega = 0.001$ and $\omega = 0.4$.
5. The shape of convergence lines of the energies T on subdivision of cells (Fig. 17) is very significant. Three of these lines descend, as the cells are subdivided to $\frac{1}{2}$ and $\frac{1}{4}$ sizes, and two ascend on the way to the exact value of T . Models with the best type of cells ($\omega = 0.2$) have the flattest convergence line, because their values of T are the closest to the exact.

6. Confirming the theoretical conclusion reached earlier, convergence lines of models constructed of different types of cells, do not intersect on the way to the true value of T , as the cells are subdivided.
7. The advantage of cells with a variable parameter ω lies in availability of the type of cell most suitable to the problem in question, having precision in mind. If one kind of cell in the model results in an ascending convergence line, and another — in descending, the cell, characterized by the best T , must lie somewhere in between. To obtain a comparable precision with models constructed of no-bar cells, their size must be made very fine, and the computer solution lengthy.

Notation

A	without and with subscripts and superscripts, — bar areas.
E	modulus of elasticity.
$[K], [K_o]$	stiffness matrix of cell in x, y and r, t coordinates respectively.
$[L]$	transformation matrix.
P	acting load; with number subscripts, — fractions of it.
R	radius of plate.
T	total energy.
U	energy of deformation.
V	potential energy.
X, Y	with and without subscripts, — corner forces in cell.
X, Y	with subscripts and superscripts, — terms of stiffness matrix.
a_1, a_2	lengths of parallel bases of trapezoidal cell.
c	coefficient in expression for nodal displacement.
h	height of cell.
k, k_1	ratios describing the shape of cell.
n	number of circumferential rows of cells in model.
r	polar coordinate, radius.
r, t	structure coordinate axes.
t	plate thickness.
u, v	with and without subscripts, — nodal displacements.
u_o, v_o	remaining distances in Fig. 12.
x, y	cell coordinate axes.
α	base angle in the cell.
γ_{xy}	unit shear strain.
δ	nodal displacement.
ϵ_x, ϵ_y	normal unit strains.
η	a parameter.
θ	polar coordinate; angle of bar A_3 with horizontal.
μ	Poisson's ratio.
r, ω	parameters.
$\tau_{r\theta}$	shear stress.
ϕ	angle subtended by cell.

Acknowledgment

The research forming the basis of this work was conducted with financial assistance of the National Research Council of Canada, and this is gratefully acknowledged. The authors are also thankful to S.L. Lipson, the Head of the Department of Civil Engineering and A.G. Fowler, the Associate Director of the Computer Centre, of the University of British Columbia, for provision of computer facilities. Thanks are also expressed to the former graduate students in the Department of Civil Engineering, H.G. Charania, C.I. Mathew and Rajan Sen for some of the computer work.

Application with the view to safety and economy

With introduction of digital computer the method of Finite Element has brought into engineering practice a reliable numerical procedure for solution of numerous, hitherto insoluble, problems of practical importance, related to analyses of stresses, vibrations and instability of structures composed of continuous elastic material. Among the applications may be mentioned tall buildings depending for their strength and stability on shear walls, coverings of large areas by shells of spherical, cylindrical and other shapes and elements of modern aircraft.

In each case the structure under investigation is replaced by a model composed of an assembly of polygonal units, called finite elements or cells, of repeated pattern, planar in shape (usually rectangular, trapezoidal or triangular) or three dimensional. Planar cells may be capable of resisting stresses lying in their planes only, or flexural stresses, or both planar and flexural.

The displacements and stresses found by the computer are approximate, and their precision depends on the fineness of subdivision and the type of cells. Models made of fine cells in general give better results, but require longer computer time, and their precision may suffer from too great a number of simultaneous equations and the resultant unfavourable effect of rounding off errors by the computer, requiring special procedures for counteracting them.

Some finite elements are better than others, and the unfavourable effects mentioned here may be less pronounced, even with coarser cells. Cells may be of bar or no-bar types.

As the model is repeatedly subdivided into smaller units of the same shape and type, the solution, in all its aspects, i.e., in displacements, stresses and the energy of the system, converges gradually to the true values. Better cells are the ones, whose lines of such convergence are quite flat, i.e., whose energy, even in a coarse model, is not far from the true one.

The advantage of the cell proposed in this work lies in provision of a variable parameter, whose better value for the particular problem is found by trial to make the energy convergence line fairly flat.

The cells used in the present study are of the bar type, in the shape of equilateral trapezoid, and are suitable for solving plane stress or plane strain problems in a body, whose geometry may be described conveniently in polar

coordinates. Among suitable examples may be mentioned plane stress in a plate with a circular hole and stress analysis in rock around a circular tunnel.

Rectangle is a special case of trapezoid, and so the theory proposed here may be extended to rectangles.

The application of the theory is demonstrated on an example, whose exact theoretical solution is available.

References

1. CHARANIA, H.G.: Plane Stress Analysis with Isosceles Trapezoidal Bar Cells. Thesis for the Degree of Master of Applied Science in Civil Engineering, the University of British Columbia, Canada, 1968.
2. HRENNIKOFF, A.: Framework Method and its Technique for Solving Plane Stress Problems. Publications, International Association for Bridge and Structural Engineering, Vol. 9, 1949.
3. HRENNIKOFF, A.: The Finite Element Method in Application to Plane Stress. Publications, International Association for Bridge and Structural Engineering, Vol. 28-II, 1968.
4. HRENNIKOFF, A., and AGRAWAL, K.M.: Superior Rectangular Bar Cells in Plane Stress. Conference on "Symmetry, Similarity and Group-Theoretic Methods in Mechanics", the University of Calgary, Alberta, Canada, August 1974.
5. TIMOSHENKO, S.: Theory of Elasticity. McGraw Hill Book Co. Inc., New York, 1934.

Summary

Finite elements in the shape of isosceles trapezoids, formed of several elastic bars are proposed for analysis of plates in plane stress, when the plate geometry can be conveniently described in polar coordinates. The elements used are endowed with some distinctive features and possess a variable parameter contributing to precision of results. Stiffness matrix of the cell is derived, and the application is demonstrated on analysis of displacements of a plate in the shape of a circular sector with central cut-out, whose theoretical solution is available.

Comparison with the theoretical results shows the superiority of the proposed cell over the no-bar cell. A method for selection of a proper value for the variable parameter is suggested.

Résumé

On propose d'utiliser des éléments finis en forme de trapèzes isocèles de plusieurs barres élastiques, afin d'étudier des plaques chargées dans leur plan, lorsqu'il est indiqué de décrire la géométrie de la plaque par des coordonnées polaires. Les éléments employés sont dotés de certaines propriétés caractéristiques pour améliorer la précision. On obtient la matrice de rigidité de l'élément et on applique cette théorie à l'étude des déplacements d'une plaque en forme de secteur circulaire avec évidement central, dont la solution théorique est connue.

La comparaison entre les résultats théoriques et ceux obtenus par l'utilisation d'éléments sans barres montre la supériorité de la cellule proposée par rapport à la cellule sans barres. On propose une méthode de sélection d'une valeur propre pour le paramètre variable.

Zusammenfassung

Finite Elemente in Form isoceler Trapezoide, bestehend aus mehreren elastischen Stäben, werden für die Berechnung in ihrer Ebene belasteter Platten vorgeschlagen, wenn sich die Plattengeometrie in Polarkoordinaten zweckdienlich ausdrücken lässt. Die verwendeten Elemente besitzen gewisse unterschiedliche Merkmale und einen veränderlichen Parameter, der zur Genauigkeit der Resultate beiträgt. Für die Zelle wird die Steifigkeitsmatrix abgeleitet und ihre Anwendung beim Berechnen der Verschiebung einer Platte in Form eines Kreissektors mit zentrischem Ausschnitt gezeigt, dessen theoretische Lösung verfügbar ist.

Vergleiche mit den theoretischen Resultaten zeigen die Vorzüge der vorgeschlagene Zelle gegenüber der stablosen Zelle. Es wird eine Methode zur Auswahl eines Eigenwertes für en veränderlichen Parameter vorgeschlagen.

Leere Seite
Blank page
Page vide

Fatigue Strength of Form-Reinforced Composite Slabs for Bridge Decks

Résistance à la fatigue de plaques composites en béton armé pour tabliers de ponts

Ermüdungsfestigkeit von Stahlbeton-Verbundplatten für Brückenfahrbahnen

R. P. JOHNSON

University of Warwick, Coventry, England.

J. J. CLIMENHAGA

John Stephenson and Associates, Toronto,
Canada.

Introduction

There are several advantages in using corrugated steel permanent formwork for the construction of concrete bridge decks and floor slabs, rather than conventional timber or steel formwork. Erection is quicker, and no shoring or dismantling are required. If adequate shear connection is provided, the formwork can also act as reinforcement for the deck slab.

In North America, corrugated steel decking is widely used as formwork for floors in buildings, and is designed to act compositely with the concrete. Design is usually based upon safe-load tables supplied by the decking manufacturer, who derives them empirically from his own tests. There is little published information on fundamental research into this type of construction. In the only report on fatigue behaviour known to the authors [1] results of six tests are presented, but insufficient data are given to permit their analysis in terms of bond and bearing stresses on dimples in the shear spans.

An experimental study of the stiffness and static and fatigue strength of composite slabs reinforced with two types of corrugated steel decking is summarised in this paper, and recommendations for design are given. A full report on the work is available [2].

The primary aim of the tests was to find out if "form-reinforced" concrete slabs are suitable for use in the decks of highway bridges. The design of the test specimens was based on criteria laid down in 1970 by the Bridges Engineering Division of the Department of the Environment. Those that influenced the design of the test specimens are:

1. Range of spans, 1.8 to 3.6 m (6 ft to 12 ft).
2. Overall depth of slab not less than 0.18 m (7 in).
3. The metal decking alone must be capable of carrying its own weight, that of the concrete slab, and in addition a load of 9 kN (2,000 lb) applied over a circular area 0.6 m (2 ft) in radius.

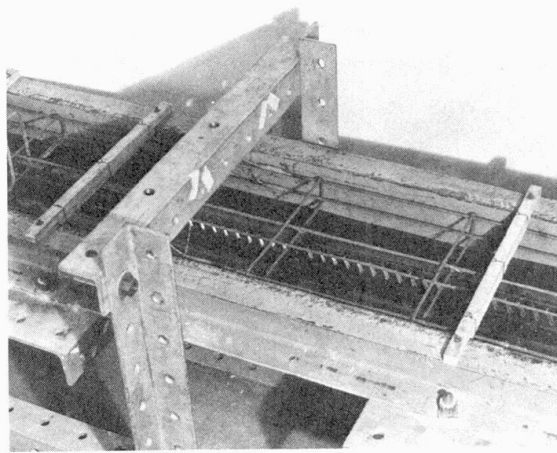


Fig. 2. Specimen DS3 before casting.

is quite small. This suggested that shear connectors could be welded to the tops of the corrugations. Thus the first two profiles tested (Figs. 1 and 3) were determined by the fabrication facilities readily available. All linear dimensions are two-thirds full size, except the sheet thickness (1.6 mm). In the first group of four specimens (DS1 to 4), the dimples (Fig. 2) were pressed individually. The second group of specimens, MS1 to 4, were made to the same design as Group 1, except that welded-bar shear connectors (Figs. 3 and 9) were used in place of dimples.

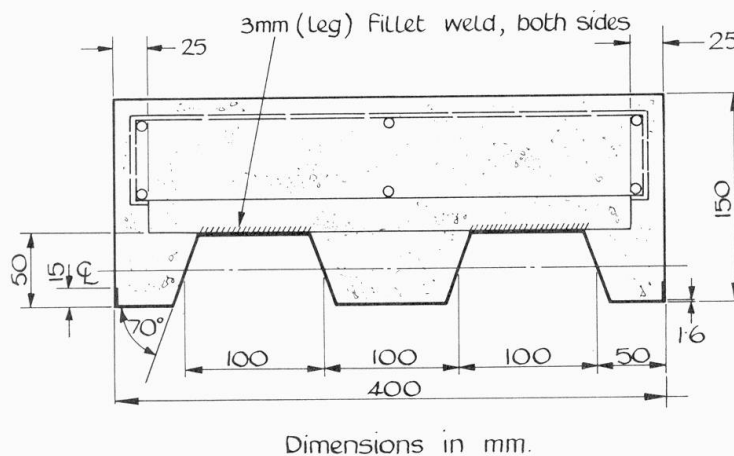


Fig. 3. Typical cross section of specimens MS1 to MS4.

The maximum length of plate that could be corrugated was 1.22 m. Longer units were required for the tests, so 2.44-m lengths were made by butt welding the shorter pieces together. This was not a preferred method of fabricating specimens for fatigue tests, but only one test result, to be described later, was influenced by it.

A third group of specimens (DS5 to 14) using proprietary galvanised decking made in North America was also tested. The corrugated sheets were similar to those of Group 1, except that the dimples projected about 0.9 mm into the concrete, instead of 4.0 mm.

This projection was insufficient to transfer longitudinal shear after breakdown of bond in the fatigue tests, and it was concluded that these sheets were unsuitable for the loading specified. These results are given elsewhere [2].

Design of specimens. It was decided to test simply supported specimens representing a strip of bridge deck spanning transversely between longitudinal girders, and to use symmetrical two-point loading (Fig. 1c).

In designing the specimens of Groups 1 and 2, it was found that the flexural strength of the steel section was determined by the longest span and loading condition [3] above. Maximum longitudinal shear in the composite section is that due to a wheel load. It was assumed that the critical parameter of interaction was the bearing stress, f_g , on the projected area of the dimples or bar connectors. The allowable bearing stress due to a 90-kN wheel load was taken as $0.6u$, where u is the design cube strength (i.e. two-thirds of the specified 'works' cube strength). This led to the dimple size and spacing shown in Fig. 1 and to the use of three bar connectors 19 mm high in each shear span of specimen MS1.

Table 1. Properties of specimens

Specimen No.	Cube strength	Modular ratio, m	Calc. P for HB loading	Calculated P_u	Observed P_{ut}
	N/mm ²		kN	kN	kN
DS1	26.1	8.6	20.5	51.8	63.0
2	34.0	8.9	30.0	53.5	65.0
3	26.6	9.0	20.5	51.8	58.5
4	23.6	9.8	20.5	50.8	32.0*
MS1	25.4	9.0	33.0	51.4	33.0*
2	20.1	11.7	27.0	49.2	30.0*
3	25.1	10.1	22.0	51.4	30.0*
4	24.5	9.1	18.0	51.2	33.0*

* Fatigue failure.

Information on the concrete used and on the strength of the specimens is given in Table 1. In Group 1, the design longitudinal shear per unit length of specimen was determined by the chosen dimple size and spacing and the assumed bearing stress, since bond was neglected. Thus the design vertical shear was known for each shear span, the length of which was then chosen from consideration of the flexural strength of the specimen. In Table 1, the column 'Calc. P for HB loading' gives the load on the specimen at which the calculated bearing stress on the dimples in each shear span is $0.6u$, and 'Calculated P_u ' gives the load for flexural failure, calculated using full-interaction theory.

No attempt was made to reproduce in the steel the stresses due to 'unpropped' construction, for these are small near the supports, where the highest shear stresses occur.

Details of specimens, and test variables. In Group 1, the only planned variables were the overhang past the support points, which was 0.46 m except in DS4 (0.28 m), and the magnitude and number of the load applications, of which details

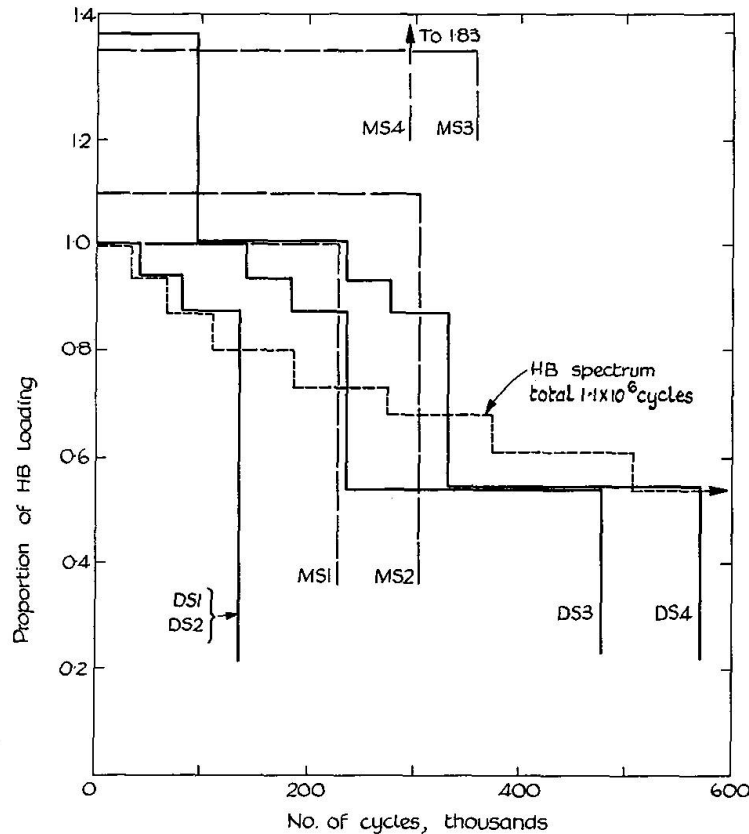


Fig. 4. Repeated loading of specimens.

are given in Table 2. The loadings are compared with the standard HB spectrum in Fig. 4. The values f_g/u in Table 2 are based on measured cube strength, and so do not correspond exactly to 0.6 at the maximum HB wheel load of 90 kN (20,200 lb).

Table 2.

Specimen No.	$N_1 \times 10^3$	f_g/u	$N_2 \times 10^3$	f_g/u	$N_3 \times 10^3$	f_g/u	$N_4 \times 10^3$	f_g/u
DS 1	—	—	55	0.52	41	0.55	41	0.59
2	—	—	55	0.46	41	0.50	41	0.53
3	240	0.32	55	0.51	41	0.55	141	0.58
4	240	0.36	55	0.57	41	0.62	141*	0.66

* Followed by 94,700 cycles at $f_g/u = 0.83$.

In DS1 to 3, the fatigue testing was followed by static tests to failure. In DS4, repeated loading at a mean bearing stress of $0.83 u$ was continued until failure.

The specimens of Group 2 differed from DS1 to 4 only in the method of shear connection and in the end overhang (0.28 m). The main variable was the intensity of loading on the bar connectors. In designing specimen MS1, it was assumed that the connector would be effective for 130% of the welded length, that f_g should not exceed $0.6 u$ and that $u = 24.2 \text{ N/mm}^2$. The weld size was governed by the plate thickness; the design of the welds is discussed later.

These assumptions led to the provision of three connectors at 216 mm pitch in each shear span of MS1 and one in each end overhang. The use of fewer and smaller connectors was studied in the other three tests. In MS2 to 4, the bar in each end overhang was omitted; in MS3 and 4 the height of the bars was reduced from 19 mm to 13 mm, and in MS4, only two bars at 254 mm pitch were provided in each shear span. An additional connector was provided in each specimen at midspan, to prevent uplift.

Table 3. Properties and Results. Group 2.

Specimen No.	Load range	f_g/u	σ_{bd}	$\bar{\sigma}$	N_u	N_c	N_f	$\frac{\log N_c}{\log N_u}$
	kN		N/mm^2	N/mm^2	10^3	10^3	10^3	
MS 1	3-33	0.60	56.1	157	102	230	230	1.17
MS 2	3-30	0.67	43.4	138	175	300	306	1.10
MS 3	3-30	0.82	43.4	115	426	303	360	0.95
MS 4	3-33	1.10	25.5	151	120	197	296	1.10

All specimens in this Group were subjected to fluctuating loads over a single load range (Table 3) until failure. The maximum load on MS1 was that corresponding to 1.0 times HB loading (Table 1). That for MS2 gave a mean bearing stress of 0.67 u , and so corresponded to 1.1 HB. Much higher bearing stresses were used in the last two tests, where the maximum loads were chosen such that the flexural stresses in steel and concrete did not exceed 0.85 f_y and 0.65 u , respectively. The columns headed f_g/u and σ_{bd} in Table 3 give the calculated mean bearing stress f_g and the maximum longitudinal flexural stress in the decking at a weld location, σ_{bd} , at these maximum loads.

Casting procedure. During casting, the metal decking was supported at its ends and third points and was coated with mould oil to inhibit bond. About 14 concrete control specimens of various types were cast and cured with each test slab.

Test Procedure

In the fatigue tests, the minimum load was about 10% of the maximum, so the stress ratio was +0.1. The rate of loading was 200 to 250 cycles/min. Before and during each test, the behaviour of the specimen was monitored by stopping the pulsator and taking sets of readings during a static "run" over the maximum load range.

Static tests to failure were conducted in the same apparatus, and were completed in from 1 to 4 hours.

Curvature, deflection, and longitudinal strains were measured at midspan in all tests. End slip was also measured in each test, and in some tests slip distribution along the shear span was recorded.

Static tests to failure were carried out on five push-out specimens in which the two types of shear connection were reproduced.

Test Results

Typical results are now given; full details are available elsewhere [2]. Data from the static test runs are labelled with the number (N) of cycles of repeated loading completed at that stage. The maximum load per jack applied to each specimen, P_{ut} , is given in Table 1.

In auxiliary tests on materials, the yield strengths in tension of the decking were found to be 257 N/mm^2 for Groups 1 and 2 and 277 N/mm^2 for Group 3; that of the reinforcement was 381 N/mm^2 . Table 1 gives results of compressive strength and stiffness tests on the concrete at the mean age of testing of the parent test specimen (29 to 31 days).

Group 1. In Fig. 5, the ratio of the applied load (P) to the calculated load for flexural failure (P_u , Table 1) is plotted against the midspan deflexion, δ , for each of the static-load tests on specimen DS3. The change from a cracked to an uncracked section occurred during the first test ($N=0$). The crack spacing in the midspan region was about 0.13 m. The curve for the final static test to failure has been zero-corrected. The bands on Fig. 6 show the ranges, for two levels of load, within which midspan strain readings during static tests fell for the whole duration of the fatigue test on this specimen. Typical slip distributions are given in Fig. 7. Results for specimens DS1, 2 and 4 are similar.

The testing of DS4 was designed to study its fatigue strength. The first 377,000 cycles of load (Table 2) simulated the upper part of the HB loading spectrum (Fig. 4). Another 100,000 cycles of loading at $f_g/u = 0.66$ were followed by 94,700 cycles at $f_g/u = 0.83$, at which time fatigue failure occurred in the butt weld in the decking.

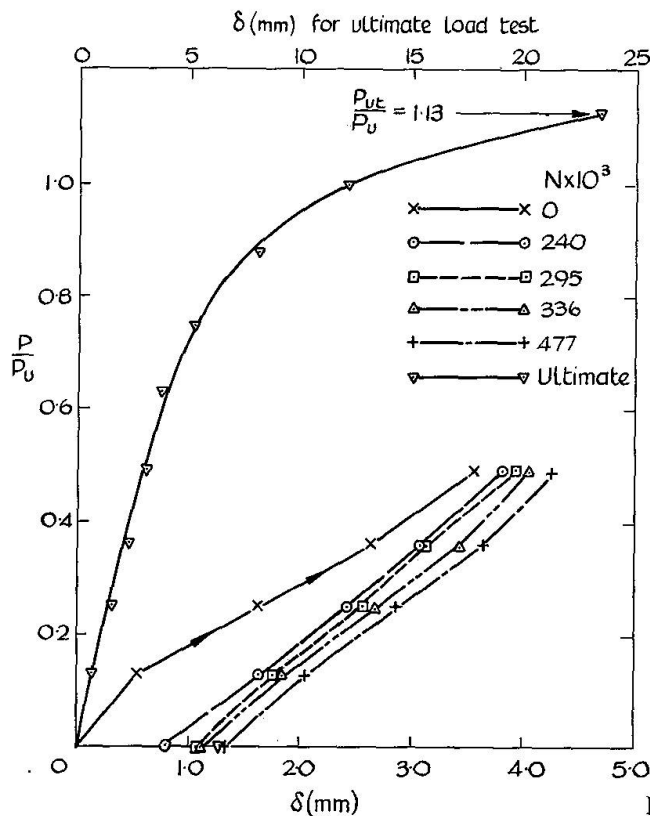
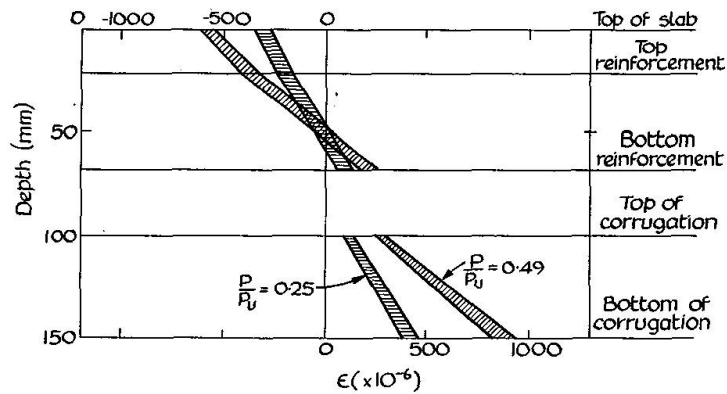
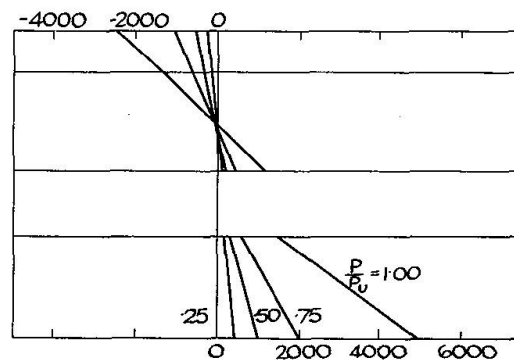


Fig. 5. P - δ curves for DS3.



(a) Strain distributions during fatigue tests



(b) Strain distributions during static test to failure

Fig. 6. Longitudinal strain distribution at midspan during fatigue tests on DS3.

In the ultimate-load tests, DS1 to 3 failed in flexure like reinforced concrete beams (Fig. 8). Slip increased during the tests (e.g. Fig. 7), but no real distress of the shear connection was observed in any of these specimens.

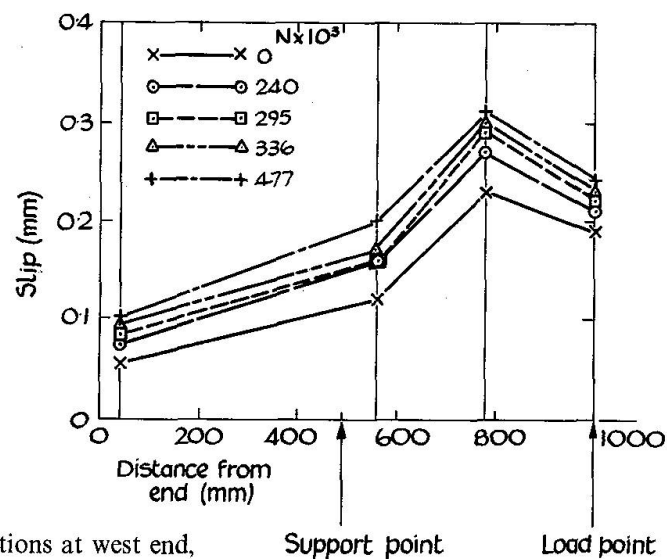


Fig. 7. Slip distributions at west end, specimen DS3.

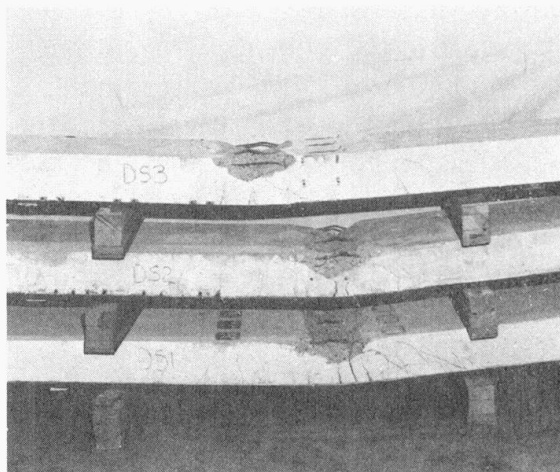


Fig. 8. Specimens DS1 to DS3 after test.

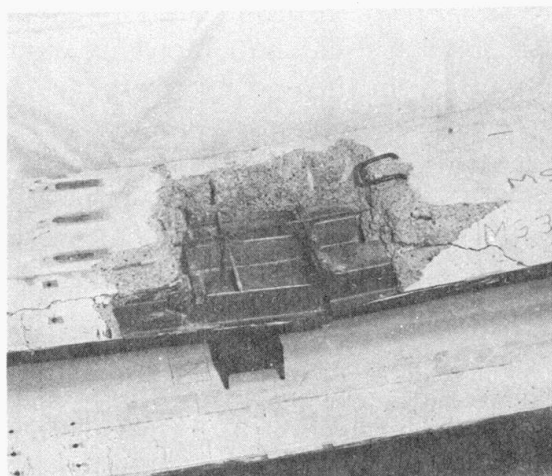


Fig. 9. Concrete removed at failure location in MS3.

Group 2. Load-deflexion curves and strain and slip distributions found in the static tests were similar to those of Group 1, and showed that repeated loading caused little deterioration of stiffness. All four specimens failed by fracture of the decking at a connector location (Fig. 9). Table 3 gives the number of cycles at failure, N_f , and at which cracks were first noticed, N_c . In MS2, 3, and 4, these occurred well in advance of failure, located at the corners of the tops of the corrugations in the heat-affected zone of the connector welds. In all three tests, they were observed at corresponding positions in both shear spans; but those in the spans that failed then increased in length more rapidly than the others.

Push-out tests. The load-slip curves for the specimens of Group 1 and Group 2 [2] were similar in shape to those for stud connectors. Failure occurred by crushing of the concrete against the dimples and distortion of the corrugations (Group 1) and by tearing of the metal decking (Group 2).

Discussion of Results

Group 1. Most of the irrecoverable deflexion of these specimens occurred during the first load cycle. The small increases in permanent set and the consistent distribution of longitudinal strains and slip show that repeated loading caused negligible deterioration at the dimple-concrete interfaces. The sets of P - δ curves show that additional cycles of load at low levels have very little effect, and suggest that the behaviour would have been much the same had the entire loading spectrum been applied.

It had been assumed in planning the tests that full HB loading should correspond to a bearing stress of $0.6 u$ on the dimples, bond being neglected. In considering this as a design value, it is helpful to compare (Fig. 4) the loading imposed in the tests with the standard HB spectrum. The spectrum down to 0.61 HB is effectively covered by the tests. Lower loads should cause bearing stresses not exceeding about $0.3 u$, which should not cause fatigue damage to the concrete.

There is evidence from test DS4 that a bearing stress of $0.7 u$ or $0.8 u$ could probably be used; but allowance must be made for the contribution to shear strength from the end overhangs (neglected in the calculations). For example, if the effective shear span was the actual span plus half the overhang length, the mean values of f_g/u in DS1 to 3 were 70% of those reported, and 80% in DS4. There should be no problem where forms are continuous over supports, but the strength of a shear span without overhang may be less than found in these tests. It is concluded that $0.6 u$ should be used in design for HB wheel loading until more evidence becomes available.

The static tests to failure showed that previous fatigue testing at bearing stresses up to $0.6 u$ causes little, if any, reduction in static strength. Both DS1 and DS2 had flexural strengths 1.21 times the value given by simple plastic theory, and the ratio for DS3 was 1.13.

Group 2. Comparisons of the results from Groups 1 and 2 show that their behaviour was similar, and that the slabs with bar connectors were slightly stiffer than those with dimples. The similarity of the distributions of slip was remarkable [2], bearing in mind that shear connection in the Group 2 specimens was provided only at two or three points in each shear span and (in MS2 to 4) not in end overhangs.

Examination of the connectors in MS3 after the test (Fig. 9) confirmed other evidence that little distress or distortion occurred at the shear connectors during fatigue testing.

It is evident from Table 3, Fig. 4, and the mode of failure that the nominal bearing stress f_g/u was not a critical parameter in these tests. In MS1 to MS3 increased bearing stress is accompanied by increased fatigue life. In MS4 no increase in the flexibility of the specimen was observed until after cracking of the decking, showing that the greatly increased bearing stress did not reduce the effectiveness of the shear connection.

The range of mean bearing stress explored was from $0.6 u$ to $1.1 u$. CP 117: Part 2 [4] limits the load per connector for HB loading to $0.4 P_w$, which corresponds to a mean bearing stress of $0.93 u$ for the bar connectors listed in Table 2 of CP 117. It is concluded that this same level of bearing stress could be used for bar connectors attached to corrugated sheeting.

It does not follow that the weld sizes should be as specified in CP 117, for in the present application each weld supports a greater length of bar, and attaches it to a plate that may be thinner than the flange of a typical girder. It can be shown [2] that the fatigue life was determined mainly by the stresses in the weld, rather than by the longitudinal stress in the decking, given as σ_{bd} in Table 3.

The Table also gives the mean stress on the weld throat, $\bar{\sigma}$, and the fatigue life N_u for a Class F detail having this maximum stress, taken from B.S. 153 [3]. For the present purpose, failure is assumed to occur in the test when the first crack is observed, given as N_c cycles in the Table. The ratios $(\log N_c / \log N_u)$ give the 'safety factor' of the weld in relation to design to B.S. 153.

When account is taken of the assumptions made above, and the inevitable scatter of the results of fatigue tests, it can be seen that there is good agreement between the test data and the predictions of B.S. 153.

It is of interest that, as assumed in this analysis, all fractures occurred on the side of a connector closer to midspan, and at the connector where the measured slip was greater, not at the connector nearest to the load point.

The ratio of weld leg length to plate thickness was 1.9, far in excess of the limit of 0.5 given in CP 117: Part 2. These results suggest that a higher limit, perhaps 1.5, could be allowed for metal decking. It is concluded that with this limitation, the method of B.S. 153 may be used for designing fillet welds to bar connectors in corrugated composite plates.

Pushout tests. In the three pushout tests on Group 1 specimens the lowest mean bearing stress at failure was $1.65 u$. This gives a generous margin above the proposed design stress of $0.6 u$ for repeated loading. These results and the static tests of Group 1 show that the design ultimate bearing stress for static loading could be increased to about $1.0 u$.

The tests on bar connectors showed that the strength was governed by the sheeting, not by bearing stress on the bars, which exceeded $1.5 u$ in both tests.

Conclusions and Recommendations for Design

The plate specimens tested were in essence two-thirds scale versions of a prototype designed to the requirements of the Department of the Environment (Ministry of Transport) for use as permanent formwork in bridge decks subjected to HA and HB loading. The purpose of the work was to develop design rules for this formwork, using it if possible as the bottom reinforcement of the deck slab.

It was assumed that the design criterion was that the shear connection should be capable of resisting the local effects of the fatigue spectrum of HB loading without significant reduction in the flexural strength of the bridge deck under static loading. Two of the three types of decking studied are believed to be satisfactory for this purpose. Tentative design rules for these (Groups 1 and 2) are now given.

1. The mean bearing stress on the projected area of dimple shear connectors as used in specimens DS1 to 4 due to 1.0 times HB wheel loading should not exceed $0.6 u$, where u is the design cube strength of the concrete. The stress should be calculated by the elastic theory, using a fully composite section and neglecting the tensile strength of concrete.
2. The corresponding stress for bar connectors as used in specimens MS1 to 4 is $0.9 u$. The effective length of each bar is the lesser of the actual length and 1.3 times the length welded to the corrugated decking.
3. The fillet welds by which bar connectors are attached to decking may be designed for fatigue in accordance with B.S. 153: Part 3B, provided that the leg length of the weld does not exceed 1.5 times the thickness of the decking, and that the coexisting longitudinal tensile stress in the decking at the weld does not exceed 50 N/mm^2 (3.2 ton/in^2).
4. The limiting value of static bearing stress on dimples at the Collapse Limit State was not determined, but is not less than $1.0 u$. When this condition is satisfied, the static flexural strength of the composite section may be taken as that given by the well-established rectangular-stress-block theory.

5. The strengthening effect of overhang of the composite plate beyond a simple support was not studied. Overhangs not less than 0.28 m were used in the tests.
6. Pushout tests for corrugated decking were devised. They are thought to give a reliable indication of the static strength of the connectors used.

Information about possible variations in the design of the sheeting used for Groups 1 and 2 may be useful. The ratio of dimple projection to sheet thickness was 2.5. That in the proprietary decking, 0.55, was found to be too small for complete interaction after repeated loading [2]. Obviously other factors, such as the shape of the dimple, are relevant: but it is thought that a successful design will have a ratio of at least 2.0. If a scaled-up version of the Group 2 sheets were made, it might be better to use relatively smaller bars and welds, for fatigue behaviour should be improved, and failure of connectors before shattering would provide warning of deterioration.

The effects of corrosion and fire have not been studied.

The choice between dimpled and undimpled-with-bars formwork will depend mainly on relative cost. Both types are believed to be suitable for use in bridge decks.

Consequences of this work

The cost of corrugated steel decking depends on the demand for it, to a far greater extent than for many other materials, because of the large capital investment needed for its manufacture. It is evident that its use in bridge decks can reduce construction costs. The safety and economy of such structures can only be ensured through an understanding of the fatigue behaviour of possible types of shear connection between the steel decking and the concrete slab. The research reported above provides guidelines for the development of commercially viable profiles and methods of shear connection for use in structures subjected to repeated loading.

Acknowledgments

The authors are grateful to the Department of the Environment, for whom the work was done, for permission to publish this paper. They also acknowledge with thanks the willing help with the experimental work given by Mr. C.J. Mason and his colleagues at Cambridge University Engineering Laboratories.

References

1. MOUW, K.W.: Fatigue Testing of Light Gage Metal Forms. Rept. ERI-348, Engineering Research Institute, Iowa State University, Jan. 1969, p. 35.
2. CLIMENHAGA, J.J., and JOHNSON, R.P.: Use of Corrugated Metal Decking as Permanent Formwork for Composite Bridge Decks. Engineering Laboratory, University of Cambridge, Nov. 1971, p. 74.
3. B.S. 153: Specification for Steel Girder Bridges. Part 3B: Stresses. British Standards Institution, 1958.
4. CP117: Composite Construction in Structural Steel and Concrete. Part 2: Beams for bridges. British Standards Institution, 1967.

Summary

Results are given of static and fatigue tests on eight composite plates, each consisting of a sheet of corrugated steel decking attached by dimple or bar shear-connectors to an in situ concrete slab. The local effects of repeated wheel loads up to 90 kN (20,200 lb) were simulated in the tests. Rules for designing two types of shear connection for composite plates in bridge decks are deduced from the results.

Résumé

On donne des résultats d'essais statiques et de fatigue opérés sur huit plaques composites dont chacune est composée d'une tôle d'acier ondulé attachée par encastrement ou par connecteurs de cisaillement sur une plaque en béton armé installée sur place. Les effets locaux dus aux charges de roue répétées jusqu'à 90 kN (20000 lb.) ont été simulés aux essais. Par les résultats obtenus on a dérivé des règles en vue de projeter deux types de connexions de cisaillement pour plaques composites de plates-formes de tabliers.

Zusammenfassung

Es werden die Ergebnisse von statischen und Ermüdungsversuchen an acht Verbundplatten mitgeteilt, wobei jede aus gewelltem Stahlblech besteht, die mittels einer Verbindung oder eines Schubverbinders an einer an Ort und Stelle vorhandenen Betondecke befestigt ist. Die örtlichen Einflüsse wiederholter Radlasten bis zu 90 kN (20000 lb) wurden bei den Versuchen simuliert. Aus den gewonnenen Resultaten wurden Regeln zum Entwurf zweier Typen von Schubverbindern für Verbundplatten an Brückenfahrbahnen abgeleitet.

Leere Seite
Blank page
Page vide

Réaction dynamique des structures soumises aux charges mobiles

Dynamic Response of Structures to Moving Loads

Dynamisches Verhalten durch bewegliche Lasten beanspruchter Bauwerke

A. KHOUDAY

Ing., M.Sc., candidat au grade de docteur ès sciences, Université Laval, Québec. Bureau d'études Lalonde, Girouard, Letendre et Associés, Montréal.

J. PROULX

Ingénieur-conseil, Ph.D., Bureau d'études Beau-lieu, Poulin et Robitaille, ex-professeur agrégé, Université Laval, Québec.

Introduction

Généralités

Le problème du comportement dynamique des structures soumises à des charges mobiles a toujours incité un intérêt spécial tant dans le domaine du génie civil [1] et mécanique que dans le domaine du génie naval et aéronautique. Dans tous ces domaines, les études théoriques, en laboratoire, et sur chantier se sont intensifiées ce dernier quart de siècle. Ces études visaient une meilleure connaissance des paramètres et du comportement de ces systèmes et une élaboration de méthodes de calcul pour estimer la valeur de leurs réponses dynamiques. Les sujets principaux de ces études étaient le pourcentage d'amplification dynamique, les effets de fatigue et la limitation des fréquences nuisibles tant aux structures qu'aux humains qui les utilisent.

La méthode proposée dans cette publication présente un outil maléable et efficace pour traiter les problèmes parfois complexes des réponses dynamiques des structures soumises à des charges mobiles. Une réponse déterministe dynamique peut être calculée en premier lieu en réduisant le système à une force mobile constante. L'écart type de cette réponse peut être aussi estimé si l'excitation mobile est due à plusieurs facteurs ou si le système mobile est complexe.

Dans la pratique courante du génie civil, il n'est pas d'usage de compléter l'analyse statique des structures par une analyse dynamique. Les différents codes fournissent plusieurs critères et facteurs pour tenir compte de l'effet dynamique. Les ponts sont peut-être l'exemple le plus important de ces genres de structures. Mais l'évolution et la diversité des modes et matériaux de construction des ponts et la tendance vers une utilisation de véhicules plus rapides et plus lourds incitent à une révision des différents codes et méthodes de calcul et à une sélection de nouveaux critères limitant les effets nocifs pouvant être causés à ces structures et aux voyageurs qui les utilisent. Les codes et méthodes de calcul utilisés actuellement

sont basés sur une conception statique de l'application de la charge et du comportement du pont. Or ni la charge ni le pont ne représentent l'aspect d'un système statique. Le véhicule se rapproche plutôt d'une force perturbatrice mobile et le pont possède des caractéristiques vibratoires propres. Les spécifications d'impact actuelles, quoique encore valables puisqu'elles représentent un pourcentage tolérable d'augmentation de la charge statique, n'ont aucune justification théorique ou expérimentale acceptable pour être appliquées à la grande diversité des ponts, présents et futurs.

Il est inutile pour des spécifications futures et générales de proposer une méthode de calcul dynamique. Une équivalence statique de l'effet dynamique et certains critères appropriés peuvent être élaborés dans le but de conserver l'aspect statique du problème et la simplification des calculs. Mais pour que de telles solutions s'avèrent justifiables, une connaissance du comportement vibratoire du système pont-véhicule, une évaluation de la grandeur des réponses dynamiques et une estimation des effets de la charge vive sur la vie de service de la structure, doivent être à la base de cette équivalence statique. La méthode proposée, à part sa contribution au domaine de la recherche se rapportant à l'étude des ponts soumis à la circulation, peut s'appliquer facilement dans le bureau d'ingénieurs pour l'étude des cas spéciaux de structures soumises à des charges mobiles.

Aperçu de la méthode

La formulation du problème dynamique des structures soumises à des charges mobiles diffère en complexité suivant que la structure est supposée de dimension finie ou infinie, ou qu'elle est représentée par un espace ou un semi-espace élastique traversé par une force à vitesses subsonique, transonique ou supersonique. L'attribution à la charge mobile des forces d'inertie et des caractéristiques dynamiques propres rend le problème plus complexe.

La méthode développée dans cette publication s'applique à une structure de forme quelconque et de dimension finie. L'amplitude, la répartition, la fonction du mouvement et le trajet de la charge sont arbitraires. La méthode est basée sur la technique des éléments finis pour calculer les valeurs et modes propres et sur l'analyse modale pour calculer la réponse. L'originalité et le fond de la méthode consistent à ne pas discrétiser les forces aux nœuds comme l'exige la technique de l'élément fini. La discrétisation des forces aux nœuds n'est nécessaire que dans le cas d'une charge mobile possédant une force d'inertie [2] ou des caractéristiques dynamiques propres et dans le cas d'un changement des caractéristiques élastiques [3] de la structure en fonction du temps. Dans ces cas, les coefficients des matrices formant l'équation dynamique du système ne sont plus constants, l'analyse modale n'est plus applicable que par étapes de petits intervalles et une solution par les méthodes de résolution numérique pas à pas est souhaitable.

Méthode classique

L'équation dynamique du système utilisant la technique des éléments finis s'écrit [4] sous la forme matricielle suivante:

$$M\ddot{U} + C\dot{U} + KU = P \quad (1)$$

La matrice colonne U représente les déplacements nodaux. Les matrices M , C et K sont les matrices de masses, d'amortissement et de rigidité de la structure assemblée. La matrice colonne P représente les charges nodales équivalentes. En appliquant l'analyse modale et en supposant que la matrice d'amortissement est proportionnelle soit à la matrice des masses, soit à la matrice de rigidité, ou soit à l'amortissement critique, l'équation (1) du système devient non couplée et prend la forme suivante:

$$\bar{M}\ddot{Q} + \bar{C}\dot{Q} + \bar{K}Q = \bar{P} \quad (2)$$

Les matrices \bar{M} , \bar{C} et \bar{K} sont diagonales et égales respectivement à $F^T M F$, $F^T C F$ et $F^T K F$. La matrice colonne Q représente les amplitudes modales (coordonnées généralisées) et est égale à $F^{-1}U$. \bar{P} est la matrice colonne des forces en coordonnées généralisées et est égale à $F^T P$. F est la matrice des modes propres et F^T sa transposée. Le retour aux coordonnées de la structure s'effectue par une prémultiplication des coordonnées généralisées par la matrice des modes propres F .

La solution de l'équation (2), quoiqu'elle diffère peu, suivant l'hypothèse faite au sujet de l'amortissement, s'exprime toujours sous la forme d'une intégrale de Duhamel [4]. Dans le cas d'une charge mobile concentrée ou d'une charge mobile répartie sur une surface limitée, la réponse de la structure est souvent calculée par l'une des deux procédures suivantes. Dans la première procédure, la matrice colonne \bar{P} est formée en premier lieu par assemblage, combinaison et superposition des forces nodales dues au déplacement de la charge sur la structure, puis l'équation (2) est résolue. Dans la seconde procédure, la réponse de la structure en coordonnées généralisées est une superposition des réponses dues au parcours de la charge sur chaque élément à part. Dans cette dernière procédure, les conditions finales de déplacement et de vitesse sont à noter au moment du départ de la charge de chaque élément traversé pour être prises en considération dans la superposition.

Méthode proposée

La modification proposée à la méthode de calcul basée sur la technique des éléments finis se situe au niveau du calcul des forces en coordonnées généralisées, soit la matrice colonne \bar{P} . Cette matrice est calculée à l'aide de la notion de «modes-trajet» et d'une manière équivalente à celle utilisée pour une structure à milieu continu. L'équation (2) prend à ce moment la forme suivante:

$$\bar{M}\ddot{Q} + \bar{C}\dot{Q} + \bar{K}Q = \bar{P} \quad (3)$$

La matrice colonne \bar{P} représente les forces en coordonnées généralisées et est calculée par une intégration s'étendant sur la structure:

$$\bar{P}(t) = \iiint_A p(x, y, z, t) \mathcal{F}(x, y, z) dx dy dz \quad (4)$$

$p(x, y, z, t)$ est une fonction représentant le chargement. $\mathcal{F}(x, y, z)$ est une matrice colonne dont chaque élément représente la forme d'un mode propre.

Charge concentrée

Considérons le cas d'une charge concentrée se déplaçant suivant une fonction de mouvement $s = g(t)$ sur un trajet déterminé s . Soit $p(t)$ la fonction représentant l'amplitude de cette charge. La fonction représentant le chargement peut s'écrire sous la forme suivante:

$$p(x, y, z, t) = \delta[x - g_x(t)] \delta[y - g_y(t)] \delta[z - g_z(t)] [p_x(t), p_y(t), p_z(t), p_{xx}(t), p_{yy}(t), p_{zz}(t)] \quad (5)$$

où δ est la fonction Dyrac et g_x , g_y et g_z sont des fonctions représentant les composantes du mouvement par rapport aux coordonnées de la structure. Les fonctions p_z et p_{zz} , par exemple, représentent respectivement l'amplitude d'une force et d'un moment par rapport à z . Les fonctions p_x , p_y ... p_{zz} peuvent être distinctes et ne résultent pas nécessairement d'une simple projection d'une force maîtresse sur ces composantes.

En remplaçant dans l'équation (4) $p(x, y, z, t)$ par sa valeur en (5) et en effectuant l'intégrale, on obtient:

$$\bar{P}(t) = \bar{F}_x(t)p_x(t) + \bar{F}_y(t)p_y(t) + \dots + \bar{F}_{zz}(t)p_{zz}(t) \quad (6)$$

L'équation (6) peut se mettre sous la forme condensée suivante:

$$\bar{P}(t) = \sum_i \bar{F}_i(t) p_i(t) \quad (7)$$

$$i = x, y, z, xx, yy, zz.$$

$$\bar{F}_i(t) = \hat{F}_i[g(t)] \quad (8)$$

où $\bar{F}_i(t)$ sont des matrices colonnes qui s'obtiennent de $\hat{F}_i(s)$ par une transformation d'échelle décrite plus loin; les matrices colonnes $\hat{F}_x(s)$, $\hat{F}_y(s)$ et $\hat{F}_z(s)$ représentent respectivement les composantes x , y et z de la déformation modale de la structure le long du trajet de la charge; $\hat{F}_{xx}(s)$, $\hat{F}_{yy}(s)$ et $\hat{F}_{zz}(s)$ sont les dérivés de $\hat{F}_x(s)$, $\hat{F}_y(s)$ et $\hat{F}_z(s)$ par rapport à x , y et z respectivement.

L'équation (7) est facile à calculer. Les composantes $\hat{F}_i(s)$ des modes propres le long du trajet sont déterminées à l'aide des coordonnées du trajet, des déplacements nodaux en chaque mode des éléments traversés, de la matrice des polynômes d'interpolation définissant les déplacements à l'intérieur des éléments et des matrices de transformation des coordonnées locales en coordonnées globales. Les valeurs de ces composantes sont généralement calculées à des intervalles égaux ds du trajet. Chaque élément des matrices colonnes $\hat{F}_i(s)$ est au fond un vecteur représentant la discrétisation d'un mode le long du trajet. Les matrices colonnes $\bar{F}_i(t)$ sont obtenues de $\hat{F}_i(s)$ par une transformation de l'échelle des abscisses $s = g(t)$. Les éléments de $\bar{F}_i(t)$ sont aussi des vecteurs. Leurs valeurs correspondent généralement à des intervalles de temps égaux dt . Il est très probable que les points de discrétisation des modes le long du trajet à des intervalles égaux de distance ds ne correspondent pas avec les mêmes points de discrétisation à des intervalles égaux de temps dt . Dans ces cas, une simple interpolation entre les points discrétisés peut bien se faire sans apporter une différence significative au niveau des réponses.

Charge répartie

Dans le cas d'une charge ayant une dimension négligeable dans le sens du mouvement et une dimension définie dans le sens perpendiculaire (fig. 1), une solution par discrétisation de cette charge sur un faible nombre de trajets est à suggérer.

Le cas d'une charge d'une dimension non négligeable dans la direction du mouvement (fig. 2) peut aussi être traité sans difficulté et s'effectue de la manière suivante: soit $h_i(q)$ la fonction définissant la répartition de la charge suivant la composante i où q appartient à un système d'axe mobile propre à la charge.

$$q = s - g(t) \quad (9)$$

Soit $\bar{h}_i(q)$ l'image de $h_i(q)$ par rapport à l'axe des ordonnées du système d'axe mobile, et soit $\bar{h}_i(q)$ la translation de cette image dans la partie positive des abscisses. L'équation (8) prendra la forme générale suivante:

$$\bar{F}_i(t) = \bar{F}_i [g(t)] \quad (10)$$

où pour une charge concentrée:

$$\bar{F}_i(s) = \hat{F}_i(s) \quad (10a)$$

et pour une charge répartie:

$$\bar{F}_i(s) = \int_0^s \bar{h}_i(\xi) \hat{F}_i(s - \xi) d\xi \quad (10b)$$

L'équation (10b) se calcule facilement par une convolution numérique entre vecteurs. Le premier vecteur représente la discrétisation de l'image de la charge après translation. Le deuxième vecteur est à tour de rôle un des éléments de la matrice colonne $\hat{F}_i(s)$.

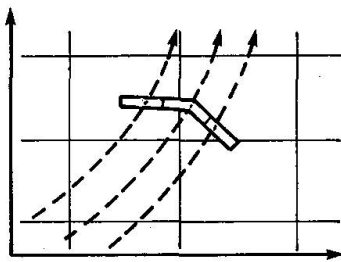


Fig. 1. Charge discrétisée sur trois trajets.

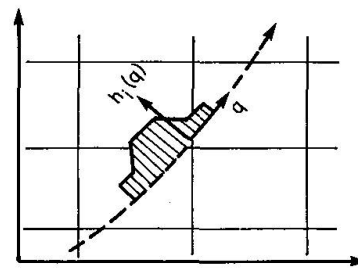


Fig. 2. Charge répartie dans la direction du mouvement.

Charge d'amplitude aléatoire

Le cas d'une charge mobile d'amplitude aléatoire peut se traiter en utilisant les mêmes notions. Supposant que la charge possède une seule composante dans la direction z et que la covariance de l'amplitude de cette composante soit $C_{pp}(t_1, t_2)$.

L'élément j, k de la matrice $C_{\overline{pp}}$ des covariances des forces en coordonnées généralisées s'écrit sous la forme suivante:

$${}_{j, k} C_{\overline{pp}}(t_1, t_2) = {}_j \overline{F}_z(t_1) {}_k \overline{F}_z(t_2) C_{pp}(t_1, t_2) \quad (11)$$

ou ${}_j \overline{F}_z$ représente l'élément j de la matrice colonne \overline{F}_z .

Conclusion

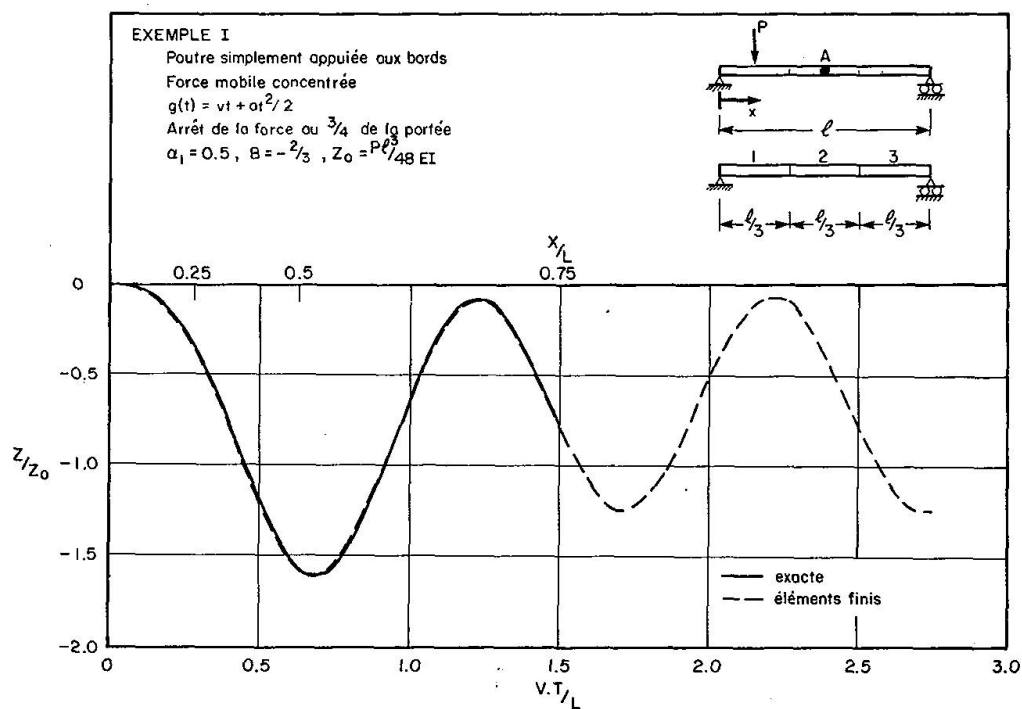
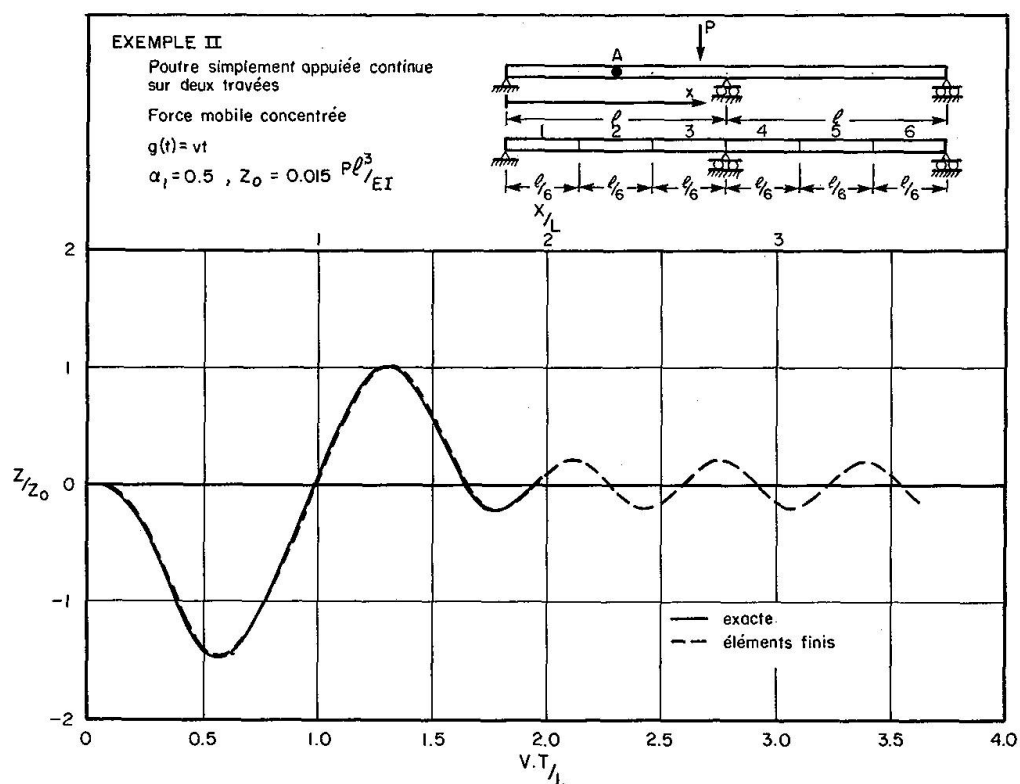
L'avantage de la méthode exposée réside dans la notion des «modes-trajet» $\hat{F}_i(s)$. Une fois ces «modes-trajet» déterminés et bien discrétisés, des cas de charges de fonctions différentes de répartition et de mouvement parcourant le même trajet peuvent être traités sans revenir à toutes les caractéristiques de la structure (éléments traversés, calcul des forces nodales équivalentes, assemblage...). L'analyse des cas de charges mobiles réparties sur une surface limitée ne présente aucune difficulté. Tandis que dans la technique des éléments finis le calcul des forces équivalentes aux nœuds pour des cas pareils demande une intégration spéciale s'étendant sur la partie chargée de chaque élément traversé. Ce genre de calcul demande différentes opérations et est parfois compliqué, vu que la partie chargée de chaque élément varie en fonction du temps et la répartition de la charge mobile se fait sur plusieurs éléments. Dans le cas de l'analyse aléatoire, aucune notion supplémentaire n'est requise. Tandis que la méthode de charges équivalentes aux nœuds présente un handicap pour l'analyse aléatoire des charges mobiles.

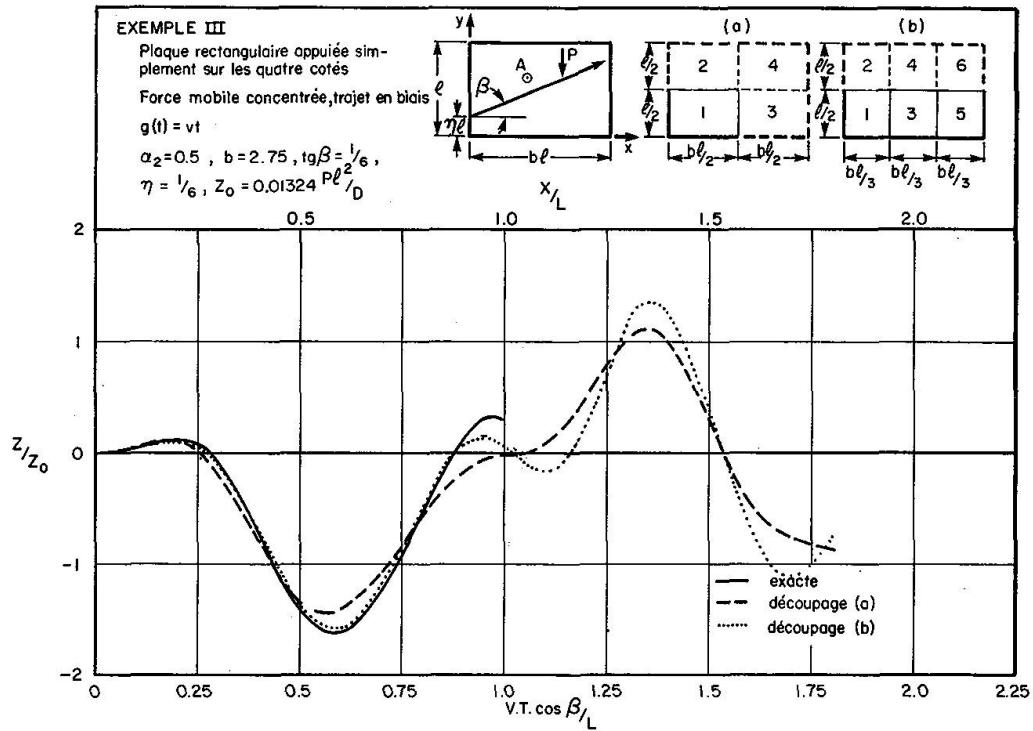
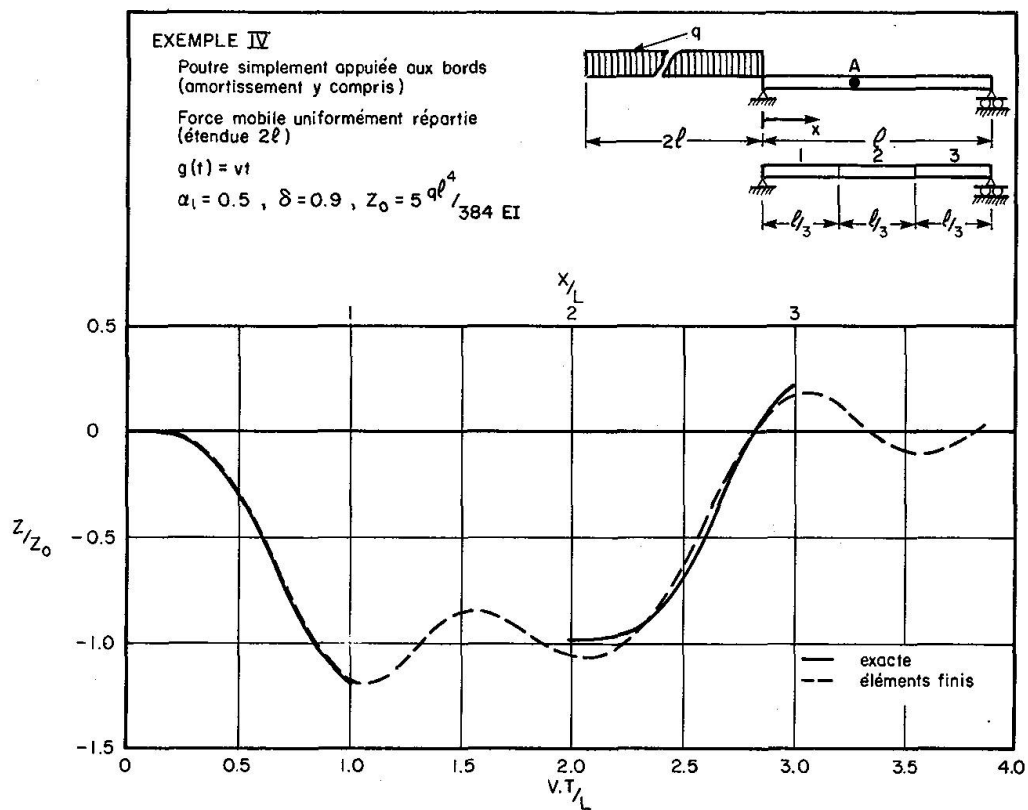
Exemples numériques

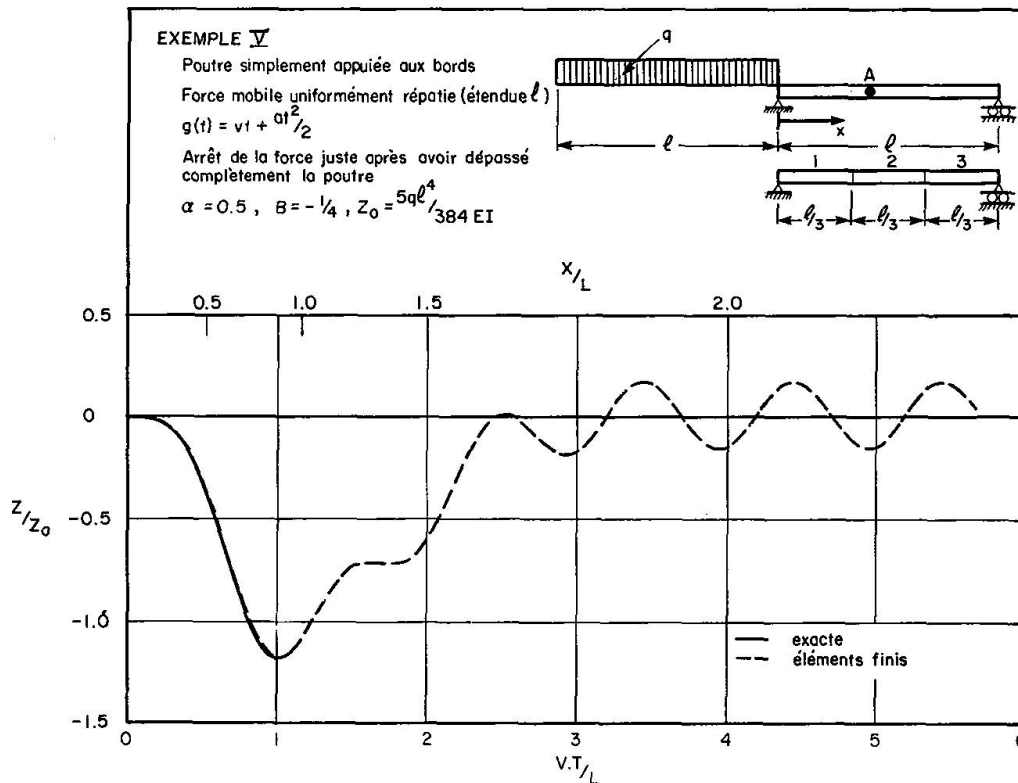
Des cas très simples mais représentatifs ont été fournis comme exemples. Le choix de ces cas a été restreint par la pénurie des solutions exactes. Des éléments très simples comme l'élément poutre à quatre degrés de liberté [4] (un déplacement et une rotation à chaque nœud) et l'élément plaque à seize degrés de liberté de Bogner [5] ont été utilisés. Le «mode-trajet» de chaque exemple a été discrétisé en cinquante points. La formulation des solutions exactes des cas traités se trouve dans l'excellent ouvrage de FRYBA [6]. Des exemples supplémentaires sont traités ailleurs [7]. L'exactitude des réponses est vraiment satisfaisante malgré la simplicité des éléments et le très faible nombre de découpages.

Notations pour les exemples numériques

a	accélération.
B	al/v^2 .
D	rigidité en flexion de la plaque.
EI	rigidité en flexion de la poutre.


 Fig. 3. Déflexion du point A ($x = 0.45 l$) (contribution des premiers quatre modes).

 Fig. 4. Déflexion du Point A ($x = 0.48 l$) (contribution des premiers cinq modes).

Fig. 5. Déflexion du point A ($x = 1.25 l$, $y = 0.60 l$) (contribution des premiers cinq modes).Fig. 6. Déflexion du point A ($x = 0.45 l$) (contribution des premiers quatre modes).


 Fig. 7. Déflexion du point A ($x = 0.45 l$) (contribution des premiers quatre modes).

$g(t)$	fonction du mouvement de la force.
P	valeur de la force concentrée.
q	valeur de la force uniformément répartie par unité de longueur.
u_1	masse par unité de longueur.
u_2	masse par unité de surface.
v	vitesse.
z	déflexion due au passage de la force.
z_0	déflexion de référence.
δ	décroissement logarithmique de l'amortissement.
α_1	$\frac{vl}{\pi} \sqrt{\frac{u_1}{EI}}$
α_2	$\frac{b \cos \beta vl}{1 + b^2} \frac{1}{\pi} \sqrt{\frac{u_2}{D}}$
l, x, b, β, η	paramètres désignés sur les figures.

Références

1. KHOUDAY, A.: Introduction au problème dynamique des ponts routiers soumis à la circulation. Thèse de maîtrise, Département de génie civil, Université Laval, Québec, Canada, août 1971.
2. YOSHIDA, D.M., and WEAVER, W., Jr.: Finite Element Analysis of Beams and Plates with Moving Loads. Publications, International Association for Bridge and Structural Engineering, v. 31-1, 1971.
3. GHAJARI, H.N.: Dynamic Response of Elastic-Perfectly Plastic Rectangular Plates, Ph.D. thesis, Department of Civil Engineering, New York University, April 1971.
4. PRZEMIENIECKI, J.S.: Theory of Matrix Structural Analysis. McGraw-Hill Inc., New York, 1968.
5. BOGNER, F.K., FOX, R.L., and SCHMIT, L.A.: The Generation of Inter-Element-Compatible Stiffness and Mass Matrices by the Use of Interpolation Formulas. AFFDL-TR-66-80, Conference on Matrix Methods in Structural Mechanics, Wright-Patterson Air Force Base, Ohio, October 1965.
6. FRYBA, L.: Vibration of Solids and Structures under Moving Loads. Noordhoff International Publishing, Groningen, The Netherlands, 1972.
7. KHOUDAY, A.: Réponse dynamique et probabiliste des structures soumises à des charges mobiles. Thèse de doctorat, Département de génie civil, Université Laval, Québec, Canada (en rédaction).

Résumé

Une méthode de calcul est exposée en vue de la détermination des réactions dynamiques et probabilistes d'une structure d'une forme quelconque soumise à des charges mobiles arbitraires. La méthode est basée sur la technique des éléments finis et de l'analyse modale. Les forces appliquées sur la structure ne sont pas remplacées par des forces équivalentes aux nœuds. Des exemples numériques sont fournis. Ces exemples comprennent les cas de poutres, de plaques, de forces concentrées ou réparties, de mouvements avec accélération et de matériau ayant de l'amortissement.

Zusammenfassung

Ziel des behandelten Verfahrens ist die Untersuchung des dynamischen und probabilistischen Verhaltens eines Bauwerks unter beliebiger beweglicher Belastung. Die Lösung des Problems erfolgt mittels der Methode finiter Elemente und der Modalanalyse. Die Untersuchung des Bauwerkes wird durchgeführt, ohne die gegebenen Lasten auf Knotenlasten zu reduzieren. Es werden Zahlenbeispiele mit Anwendung auf Balken und Platten unter verteilter und Punktbelastung angeführt, sowie die Dämpfung des Materials und die Lastbeschleunigung berücksichtigt.

Summary

This paper describes a method to evaluate the dynamic and probabilistic response of a structure to an arbitrary moving load. To solve the problem, finite element techniques combined with nodal analysis are used. In the analysis of the

structure, the applied loads are not transformed into equivalent nodal loads. Numerical examples such as beams and plates subjected to uniform and concentrated loads, damping of the structure and acceleration of the load are included in the study.

Leere Seite
Blank page
Page vide

Structures en poutres-caissons reliées par des dalles *

Structures of Box-Girders Joint Together by Slabs

Kastenträger-Brücken mit untereinander verbundenen Platten

S. KLIMINSKI

Docteur-Ingénieur

(Entreprises SPIE-BATIGNOLLES France)

Préface

La détermination des contraintes et des déformations dans les profils minces fermés que constituent les poutres-caissons ne relève pas de théories élémentaires; à vouloir simplifier le problème à coups d'hypothèses, difficiles à justifier, on court le risque d'ignorer dans quelle mesure on ne s'écarte pas trop de la réalité. A une époque où les ponts courbes deviennent de plus en plus nombreux, où les parois des poutres-caissons sont de plus en plus minces, il importait que le comportement de telles poutres soit étudié en prenant essentiellement en compte:

- la flexion transversale des parois,
- la contrainte normale longitudinale engendrée par la torsion non uniforme.

C'est le travail qu'a entrepris d'effectuer M. Kliminski, et pour avoir suivi pas à pas son élaboration, j'ai pu me rendre compte de l'effort continu et passionné qu'a dû fournir l'auteur pour arriver à la volumineuse thèse soutenue récemment.

C'est un résumé de ce travail que je suis heureux de présenter ici, convaincu que tous ceux qui sont intéressés par le calcul de telles structures sauront y trouver à la fois des renseignements directement utilisables et matière à réflexion.

P.M. Géry

Professeur à l'Ecole nationale Supérieure des mines
et au Conservatoire national des arts et métiers.

* Extraits d'une thèse de doctorat soutenue le 22 septembre 1971, à la Faculté des sciences de Paris, devant le jury composé de MM. les professeurs: R. Siestrunck (Président), R. Vichnievsky, P. Géry, D. Ceylon.

Introduction

Utilisées fréquemment comme structures d'ouvrages d'art, en métal ou béton précontraint, les poutres-caissons sont une source de calculs parfois complexes.

Lorsqu'il s'agit d'ouvrages en béton précontraint, ces poutres-caissons sont maintenant très souvent reliées transversalement par le seul intermédiaire de dalles souples. Actuellement, la résolution de telles structures ainsi définies est conduite, compte tenu de:

- la rigidité à la torsion des poutres-caissons, la torsion étant supposée uniforme;
- la rigidité à la flexion des dalles de liaison.

Pour des systèmes composés de deux poutres-caissons, ces hypothèses de calculs semblent fournir des résultats satisfaisants. Cependant, appliquées à plusieurs poutres-caissons, celles-ci deviennent caduques.

Deux sollicitations importantes sont en effet négligées:

- 1° La flexion transversale des parois de caissons.
- 2° La torsion qui engendre une contrainte normale longitudinale.

L'objet de cette recherche est d'analyser le comportement de structures en plusieurs poutres-caissons, qui peuvent être classées, de par leurs dimensions, dans la catégorie des pièces longues en voile mince, en considérant les deux sollicitations précitées comme fondamentales.

Définition du problème

Les sections transversales des structures comprennent n caissons ($n \geq 2$). Chaque caisson est symétrique au moins par rapport à son axe vertical. Les caissons sont liés entre eux par des dalles pouvant être de longueur différente. Ainsi, la section transversale a la forme ci-dessous:

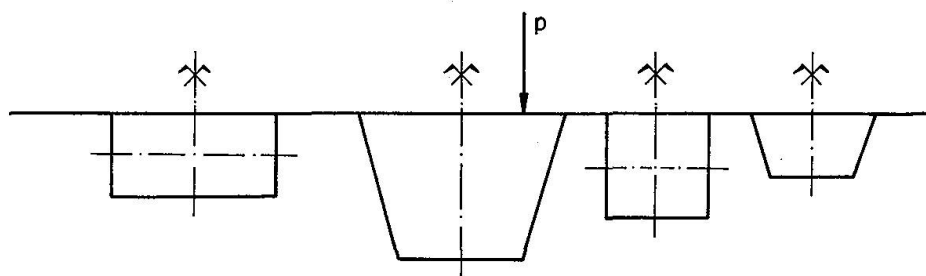


Fig. 1

Les axes longitudinaux des structures d'inertie constante sont rectilignes. Aux deux extrémités de la travée étudiée, les sections transversales sont unies par des diaphragmes. Ceux-ci sont, le plus souvent, inextensibles dans le plan vertical et normal à l'axe longitudinal des structures. Ils sont, par contre, souples à la torsion. Ainsi les sections extrêmes des structures sont parfaitement encastrees à la torsion et chaque poutre-caisson est encastree élastiquement à la flexion.

La charge appliquée est une charge verticale p , uniformément répartie dans le sens longitudinal, et ponctuelle transversalement (fig. 1).

La position de la charge étant variable transversalement.

Sous une telle charge, la structure est soumise à la flexion et à la torsion.

Si la flexion ne pose pas de problème majeur, la torsion apparaît, en revanche, complexe. En effet, nous avons le phénomène de torsion non uniforme. Les sections transversales sont encastrees à leurs extrémités (gauchissement empêché), et cet encastrement engendre des réactions longitudinales qui sont équilibrées par des contraintes normales.

Nous décomposons la structure, par des coupures effectuées au milieu de chaque dalle de liaison, parallèlement à l'axe longitudinal.

D'une manière générale, nous obtenons ainsi des profils dissymétriques d'un caisson à deux porte-à-faux. La dissymétrie est créée par la longueur différente des porte-à-faux.

Etat des contraintes et déformations – Convention de signes

Soit une tranche de poutre-caisson à deux porte-à-faux, soumise à la compression, flexion et torsion non uniformes.

Les axes Ox et Oy se trouvent dans le plan d'une section transversale, et ce sont ses axes principaux d'inertie (fig. 2).

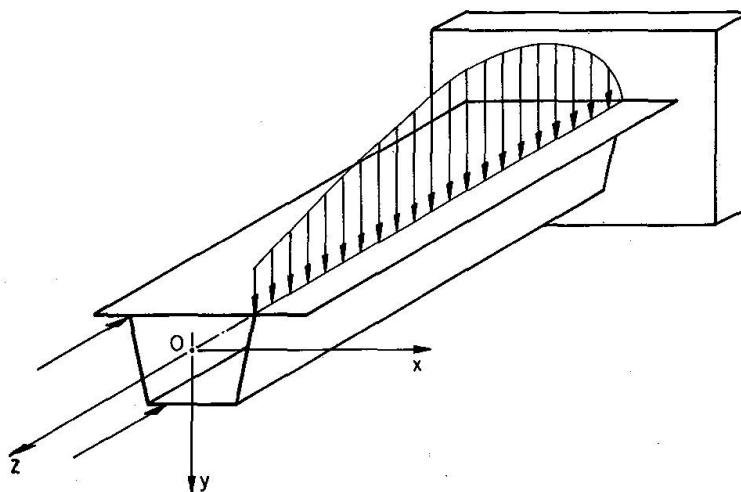


Fig. 2

Suivant les hypothèses de VLASSOV, nous pouvons exprimer l'allongement longitudinal relatif ε , compté positivement suivant la direction de l'axe Oz :

$$\varepsilon = \frac{1 - \nu^2}{E} \sigma, \quad \varepsilon = \frac{\sigma}{E_1}$$

et la déformation de distorsion, comptée positivement, contrairement au sens trigonométrique, par:

$$\gamma = \frac{\tau}{G}$$

Il faut maintenant déterminer les contraintes σ et τ .

Pour les profils ouverts, cette détermination se fait à l'aide des formules suivantes développées par VLASSOV:

$$\sigma = \frac{N}{A} + \frac{M_x}{I_x} \cdot y - \frac{M_y}{I_y} \cdot x + \frac{B}{I_\omega} \cdot \omega \quad (1)$$

$$\tau = - \left(\frac{T_y \cdot S_x}{I_x \cdot \delta} + \frac{T_x \cdot S_y}{I_y \cdot \delta} + \frac{M_\omega \cdot S_\omega}{I_\omega \cdot \delta} \right) \quad (2)$$

Le sens des symboles est expliqué en notations.

L'effort normal N est compté positif quand il est dirigé le long de l'axe O_z .

Les moments (M_x) et (M_y) sont positifs quand leurs vecteurs ont les directions des axes O_x et O_y .

On donne au moment de torsion C le signe positif comme sur la fig. 3.

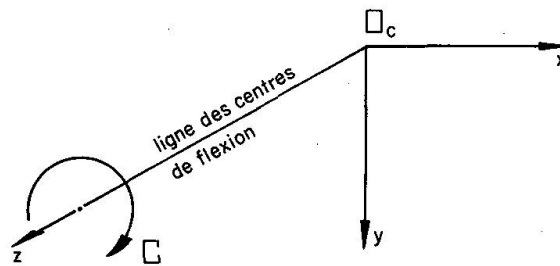


Fig. 3

On voit qu'avec la torsion non uniforme une nouvelle force généralisée apparaît dans les formules: c'est le bimoment B . Contrairement à un moment, le bimoment représente une force statiquement équivalente à zéro.

Le moment de torsion fléchi (M_ω) est lié avec le bimoment par la relation: $M_\omega = \frac{dB}{dz}$.

Pour les profils fermés, on peut déterminer ces contraintes par les formules semblables, développées par OUMANSKY, OURBAN [26], [27], [30] et [33]:

$$\sigma = \frac{N}{A} + \frac{M_x}{I_x} \cdot y - \frac{M_y}{I_y} \cdot x + \frac{B}{I_{\hat{\omega}}} \cdot \hat{\omega} \quad (3)$$

$$\tau = \frac{C}{\Omega \cdot \delta} - \left(\frac{T_y \cdot \hat{S}_x}{I_x \cdot \delta} + \frac{T_x \cdot \hat{S}_y}{I_y \cdot \delta} + \frac{M_{\hat{\omega}} \cdot S_{\hat{\omega}}}{I_{\hat{\omega}} \cdot \delta} \right) \quad (4)$$

La différence entre ces formules et celles des profils ouverts porte sur les caractéristiques géométriques. En outre, dans la formule de contraintes tangentielles, on rencontre un terme supplémentaire, qui exprime la torsion uniforme. Il apparaît cependant que, dans le cas du profil étudié pour le calcul des contraintes, on ne peut utiliser aucune de ces formules, parce que:

- 1° Le profil en question est découpé dans une section transversale continue.
- 2° Le profil est composé, car il est constitué en même temps par un profil fermé et deux profils ouverts.

Nous déterminons les contraintes pour un tel profil, compte tenu de la ressemblance des formules (1), (2) avec (3) et (4).

Il est à remarquer que, dans les nouvelles formules, certains termes vont disparaître. Soit une poutre-caisson à deux porte-à-faux, dont la section transversale est découpée dans une section continue. L'effet des coupures est remplacé par (q) et (m), comme sur la fig. 4. (Nous négligeons les glissements longitudinaux au droit des coupures.)

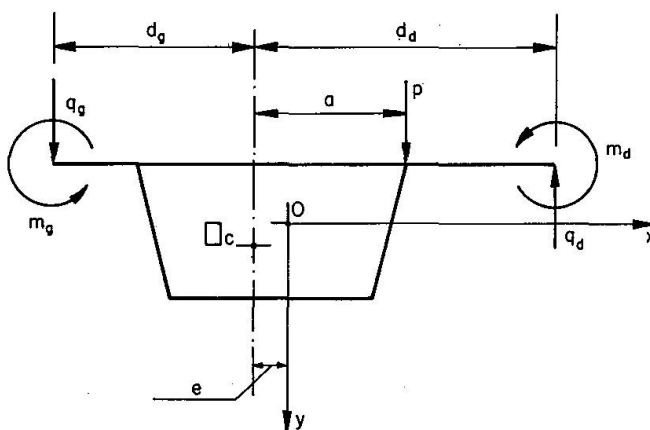


Fig. 4

Considérons les axes Oxy comme les axes principaux d'inertie. En effet, nous pouvons admettre, avec une bonne approximation, que ces axes sont verticaux et horizontaux. La dissymétrie de la section est provoquée seulement par la longueur différente des porte-à-faux. Or, l'application numérique montre que dans ce cas les axes principaux d'inertie sont quasiment verticaux et longitudinaux. Ceci confirme l'étude de M. RENARD [20], dans laquelle la différence de longueur des porte-à-faux atteint 3 m, ce qui est d'ailleurs difficilement réalisable en pratique.

Les formules relatives aux contraintes du profil étudié, avec les nouvelles notations sectorielles, prennent la forme suivante:

$$\sigma = \frac{M}{I} \cdot y + \frac{B}{I_{[\omega]}} \cdot [\omega] \quad (5)$$

$$\tau = \frac{C}{\Omega \cdot \delta} - \frac{T \cdot \hat{S}_x}{I_x \cdot \delta} - \frac{M_{[\omega]} \cdot \Gamma}{I_{[\omega]} \cdot \delta} \quad (6)$$

Dans ces formules $[\omega]$, $I_{[\omega]}$, \hat{S}_x et Γ dépendent de la section transversale. B et $M_{[\omega]}$, par contre, dépendent de la longueur, et se déterminent de l'équation de torsion non uniforme.

Avant de définir ces grandeurs, nous analysons l'hyperstaticité des structures.

Inconnues hyperstatiques

Soit un système plan à (n) caissons reliés par des dalles, soumis aux forces extérieures quelconques.

Un tel système est à la fois hyperstatique intérieur et extérieur. En effet, chaque caisson représente un portique fermé, trois fois hyperstatique — l'hyperstaticité intérieure.

Pour lever totalement l'hyperstaticité du système, il faut pratiquer des coupures dans chaque dalle de liaison. On crée, ainsi, trois inconnues hyperstatiques par coupure — l'hyperstaticité extérieure. Chaque coupure implique l'introduction de trois inconnues hyperstatiques, qui sont:

- effort tranchant q , — q ;
- effort normal N , — N ;
- moment fléchissant m , — m .

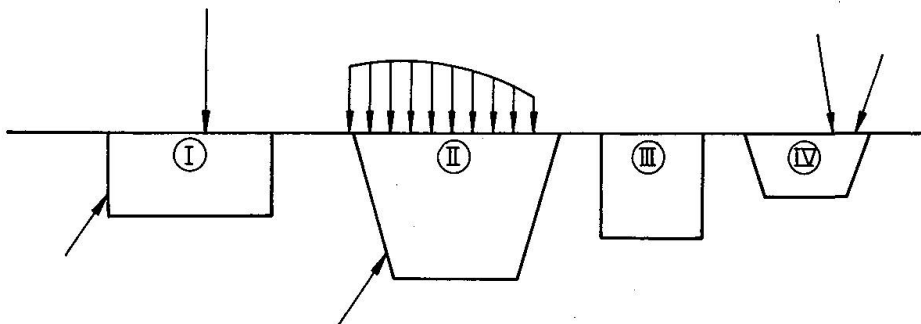


Fig. 5

Le système de la fig. 5 aura les inconnues hyperstatiques représentées sur la fig. 6.

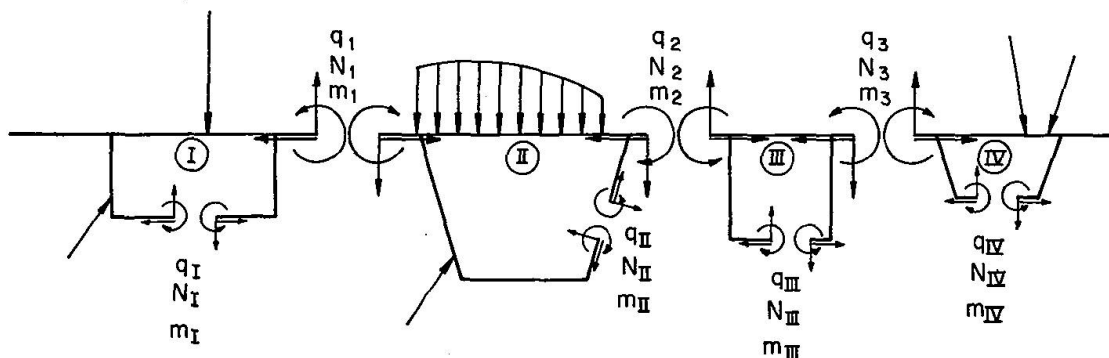


Fig. 6

Le degré d'hyperstaticité total du système peut être exprimé par la formule:
 $3n + 3(n - 1)$, n étant le nombre des caissons.

Pour quatre caissons, par exemple (fig. 5 et fig. 6), le degré d'hyperstaticité est: $3 \times 4 + 3 \times (4 - 1) = 12 + 9 = 21$, car $n = 4$. Il y a 12 inconnues hyperstatiques intérieures et 9 inconnues hyperstatiques extérieures.

Pour un seul caisson ($n = 1$), nous avons:

$3 \times 1 + 3 \times (1 - 1) = 3$. En effet, le système ne possède que trois inconnues hyperstatiques intérieures.

Dans les cas courants, les structures en question sont soumises aux charges verticales seules. Ceci réduit le nombre total des inconnues hyperstatiques. A chaque coupure de la dalle de liaison, l'effort normal N devient nul.

Le degré d'hyperstaticité du système s'exprime par la formule suivante:

$3n + 2(n - 1)$, où (n) est également le nombre de caissons.

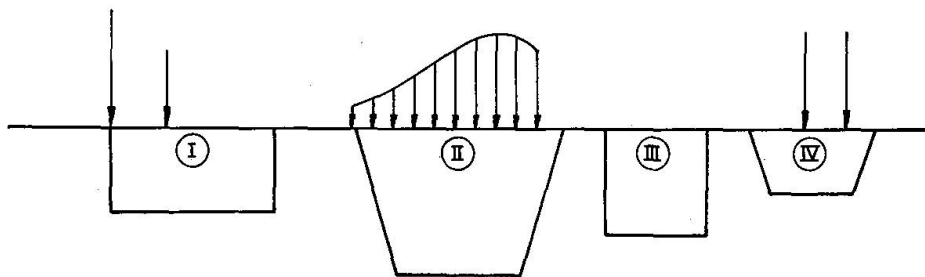


Fig. 7

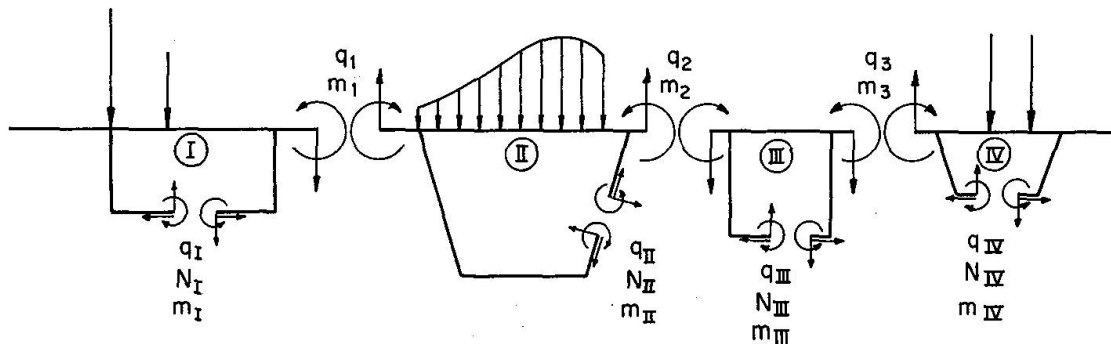


Fig. 8

Pour le système de la fig. 7, le nombre d'inconnues hyperstatiques est: $3 \times 4 + 2(4 - 1) = 18$, car $n = 4$. Il y a toujours 12 inconnues hyperstatiques intérieures et 6 inconnues hyperstatiques extérieures.

Les structures le plus souvent rencontrées ont les sections transversales symétriques, et de cette symétrie découle une simplification importante:

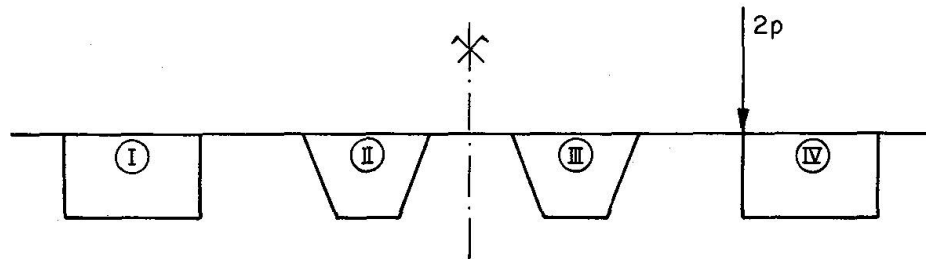


Fig. 9

En effet, nous pouvons décomposer la charge extérieure selon le procédé de la symétrie et de l'antisymétrie. Ceci réduit le nombre d'inconnues hyperstatiques (fig. 10 et 11).

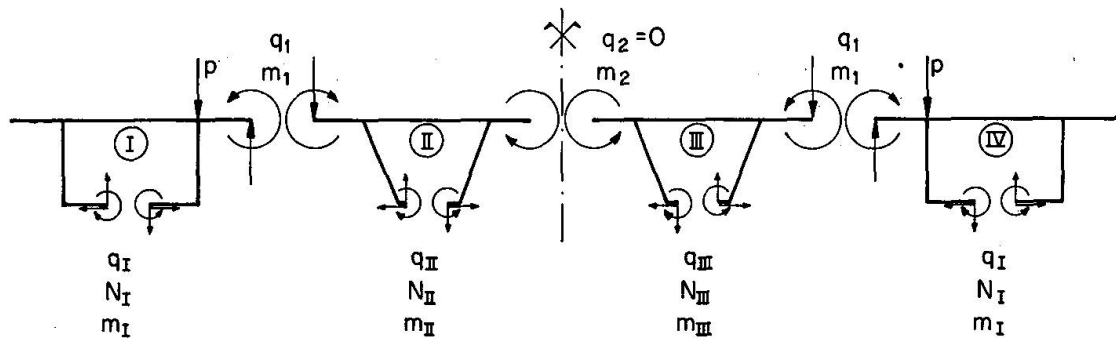


Fig. 10. Chargement symétrique.

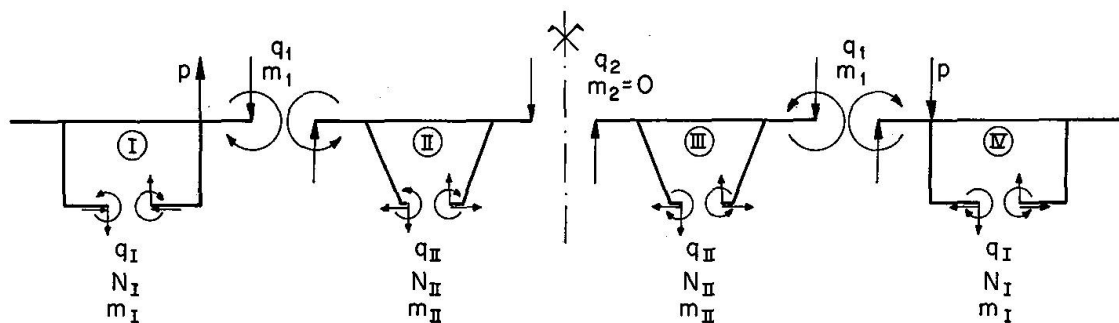


Fig. 11. Chargement antisymétrique.

Jusqu'à présent, nous avons analysé l'hyperstaticité des systèmes plans (sections transversales des structures). Il apparaît cependant que les structures étudiées forment des systèmes spatiaux. En conséquence, toutes les inconnues hyperstatiques ne sont

pas des nombres mais des fonctions de la longueur (z). Pour simplifier le problème nous séparons les inconnues intérieures et extérieures.

Résumons la marche à suivre en nous reportant au caisson ① de la fig. 10.

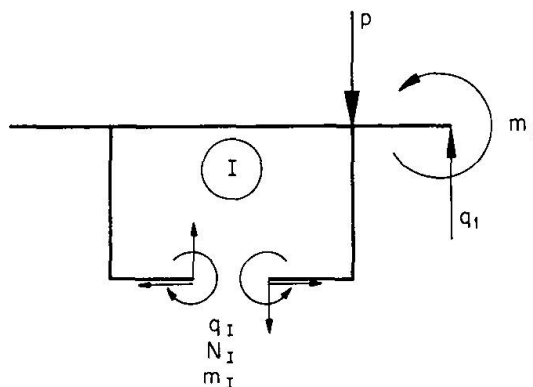


Fig. 12

On détermine d'abord les inconnues hyperstatiques intérieures (q_I), (N_I) et (m_I), dues aux charges extérieures; les inconnues (q_1) et (m_1) étant considérées aussi comme les charges extérieures.

Afin de pouvoir considérer le caisson comme un système plan, il faut déterminer les forces axiales qui apparaissent dans les parois. Ces forces proviennent de la différence des cisaillements sur deux faces d'une tranche élémentaire (dz) (fig. 13), et la tranche unitaire se comporte comme un portique élastique.

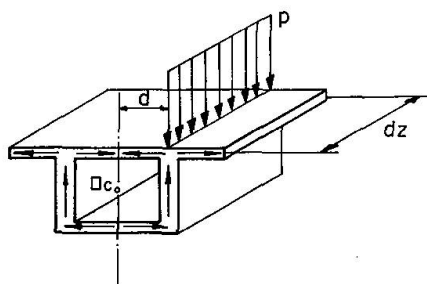


Fig. 13.

Les cisaillements en question sont définis par la formule (6), dans laquelle le dernier terme exprime les cisaillements provenant de la torsion non uniforme. Nous négligeons ce terme dans le calcul des inconnues hyperstatiques.

Si l'on voulait tenir compte de ces cisaillements, il faudrait définir le moment de torsion fléchi. Celui-ci ne peut pas être déterminé autrement que par la résolution de l'équation de torsion non uniforme. Comme le moment extérieur de torsion (c) dépend de valeurs (q)₁ et (m)₁, il se trouve que l'on aurait pour une équation trois inconnues:

$$(\Theta), (q)_1 \text{ et } (m)_1$$

Il est donc impossible de déterminer par cette équation le moment de torsion fléchi, indispensable à la définition de telles contraintes.

Ensuite nous rendons le système isostatique. Nous avons donc trois états unitaires dus aux charges extérieures (fig. 14).

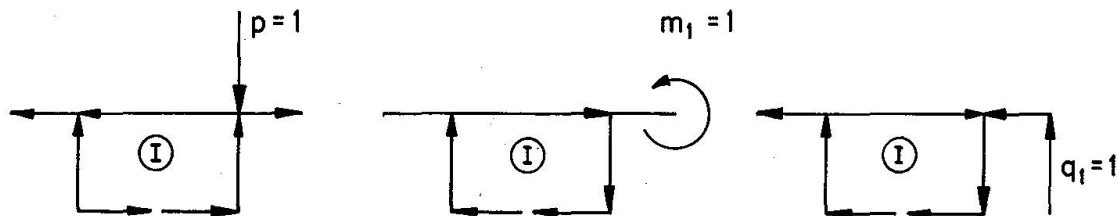


Fig. 14

A chacun de ces trois états sont associés trois états unitaires relatifs aux inconnues q_I , N_I et m_I (fig. 15).

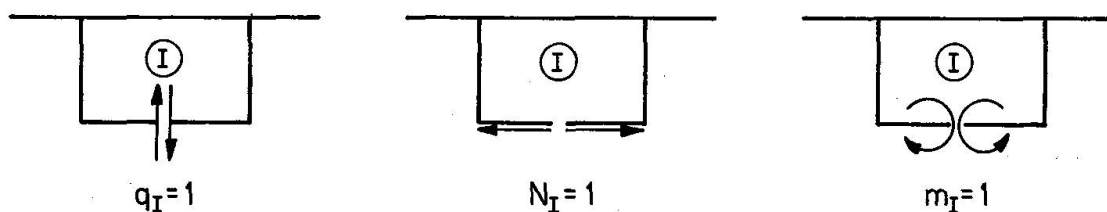


Fig. 15

Les inconnues recherchées (q_I), (N_I) et (m_I) se déterminent à partir d'un système de trois équations linéaires, dont la forme matricielle est:

$$\begin{bmatrix} a_{11} & a_{21} & a_{31} \\ a_{12} & a_{22} & a_{32} \\ a_{13} & a_{23} & a_{33} \end{bmatrix} \times \begin{bmatrix} q_I \\ N_I \\ m_I \end{bmatrix} + \begin{bmatrix} A_{1P} \\ A_{2P} \\ A_{2P} \end{bmatrix} = \begin{bmatrix} 0 \\ 0 \\ 0 \end{bmatrix}$$

La matrice (a_{ij}) est indépendante du système des forces extérieures, et elle est symétrique ($a_{ij} = a_{ji}$). Les coefficients (a_{ij}) et (A_{ip}) se calculent habituellement par les intégrales de MOHR.

Les moments fléchissants réels dans les parois sont à multiplier par les valeurs réelles de (p), (m_1) et (q_1). Ces deux derniers étant les inconnues hyperstatiques extérieures à déterminer.

Déterminons d'abord les inconnues hyperstatiques extérieures pour une travée isostatique.

La poutre est soumise à la charge extérieure (p), d'excentricité constante (d) (fig. 16).

Puisque la poutre est isolée, il faut rétablir la continuité transversale de la structure en appliquant, le long de la coupure, des inconnues hyperstatiques $q_{(z)}$ et $m_{(z)}$.

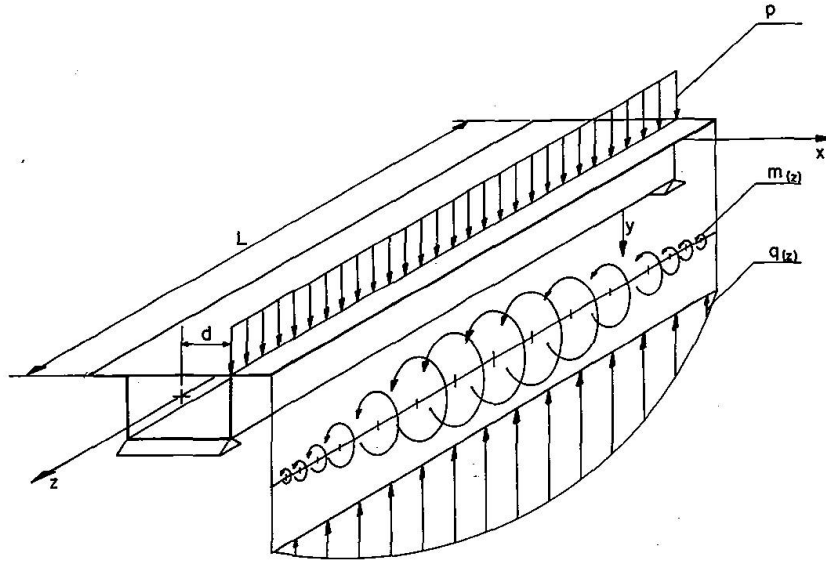


Fig. 16

Nous développons la charge extérieure (p) et les fonctions $q(z)$ et $m(z)$, en séries de FOURIER :

$$p = \sum_{n=1}^{n=\infty} p_n \cdot \sin \frac{(2n-1)\pi z}{L} \text{ avec } p_n = \frac{4p}{\pi} \frac{1}{(2n-1)}$$

$$q(z) = \sum_{n=1}^{n=\infty} q_n \cdot \sin \frac{(2n-1)\pi z}{L} \text{ avec } q_n = \text{inconnue}$$

$$m(z) = \sum_{n=1}^{n=\infty} m_n \cdot \sin \frac{(2n-1)\pi z}{L} \text{ avec } m_n = \text{inconnue}$$

Pour écrire que les déplacements sont nuls, au droit de la coupure, il faut considérer une force et un couple auxiliaire qui correspondent à $q(z)$ et $m(z)$.

La somme des travaux de la force ou du couple auxiliaire unités, dans les déplacements dus aux inconnues $q(z)$ et $m(z)$, et à la charge extérieure, doit être nulle. Ceci se traduit par un système d'équations linéaires (autant d'équations que d'inconnues) que nous pouvons exprimer sous forme matricielle :

$$[a] \cdot [x] + [A] = [0]$$

La matrice $[a]$ se compose de quantités (a_{ij}) qui représentent le travail de la force auxiliaire (i) dans les déplacements dus à une force unitaire (j) , relative à l'inconnue hyperstatique (j) . Cette matrice ne dépend pas du système des forces extérieures. Elle est symétrique $(a_{ij}) = (a_{ji})$.

La matrice $[x]$ est une matrice colonne des inconnues $(q_1); (m_1); (q_2); (m_2)$, etc.

La matrice $[A]$ est une matrice colonne des quantités (A_{ip}) , qui représentent le travail de la force auxiliaire (i) dans les déplacements dus aux forces extérieures (p) .

Les quantités (a_{ij}) sont des sommes de trois termes:

$$a_{ij} = (a_{ij})_1 + (a_{ij})_2 + (a_{ij})_3$$

$(a_{ij})_1$ provient de la flexion longitudinale verticale.

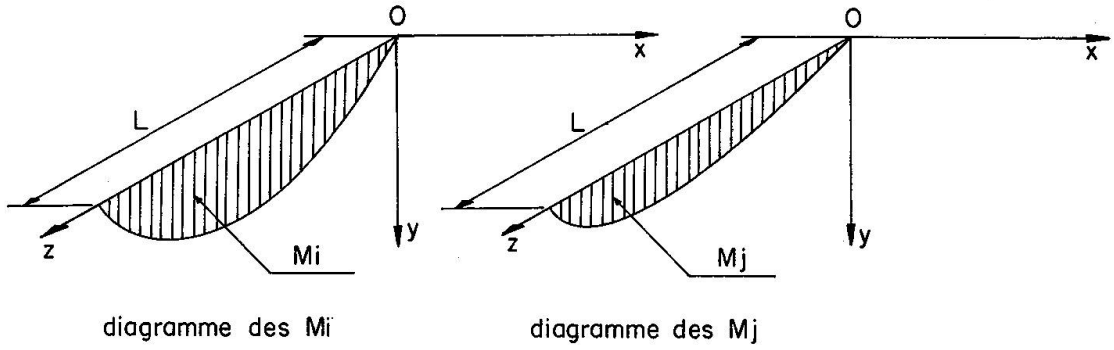


Fig. 17

$$(a_{ij})_1 = \int_0^L \frac{M_i \cdot M_j}{EI} dz \quad (7)$$

$(a_{ij})_2$ représente le travail de torsion uniforme.

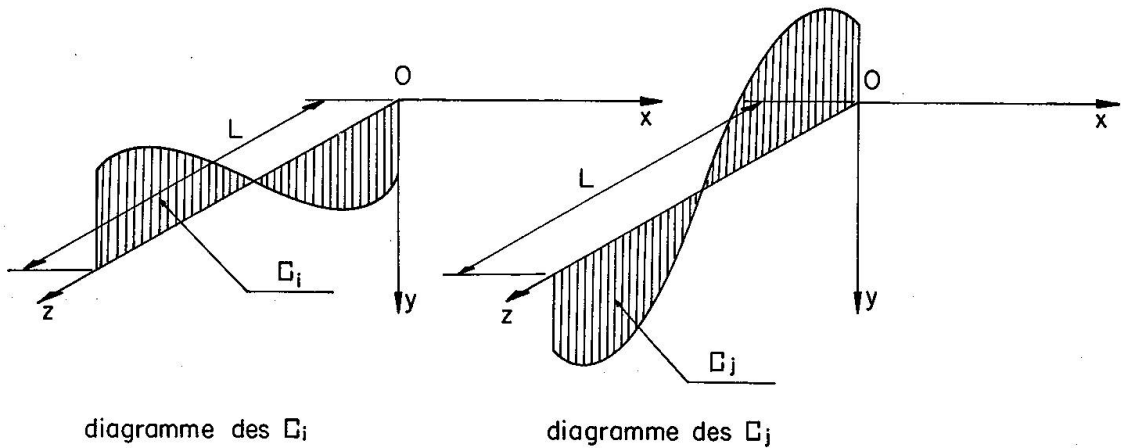


Fig. 18

$$(a_{ij})_2 = \int_0^L \frac{C_i \cdot C_j}{GI_d} dz \quad (8)$$

$(a_{ij})_3$ représente le travail de flexion transversale qui provient de la déformation des dalles de liaison et des parois des caissons. Nous avons dans ce cas l'intégrale double étendue au contour (s) de la section, et à la longueur (L) de la travée.

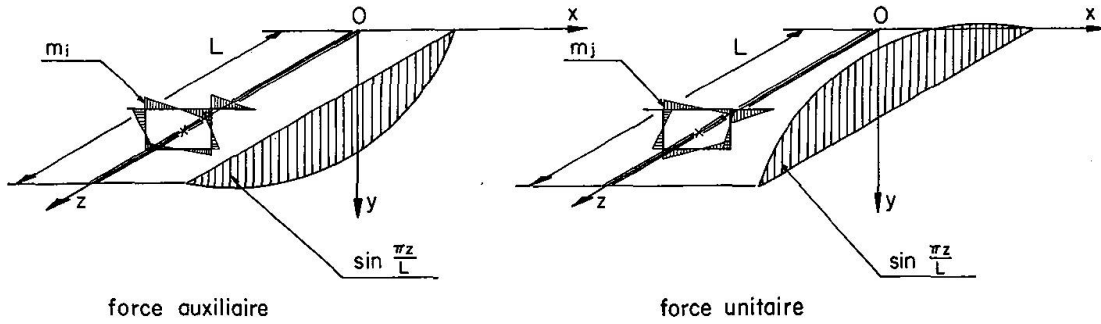


Fig. 19

$$(a_{ij})_3 = \int_0^L \int_s \frac{m_i \cdot m_j}{EI(s)} ds dz \quad (9)$$

dans laquelle $I(s)$ concerne l'inertie des parois.

De même chaque (A_{iP}) est la somme de trois termes :

$$A_{iP} = (A_{iP})_1 + (A_{iP})_2 + (A_{iP})_3$$

Le calcul de chaque terme se fait de la même façon que celui des (a_{ij}) . Les diagrammes de moments relatifs à la force auxiliaire sont les mêmes; les diagrammes de moments dus à la force unitaire sont remplacés par les diagrammes des moments dus aux forces extérieures.

Les intégrales (7), (8), (9) concernent toute la section de la structure.

Un ou plusieurs $(a_{ij})_n$ ou $(A_{iP})_n$ peuvent être nuls, en raison de la symétrie de la section transversale et de la symétrie des charges.

Pour une travée encastree élastiquement à la flexion à ses deux extrémités, le problème consiste à rechercher les fonctions $q(z)$ et $m(z)$ correspondant à des moments d'encastrement.

On procède de la même façon que dans le cas de la travée isostatique. La charge extérieure étant le moment d'encastrement appliqué aux abouts de la travée.

On détermine enfin les inconnues (q) et (m) comme la somme de deux effets: celui de la charge (p) et celui des moments d'encastrement.

Un tel calcul permet de déterminer les valeurs des inconnues q et m , au milieu de la travée (les coefficients inconnus q_n et m_n se déduisent du coefficient p_n qui caractérise la charge extérieure).

Par contre, nous ne connaissons pas l'équation de la courbe suivant laquelle sont réparties les inconnues $q(z)$ et $m(z)$ le long de la travée. Nous savons que les courbes sont symétriques par rapport au milieu de la travée ($p = C_{ic}$), et obtiennent zéro aux extrémités (fig. 20).

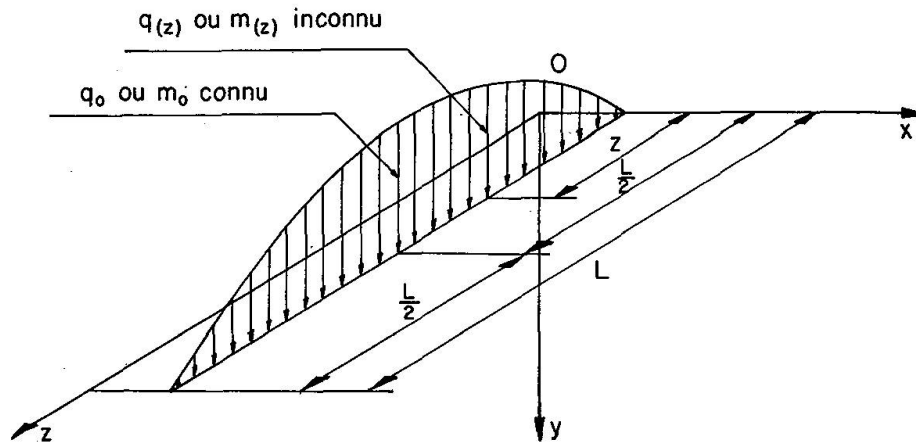


Fig. 20

Nous supposons que les fonctions inconnues sont réparties, soit suivant une loi sinusoïdale, soit suivant une parabole du deuxième degré. Seules l'application numérique et la vérification expérimentale peuvent démontrer quelle est la fonction qui répond le mieux à ce problème.

Hypothèses de la torsion

Pour la détermination des inconnues hyperstatiques, nous avons été obligés de simplifier le problème en considérant la torsion comme uniforme, mais à partir de maintenant nous adoptons les hypothèses de OUMANSKY et BENSCOTER. Ces auteurs ont défini une «fonction de gauchissement».

Les hypothèses se définissent ainsi:

- 1° Le contour de la section transversale est considéré comme indéformable. Pour les constructions en métal, cette indéformabilité est assurée par les raidisseurs transversaux. On adopte cette hypothèse également même pour les pièces sans raidisseur qui ont des parois plus épaisses: les profilés laminés, par exemple [16], [26] et [33].
Dans les constructions en béton précontraint, la section est constituée de voiles relativement épais. Les intersections des âmes et des hourdis sont renforcées par des goussets dans lesquels on loge des câbles. Ceci assure l'indéformabilité du contour même en cas de constructions peu entretoisées.
- 2° Les contraintes normales longitudinales dues à la torsion non uniforme sont réparties dans la section de la même façon que le gauchissement dans le cas de torsion uniforme.
- 3° Les contraintes de cisaillement sont uniformément distribuées sur toute l'épaisseur de la paroi. Cette hypothèse concerne les pièces longues à parois minces, dont les dimensions sont telles que:

$$\frac{\delta}{a} \leq 0,1, \quad \frac{a}{L} \leq 0,1$$

δ : épaisseur de la paroi

a : hauteur de la paroi

L : longueur de la barre.

Pour les constructions précontraintes, on néglige l'effet des câbles sur la rigidité à la torsion. Selon VLASSOV [32], pour les pièces précontraintes au lieu de GI_d relative aux sections non précontraintes, il faudrait prendre:

$$GI_d - R \cdot \Xi$$

où:

I_d = le moment d'inertie relatif à la torsion uniforme,

R = la résultante des forces de précontrainte,

Ξ = l'expression qui dépend de la géométrie de la section et de la position du point d'application de R .

Ce problème, à notre connaissance, n'a été traité que par VLASSOV pour une barre de section ouverte dans laquelle le tracé du câble est rectiligne. Il faut cependant remarquer que, lorsque la section est composée d'éléments fermés et ouverts, l'effet de câbles est moindre.

Rappel des caractéristiques géométriques sectorielles

Comme nous l'avons déjà remarqué, les caractéristiques sectorielles définissent le gauchissement des sections. Nous rappelons la définition de ces caractéristiques. Elles correspondent, dans leur appellation, à celles qui sont données par les principaux auteurs ayant pris part à l'élaboration de la théorie classique des barres à parois minces. Parmi ces auteurs, on peut citer particulièrement VLASSOV et WAGNER.

Profils ouverts

— Surface sectorielle $[L]^2$, appelée aussi coordonnée sectorielle.

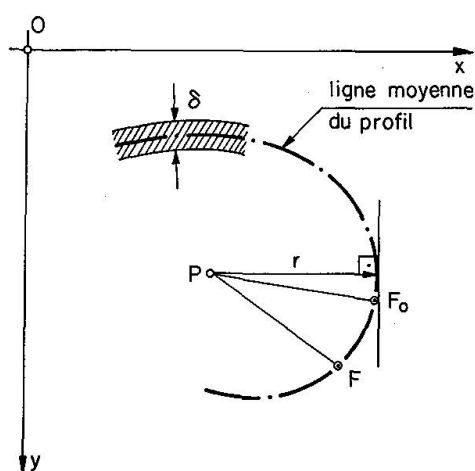


Fig. 21

Soit: P = un pôle arbitraire,
 PF_0 = rayon initial,
 PF = rayon mobile.

Conformément à la fig. 21, la surface sectorielle est définie par l'intégrale:

$$\omega = \int_0^s r ds$$

La surface sectorielle est comptée comme positive, si le rayon mobile PF qui l'engendre tourne dans le sens trigonométrique vu selon Oz .

- *Moment statique sectoriel* $[L]^4$; il est donné par: $S_\omega = \int_A \omega dA$.
- *Moments linéaires sectoriels* $[L]^5$; ils sont donnés par les intégrales:
 $S_{\omega y} = \int_A x \omega dA$, $S_{\omega x} = \int_A y \omega dA$.
- *Moment d'inertie sectoriel* $[L]^6$; il s'exprime par l'intégrale: $I_\omega = \int_A \omega^2 dA$

Profils fermés

Les caractéristiques sectorielles des profils fermés ont été établies par les auteurs russes [26], [27], [30] et [33] et ont pour but d'élargir la théorie de VLASSOV concernant les profils ouverts.

— *Surface sectorielle des profils fermés*: appelée aussi surface de gauchissement. Elle s'établit par l'analyse d'un profil fermé soumis à la torsion uniforme (le gauchissement est libre) et s'exprime par l'expression:

$$\hat{\omega} = \omega - \Omega \frac{\int_0^s \frac{ds}{G\delta}}{\oint \frac{ds}{G\delta}}$$

Les autres caractéristiques ont la même forme que celles des profils ouverts.

Centre de flexion

La surface sectorielle des profils ouverts et fermés que l'on trouve dans les formules (1) et (3) est calculée par rapport au *centre de flexion*, également appelé *centre de cisaillement*.

La position du centre de flexion dépend uniquement des caractéristiques géométriques de la section transversale, et sa détermination, pour les profils ouverts ou fermés, se fait aisément à partir d'un pôle arbitraire P (fig. 22).

$$\begin{aligned} b_x - a_x &= -\frac{1}{I_x} \int_A y \omega_P dA \\ b_y - a_y &= \frac{1}{I_y} \int_A x \omega_P dA \end{aligned} \tag{10}$$

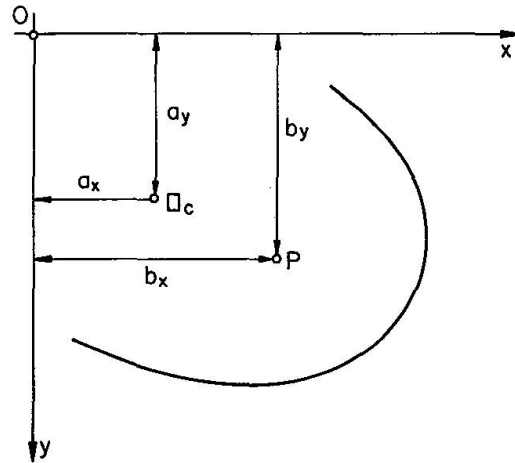


Fig. 22

Caractéristiques sectorielles des profils composés d'éléments fermés et ouverts

Pour définir les caractéristiques sectorielles des profils composés d'éléments fermés et ouverts, il faut définir la surface sectorielle qui se compose dans ce cas de trois paramètres:

- de la surface sectorielle du profil fermé $\hat{\omega}$, et
- des surfaces sectorielles de profils ouverts ω .

Considérons le profil étudié comme indépendant (les extrémités des porte-à-faux sont définies par les coupures).

Nous prenons en compte l'égalité de gauchissement suivant les arêtes $I - I'$ et $II - II'$ (fig. 23) pour le caisson et les porte-à-faux.

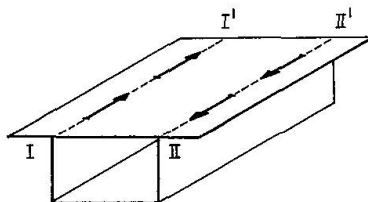


Fig. 23

Notons qu'un raisonnement semblable est fait pour l'étude de la torsion d'une coque de navire ayant une structure composée. La coque est soumise à la torsion par une vague braise rencontrée par le navire [22], [27].

La torsion étant non uniforme, conformément aux hypothèses, le gauchissement doit être exprimé par la fonction de gauchissement:

$$\zeta = -[\omega] \cdot \frac{d\vartheta}{dz} \quad (11)$$

On voit que le gauchissement de la section est proportionnel à la surface sectorielle. Pour qu'il y ait l'égalité de gauchissement à la naissance des porte-à-faux, il faut que les surfaces sectorielles calculées pour les parties fermées et

ouvertes soient égales aux points I et II (fig. 23). Cette condition nous conduit à exprimer la surface sectorielle des parties ouvertes par:

$$|\omega| = \int_0^s r ds + D_0$$

Les autres caractéristiques sectorielles qui concernent les profils composés se calculent à partir de la surface sectorielle. Celle-ci se compose de $\hat{\omega}$ et de la nouvelle valeur pour la partie ouverte déterminée ci-dessus $|\omega|$. Nous avons donné leurs symboles en notations.

Déterminons maintenant la position du point sectoriel nul, et celle du centre de flexion.

Connaissant le gauchissement, on peut écrire pour la contrainte normale:

$$\sigma = E_1 \cdot \frac{d\zeta}{dz}$$

et, compte tenu de (11), nous avons:

$$\sigma = -[\omega] \cdot \frac{d^2 \vartheta}{dz^2} \cdot E_1 \quad (12)$$

La barre est soumise uniquement à un moment de torsion, la contrainte σ doit donc satisfaire aux équations d'équilibre:

$$\left. \begin{aligned} N &= \int_A \sigma dA = 0 \\ M_y &= \int_A \sigma x dA = 0 \\ M_x &= \int_A \sigma y s dA = 0 \end{aligned} \right\} \quad (13)$$

En introduisant (12) dans les équations (13), on trouve:

$$\boxed{\begin{aligned} \int_A [\omega] dA &= 0 \\ \int_A [\omega] x dA &= 0 \\ \int_A [\omega] y dA &= 0 \end{aligned}} \quad (14)$$

Le problème est ramené à celui des profils ouverts. Les équations (14) permettent de trouver le point où le gauchissement est nul, et les coordonnées du centre de flexion s'expriment par les formules [10].

Cisaillements d'«effort tranchant» et de «torsion»

On détermine les caractéristiques \hat{S}_x et Γ , indispensables pour la définition des contraintes tangentielles, par l'analyse des contraintes dues à l'effort tranchant et à la torsion.

Soit une tranche de poutre-caisson à deux porte-à-faux, fléchié dans un plan parallèle au plan (O_y, O_z) par un moment (M) (fig. 24). Déterminons les cisaillements d'«effort tranchant» (T) provenant de cette flexion.

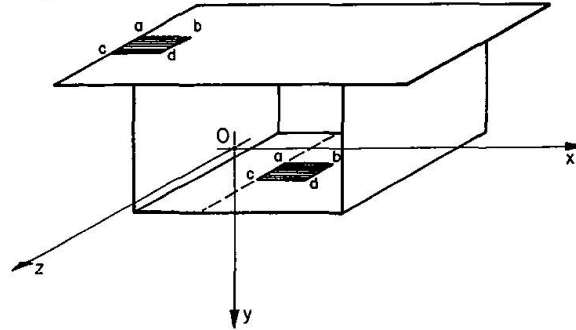


Fig. 24

Soit $abcd$ l'élément découpé dans la paroi en deux endroits différents (fig. 25).

- 1° Le côté ac est confondu avec le bord de l'un des porte-à-faux.
- 2° L'élément est situé dans un des plans de la poutre-caisson (ac restant // à l'axe Oz).

Partant du point a , nous déterminons les flux de cisaillements pour un point couvrant b .

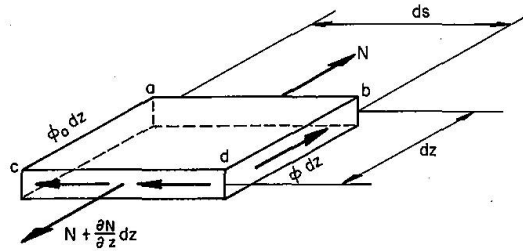


Fig. 25

L'équilibre de l'élément $abcd$ implique que:

$$\frac{\partial N}{\partial z} = \phi - \phi_o \rightarrow \phi = \frac{\partial N}{\partial z} + \phi_o$$

D'autre part, en prenant l'équation due à NAVIER, nous obtenons pour le flux de cisaillement:

$$\phi = \frac{T \cdot S_x}{I_x} + \phi_o \quad (15)$$

Le long des bords libres des porte-à-faux, les tensions tangentielles sont nulles ($\Phi_o = 0$), nous avons:

$$\boxed{\Phi = \frac{T \cdot S_x}{I_x}} \quad (16)$$

Le caisson, par contre, est un profil fermé et il faut déterminer le flux supplémentaire constant Φ_o . Pour calculer ce flux, on pratique une coupure passant par le côté ac de l'élément $abcd$.

Considérons le point (P) de position quelconque comme le centre de flexion d'un profil fermé (fig. 26).

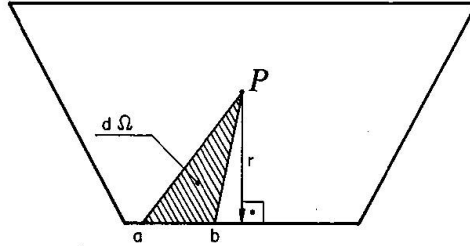


Fig. 26

Le moment de torsion autour de l'axe parallèle à Oz , et passant par P , est tel que:

$$C = \oint \Phi r ds \quad (17)$$

Compte tenu de la relation (15), la relation (17) devient:

$$C = \oint \frac{T \cdot S_x}{I_x} r ds + \oint \Phi_o r ds$$

d'où:

$$\Phi_o = \frac{C}{\oint r ds} - \frac{\frac{T}{I_x} \oint S_x r ds}{\oint r ds} \quad (18)$$

Puisque le plan de sollicitation passe par P , $C = 0$, et l'expression (18) devient:

$$\Phi_o = -\frac{1}{\Omega} \cdot \frac{T}{I_x} \oint S_x r ds$$

et l'équation (15) s'écrit:

$$\Phi = \frac{T}{I_x} \left(S_x - \frac{1}{\Omega} \oint S_x r ds \right)$$

Celle-ci peut être exprimée sous la forme suivante:

$$\boxed{\Phi = \frac{T \cdot \hat{S}_x}{I_x}} \quad (19)$$

dans laquelle le moment statique pour les profils fermés est:

$$\boxed{\hat{S}_x = S_x - \frac{1}{\Omega} \oint S_x r ds} \quad (20)$$

A l'aide des formules (16), (19) et (20), nous pouvons déterminer les cisaillements dus à l'effort tranchant en tout point de la paroi du profil étudié.

Remarque: Pour la détermination des cisaillements d'«effort tranchant», dans un profil composé, les principes de la résistance des matériaux classiques, sont encore applicables. En effet, dans la partie fermée du profil, dans laquelle on a pratiqué une coupure, les cisaillements sont entièrement déterminés par la statique. Cela signifie que le système est isostatique du point de vue de ses liaisons internes, et il est strictement complet.

D'autre part, le profil ainsi composé est hyperstatique, car à l'aide d'une coupure nous avons déterminé le profil d'abord ouvert, et ensuite fermé.

Cette hyperstaticité est du premier degré.

L'examen d'une tranche de poutre-caisson à deux porte-à-faux encastrée à une extrémité, et soumise à un moment de torsion à l'autre extrémité, conduit à la définition de cisaillements de «torsion» et de la valeur sectorielle Γ .

Ecrivant l'équation d'équilibre de l'élément $abcd$ découpé en deux endroits, comme dans le cas précédent, et compte tenu de l'expression (12), nous avons:

Pour les porte-à-faux:

$$\tau = \vartheta''' \cdot E_1 \cdot \frac{1}{\delta} \cdot S_{[\omega]}$$

Pour le caisson:

$$\tau = \frac{C}{\Omega \cdot \delta} + \vartheta''' \cdot \frac{E_1}{\delta} \cdot \Gamma$$

où:

$$\Gamma = S_{[\omega]} - \frac{1}{\Omega} \oint S_{[\omega]} r ds$$

Remarque: Pour la partie fermée du profil, les contraintes de cisaillement se composent de celles de la torsion uniforme et de celles provenant de la torsion non uniforme. Ces dernières dépendent de la dérivée troisième de la fonction de gauchissement ϑ et sont réparties de la même façon que la caractéristique sectorielle Γ .

La valeur Γ concerne le contour entier du profil (parties fermées et ouvertes), bien qu'elle provienne de l'intégration des déplacements le long de la partie fermée seulement. Ceci provient de la valeur $[\omega]$, dont l'intégrale est étendue sur le contour entier.

Equation différentielle de torsion non uniforme

Pour connaître l'état de contraintes et de déformations dans une pièce soumise à la torsion non uniforme, il est indispensable de définir le bimoment et le moment de torsion fléchi. Ces deux grandeurs liées à l'angle de torsion et à la fonction de gauchissement se déterminent à partir de l'équation différentielle de torsion non uniforme.

Pour la première fois, le problème de torsion non uniforme a été mis en équation par TIMOSHENKO (1905), dans le cas particulier d'une poutre en «I». Plus tard (1926), WEBER a complété cette équation pour la même section, mais asymétrique. Ce sont WAGNER (1929) et VLASSOV qui ont généralisé l'équation. Ils l'ont rendue valable pour toutes les sections ouvertes, en lui donnant la forme:

$$\left. \begin{aligned} \Theta^{IV} - k^2 \Theta^{II} &= \eta \cdot c \\ k^2 &= \frac{GI_s}{E_1 I_\omega}, \quad \eta = -\frac{1}{E_1 I_\omega} \end{aligned} \right\} \quad (21)$$

avec:

Pour les sections fermées, ce sont les problèmes d'aviation qui ont principalement développé la théorie de torsion. Dans une première théorie technique de torsion des profils fermés, on a appliqué l'équation (21). Les modifications ont porté seulement sur les caractéristiques sectorielles (voir exemple: l'étude de BORNSCHEUR [4]).

Les études de OUMANSKY [30], et BENSCOTTER [10] sont plus exactes. Ces auteurs introduisent dans l'équation une deuxième fonction — fonction de gauchissement ϑ . La nouvelle équation a la forme:

$$\left. \begin{aligned} \Theta^{IV} - k^2 \Theta^{II} &= \eta \cdot c \\ k^2 &= \frac{GI_d}{E_1 I_\omega} \cdot \mu, \quad \eta = -\frac{1}{E_1 I_\omega} \cdot \mu \end{aligned} \right\} \quad (22)$$

avec:

on voit que les termes k^2 et η sont multipliés par le coefficient de gauchissement μ .

En ce qui concerne les profils composés d'éléments fermés et ouverts, on connaît l'équation établie par rapport à la fonction de gauchissement [10]. Il est sans doute préférable d'étudier ces profils de la même façon que les profils ouverts et fermés, c'est-à-dire à l'aide d'une équation semblable à celle (21) ou (22).

Nous établissons maintenant une telle équation, ou plus précisément nous transformons les termes k et η , en analysant la répartition des contraintes dans toutes les parties du profil composé.

Conformément aux hypothèses, nous introduisons en plus de Θ une nouvelle fonction: ϑ .

Pour deux inconnues, deux équations sont indispensables.

— La première se déduit de la condition de continuité des déplacements longitudinaux, le long du contour de la partie fermée:

$$\oint \frac{\partial u}{\partial s} ds = 0$$

et elle s'exprime:

$$\vartheta^{IV} \cdot \frac{E_1}{G} \cdot \oint \frac{\Gamma}{\delta} ds - \Theta^{II} \cdot \Omega = -c \cdot \frac{1}{G\Omega} \cdot \oint \frac{ds}{\delta} \quad (23)$$

— La deuxième équation provient de l'équilibre du moment de torsion C par les contraintes $\int_A \tau \cdot \delta \cdot r ds$:

$$\Theta^I - \mu \cdot \vartheta^I = \frac{C}{GI_o} \quad (24)$$

Dans cette équation $\mu = (1 - \frac{I_d}{I_o})$ étant le coefficient de gauchissement, avec:

$$I_d = \frac{\Omega^2}{\oint \frac{ds}{\delta}} \quad \text{qui caractérise la torsion uniforme des profils fermés, et}$$

$$I_o = \int_A r^2 \delta ds \quad \text{qui concerne toute la section du profil composé (parties fermées et ouvertes).}$$

En dérivant trois fois (24), nous avons la relation entre les deux fonctions:

$$\vartheta^{IV} = \frac{\Theta^{IV}}{\mu} \quad (25)$$

Introduisons (25) dans (23); nous avons ainsi l'équation différentielle recherchée par rapport à l'angle de torsion:

$$\Theta^{IV} - k^2 \Theta^{II} = \eta \cdot c$$

dans laquelle:

$$k^2 = \frac{\mu \cdot G}{E_1} \cdot \frac{\Omega}{\oint \Gamma \frac{ds'}{\delta}} \quad \eta = - \frac{\mu}{E_1} \cdot \frac{\oint \frac{ds}{\delta}}{\Omega \oint \Gamma \frac{ds}{\delta}}$$

(26)

Pour vérifier l'équation établie, nous l'avons appliquée au profil fermé, en remarquant que, pour un tel profil $\Gamma = S_{\omega} - \frac{1}{\Omega} \oint S_{\omega} r ds$. Ainsi nous avons obtenu l'équation (22). L'équation (26) avec ses termes k et η est donc correcte.

Résolution de l'équation de torsion non uniforme

Pour la résolution de l'équation (26), nous utilisons la méthode des *paramètres initiaux*, appliquée par VLASSOV au calcul des voiles à profils ouverts [32].

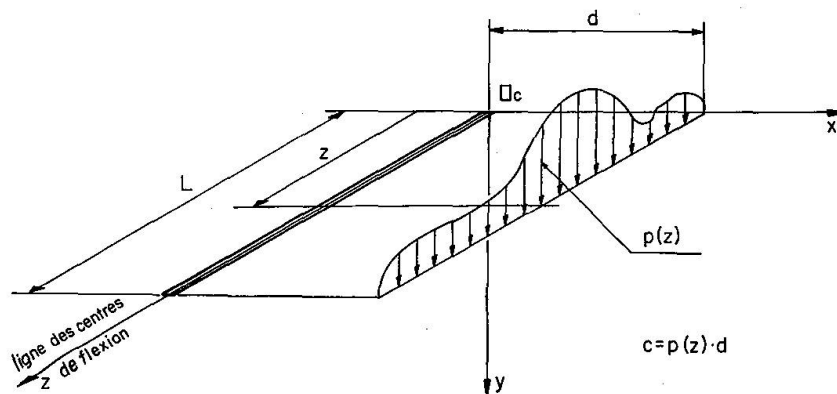


Fig. 27

La matrice définissant les quatre facteurs fondamentaux pour une charge continue à répartition quelconque et d'excentricité constante (fig. 27) s'écrit:

	Θ_o	Θ_o^I	$-B_o \frac{\oint \Gamma_{\frac{ds}{s}}}{G\Omega I_{[0]}}$	$-C_o \cdot \frac{1}{GI_d}$	$-\frac{1}{GI_d}$
$\Theta_{(z)}$	1	$\frac{Sh\,kz}{k}$	$Ch\,kz - 1$	$\frac{Sh\,kz}{k} - z$	$\frac{1}{k} \int_0^z c(kz - Sh\,kz) dz$
$\Theta_{(z)}^I$	0	$Ch\,kz$	$k\,Sh\,kz$	$Ch\,kz - 1$	$\int_0^z c(1 - Ch\,kz) dz$
$\Theta_{(z)}^H$	0	$k\,Sh\,kz$	$k^2\,Ch\,kz$	$k\,Sh\,kz$	$-k \int_0^z c \cdot Sh\,kz\,dz$
$\Theta_{(z)}^{II}$	0	$k^2\,Ch\,kz$	$k^3\,Sh\,kz$	$k^2\,Ch\,kz$	$-k^2 \int_0^z c \cdot Ch\,kz\,dz$

Les paramètres initiaux Θ_o , Θ_o^I , B_o et C_o s'expriment par les constantes d'intégration de l'équation différentielle, et doivent donc être déterminés par les conditions aux limites, imposées aux extrémités de la pièce ($z = 0$ et $z = L$).

Les sections extrêmes sont encastées à la torsion ($\Theta = 0$), et elles restent planes ($B \neq 0$), donc pour $z = 0$ et $z = L$ $\Theta = \Theta^I = 0$.

Nous obtenons dans une section $z = C^c$, pour les cas de charge étudiés, les formules suivantes:

a) *Moment de torsion uniformément réparti, $c = p \cdot d$ (fig. 27):*

$$\begin{aligned}
 \Theta_{(z)} &= \frac{pdL}{2kGI_d} \left[\frac{kz(L-z)}{L} - \frac{2\,Sh\,\frac{k(L-z)}{2} \cdot Sh\,\frac{kz}{2}}{Sh\,\frac{kL}{2}} \right] \\
 \Theta_{(z)}^I &= \frac{pdL}{2GI_d} \left[\frac{L-2z}{L} - \frac{Sh\,k(\frac{L}{2}-z)}{Sh\,\frac{kL}{2}} \right] \\
 \Theta_{(z)}^H &= \frac{pdL}{2GI_d} \left[\frac{Ch\,k(\frac{L}{2}-z)}{Sh\,\frac{kL}{2}} - \frac{2}{kL} \right] \\
 \Theta_{(z)}^{II} &= \frac{pdL}{2GI_d} \cdot \frac{Sh\,k(z-\frac{L}{2})}{Sh\,\frac{kL}{2}}
 \end{aligned}$$

b) *Moment de torsion réparti suivant une sinusoïde, avec l'origine du système d'axes $\square_c x y z$ en milieu de la travée $c = c_o \cdot \cos(\frac{\pi z}{L})$, $c_o = q(\frac{L}{2}) \cdot d$, ou $c_o = m(\frac{L}{2})$ (§ 5):*

$$\Theta_{(z)} = \frac{c_o}{GI_d} \cdot \frac{2L}{k} \left[\frac{1}{\pi} \left(\frac{kL}{2} - kz \sin \frac{\pi z}{L} - \frac{kL}{\pi} \cos \frac{\pi z}{L} \right) - \frac{\pi}{k^2 L^2 + \pi^2} \left(Sh \frac{kL}{2} - Sh kz \cdot \sin \frac{\pi z}{L} - \frac{kL}{\pi} \cdot Ch kz \cdot \cos \frac{\pi z}{L} \right) - 2 \cdot \left(\frac{1}{\pi} - \frac{\pi}{k^2 L^2 + \pi^2} \cdot Ch \frac{kL}{2} \right) \cdot \frac{Sh k(\frac{L+2z}{4}) \cdot Sh k(\frac{L-2z}{4})}{Sh \frac{kL}{2}} \right]$$

$$\Theta_{(z)}^I = \frac{c_o}{GI_d} \cdot 2L \left[\frac{\pi}{k^2 L^2 + \pi^2} \left(Ch kz \cdot \sin \frac{\pi z}{L} + \frac{kL}{\pi} Sh kz \cdot \cos \frac{\pi z}{L} \right) - \frac{1}{\pi} \sin \frac{\pi z}{L} - \left(\frac{\pi}{k^2 L^2 + \pi^2} \cdot Ch \frac{kL}{2} - \frac{1}{\pi} \right) \cdot \frac{Sh kz}{Sh \frac{kL}{2}} \right]$$

$$\Theta_{(z)}^{II} = \frac{c_o}{GI_d} \cdot 2kL \left[\frac{\pi}{k^2 L^2 + \pi^2} \left(Sh kz \cdot \sin \frac{\pi z}{L} + \frac{kL}{\pi} Ch kz \cdot \cos \frac{\pi z}{L} - \frac{kL}{\pi} \right) - \left(\frac{\pi}{k^2 L^2 + \pi^2} \cdot Ch \frac{kL}{2} - \frac{1}{\pi} \right) \cdot \frac{Ch kz}{Sh \frac{kL}{2}} \right]$$

$$\Theta_{(z)}^{III} = \frac{c_o}{GI_d} \cdot 2k^2 L \left[\frac{\pi}{k^2 L^2 + \pi^2} \left(Ch kz \cdot \sin \frac{\pi z}{L} + \frac{kL}{\pi} Sh kz \cdot \cos \frac{\pi z}{L} \right) - \left(\frac{\pi}{k^2 L^2 + \pi^2} \cdot Ch \frac{kL}{2} - \frac{1}{\pi} \right) \cdot \frac{Sh kz}{Sh \frac{kL}{2}} \right]$$

c) *Moment de torsion réparti suivant une parabole, avec l'origine du système d'axes $\square_c x y z$ en milieu de la travée, $c = c_o \cdot \left(1 - \frac{4z^2}{L^2}\right)$, $c_o = q(\frac{L}{2}) \cdot d$, ou $c_o = m(\frac{L}{2})$ (§ 5):*

$$\Theta_{(z)} = \frac{c_o}{GI_d} \cdot \frac{2}{k^2} \left[k^2 z^2 \cdot \left(\frac{z^2}{L^2} - \frac{1}{2} \right) + \frac{k^2 L^2}{16} + \frac{8}{k^2 L^2} - \left(\frac{8}{k^2 L^2} + \frac{4z^2}{L^2} - 1 \right) \cdot Ch kz + \frac{8z}{kL^2} Sh kz - \left(\frac{4}{kL} + \frac{kL}{3} \right) \cdot Th \frac{kL}{4} + \left(\frac{8}{k^2 L^2} Sh \frac{kL}{2} + \frac{kL}{3} - \frac{4}{kL} \cdot Ch \frac{kL}{2} \right) \cdot \frac{Ch kz - 1}{Sh \frac{kL}{2}} \right]$$

$$\Theta_{(z)}^I = \frac{c_o}{GI_d} \cdot \frac{2}{k} \left[kz \cdot \left(\frac{4z^2}{3L^2} - 1 \right) + \left(1 - \frac{8}{k^2 L^2} - \frac{4z^2}{L^2} \right) \cdot Sh kz + \frac{8z}{kL^2} Ch kz + \left(\frac{8}{k^2 L^2} Sh \frac{kL}{2} + \frac{kL}{3} - \frac{4}{kL} Ch \frac{kL}{2} \right) \cdot \frac{Sh kz}{Sh \frac{kL}{2}} \right]$$

$$\Theta_{(z)}^{II} = \frac{c_o}{GI_d} \cdot 2 \cdot \left[\frac{2}{k^2 L^2} - 1 + \left(1 - \frac{8}{k^2 L^2} - \frac{4z^2}{L^2} \right) \cdot Ch kz + \frac{8z}{kL^2} Sh kz + \left(\frac{kL}{3} - \frac{4}{kL} Ch \frac{kL}{2} + \frac{8}{k^2 L^2} Sh \frac{kL}{2} \right) \cdot \frac{Ch kz}{Sh \frac{kL}{2}} \right]$$

$$\Theta_{(z)}^{III} = \frac{c_o}{GI_d} \cdot 2k \cdot \left[\left(1 - \frac{8}{k^2 L^2} - \frac{4z^2}{L^2} \right) \cdot Sh kz + \frac{8z}{kL^2} \cdot Ch kz - \left(\frac{4}{kL} Ch \frac{kL}{2} - \frac{8}{k^2 L^2} Sh \frac{kL}{2} - \frac{kL}{3} \right) \cdot \frac{Sh kz}{Sh \frac{kL}{2}} \right]$$

Application numérique et vérification expérimentale

Nous appliquons la théorie exposée dans les paragraphes précédents à un pont à quatre caissons, récemment construit: le Pont de Courbevoie, sur la Seine, dont la coupe transversale est donnée sur la fig. 28*. C'est un portique ouvert à trois travées (40 + 60 + 40 m). La travée étudiée est celle de 60 m.

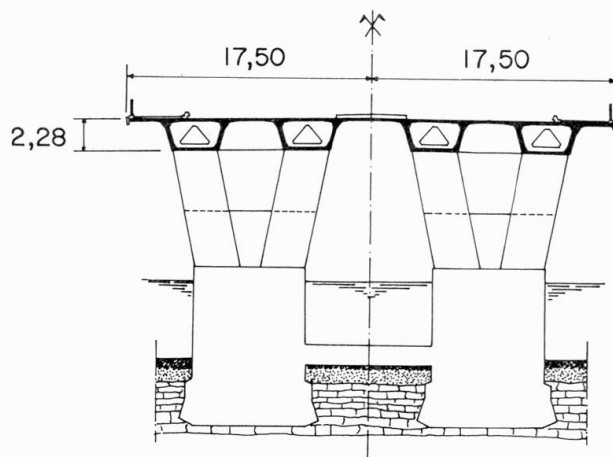


Fig. 28

La section d'un caisson est définie sur la fig. 29. La disymétrie est créée par la différence de longueur des porte-à-faux ($e_1 \neq e_2$).

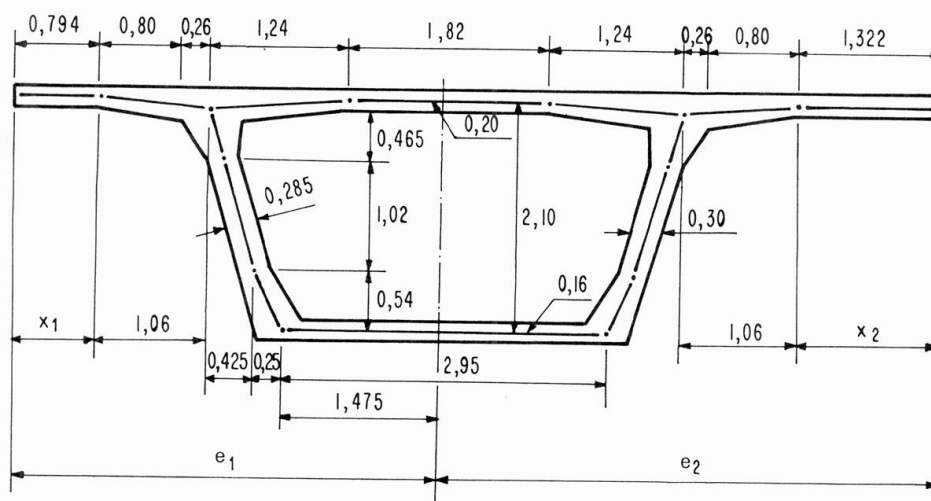


Fig. 29

Les mesures de déformations effectuées au cours des épreuves de cet ouvrage ont mis en doute les hypothèses habituelles de calcul.

*Pont construit par l'entreprise Campenon Bernard. Au moment de l'étude, l'auteur était ingénieur au Service régional de l'Équipement de la Région parisienne.

Au cours des épreuves, nous avons utilisé des camions de 35 t en mesurant les flèches et rotations au milieu de chaque poutre-caisson, pour les trois cas de charge suivants:

- 1° 8 files de 4 camions (toute la largeur de 26 m chargée).
- 2° 4 files de 4 camions (deux poutres-caissons latérales chargées).
- 3° 2 files de 4 camions (une seule poutre-caisson latérale chargée).

Ces trois cas de charge sont considérés dans l'application numérique.

Afin de ne pas prolonger l'exposé, nous nous bornons à donner les résultats essentiels:

- de la répartition des charges entre les poutres-caissons,
- de la torsion considérée comme non uniforme.

Les lignes d'influence pour les inconnues hyperstatiques à mi-travée isostatique sont données sur les fig. 30, 31, 32 et 33.

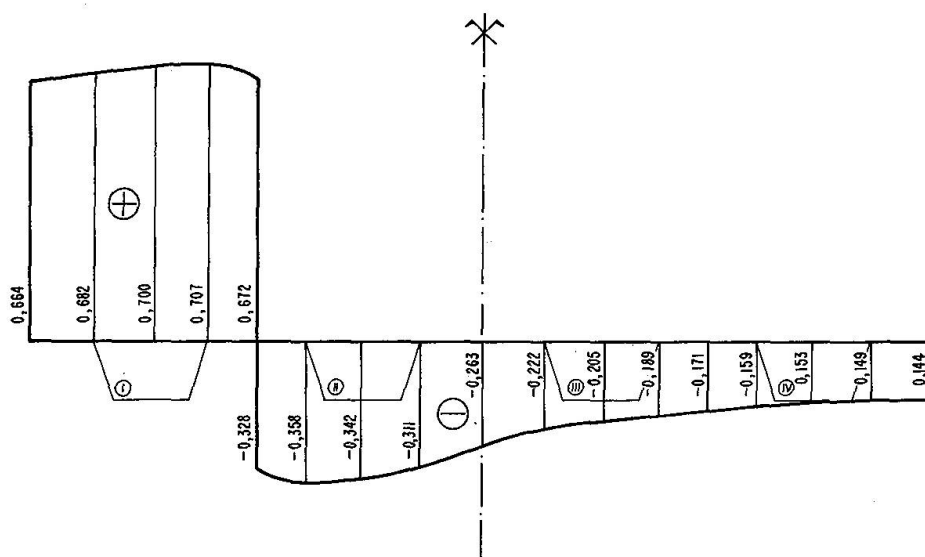


Fig. 30

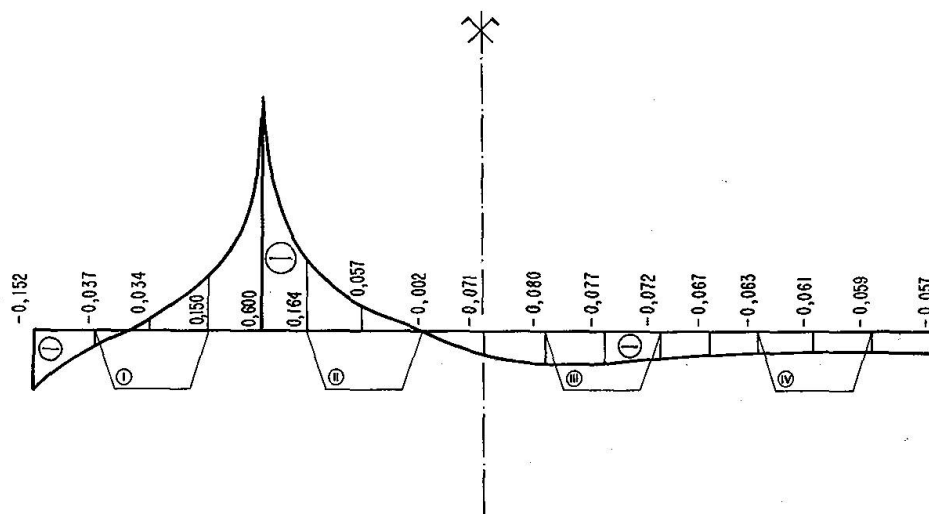


Fig. 31

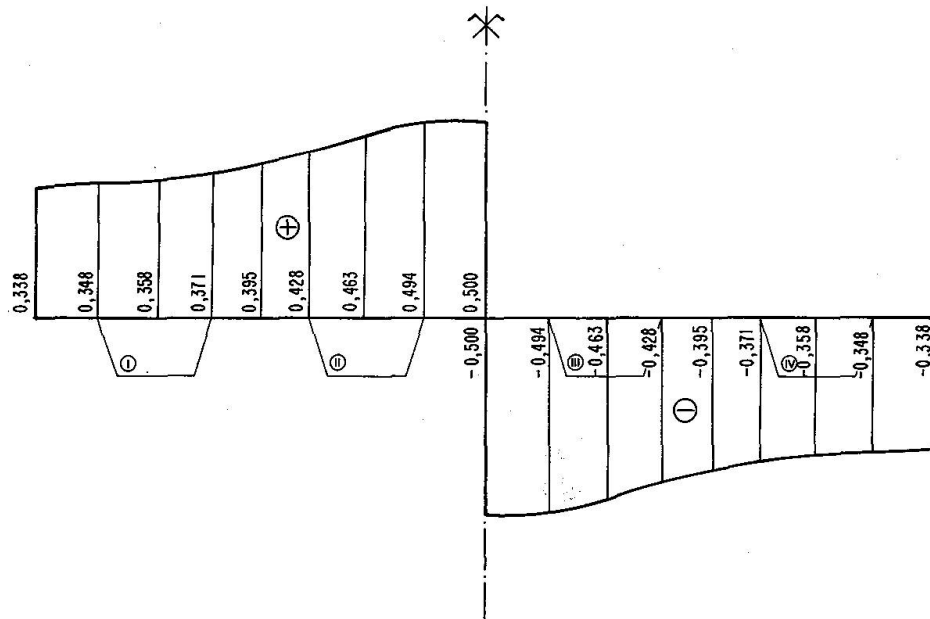


Fig. 32

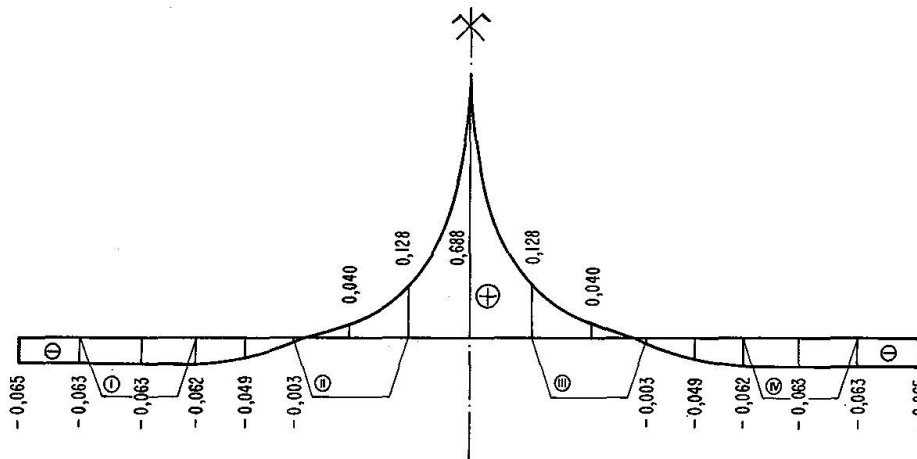


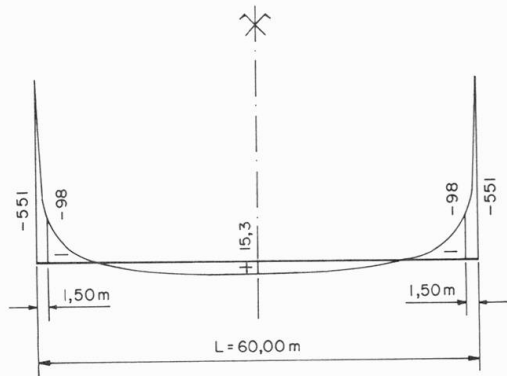
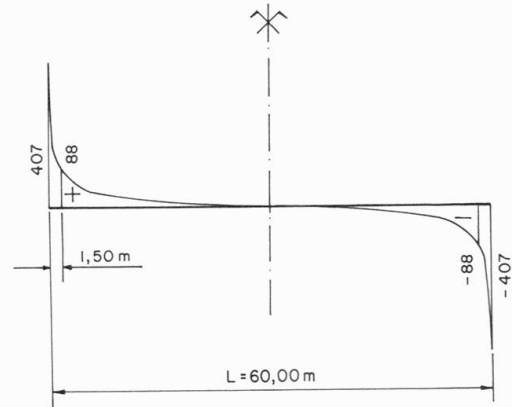
Fig. 33

Sur les fig. 34 et 35 sont donnés les diagrammes des bimoment et moment de torsion fléchié pour une poutre-caisson latérale. Ces diagrammes correspondent à la surcharge réglementaire A (1) répandue sur toute la longueur (60 m), et toute la largeur de chaussée (26 m); les inconnues hyperstatiques étant réparties suivant la loi sinusoïdale.

Les contraintes σ et τ dues au gauchissement empêché sont représentées sur les fig. 36 et 37. Les valeurs entre les parenthèses correspondent au troisième cas de charge d'épreuves — la charge la plus excentrée.

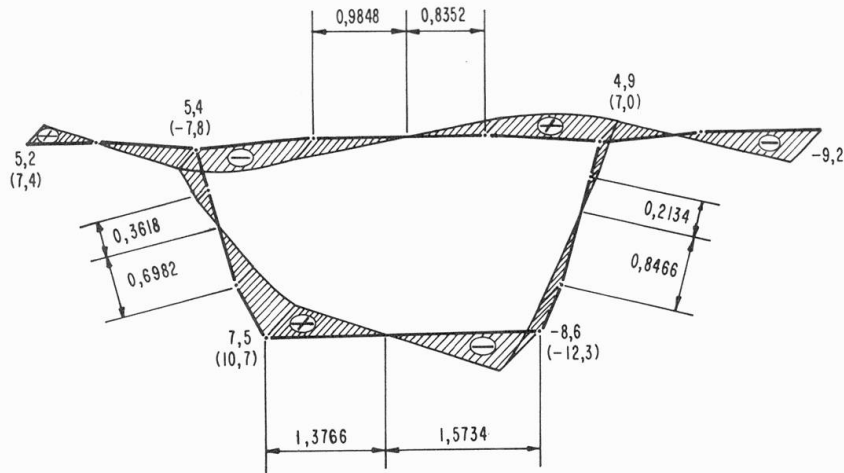
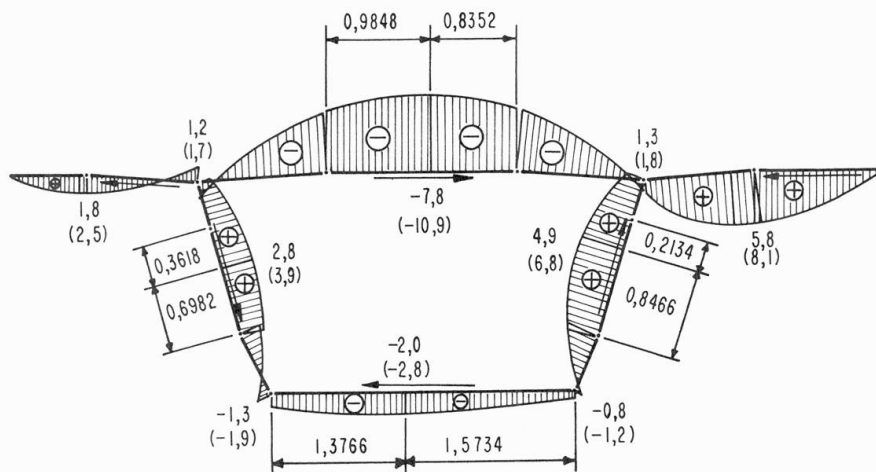
Les contraintes en question sont réparties suivant le contour de la section de la même façon que les valeurs sectorielles $[\omega]$ et Γ .

La section considérée est celle du voisinage des appuis ($z = 1,5$ m ou $z = 58,5$ m).

Fig. 34. Diagramme du bimoment B (en Tm^2).Fig. 35. Diagramme du moment de torsion fléchi M_ω (en Tm).

Dans la section à mi-portée $M_\omega = 0$, donc $\tau = 0$.

La valeur du bimoment B est faible. Les contraintes δ ne dépassent pas en valeur absolue 2 kg/cm^2 .

Fig. 36. Contraintes normales $\sigma = \frac{B_{[\omega]}}{I_{[\omega]}}$ en kg/cm^2 .Fig. 37. Contraintes de cisaillement $\tau = \frac{M_\omega \cdot \Gamma}{I_{[\omega]} \cdot \delta}$ en kg/cm^2 .

Conclusions

D'une façon générale, les résultats de cette recherche sont très satisfaisants.

La flexion transversale des parois de caissons, prise en compte dans le calcul des inconnues hyperstatiques, modifie sensiblement le comportement des structures.

En ce qui concerne la répartition des inconnues hyperstatiques, le long de la travée, on peut admettre, avec une bonne approximation, que ces inconnues sont réparties suivant une sinusoïde.

C'est du point de vue de la torsion que l'étude est la plus intéressante.

Les mesures des rotations au milieu de chaque poutre-caisson donnent des valeurs supérieures de 30% environ, comparativement à celles trouvées par la méthode classique de calcul, et ces mesures confirment nos résultats de calcul.

La torsion est en effet non uniforme, et les principes de la théorie des barres à parois minces sont parfaitement applicables au calcul des structures en béton précontraint composées de poutres-caissons.

Les contraintes supplémentaires dues à la torsion non uniforme, ignorées dans la méthode de calcul classique, peuvent avoir de graves conséquences sur le comportement de ce genre de structures, et surtout dans les ponts courbes, où la sollicitation à la torsion est plus accentuée.

L'importance de ce problème devient à l'heure actuelle plus grande, du fait de l'évolution de la préfabrication, qui conduit à la production d'éléments de construction ayant des parois de plus en plus minces.

Notations

A	section transversale.
B	bimoment.
C	moment de torsion.
c	moment de torsion par unité de longueur.
D_o	constante relative aux caractéristiques sectorielles des profils composés.
E	module d'élasticité longitudinale.
ν	coefficient de Poisson.
E_1	module d'élasticité réduit de la traction longitudinale ($E_1 = \frac{E}{1 - \nu^2}$).
G	module d'élasticité transversale.
I_x, I_y	moment d'inertie par rapport aux axes Ox et Oy .
I_s, I_d	moment d'inertie à la torsion uniforme d'un profil: ouvert, fermé.
I_o	moment d'inertie polaire.
μ	coefficient de gauchissement.
$\omega, \hat{\omega}, [\omega]$	surface sectorielle d'un profil: ouvert, fermé, composé.
Ω	double de l'aire comprise à l'intérieur de la ligne moyenne d'un profil fermé.
$I_\omega, I_{\hat{\omega}}, I_{[\omega]}$	moment d'inertie sectoriel d'un profil: ouvert, fermé, composé.
L	longueur de la portée étudiée.
M	moment fléchissant agissant dans le plan parallèle au plan Oy, Oz .
M_ω	moment de torsion fléchie.

N	effort normal.
O	centre de gravité.
\square_c	centre de flexion.
r	longueur de la perpendiculaire abaissée du centre de flexion sur la tangente au contour.
$S_x, S_y, \hat{S}_x, \hat{S}_y$	moments statiques par rapport aux axes Ox et Oy d'un profil: ouvert, fermé.
S_ω, S_ϕ	moment statique sectoriel d'un profil: ouvert, fermé.
s	abscisse curviligne d'un point de l'arc.
s_o	périmètre suivant la ligne moyenne d'un profil fermé.
T	effort tranchant agissant dans le plan parallèle au plan Oy, Oz .
u	déplacement dans la direction z .
v	déplacement dans la direction de la tangente au contour.
δ	épaisseur de la paroi.
Φ	flux de cisaillement.
Θ	angle de torsion.
σ	contrainte normale.
ζ	gauchissement.
ϑ	fonction de gauchissement (caractérisant la torsion non uniforme).
τ	contrainte de cisaillement.
\oint	intégrale étendue sur tout le contour d'un profil fermé.

Considérations pratiques

Nous donnons ici quelques remarques pratiques concernant les conséquences de la torsion non uniforme vis-à-vis du dimensionnement des armatures des ponts à poutres-caissons en béton précontraint.

Il convient de constater que les contraintes maximales dues à la torsion non uniforme se situent au voisinage des appuis.

Dans le cas des ponts droits, les calculs classiques ignorent ces contraintes — de l'ordre de quelques bars — et il n'est pas prévu d'armatures passives pour les reprendre.

Le diagramme (fig. 36) des contraintes normales conduit à renforcer les armatures longitudinales dans les zones de goussets et de porte-à-faux et le diagramme (fig. 37) des contraintes tangentielles à renforcer les armatures transversales au milieu des hourdis et des âmes.

Pour les ponts courbes, on ne peut pas séparer les termes de flexion et de torsion qui sont liés par la même équation; il en résulte que les conséquences de la torsion non uniforme sont plus importantes, puisqu'elle influe sur l'état général des contraintes et des déformations. Ainsi les flèches mesurées en travées sont en réalité plus importantes que celles trouvées par un calcul classique.

D'autre part, dans une poutre-caisson large à plusieurs cellules, où l'effet de gauchissement est important, les contraintes supplémentaires normales et tangentielles peuvent atteindre quelques dizaines de bars. Un calcul automatique tridimensionnel permet de mettre en évidence l'existence de ces contraintes. Un tel tablier

dimensionné suivant les formules habituelles manquera non seulement d'armatures passives, mais aussi de précontrainte, d'où risque de fissures.

Il semble que l'effet nuisible de la torsion non uniforme aussi bien dans le cas des ponts droits que courbes pourrait être considérablement diminué par une différente conception des entretoises d'appui.

Une simple diminution de l'épaisseur des entretoises, voire leur suppression dans certains cas, pourrait améliorer le comportement des ponts en béton précontraint et, en plus, apporter de l'économie au projet.

Nous nous proposons de traiter ce problème prochainement dans une étude étendue sur plusieurs types de ponts.

Remerciements

J'exprime ma reconnaissance à M. R. *Siestrunck*, professeur à la Faculté des sciences de l'Université de Paris, qui m'a aidé à porter cette recherche devant la Faculté des sciences et qui a accepté de présider le jury d'examen.

Le sujet de cette étude a été accepté par M. P. *Géry*, professeur à l'Ecole des Mines et au Conservatoire national des arts et métiers, et le travail réalisé sous sa direction.

Je tiens à l'assurer de ma reconnaissance.

Je remercie M. R. *Vichnievsky*, professeur à la Faculté des sciences de l'Université de Paris, qui a accepté de faire partie du jury d'examen.

Je remercie également M. D. *Ceylon*, ingénieur en chef des Ponts et Chaussées, professeur au Centre des hautes études de la construction, pour le profit que j'ai retiré de ses suggestions, et qui a bien voulu faire partie du jury d'examen.

Cette étude a été entreprise au Service régional de l'Equipement de la Région parisienne.

Je tiens à exprimer ma gratitude à M. G. *Rondard*, ingénieur des Travaux publics de l'Etat, qui m'a accueilli dans son service.

Que toute sa subdivision trouve ici ma sympathie pour sa collaboration et son aide amicale.

Je tiens enfin à remercier M. G. *Wianecki*, docteur ès sciences, chargé de la Section aérodynamique de l'I.T.B.T.P., J. *Bródka*, Docteur ès sciences, chef de la Section Constructions métalliques de l'Institut technique de Varsovie, pour leur aide amicale et efficace.

Bibliographie

1. BAZANT: Pièces longues à voiles épais et calcul des ponts à section déformable. Annales des Ponts et Chaussées, N° 3, 1968.
2. BECK, SCHÄFER: Die Berechnung von Hochhäusern durch Zusammenfassung aller aussteifenden Bauteile zu einem Balken. Der Bauingenieur, Nr. 3, 1969.
3. BLEICH: Non-Linear Distribution of Bending Stresses due to Distortion of the Cross Section. Journal of the Applied Mechanics, 1;3, 1953.
4. BORNSCHEUER: Beispiel und Formelsammlung zur Spannungsberechnung dünnwandiger Stäbe mit wölbbehindertem Querschnitt. Der Stahlbau, Nr. 12, 1952; Nr. 2, 1953.

5. COURBON: Résistance des matériaux. Paris, Dunod, 1964.
6. COURTAND et LEBELLE: Formulaire du béton armé. Paris, I.T.B.T.P., 1962.
7. DABROWSKI: Distribution non linéaire des contraintes due à la déformation de la section dans les poutres raidies, soumises à la flexion (en polonais). *Rozprawy Inzynierskie, Zeszyt 3*, 1954.
8. DABROWSKI: Torsion des ponts et des constructions hydrauliques à parois minces et section fermée (en polonais). *Rozprawy Inzynierskie, Zeszyt 2*, 1958.
9. DZIEWOLSKI: Etude théorique et expérimentale d'une poutre en caisson asymétrique avec deux appendices. Publication préliminaire de l'A.I.P.C., 7^e Congrès, Rio de Janeiro, 1964.
10. DZIEWOLSKI: Torsion non uniforme des poutres à parois minces et à profils composés d'éléments fermés et ouverts. *Construction métallique*, N° 2, 1964.
11. GOSCHY: Der Kastenträger ohne Zwischenschotte, Berechnung auf Torsion. *Die Bautechnik*, Nr. 5, 1966.
12. HENRY: Le viaduc courbe de la Porte de Paris à Saint-Denis. *Annales de l'I.T.B.T.P.*, N° 11, 1967.
13. ISNARD: Formulaire de l'Ingénieur. Paris, Eyrolles, 1964.
14. KLIMINSKI: Calcul des ponts courbes métalliques compte tenu du gauchissement des sections transversales. *Annales des Ponts et Chaussées*, N° 5, 1970.
15. LAREDO: Théorie générale du comportement mécanique des grandes structures dans l'espace. *Travaux*, N° 6, 1967.
16. LORINGOVEN: Torsion des poutres. Stage de perfectionnement technique, C.T.I.C.M., N° 1, 1967.
17. MANDEL: Détermination du centre de torsion à l'aide du théorème de réciprocité. *Annales des Ponts et Chaussées*, N° 3, 1948.
18. MARGUERRE: Über die Beanspruchung von Plattenträgern. *Die Bautechnik*, Nr. 8, 1952.
19. MASSONNET: Résistance des matériaux. Paris, Dunod, 1962.
20. MATHIVAT: Reconstruction du pont de Choisy-le-Roi. *Travaux*, N° 1, 1966.
21. MATHIVAT: Boulevard périphérique – Franchissement de la Seine, pont aval. *Annales de l'I.T.B.T.P.*, N° 10, 1968.
22. NALESZKIEWICZ: Etudes préliminaires de la torsion d'une coque de navire sous la vague biaise (en polonais). *Rozprawy Inzynierskie, Zeszyt 34*, 1955.
23. NOWACKI: Mécanique des constructions (en polonais). Varsovie, P.W.N., 1967.
24. REISSNER: Analysis of Shear Lag in Box Beams by the Principle of Minimum Potential Energy. *Quarterly of Applied Mathematics*, No. 3, 1946.
25. RENARD: Etude des ponts courbes. *Annales des Travaux publics de Belgique*, N° 1, 1967.
26. RUTECKI: Résistance des matériaux appliquée aux constructions à parois minces (en polonais). Varsovie, P.W.N., 1957.
27. RUTECKI: Ossatures portantes composées de parois minces (en polonais). Varsovie, P.W.N., 1966.
28. STÜSSI: Centre de cisaillement et torsion. *Mémoires de l'A.I.P.C.*, Vol. 12, 1952.
29. TERRINGTON: The Torsion Centre of Girders. *Engineering*, Vol. 178. No. 11, 1954.
30. URBAN: Théorie et calcul des constructions aéronautiques en parois minces (en russe). Moscou, 1956.
31. VIRCİK: Beitrag zur Berechnung des statischen Momentes als Querkraft bei dünnwandigen Querschnitten. *Der Bauingenieur*, Nr. 5, 1970.
32. VLASSOV: Pièces longues en voiles minces. Paris, Eyrolles, 1962.
33. WEISS: Dimensionnement des constructions métalliques composées des barres, selon la théorie des structures à parois minces (en polonais). Varsovie, *Inzynieria i Budownictwo*, 1962.
34. WELLER: Modern Mathematics for the Engineer. New York, 1956.
35. WINTER: Stress Distribution in and Equivalent Width of Flanges of Wide Thin-Wall Steel Beams. National Advisory Committee for Aeronautics, Note 784, Washington, No. 11, 1940.

Résumé

L'étude concerne les systèmes spatiaux élastiques rencontrés dans la construction actuelle des ponts.

Le problème porte principalement sur une section transversale, composée de caissons liés entre eux par des dalles de différentes longueurs. Les structures ne sont entretoisées que sur appuis.

Pour la définition des inconnues hyperstatiques, on tient compte de la flexion transversale des parois de caissons et, pour la torsion, de la fonction de gauchissement.

Zusammenfassung

Die Untersuchung behandelt räumliche elastische Systeme wie sie im heutigen Brückenbau auftreten. Das Problem bezieht sich hauptsächlich auf einen aus Kasten zusammengesetzten transversalen Querschnitt, die untereinander durch verschieden lange Betonplatten verbunden sind. Das Bauwerk ist nur an den Auflagestellen ausgesteift.

Zwecks Definition der statisch unbestimmten Unbekannten werden die transversale Biegung der Kastenwände, sowie die Krümmungsfunktion für die Torsion berücksichtigt.

Summary

The study deals with spatial elastic systems in actual bridge construction. The problem relates mainly on a transversal section composed by boxes joint together by concrete slabs of different lengths. The structure is only stiffened on the supports.

With a view of defining the statically undetermined unknowns the transversal flexion of the box wall and the function of the curvature for the torsion are taken into consideration.

Critical Loads of Building Frames

Charges critiques de constructions en cadres

Kritische Lasten von Rahmentragwerken

T. VAN LANGENDONCK

Professor catedrático

Escola Politécnica, Universidade de São Paulo

Introduction

The theoretical solution of the problem of finding the critical load of orthogonal building structures within the elastic range is already known. In practice, however, the determination of that load — excepting very simple cases — is difficult, for it involves the solution of a great number of transcendental equations. It is sufficient for the Structural Engineer the knowledge of the approximate value of that load, if it leads to an acceptable safety factor. Therefore, if a simple method is known that yields a sufficiently approximate answer, the exact solution may be waved. The conventional simplistic procedure consisted in finding the buckling load of the columns of the building, one by one, and assuming that the effect of the link with the remainder of the structure could be represented by a single buckling length. In this article a method of solution¹ is suggested which lies between the simplistic and the theoretically exact solution. “Theoretically” exact since even the most complicated solution mentioned above, with the transcendental equations, does not avoid certain facts that lead to discrepancies in relation to the actual structure, due to the lack of knowledge of certain values and the way of considering certain factors, such as: the value of the modulus of elasticity E , the effects of the beam-column connections and of the rigidity of the slabs, the uncertainty of the load distribution, the heterogeneity of the material, in particular if it is reinforced concrete.

Hypothesis

Consider a plane structure with several vertical columns fixed at the same level at the lower end, and m stories with horizontal uninterrupted beams². The cross section of the columns remains constant within each story, but it may vary from one

¹ The method originated from another more elementar one which considers only one of the various systems of stacked columns of the building, with only one parameter to be determined; it has been suggested by the Author several years ago [1].

² If it happens that some of the columns, and attached girders, do not extend all the way to the top of the structure, the method may still be applied if we assume that they do exist, but with $I = 0$.

story to another; there are no restrictions to the beam sizes, and the loads — assumed vertical — are applied at the joints of the structure without any intensity relations among them¹.

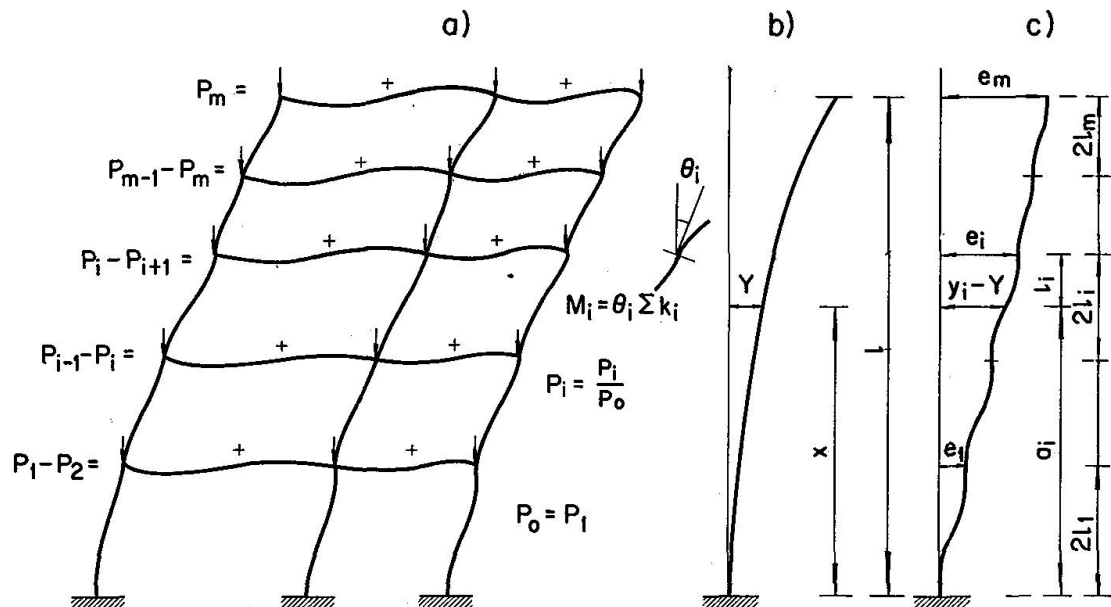


Fig. 1.

The simplifying hypothesis consists in assuming for the elastic curves of the deformed columns, which remain within elastic range until buckling, a combination of two curves (Fig. 1a): one corresponding to the deformation resulting by disregarding the floor girders (Fig. 1b), the other by assuming girders of infinite rigidity (Fig. 1c). The relative magnitude of the respective displacements is evaluated in such a manner as to result minimum buckling load.

Since the method is based on the assumption of a certain shape of the deflection curve of the structure, with a few parameters to be determined by comparing energies — it will yield a larger value than the correct one. In order to stay on the safe side a reduction coefficient for the deformation energy is used, thus resulting, for the majority of the less favorable cases, a strength which is nearly the correct one, but in other cases might yield safety factors in excess of 20% when the assumed curve resembles the correct one (as in the case of the buckling of isolated columns in two adjacent floors, mentioned ahead, where Euler's formula would be applicable).

¹ The loads applied on the girders are transferred to the columns, without significant influence on the structural instability. A closer look will be taken regarding this aspect in a later publication, including the action of horizontal loads as well as the deformability at the supports.

Deflection Curve

The deflection curve of the column shall be the one defined along each portion between floors by

$$y_i = e_{i-1} + c_i \left[2 + 3 \frac{x - a_i}{l_i} - \left(\frac{x - a_i}{l_i} \right)^3 \right] l_o + Y, \quad (4)$$

the three terms of the second member representing, respectively:

- the displacement of the starting joint in the portion of the structure with rigid girders (e_{i-1}),
- the complement of this displacement along that portion (the equation of the cubic parabola was used because — as it is known — it adjusts itself very well to the corresponding sine wave) including the factor c_i , to be determined,
- the displacement (Y) of the column (without girders) assumed fixed at the lower end and free at the top.

For the latter, any curve that satisfies the boundary conditions can be used; however, for simplicity, a cubic parabola will again be used:

$$Y = \frac{x^2}{l_o^2} (Kl - x) \quad (5)$$

This equation assumes fixity at the bottom; the condition at the top is characterized by the parameter K , which varies from $K = 1,5$ (infinitely rigid beam at the top) to $K = 3$ (rigidity zero of the beam at the top). A better value of K could be obtained assuming it being a new parameter to be determined along with c_i ; however, in the case of buildings, as long as the beams at the top are not stronger than the ones below, which is usual, one may take $K = 3$, as has been done in the present article. For any other value of K it is sufficient to substitute λ by $K\lambda/3$ in the formulas (9)¹.

Since the assumed line is not the real one, which is the most unfavorable, the proposed equation will lead to a larger critical load; in order to compensate for this error it is suitable to multiply the coefficient c_i , which appears in the expression of the deformation energy of the column, by $\sim 0,9$. This explains, in the equations for B_i and C_i presented further, the coefficient 1,8 (instead of 2), and 0,8 ($\sim 0,9^2$), respectively.

Buckling Load

It is a known fact that the buckling load of a member may be obtained by establishing the equivalence between the developed energy and the summation of energies from the reaction forces and the deformation of the member; i.e. (the summations extend between $i = 1$ and $i = m$):

$$\frac{1}{2} \sum P_i I_i^* = \frac{E}{2} \sum I_i I_i^{**} + \frac{1}{2} \sum M_i \theta_i \quad (6)$$

¹ Only λ ; the λ_i remain the same.

If the assumed deflection curve is correct, this equation would yield the buckling load (by substituting P_i by $p_i P_o$, I_i by $j_i I_o$, M_i by $\theta_i \sum k_i$, θ_i by $Y'_{a_i+l_i}$):

$$P_o = \frac{\sum l_o^2 j_i I_i^{**} + \sum (l_o^2 \sum k_i / EI_o) Y_{a_i+l_i}'^2}{\sum p_i I_i^*} \frac{EI_o}{l_o^2} \quad (7)$$

or:

$$P_o = \frac{A + B + C}{A' + B' + C'} \frac{EI_o}{l_o^2} = G \frac{EI_o}{l_o^2} \quad (8)$$

with A, B, C, A', B' and C' as defined in (1) and (2), and also:

$$\begin{aligned} A_i &= \lambda j_i [3(\lambda - \alpha_i)^2 + \lambda_i^2] + \frac{3}{8} \kappa_i (\alpha_i + \lambda_i)^2 (2\lambda - \lambda_i - \alpha_i)^2 \\ B_i &= 1,8 j_i, \quad C_i = 0,8 \frac{j_i}{\lambda_i^3} \\ A'_i &= p_i \lambda_i \left[\frac{3}{4} (\alpha_i^4 + 2\alpha_i^2 \lambda_i^2 + 0,2\lambda_i^4) - 3\lambda \alpha_i (\alpha_i^2 + \lambda_i^2) + \lambda^2 (3\alpha_i^2 + \lambda_i^2) \right] \\ B'_i &= p_i (2\lambda \alpha_i - \alpha_i^2 - 0,2\lambda_i^2), \quad C'_i = 0,4 \frac{p_i}{\lambda_i} \end{aligned} \quad (9)$$

The problem will have been solved when the expression (8) reaches its minimum value, which can be accomplished by assigning adequate values to the coefficients c_i , obtained from the following equations:

$$\frac{B_i + 2C'_i c_i}{B'_i + 2C'_i c_i} = G. \quad (10)$$

For the solution of this system of equations, assign values G_o for G (neither larger than A/A' nor larger than the smaller of the quotients C_i/C'_i) and determine the corresponding c_i values¹:

$$c_i = \frac{1}{2} \frac{B'_i G_o - B_i}{C_i - C'_i G_o}; \quad (11)$$

the substitution of these c_i values in (3) will lead to the corresponding G values. If they do not match with the assumed G_o values, the process should be repeated by assigning another value to G_o (equal, for instance, to the preceding value of G , but never greater than any of the mentioned limiting values A/A' and C_i/C'_i), until $G_o = G$. Usually a few trials will suffice (the plotting of curves $G = f(G_o)$ and their intersection with the line $G = G_o$ will aid in reducing the number of trials).

¹ The limit A/A' results from all c_i values equal to zero, which would be the solution of the problem if the beams had no effect on the buckling load. The limit C_i/C'_i , which is a minimum for a certain value $i = i_o$, corresponds to $c_{i_o} = \infty$ meaning isolated buckling of the columns of the floor i_o . In this case the buckling load should be given by Euler's formula; however the value will be smaller, since the idea is to remain on the safe side by using the reduction coefficient 0,9 while calculating the deformation energy (refer to the last observation of item *Deflection Curve*).

The problem will have been solved when the value of G has been found, since the critical load is equal to:

$$P_o = G \frac{EJ_o}{l_o^2} \quad (12)$$

The precision will be shown by comparing results already known with the ones obtained using the method being presented.

1st Example

The extreme case of a structure with beams with zero rigidity will be presented in this example. Therefore the column is isolated and subjected to a concentrated load at the top end of each of the two portions, each with its own cross section. Three cases with different dimensions will be considered (Fig. 2).

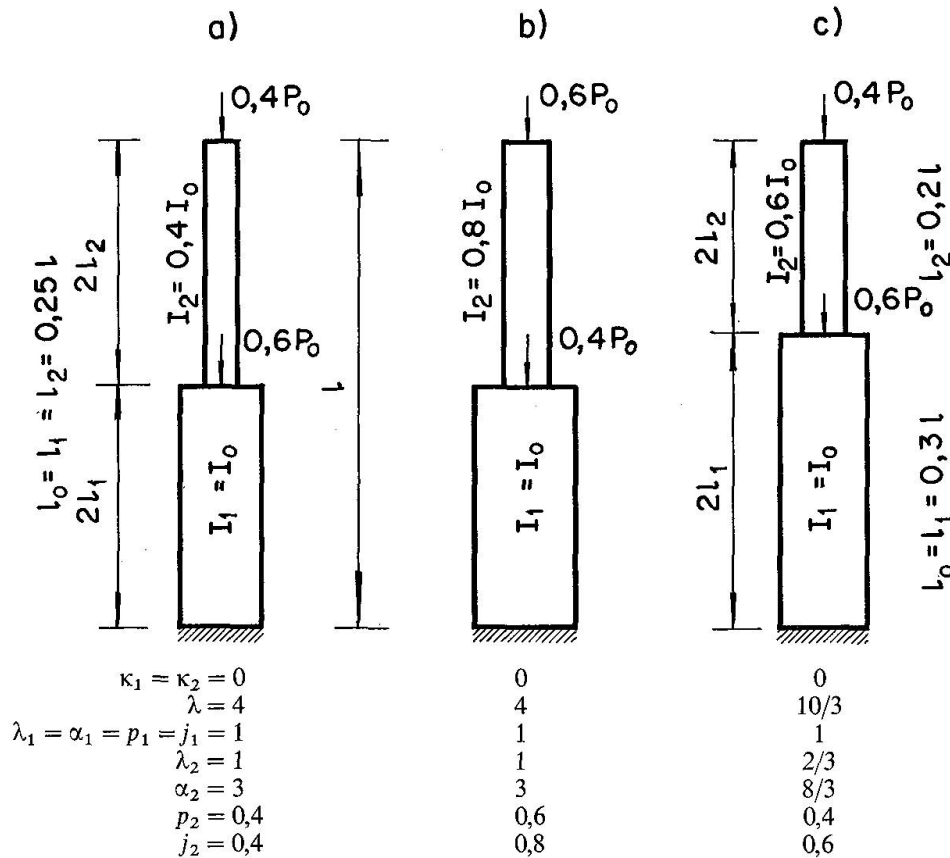


Fig. 2.

In the first case, $A/A' = 0.2757$, $C_1/C'_1 = 1$, $C_2/C'_2 = 1$. Assigning the smaller of these values (0.275) to G_o , from (11), $c_1 = 0.0507$ and $c_2 = 1.645$, resulting $G = 0.269$ if we replace these values in (3). Repeating the process, starting with $G_o = 0.269$, will lead to $c_1 = 0.081$, $c_2 = 1.575$, $G = 0.269$. This value replaced in (11) yields the final answer:

$$a) P_o = 0.269 \frac{EJ_o}{l_o^2}$$

The exact answer [5] is $G = 0,253$, i.e., 6% smaller. For the other two cases the discrepancy is much smaller, the results being obtained in a similar manner:

- b) $G = 0,222$ (instead of [5]: 0,221)
- c) $G = 0,367$ (instead of [5]: 0,366).

2nd Example

Three different story heights and two columns, as shown in Fig. 3. $A/A' = 46,13$ and the smallest value C_i/C'_i , for $i = 1$, equals 18,75. Assuming G_o equal to 18 and then 17, $G = G_o$ for the latter, thus the answer is $G = 17$. Other authors found, for the same problems, the values 16,84 [3] and 16,93 [4]. The latter one shows also the buckling mode, i.e., the relative floor displacements under the buckling load: 1, 0,924 and 0,621, respectively at the top, 3rd and 2nd floor level.

The buckling mode can also be determined by using formulas presented herein. With $G = 17$, $c_1 = 45,43$, $c_2 = 6,45$ and $c_3 = 3,65$; correspondingly:

$$\begin{aligned} \frac{e_1}{l_o} &= 4c_1 = 181,7, & \frac{e_2}{l_o} &= \frac{e_1}{l_o} + 4c_2 = 207,5 \\ & & \frac{e_3}{l_o} - \frac{e_2}{l_o} + 4c_3 &= 222,1 \end{aligned}$$

and also the respective Y values (5):

$$\begin{aligned} \frac{Y_1}{l_o} &= \frac{240^2}{150^3} (3 \times 570 - 240) = 25,1 \\ \frac{Y_2}{l_o} &= \frac{420^2}{150^3} (3 \times 570 - 420) = 67,4 \\ \frac{Y_3}{l_o} &= \frac{570^2}{150^3} (3 \times 570 - 570) = 109,7 \end{aligned}$$

with $(Y_3 + e_3)/l_o = y_3^*/l_o = 331,8$, and the relative values:

$$\frac{y_3^*}{y_3^*} = 1 \qquad \frac{y_2^*}{y_3^*} = 0,829 \qquad \frac{y_1^*}{y_3^*} = 0,623.$$

3rd Example

Five stories equally high, $h = 2l_o$ each, one single load applied at the top, girders on both sides, and $(l_v I_o)/(l_o I_v) = 3$:

$$\begin{array}{ccccc} \lambda_i = 1, & \alpha_1 = 2i - 1, & \lambda = 10, & p_i = 1, & j_i = 1 \\ c_1 = 13,7 & c_2 = 40,3 & c_3 = 60,2 & c_4 = 73,5 & c_5 = 80,1. \end{array}$$

Therefore:

$$P_o = 0,80 EJ_o/l_o^2 \text{ since } G = 0,798 \text{ (exact value [2]: 0,77).}$$

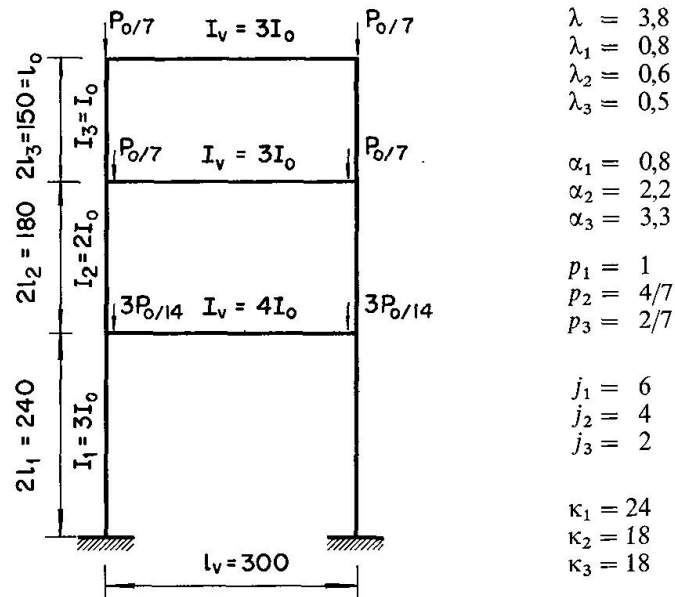


Fig. 3.

4th Example

Five stories and three different columns, see Fig. 4. Proceeding as in the previous examples:

$c_1 = 186,7$, $c_2 = 39,6$, $c_3 = 29,1$, $c_4 = 36,6$, $c_5 = 11,0$,
 $G = 30,5$ (as compared to 28,7 in [6], 30,3 in [3] and 31,4 in [4]).

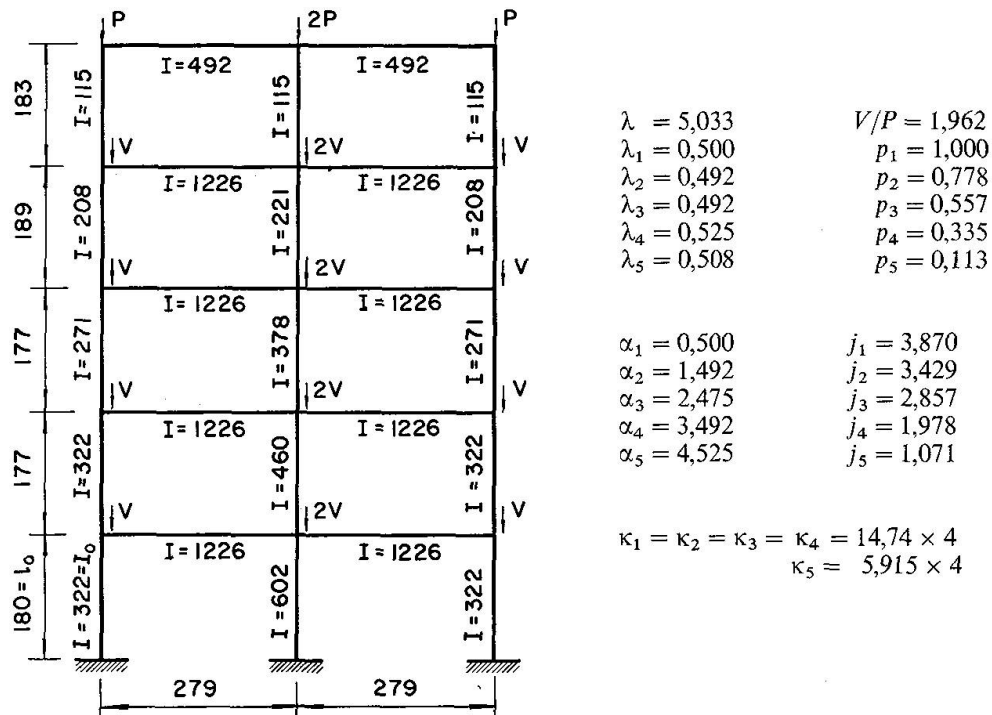


Fig. 4.

5th Example

This example considers the less common case of the upper beam being more rigid than the others; therefore, assume $K = 1,5$ in (5), which corresponds to substituting λ by $K\lambda/3 = 0,5\lambda$ in (9). Using again the example shown in Fig. 3, and changing the value of I_v of the upper beam from $3I_o$ to $20I_o$, among the values shown on Fig. 3 only κ_3 changes from 18 to 120 (besides the substitution of $\lambda = 3,8$ by $0,5\lambda = 1,9$ in the formulas).

The result thus obtained $G = 15,1$ is 10,3% smaller than the exact one.

Notations

The stories are numbered 1 through m , starting from below; therefore the properties related to the portion of the column between the foundation and the first floor shall be identified by the subscript 1, and so forth. The properties related to the joints (column-girder intersection) shall have the same subscript of the adjacent column below. The notation is as follows (Fig. 1):

$$A = \sum A_i, \quad B = \sum B_i c_i, \quad C = \sum C_i c_i^2 \quad (1)$$

$$A' = \sum A'_i, \quad B' = \sum B'_i c_i, \quad C' = \sum C'_i c_i^2 \quad (2)$$

$A_i, B_i, C_i, A'_i, B'_i, C'_i$ = values defined in (9).

a_i distance from the lower end to the center of segment i of the column.

c_i coefficient, to be determined, representing the relative sidesway magnitude at the various floors.

E modulus of elasticity of the material.

e_i displacement of joint i in the structure with rigid girders.

$$G = (A + B + C)/(A' + B' + C') \quad (3)$$

$$I_i^* = \int_{a_i - l_i}^{a_i + l_i} y^2 dx, \quad I_i^{**} = \int_{a_i - l_i}^{a_i + l_i} y_i'^2 dx.$$

i subscript referring to the generic column portion between two floors.

I_v moment of inertia of beam cross section.

I_i summation of the moments of inertia of the cross sections of the portions i of the columns.

I_o moment of inertia of a section used as reference.

j_i I_i/I_o .

K parameter.

k_i coefficient characterizing the rigidity of the joints i ($k_i = M_i/\theta_i$)¹.

$\sum k_i$ summation of all k_i with the same subscript i .

¹ For instance, at a joint with only one girder (end columns) of length l_v and constant cross section with moment of inertia I_v , $k_i = 6EI_v/l_v$; should two girders be present, the summation of the corresponding $6EI_v/l_v$ yields the value of k_i .

l	total column length.
l_i	length of the portion i of the column, divided by 2.
l_o	reference length.
l_v	length of girder.
M_i	moments at the supports of the girders, at the joints i .
P_i	summation of the loads applied above the joints i (including the ones applied at these joints).
P_o	total buckling load ($= P_1$), to be determined.
p_i	P_i/P .
x	distance of a section from the lower end of a column.
Y	portion of the horizontal displacement of the column (function of x), for the case of total absence of girders (Fig. 1 b).
Y_i	value of Y at the joint i .
y_i	horizontal displacement of the column at x , in the segment i ($a_i - l_i < x < a_i + l_i$).
y_i^*	horizontal displacement of joint i .
α_i	a_i/l_o .
θ_i	$Y'_{a_i+l_i} =$ angular displacement at joint i .
κ_i	$(\sum k_i)l_o/EI_o$.
λ	l/l_o .
λ_i	l_i/l_o .

The derivatives in respect to x are indicated by an accent (y' , y'' , Y' , Y''). The values of these derivatives for particular values of x are identified by using these as subscripts (for instance, Y' for $x = a_1$ will be represented by Y'_{a_1}).

Remark concerning Economy

The method proposed in the present article for calculating the buckling load of the structure permits to obtain it with a sufficient approximation and in a much simpler and economical manner than by the general method.

Therefore, without spending a great deal of his time and of the computer, the proposed method will yield the Structural Engineer a fairly accurate solution of the problem.

References

1. LANGENDONCK, T. van: Pilares de edificios de vários andares. La Ingenieria, Buenos Aires, Dec. 1969, p. 152.
2. BLEICH, Friedrich: Buckling Strength of Metal Structures. Mc Graw-Hill, 1952.
3. MC MINN, S.J.: Matrices for Structural Analysis, John Wiley, New York, 1962.
4. FIGUEIREDO, R.G.: Sobre a instabilidade elástica de pórticos tridimensionais de edificios. Esc. Eng. de São Carlos, 1972.
5. LANGENDONCK, T. van: Eine Numerische Lösung des Knickproblems. I.A.B.S.E., Publications, XIV, 1954, p. 111.
6. BOWLES, R.E., and MERCHANT, W.: Critical Load of Tall Building Frames. The Structural Engineer, June, 1958, p. 187.

Summary

The Author proposes a simplified method for the determination of the critical load of orthogonal building structures, assuming plane buckling. The method presented, although much easier to apply than most of the exacting ones — which require the use of large computers — is sufficiently accurate.

Résumé

L'auteur propose une méthode simplifiée pour la détermination de la charge critique aux structures orthogonales, en assumant le voilement en plaine. La méthode présentée, bien que plus facilement applicable que la plupart des méthodes exactes qui demandent l'application de grands ordinateurs, s'avère suffisamment exacte.

Zusammenfassung

Der Verfasser schlägt eine vereinfachte Methode zur Bestimmung der kritischen Last an rechteckigen Tragwerken unter Annahme der Beulung in einer Ebene vor. Die vorgelegte Methode, obschon weit leichter anwendbar als die meisten genauen Verfahren, welche die Verwendung grosser Computer erfordern, erweist sich als hinreichend genau.

The Analysis of Thin, Thick and Sandwich plates by the Finite Strip Method

Analyse de plaques minces, épaisses et sandwich par la méthode des bandes finies

Berechnung dünner, dicker und Sandwichplatten mittels der finiten Streifenmethode

A. S. MAWENYA

University of Dar-es-Salaam, P.O. Box 35131, Dar-es-Salaam, Tanzania.

Introduction

The use of the finite strip method for analysing elastic plates is well established [1–3]. The method, which is similar in principle to the finite element technique, assumes the plate to be an assemblage of narrow longitudinal strips and defines the displacement field in terms of one-way slab functions across the width of the strip and basic series function in the longitudinal direction.

Previous formulations of the finite strip method for the analysis of plate bending have invariably used slab functions which constrain the plate to obey the Kirchhoff's normality hypothesis. Consequently, no allowance is made for the effects of transverse shear deformations. In thick and sandwich plate situations the influence of transverse shear on the deformations and stresses is quite significant and cannot be neglected in the analysis.

In this paper finite strip formulations are presented for the elastic analysis of rectangular and curved plates with opposite simply supported ends. The formulations involve transverse shear deformation which is included in the analysis by discarding the Kirchhoff's normality hypothesis and specifying independently the transverse displacement and normal rotations of the plate.

Finite Strip Formulation of Rectangular Plates

A detailed description of the ingredients required for the implementation of the finite strip method in the analysis of plate bending has been given by Cheung [1]. The essential steps involved in deriving the stiffness and load matrices of a rectangular finite strip in which the effects of transverse shear deformation are considered, are now given.

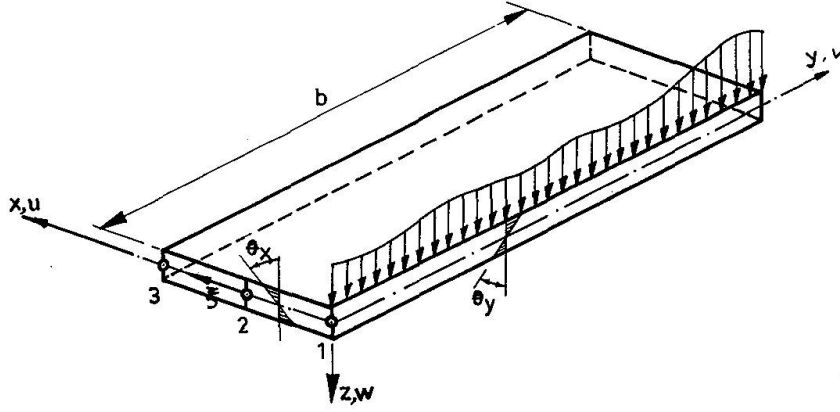


Fig. 1. Rectangular finite strip.

Figure 1 shows a typical finite strip with three nodal lines. The deformation of the plate is defined in terms of the transverse displacement w , and the rotations θ_x and θ_y of the normal to the reference xy -plane. The variables w , θ_x and θ_y are independently specified so that plate normals are not constrained to remain normal during deformation as in the classical thin plate theory. This permits the plate to experience transverse shear deformations although the transverse cross-sections of the plate do not warp out of their plane during deformation.

The displacement vector at any point (x, y, z) of a simply supported strip can then be written in series form as [4]

$$\begin{aligned} u &= -z \sum_{l=1}^{\infty} \sum_{i=1}^n N_i \theta_{xi}^l \sin \frac{l\pi y}{b} \\ v &= -z \sum_{l=1}^{\infty} \sum_{i=1}^n N_i \theta_{yi}^l \cos \frac{l\pi y}{b} \\ w &= \sum_{l=1}^{\infty} \sum_{i=1}^n N_i w_i^l \sin \frac{l\pi y}{b} \end{aligned} \quad (1)$$

where n denotes the number of nodal lines per strip; and the vector of the nodal-line displacement amplitudes is prescribed for the l^{th} harmonic as

$$\{\delta_i^l\} = \{w_i^l, \theta_{xi}^l, \theta_{yi}^l\}^T \quad (2)$$

The shape functions N_i are simple Lagrangian interpolation functions corresponding to those of an n -noded beam element. In this paper only parabolic shape functions will be considered for which

$$n = 3, N_1 = -\frac{1}{2}s(1-s), N_2 = 1-s^2 \text{ and } N_3 = \frac{1}{2}s(1+s) \quad (3)$$

At $y = 0$ or $y = b$ we shall always have

$$w = u = \frac{\delta v}{\delta y} = 0$$

which corresponds to simply supported boundary conditions.

For orthotropic situations the constitutive relation is given by

$$\begin{Bmatrix} M_x \\ M_y \\ M_{xy} \\ Q_x \\ Q_y \end{Bmatrix} = \begin{bmatrix} D_x & D_1 & 0 & 0 & 0 \\ D_1 & D_y & 0 & 0 & 0 \\ 0 & 0 & D_{xy} & 0 & 0 \\ 0 & 0 & 0 & S_x & 0 \\ 0 & 0 & 0 & 0 & S_y \end{bmatrix} \begin{Bmatrix} -\frac{\delta\theta_x}{\delta x} \\ -\frac{\delta\theta_y}{\delta y} \\ -\left(\frac{\delta\theta_x}{\delta y} + \frac{\delta\theta_y}{\delta x}\right) \\ \frac{\delta w}{\delta x} - \theta_x \\ \frac{\delta w}{\delta y} - \theta_y \end{Bmatrix}$$

$$\text{or } \{M\} = [D] \sum_{l=1}^{\infty} \sum_{i=1}^n [B_i^l] \{\delta_i^l\} = [D] \sum_{l=1}^{\infty} [B^l] [\delta^l] = [D] [B] \{\delta\} \quad (5b)$$

where the strain submatrix $[B_i^l]$ is given by

$$[B_i^l] = [\bar{B}_i^l] \sin \frac{l\pi y}{b} + [\bar{\bar{B}}_i^l] \cos \frac{l\pi y}{b} \quad (6a)$$

$$\text{with } [\bar{B}_i^l] = \begin{bmatrix} 0 & -\frac{\delta N_i}{\delta x} & 0 \\ 0 & 0 & \frac{l\pi}{b} N_i \\ 0 & 0 & 0 \\ \frac{\delta N_i}{\delta x} & -N_i & 0 \\ 0 & 0 & 0 \end{bmatrix} \quad (6b)$$

$$\text{and } [\bar{\bar{B}}_i^l] = \begin{bmatrix} 0 & 0 & 0 \\ 0 & 0 & 0 \\ 0 & \frac{l\pi}{b} N_i & -\frac{\delta N_i}{\delta x} \\ 0 & 0 & 0 \\ \frac{l\pi}{b} N_i & 0 & -N_i \end{bmatrix} \quad (6c)$$

With the strain and property matrices known, the stiffness matrix of the strip can be calculated from the well known relationship [5]

$$[k] = \int [B]^T [D] [B] dx dy \quad (7a)$$

in which a typical submatrix of $[k]$ linking harmonics l and m is given by

$$[k^{lm}] = \int [B^l]^T [D] [B^m] dx dy \quad (7b)$$

The integration is carried out over the area of the strip. It is done explicitly in the longitudinal direction but it might be necessary to perform it numerically across the width of the strip. In the examples presented a 2-point Gaussian integration rule has been used for this purpose. It will be noted, however, that for the exact integration of equations (7) a 3-point Gaussian rule is needed; but in accordance with the recommendations of reference [4], a lower 2-point rule has been adopted in order to improve the strip performance and to eliminate the spurious shear effects inherent in this type of formulation. Numerical integration also facilitates the treatment of variable thickness [4].

The loading on the plate must be resolved into basic series function in the longitudinal direction. For instance, a distributed transverse loading of intensity q can be expressed in a series form as

$$q = \sum_{l=1}^{\infty} q^l \sin \frac{l\pi y}{b} \quad (8)$$

The consistent load vector corresponding to this loading can be obtained from the virtual work principle [5] as

$$\{F^l\} = - \int [N_1, 0, 0, N_2, 0, 0, \dots]^T q^l \sin^2 \frac{l\pi y}{b} dx dy \quad (9)$$

for the l^{th} harmonic.

Extension to Curved Plate Situations

The formulation can easily be extended to deal with curved strips generated by sweeping the section along a circular arc as shown in Figure 2.

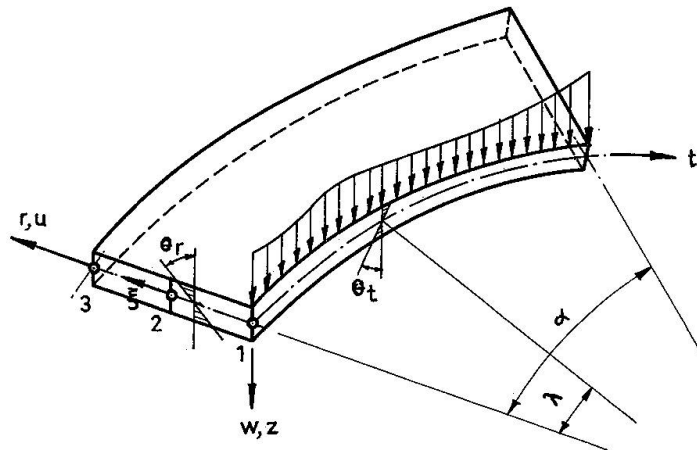


Fig. 2. Curved finite strip.

The variable co-ordinate y is replaced by an angle λ and the span b by an angle α , and the displacements are described by equation (1) now interpreted in polar co-ordinates as follows:

$$\begin{aligned} u &= -z \sum_{l=1}^{\infty} \sum_{i=1}^n N_i \theta_{ri}^l \sin \frac{l\pi\lambda}{\alpha} \\ v &= -z \sum_{l=1}^{\infty} \sum_{i=1}^n N_i \theta_{ti}^l \cos \frac{l\pi\lambda}{\alpha} \\ w &= \sum_{l=1}^{\infty} \sum_{i=1}^n N_i w_i^l \sin \frac{l\pi\lambda}{\alpha} \end{aligned} \quad (10)$$

The constitutive relationship has also to be changed into polar co-ordinates, and for orthotropic situations it becomes

$$\begin{Bmatrix} M_r \\ M_t \\ M_{rt} \\ Q_r \\ Q_t \end{Bmatrix} = \begin{bmatrix} D_r & D_1 & 0 & 0 & 0 \\ D_1 & D_t & 0 & 0 & 0 \\ 0 & 0 & D_{rt} & 0 & 0 \\ 0 & 0 & 0 & S_r & 0 \\ 0 & 0 & 0 & 0 & S_t \end{bmatrix} \begin{Bmatrix} -\frac{\delta\theta_r}{\delta r} \\ -\frac{1}{r} \left(\theta_r - \frac{\delta\theta_t}{\delta\lambda} \right) \\ -\frac{1}{r} \left(\frac{\delta\theta_r}{\delta\lambda} + r \frac{\delta\theta_t}{\delta r} - \theta_t \right) \\ \frac{\delta w}{\delta r} - \theta_r \\ \frac{1}{r} \frac{\delta w}{\delta\lambda} - \theta_t \end{Bmatrix} \quad (11)$$

The strain submatrices $[\bar{B}_i^l]$ and $[\bar{B}_i^t]$ therefore become

$$[\bar{B}_i^l] = \begin{bmatrix} 0 & -\frac{\delta N_i}{\delta r} & 0 \\ 0 & -\frac{N_i}{r} & \frac{l\pi}{r\alpha} N_i \\ 0 & 0 & 0 \\ \frac{\delta N_i}{\delta r} & -N_i & 0 \\ 0 & 0 & 0 \end{bmatrix} \quad (12a)$$

and

$$[\bar{B}_i^t] = \begin{bmatrix} 0 & 0 & 0 \\ 0 & 0 & 0 \\ 0 & -\frac{l\pi}{r\alpha} N_i & -\frac{\delta N_i}{\delta r} + \frac{N_i}{r} \\ 0 & 0 & 0 \\ \frac{l\pi}{r\alpha} N_i & 0 & -N_i \end{bmatrix} \quad (12b)$$

Numerical Examples

In order to verify the accuracy of the formulation, a uniformly loaded simply supported square sandwich plate having flexural and shear rigidities of D and $\frac{100D}{a^2}$, respectively, is first considered. Because of symmetry only a half of the plate divided into one, two and three strips is analysed, with the strips running parallel to the y -axis. Results of the maximum deflections, shearing forces, bending and twisting moments are given in Table 1, for various numbers of strips at different harmonic terms. It can be seen that the results converge rapidly as both the number of strips and the harmonic terms increase. The solution obtained using 3 strips with 4 harmonics agrees closely with that given by PLANTEMA [6].

Table 2 shows a convergence study involving a thin, isotropic, simply supported square plate also analysed using one, two and three longitudinal strips.

Table 3 shows a study of a uniformly loaded, orthotropic, simply supported square plate analysed using two strips in a symmetric half of the plate with four harmonic terms. Two cases of orthotropy were considered with the stiffness rigidities given in Table 3.

Table 1. Maximum deflection, moments and shearing forces for a square simply supported sandwich plate under uniform loading.

No. of strips	No. of harmonics	Central deflection w_{\max}	Central bending moments		Twisting moment $(M_{xy})_{\max}$	Shearing forces at mid-edges	
			$(M_x)_{\max}$	$(M_y)_{\max}$		$(Q_x)_{\max}$	$(Q_y)_{\max}$
1	1	0.00495	0.0577	0.0549	0.0319	0.487	0.242
	2	.00486	.0562	.0503	.0336	.460	.278
	3	.00487	.0564	.0512	.0339	.468	.287
	4	.00487	.0563	.0509	.0341	.464	.291
2	1	0.00489	0.0502	0.0520	0.0309	0.425	0.244
	2	.00479	.0487	.0475	.0326	.387	.288
	3	.00481	.0491	.0485	.0329	.398	.304
	4	.00480	.0489	.0481	.0331	.393	.312
3	1	0.00489	0.0496	0.0518	0.0305	0.401	0.244
	2	.00479	.0481	.0473	.0322	.359	.288
	3	.00480	.0484	.0483	.0326	.373	.304
	4	.00480	.0483	.0479	.0327	.367	.312
Exact solution [6]		0.00480	0.0479		0.0325	0.338	
Multiplier		$\frac{qa^4}{D}$	qa^2		qa^2	qa	

Table 2. Central deflection, moments and edge shears for an isotropic, square, simply supported thin plate under uniform loading

($\mu = 0.3$, $\frac{h}{a} = 0.01$, total number of harmonics terms = 4)

No. of strips	Central deflection w_{\max}	Central bending moments		Shearing forces at mid-edges	
		$(M_x)_{\max}$	$(M_y)_{\max}$	$(Q_x)_{\max}^1$	$(Q_y)_{\max}$
1	0.00415	0.0563	0.0509	0.315	0.291
2	0.00407	0.0489	0.0481	0.328	0.312
3	0.00407	0.0482	0.0479	0.332	0.312
Thin plate solution [1]	0.00406	0.0479		0.338	
Multiplier	$\frac{qa^4}{D}$	qa^2		qa	

¹ Values interpolated from those obtained at the integration points.

Table 3. Central deflection and moments for an orthotropic, square, simply supported plate under uniform loading.

Source	Central deflection w_{\max}		$(M_x)_{\max}$		$(M_y)_{\max}$	
	A	B	A	B	A	B
Present solution	0.00153	0.000633	0.0178	0.00812	0.0774	0.0991
Ref. [1]	0.00153	0.000633	0.177	0.00833	0.0777	0.0995
Exact solution [7]	0.00152	0.000633	0.178	0.00838	0.774	0.0993
Multiplier	$\frac{qa^4}{D_x}$		qa^2		qa^2	

Elastic properties

Case A: $D_y = 5.0625D_x$, $D_1 = 0.375D_x$, $D_{xy} = 0.9375D_x$, $S_x = S_y = \infty$.

Case B: $D_y = 16D_x$, $D_1 = \frac{2}{3}D_x$, $D_{xy} = \frac{5}{3}D_x$, $S_x = S_y = \infty$.

Conclusion

Finite strip formulations which involve transverse shear deformation have been presented for the elastic analysis of rectangular and curved plates. The examples presented demonstrate the accuracy and versatility of the formulation.

Nomenclature

a, b	width and length of rectangular plate.
D	flexural rigidity of isotropic plate.
D_x, D_y, D_{xy} D_r, D_t, D_{rt}	} plate rigidities in flexure and torsion.
h	plate thickness.
M_x, M_y, M_{xy} M_r, M_t, M_{rt}	} bending and twisting moments.
q	distributed transverse loading.
Q_x, Q_y Q_r, Q_t	} transverse shearing forces.
r, t	radial and tangential directions, respectively, of curved strip.
s	local natural dimensionless co-ordinate.
S_x, S_y S_r, S_t	} transverse shear rigidities of an orthotropic plate.
u, v, w	components of displacement parallel to the x -, y - and z - axes respectively.
x, y, z	rectangular co-ordinates.
α	angle subtended by curved plate.
θ_x, θ_y θ_r, θ_t	} normal rotations of plate cross-section.
λ	angular co-ordinate.
ν	Poisson's ratio of isotropic material.
$\{F\}$	nodal force vector.
$\{M\}$	stress resultants vector.
$\{\delta\}$	displacement vector.
$[B]$	matrix connecting strains and displacements of a strip.
$[D]$	property matrix.
$[k]$	stiffness matrix of strip.
$[N]$	$[N_1, N_2, N_3, \dots]$ shape function matrix.

Practical Application and Scope

The formulations presented in this paper extend the finite strip method to the analysis of plate structures which undergo considerable transverse shear deformation and cannot therefore be treated by the conventional finite strip approach [1, 2] which is based on customary thin plate theory. Examples of such structures occur frequently in bridge construction. They include sandwich plates and slabs bridges with relatively high depth to span ratio, as well as voided slabs and multicell bridge decks that can be idealized by an equivalent homogeneous material. These structures are being used in increasing numbers in modern highway systems and the application of the finite strip technique to their analysis is of particular interest.

The formulations presented are such that their accuracy is superior to the conventional finite strip and are likely to be adopted as standard in the analysis of straight and curved bridge decks. However, in order to derive their full benefits, care must be taken in programming so as to utilize all possible short cuts and reduce computing time. Reference 4 discusses some useful short cuts that can be achieved in the practical implementation of simply supported finite strips.

Although the present formulation is restricted to simply supported end conditions, Fourier transforms corresponding to a variety of other boundary conditions could be adopted. Also the treatment of intermediate supports follows well established procedures which could be readily incorporated into the formulation.

References

1. Y.K. CHEUNG: The Finite Strip Method in the Analysis of Elastic Plates with Opposite Simply Supported Ends. *Proc. Inst. Civ. Engrs.*, 40, pp. 1-7, 1968.
2. Y.C. LOO and A.R. CUSENS: A Refined Finite Strip Method for the Analysis of Orthotropic Plates. *Proc. Inst. Civ. Engrs.*, 48, pp. 85-91, 1971.
3. Y.K. CHEUNG and M.S. CHEUNG: Static and Dynamic Behaviour of Rectangular Plates using Higher Order Finite Strips. *Building Science*, 7, pp. 151-158, 1972.
4. A.S. MAWENYA: Finite Element Analysis of Sandwich Plate Structures. Ph. D. thesis, University of Wales, Swansea, 1973.
5. O.C. ZIENKIEWICZ: The Finite Element Method in Engineering Science. 2nd Edition, McGraw-Hill, 1971.
6. F.J. PLANTEMA: Sandwich Construction: The Bending and Buckling of Sandwich Beams, Plates and Shells. John Wiley, 1966.
7. S. TIMOSHENKO and S. WOINOWSKY-KRIEGER: Theory of Plates and Shells. 2nd Edition, McGraw-Hill, 1959.

Summary

Finite strip formulations are developed for the elastic analysis of transversely loaded rectangular and curved plates with opposite simply supported ends. The formulations involve transverse shear deformation which is included in the analysis by discarding the Kirchhoff's normality law used in classical thin plate theory. Numerical examples are presented which demonstrate the applicability of the formulation to thin, thick and sandwich plates.

Résumé

Des formulations par bandes finies sont développées pour l'analyse élastique de plaques rectangulaires et courbes chargées transversalement et supportées aux extrémités. Les formulations comprennent le cisaillement transversal qui est compris

dans le calcul en laissant la loi de Kirchhoff de côté telle qu'elle est appliquée dans la théorie classique des plaques minces. Des exemples numériques sont présentés, montrant le champ d'application de la formulation sur des plaques minces, épaisses et sandwich.

Zusammenfassung

Für die elastische Berechnung transversal belasteter rechteckiger und gekrümmter Platten mit entgegengesetzten einfach aufgelagerten Enden werden finite Streifenformulierungen entwickelt. Die Formulierungen schliessen transversale Schubdeformation ein, die in der Berechnung unter Ausserachtlassung des Kirchhoff'schen Normalitätsgesetzes inbegriffen ist, wie dies in der klassischen Theorie dünner Platten verwendet wird. Es werden numerische Beispiele angeführt, welche die Verwendbarkeit der Formulierung für dünne, dicke und Sandwichplatten belegen.

Hybrid Yield-Line Finite Element Analysis

Une analyse hybride des lignes de rupture moyennant la méthode des éléments finis

Eine hybride Bruchlinien-Analyse mittels der finiten Elementenmethode

A.T. RACTLIFFE

Department of Naval Architecture and Shipbuilding, University of Newcastle Upon Tyne

Introduction

Plastic yield-line analysis has proved a powerful tool in the limit design of concrete slabs under lateral loading. However it is of less value in the design of steel plates because their generally more slender proportions induce membrane stresses. These increase the load necessary to cause a given deflection and in many cases the limiting load may be considerably greater than that estimated from plastic bending alone. Thus yield-line design would be wasteful of material.

Rigorous large deflection elasto-plastic analysis is time-consuming and inconvenient. CLARKSON [1] and later YOUNG [2] described simplified approaches but these only consider infinitely long plates. Empirical formulae have been proposed [3] for plates of finite aspect ratio. These usually employ the concept of a limiting lateral load associated with a maximum allowable permanent set. JAEGER [4] developed an approximate method of analysis which involves estimating the strength of an equivalent infinitely long plate whose thickness is given by a conversion factor. HOOKE [5] presented the first genuinely two-dimensional approximate analysis and published charts from which load-deflection curves may be obtained. A rigid-plastic method has been developed by JONES [8] but in this as in all previous theoretical work except Young's the plate edges are considered to be completely restrained from in-plane movement or pull-in. Moreover, the effect of in-plane loading has not been considered.

These deficiencies are remedied by the present paper which describes a completely new method. In this, the lateral load is estimated as the sum of a first component due to plastic bending action alone calculated by orthodox yield-line analysis, plus a second component due to the membrane stresses in each of the elements bounded by the yield-lines. These elements are assumed to remain flat so that all bending is confined to the hinges. The plane stress is assumed to be uniform in each element and virtual work or strain energy principles used to analyse the plate.

Beam with End Restraint

The principle of the method is most easily explained in terms of a simple example which is relatively trivial, a rectangular beam of unit width, depth t , length b , whose ends are clamped and restrained from inward movement. Under a uniform lateral load of p_1 per unit area, simple plastic theory shows that

$$p_1 = \frac{16 M_p}{b^2}$$

where M_p is the full plastic moment, which may be modified by the presence of axial stress. Assuming that the two halves of the beam remain straight, the extension in each is δ^2/b , (see Fig. 1). This causes a tension of $2tE\delta^2/b^2$. By virtual work

$$\frac{1}{2}p_2b = \frac{2tE\delta^2}{b^2} \cdot 2 \cdot \frac{2\delta}{b}$$

i.e.

$$p_2 = \frac{16Et\delta^3}{b^4}$$

The essence of the author's proposal is that the limiting load is given by the sum of p_1 and p_2 where δ is some arbitrary standard of acceptable deflection. Clearly δ doesn't represent the actual deflection since elastic bending is ignored in the analysis. It does however give some indication of the amount of plastic bending. Its principal virtue, whatever value is actually used as a design limit, is that it provides a consistent criterion of performance for the gamut of design parameters. (The Perry-Robertson method of strut design adopts a similar heuristic approach in its treatment of initial imperfections). When we consider the limiting deflection in a plate, representation at one point is inadequate owing to the variety possible in the shape of the failure mechanism. A more significant parameter is the root of the mean square deflection denoted by $\bar{\delta}$. Using this parameter, p_2 for a beam becomes

$$p_2 = \frac{83 Et\bar{\delta}^3}{b^4} \text{ since } \bar{\delta} = \delta/\sqrt{3}$$

A reasonable value for $\bar{\delta}$ might be $b/100$.

Now the plastic moment is affected by the presence of any axial stress and is given by standard plastic theory as

$$M_p = \frac{1}{4} \sigma_Y t^2 \left[1 - \left(\frac{F_y}{\sigma_Y} \right)^2 \right] \text{ where } F_y = \frac{6 E \bar{\delta}^2}{b^2}$$

When the axial stress reaches the yield point, M_p vanishes. At the same time the membrane action becomes plastic, and assuming no work-hardening, further deflection causes a reduction in the effective modulus of elasticity so that

$$E' = \sigma_Y E / F_y$$

Replacing this reduced modulus in the expression for p_2 we have

$$p_2 = 13.8 \sigma_Y \bar{\delta} t / b^2$$

which represents the post-yield load curve when

$$\sigma_Y < 6 E (\bar{\delta} / b)^2$$

The deflected shape may not be very realistic for such an extreme condition, but the use of an RMS instead of mid-span deflection ought to improve correlation with measured data since RMS values are not so shape sensitive.

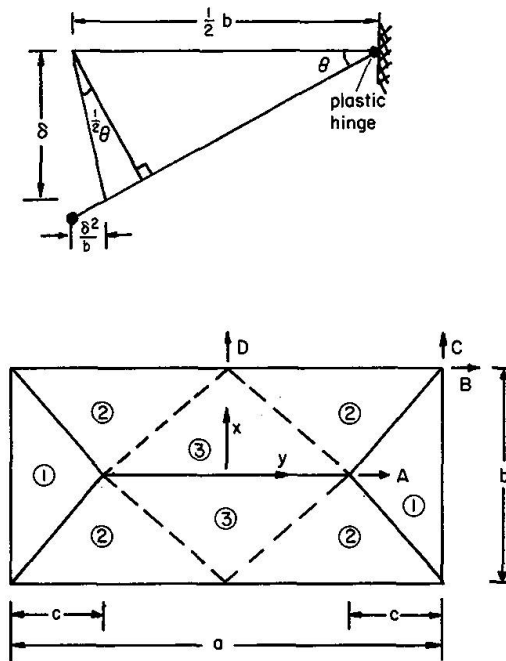


Fig. 1. Basic geometry.

The Rectangular Plate

The principle of analysis is exactly the same as for the beam but the calculation becomes more complex because membrane stresses are generated even when there is no external restraint on inward movement at the boundaries. The yield-line analysis giving p_1 uses the square Johansen yield envelope rather than the more realistic yield criteria of Tresca or von Mises. However it is considered that the loss of accuracy involved in this assumption is not sufficient to justify complicating a method, one of whose virtues is simplicity. The reader should see Ref. 6. for further discussion of the yield-line method.

The analysis of the membrane action starts by considering the finite elements formed by the pattern of hinge-lines. The full lines in Fig. 1 show a typical pitched roof mechanism. The discontinuous lines show a further division so that all elements are triangular. The in-plane displacements A , B , C and D represent the maximum number of degrees of freedom with free edges, bearing symmetry in mind. Assuming uniform strains in each element and taking into account the foreshortening due to deflection δ at the ridge line, the strains are

$$\begin{array}{lcl}
 \left. \begin{array}{l}
 \varepsilon_x = \frac{\delta^2}{2c^2} + \frac{B-A}{c} \\
 \varepsilon_y = \frac{2C}{b} \\
 \gamma_{xy} = 0
 \end{array} \right\} & & \text{in element 1} \\
 \\
 \left. \begin{array}{l}
 \varepsilon_x = \frac{2B}{a} \\
 \varepsilon_y = \frac{4cD}{ab} + \frac{4C(\frac{1}{2}a-c)}{ab} + \frac{2\delta^2}{b^2} \\
 \gamma_{xy} = \frac{4B(\frac{1}{2}a-c)}{ab} - \frac{2A}{b} + \frac{2(C-D)}{a}
 \end{array} \right\} & & \text{in element 2} \\
 \\
 \left. \begin{array}{l}
 \varepsilon_x = \frac{A}{\frac{1}{2}a-c} \\
 \varepsilon_y = \frac{2D}{b} + \frac{2\delta^2}{b^2} \\
 \gamma_{xy} = 0
 \end{array} \right\} & & \text{in element 3}
 \end{array}$$

These three equations enable the stresses to be calculated. The displacements A , B , C and D are evaluated by solving the simultaneous equations of virtual work associated with each degree of freedom. A fuller analysis is given in Appendix A. The virtual work associated with A is always zero since this point is always free. However, if there are in-plane stresses externally applied at the edges, these will contribute to the virtual work associated with B , C and D . Thus for each state of in-plane loading there will be a different solution to the four unknown displacements. In addition there are also various combinations of restraint on edge displacement. Thus if $C=D$, all edges are free to move but remain straight, reducing the number of simultaneous equations to three. If all edges are restrained against inward movement, B , C and D are all zero, a situation which might arise if the plate were heavily framed. The applied lateral load for a given value of δ can also be calculated by virtual work in terms of the displacements.

Solution for these displacements is straightforward and results have been computed for a large number of combinations of aspect ratios, boundary conditions, in-plane loading and proportions of finite elements (as defined by the parameter c in Fig. 1). These results were checked by hand calculation of some simple cases.

Yielding occurs in the membrane according to the von Mises criterion when the strain energy of distortion reaches a limit:

$$\sigma_x^2 - \sigma_x \sigma_y + \sigma_y^2 + 3 \tau_{xy}^2 = \sigma_Y^2$$

The three elements may not yield simultaneously, and for the sake of simplicity the mean strain energy of distortion is calculated for the whole plate in terms of A , B , C , D and δ . This provides a single parameter $\bar{\sigma}$, the so-called effective stress which can be compared with σ_Y . If $\bar{\sigma} > \sigma_Y$ then general yielding is established and E must be reduced by a factor $\sigma_Y/\bar{\sigma}$ in exactly the same way as already shown in the beam example.

Now the pattern of elements which gives rise to the lowest lateral load with respect to membrane action may not correspond with the pattern of plastic hinge-lines giving rise to the lowest load associated with the yield line mechanism. Thus in order to estimate the limit load, strictly we should find the value of c for which the sum $(p_1 + p_2)$ is a minimum. This is quite feasible, but tedious to the designer who wants rapid results. Fortunately, p_1 is not very sensitive to the value of c (see Fig. 2) and for the sake of simplicity, we can estimate the limit load as the sum of the minimum loads associated with plasticity and membrane action separately, i.e.

$$(p_1)_{\min} + (p_2)_{\min}$$

Even though the corresponding values of c may differ, the error in load will not be large and the strength will in any case be underestimated. The yield-line load $(p_1)_{\min}$ is obtained from Fig. 3. High in-plane stresses will modify the effective plastic moment in each direction and it may be desirable to evaluate p_1 for an appropriately affine isotropic plate as follows. If the plastic moment per unit length

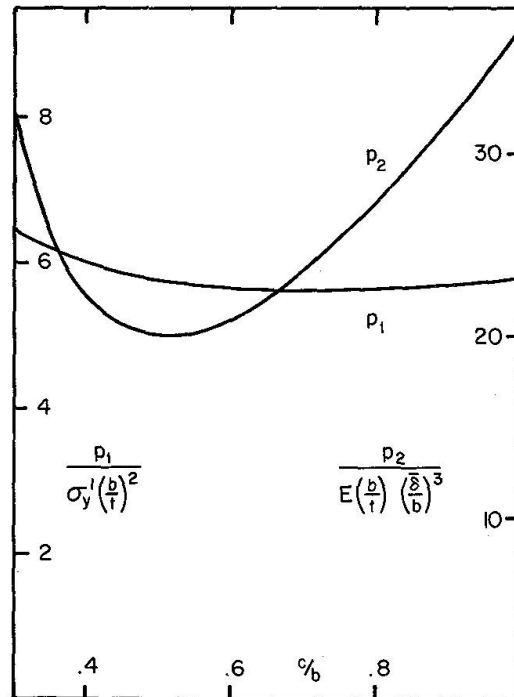


Fig. 2. Variation of p_1 and p_2 with c/b . $b/a = 0.3$, edges clamped and straight.

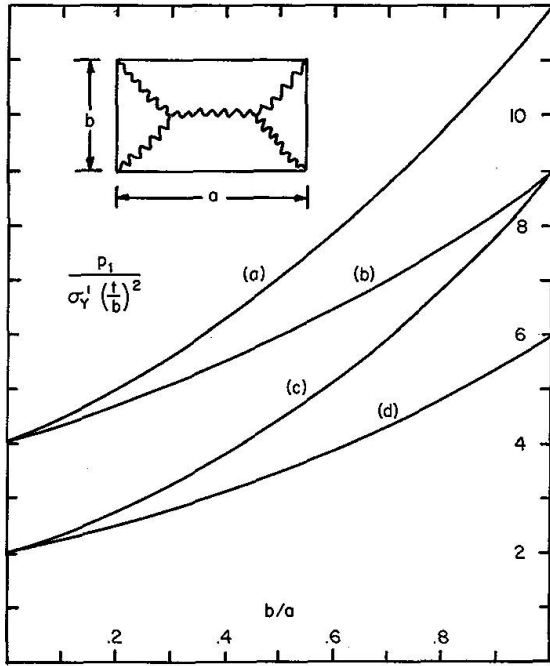


Fig. 3. p_1 given by yield-line analysis:

- (a) All edges restrained.
- (b) Long edges restrained, short edges straight.
- (c) All edges straight.
- (d) Long edges unrestrained, short edges straight.

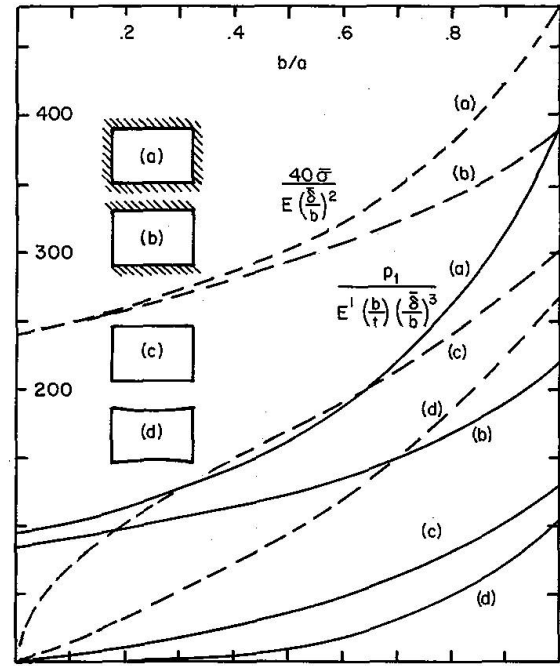


Fig. 4. p_2 (full line) and $\bar{\sigma}$ (discontinuous) due to membrane action. No in-plane loading.

- (a) All edges restrained.
- (b) Long edges restrained, short edges straight.
- (c) All edges straight.
- (d) Long edges unrestrained, short edges straight.

of plate (i.e. across the width) is M_p and that per unit width μM_p , then the so-called affine isotropic plate with M_p in both directions has a length $a/\sqrt{\mu}$. According to Johansen's Theorem, p_2 is the same for this plate as for the original one. It is shown in Appendix B that under the influence of in-plane loading and membrane action the plastic moment across the width is obtained by replacing

$$\sigma_Y \text{ by } \sigma_Y' = \frac{\sigma_Y^2 - \bar{\sigma}^2}{\sqrt{F_y^2 + \sigma_Y^2 - \bar{\sigma}^2}}$$

At the same time the aspect ratio b/a is factored by $\sqrt{\mu}$ i.e.

$$\frac{4\sqrt{F_y^2 + \sigma_Y^2 - \bar{\sigma}^2}}{\sqrt{F_x^2 + \sigma_Y^2 - \bar{\sigma}^2}}$$

Figs 4 to 7 summarise the values of $(p_2)_{\min}$ for membrane action. These have been non-dimensionalised and Poisson's ratio taken as 0.3. It is clear that for a given value of $\bar{\delta}/b$, the limiting lateral load increases under the influence of tensile in-plane forces (negative sign convention). Conversely the lateral strength is reduced by the application of compressive in-plane loading. A negative total lateral load implies instability and in such cases the in-plane loading is excessive and either it must be reduced, or the limiting value of $\bar{\delta}/b$ allowed to increase. General yielding is determined by the value of $\bar{\sigma}$ given in Figs. 4, 5 and 8. These curves were found to depend only on the type of boundary restraint and consequently it is possible to use the family of curves in Fig. 8 for any general in-plane loading.

Examples of the use of these diagrams are presented in Appendix C.

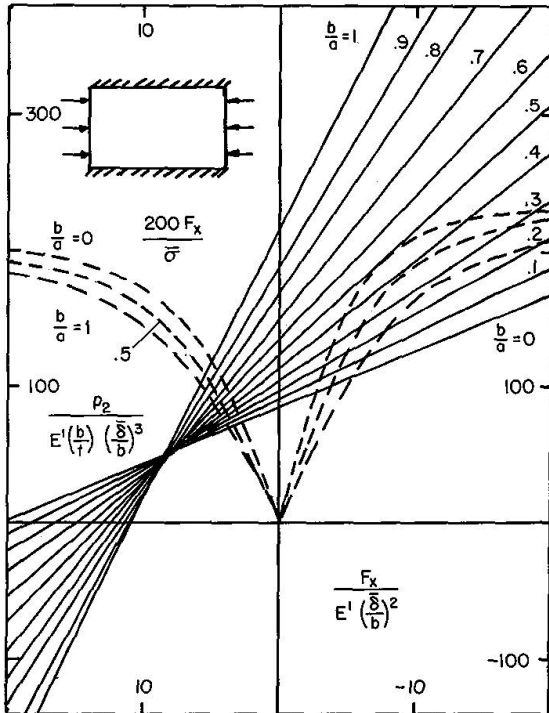


Fig. 5. p_2 (full line) and $\bar{\sigma}$ (discontinuous) with in-plane loading. Long edges restrained and short edges straight.

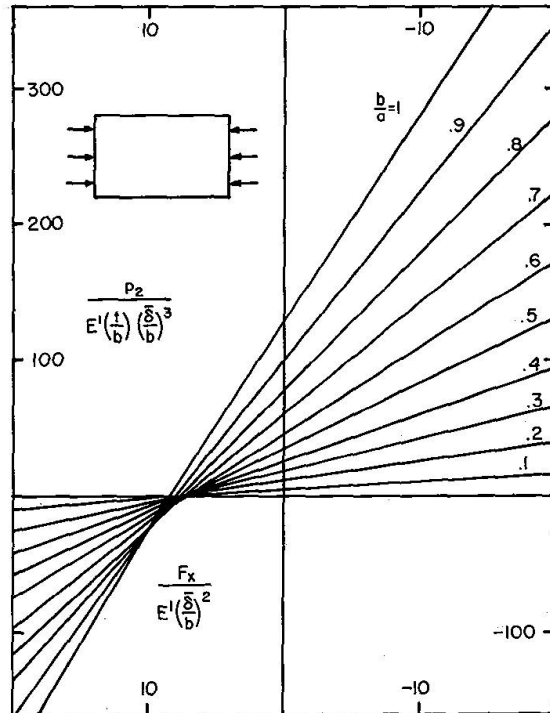


Fig. 6. (a) p_2 with all edges straight, $F_y=0$.

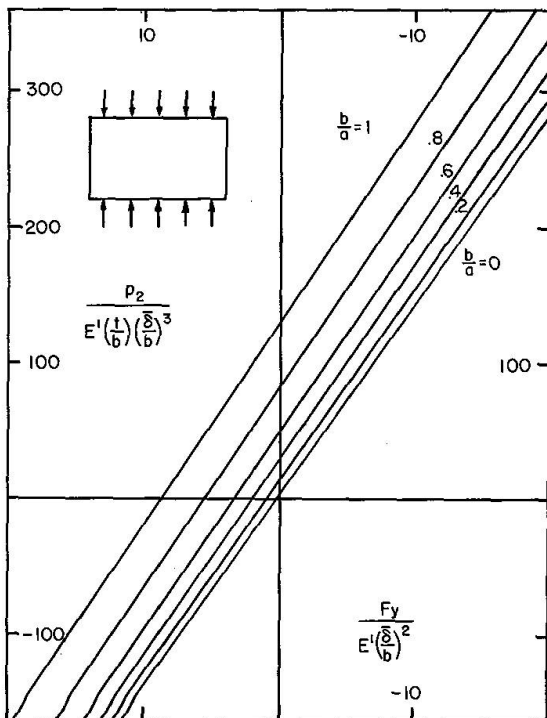


Fig. 6. (b) p_2 with all edges straight, $F_x=0$.

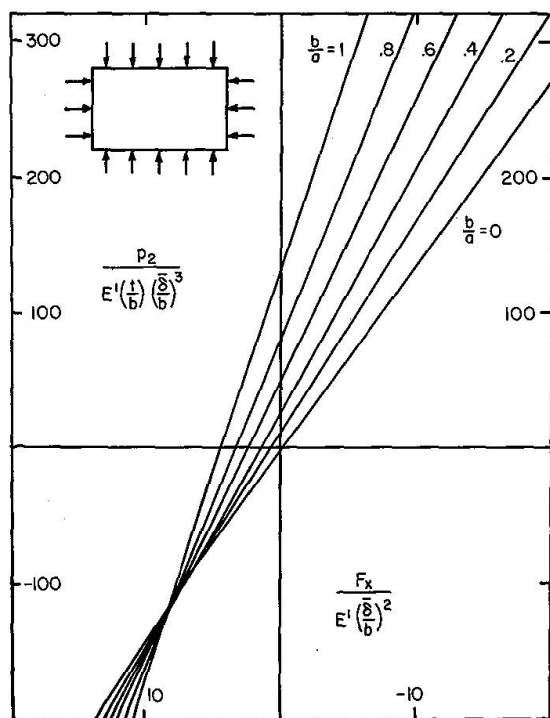
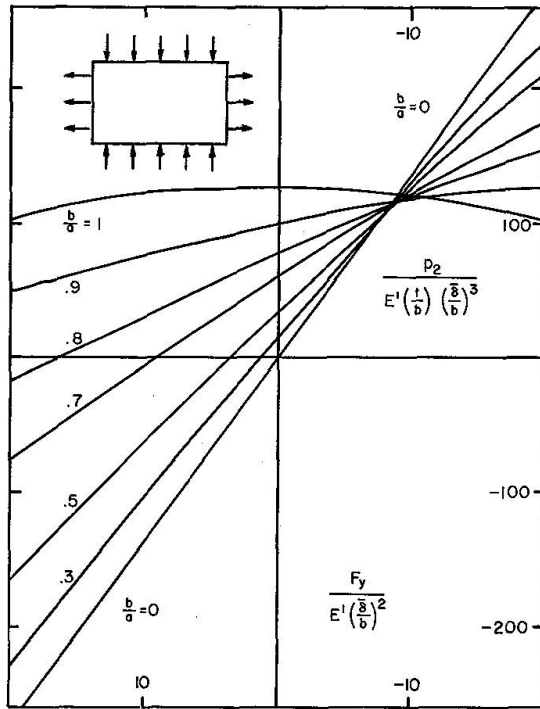
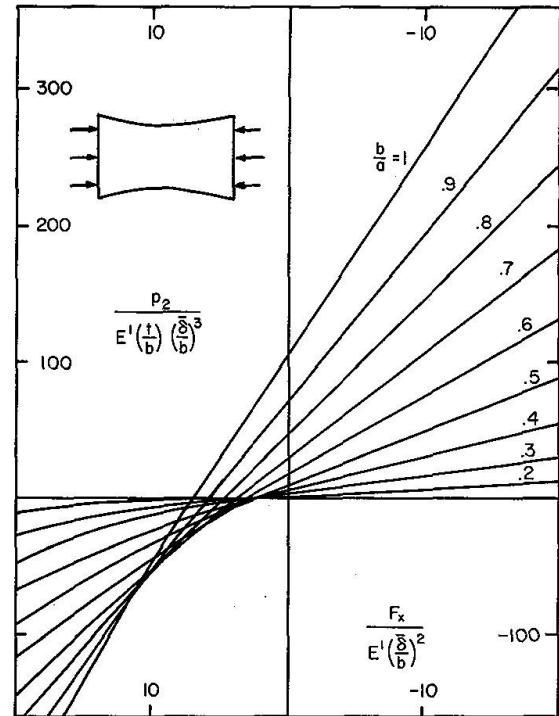
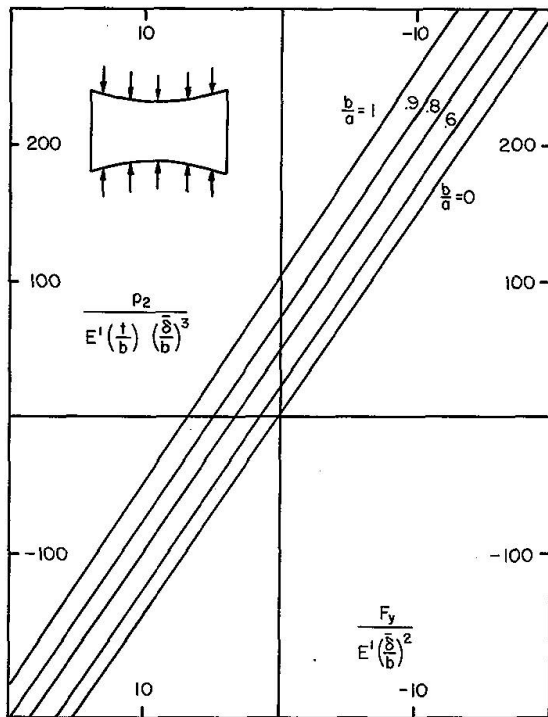
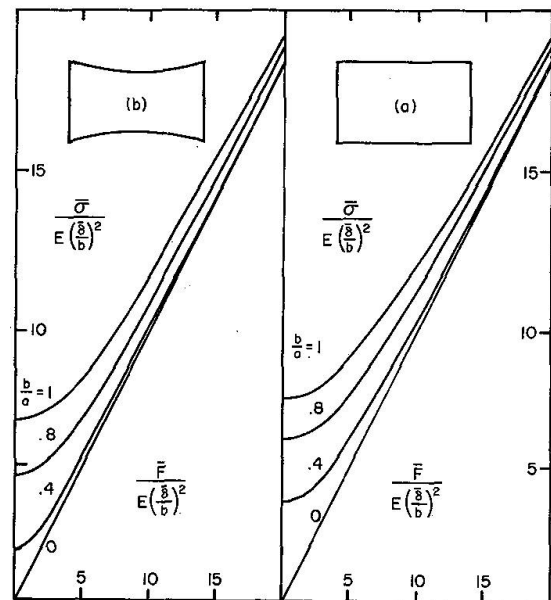


Fig. 6. (c) p_2 with all edges straight, $F_x=F_y$.

Fig. 6. (d) p_2 with all edges straight, $F_x - F_y$.Fig. 7. (a) p_2 with short edges straight, long edges unrestrained, $F_y = 0$.Fig. 7. (b) p_2 with short edges straight, long edges unrestrained, $F_x = 0$.Fig. 8. $\bar{\sigma}$ for any combination of in-plane loading, short edges straight.

$$\bar{F}^2 = F_x^2 + F_y^2 - F_x F_y + 3 F_{xy}^2$$

(a) Long edges straight.

(b) Long edges unrestrained.

Effect of Initial Imperfections

The two principal imperfections in welded steel plating are initial bowing ("hungry horse" phenomenon) and residual stresses. The latter can be estimated approximately [7] and can be idealised as uniform compression. A corresponding adjustment to F_x or F_y allows for their effect on p_2 .

Initial deflections are rather more difficult to quantify but if some nominal figure can be placed on the initial value of $\bar{\delta}_0$, p_2 should be reduced by the load associated with $\bar{\delta}_0$. In other words, the reduced value of p_2 is

$$p'_2 = p_2 [1 - (\bar{\delta}_0/\bar{\delta})^3]$$

Initial imperfections do not of course affect p_1 .

Conclusion

The method outlined in this paper enables the designer of steel plating to exploit the merits of yield-line analysis without sacrificing the reserve of strength resulting from the membrane stresses. The limiting lateral load is the sum of $(p_1)_{\min}$ and $(p_2)_{\min}$ associated with plastic bending and membrane action in relation to a nominal limiting lateral RMS deflection $\bar{\delta}$. Non-dimensional curves enable the limiting load to be rapidly estimated for rectangular plates with any symmetrical boundary conditions. The effect of membrane stress on the plastic moments, and the behaviour after the onset of general plasticity are both considered. Asymmetric boundary conditions and more complex shapes and loading can be analysed in exactly the same way, and while the computation may take slightly longer as the number of degrees of freedom increases, the method preserves its essential simplicity.

Although the effect of in-plane loading is allowed for, it is important to appreciate that this is not a buckling analysis but merely a means of estimating lateral strength, on the basis of a limiting lateral deflection. If this limiting lateral load is positive and increases with increasing deflection then buckling analysis is unnecessary since the maximum load is reached after the allowable deflection is exceeded. If the lateral load is found to decrease with increasing deflection, then design is impossible on the basis of a limiting deflection, but a more conventional buckling analysis is necessary. In-plane strength is then defined on the basis not of deflection but maximum load.

Appendix A: Finite Element Analysis of Membrane Action

The stresses in each of the three elements are calculated by Hooke's Law in terms of A , B , C , D and δ from the expressions for strain given in the main part of the paper. The virtual work associated with A is obtained by integrating the

product of each stress, and corresponding unit strain obtained by putting $A=1$ and $B=C=D=0$.

$$bc \left[\frac{-\delta^2}{2c^3} - \frac{(B-A)}{c^2} - \frac{2\nu C}{bc} \right] - a(1-\nu) \left[\frac{2B(\frac{1}{2}a-c)}{ab} - \frac{A}{b} + \frac{C-D}{a} \right] \\ + b \left[\frac{A}{\frac{1}{2}a-c} + \frac{2\nu D}{b} + \frac{2\nu\delta^2}{b^2} \right] = 0$$

In the case of B , C and D there is also work done by the stresses F_x and F_y (compressive positive) applied at the boundaries. For B , C and D respectively:

$$bc \left[\frac{\delta^2}{2c^3} + \frac{(B-A)}{c^2} + \frac{2\nu C}{bc} \right] + 2b \left[\frac{B}{a} + \frac{2\nu cD}{ab} + \frac{2\nu C(\frac{1}{2}a-c)}{ab} + \frac{\nu\delta^2}{b^2} \right] \\ + 2(1-\nu) \left(\frac{1}{2}a-c \right) \left[\frac{2B(\frac{1}{2}a-c)}{ab} - \frac{A}{b} + \frac{C-D}{a} \right] = \frac{-2F_x b(1-\nu^2)}{E} \\ bc \left[\frac{4C}{b^2} + \frac{\nu\delta^2}{bc^2} + \frac{2\nu(B-A)}{bc} \right] + 2 \left(\frac{1}{2}a-c \right) \left[\frac{4cD}{ab} + \frac{4C(\frac{1}{2}a-c)}{ab} + \frac{2\delta^2}{b^2} + \frac{2\nu B}{a} \right] \\ + b(1-\nu) \left[\frac{2B(\frac{1}{2}a-c)}{ab} - \frac{A}{b} + \frac{C-D}{a} \right] = \frac{-F_y(1-\nu^2)a}{E} \\ 2c \left[\frac{4cD}{ab} + \frac{4C(\frac{1}{2}a-c)}{ab} + \frac{2\delta^2}{b^2} + \frac{2\nu B}{a} \right] - b(1-\nu) \left[\frac{2B(\frac{1}{2}a-c)}{ab} - \frac{A}{b} + \frac{C-D}{a} \right] \\ + 2 \left(\frac{1}{2}a-c \right) \left[\frac{2D}{b} + \frac{2\delta^2}{b^2} + \frac{\nu A}{\frac{1}{2}a-c} \right] = \frac{-F_y(1-\nu^2)a}{E}$$

The net work done by any shear F_{xy} applied at the boundaries is zero, assuming the displacements remain symmetrical. This is certainly so for $b/a=1$ and 0, and there is no reason to expect a significant effect for intermediate aspect ratios.

Putting $b/a=\alpha$, $c/b=\gamma$, $\nu=0.3$ and collecting terms together we obtain the four simultaneous equations:

$$\left(\frac{A}{b} \right) \left[\frac{0.7}{\alpha} + \frac{1}{\gamma} + \frac{\alpha}{0.5-\alpha\gamma} \right] - \left(\frac{B}{b} \right) \left[\frac{1}{\gamma} + \frac{0.7-1.4\alpha\gamma}{\alpha} \right] - 1.3 \left(\frac{C}{b} \right) + 1.3 \left(\frac{D}{b} \right) = \\ = \frac{\delta^2}{b^2} \left[\frac{1}{2\gamma^2} - 0.6 \right] \quad (1)$$

$$\left(\frac{A}{b} \right) \left[\frac{1}{\gamma} + \frac{1.4(0.5-\alpha\gamma)}{\alpha} \right] - \left(\frac{B}{b} \right) \left[\frac{1}{\gamma} + 2\alpha + \frac{2.8(0.5-\alpha\gamma)^2}{\alpha} \right] - \left(\frac{C}{b} \right) \left[1.9-2.6\alpha\gamma \right] - \\ - \left(\frac{D}{b} \right) \left[2.6\alpha\gamma - 0.7 \right] = \frac{\delta^2}{b^2} \left[0.6 + \frac{0.5}{\gamma^2} + \frac{1.82F_x}{E(\delta/b)^2} \right] \quad (2)$$

$$-1.3 \left(\frac{A}{b} \right) - \left(\frac{B}{b} \right) \left[1.9-2.6\alpha\gamma \right] - \left(\frac{C}{b} \right) \left[4\gamma + 0.7\alpha + \frac{8(0.5-\alpha\gamma)^2}{\alpha} \right] \\ - \left(\frac{D}{b} \right) \left[8\gamma(0.5-\alpha\gamma) - 0.7\alpha \right] = \frac{\delta^2}{b^2} \left[\frac{0.3}{\gamma} + \frac{4(0.5-\alpha\gamma)}{\alpha} + \frac{0.9F_y}{\alpha E(\delta/b)^2} \right] \quad (3)$$

$$\begin{aligned}
& -1.3\left(\frac{A}{b}\right) + \left(\frac{B}{b}\right)\left[0.7 - 2.6\alpha\gamma\right] - \left(\frac{C}{b}\right)\left[8\gamma(0.5 - \alpha\gamma) - 0.7\alpha\right] \\
& - \left(\frac{D}{b}\right)\left[8\alpha\gamma^2 + 0.7\alpha + \frac{4(0.5 - \alpha\gamma)}{\alpha}\right] = \frac{\delta^2}{b^2}\left[\frac{2}{\alpha} + \frac{0.9F_y}{\alpha E(\delta/b)^2}\right]
\end{aligned} \quad (4)$$

These may be solved for A , B , C and D for each given value of F_x and F_y . The lateral load p_2 may then be calculated by virtual work:

$$\begin{aligned}
\frac{p_2 b(1 - \nu^2)(\frac{1}{2}a - \frac{1}{3}c)}{Et\delta} &= \delta^2 \left[\frac{b}{2c^3} + \frac{8a}{b^3} - \frac{8c}{b^3} \right] + A \left[\frac{4\nu}{b} - \frac{b}{c^2} \right] + B \left[\frac{b}{c^2} + \frac{4\nu}{b} \right] \\
&+ C \left[\frac{2\nu}{c} + \frac{8(\frac{1}{2}a - c)}{b^2} \right] + \frac{4aD}{b^2}
\end{aligned}$$

Substitution of the solutions to the simultaneous equations yields an expression for p_2 proportional to δ^3 . Now the RMS deflection $\bar{\delta}$ is given by

$$ab\bar{\delta}^2 = \delta^2 [2bc\frac{1}{6} + b(a - 2c)\frac{1}{3}]$$

Hence:

$$\begin{aligned}
\frac{p_2}{E(\frac{t}{b})(\frac{\bar{\delta}}{b})^3} &= \frac{17.32}{(1.5 - \alpha\gamma)(1 - \alpha\gamma)^{1.5}} \left\{ \frac{1}{2\gamma^3} + \frac{8}{\alpha} - 8\gamma + \left(\frac{A}{b}\right)\left[1.2 - \frac{1}{\gamma^2}\right] + \left(\frac{B}{b}\right)\left[\frac{1}{\gamma^2} + 1.2\right] \right. \\
&\left. + \left(\frac{C}{b}\right)\left[\frac{0.6}{\gamma} + \frac{8(0.5 - \alpha\gamma)}{\alpha}\right] + \frac{4}{\alpha}\left(\frac{D}{b}\right) \right\}
\end{aligned}$$

Appendix B: Effect of Membrane Stresses on Plastic Moments

Consider a hinge-line parallel to the longer side. The plastic moment per unit length is

$$\frac{1}{4}t^2\sigma'_Y \left[1 - \left(\frac{\sigma_y}{\sigma'_Y} \right)^2 \right]$$

where σ'_Y is the stress at which the material yields in the y -direction. If there are no other stresses apart from σ_y then σ'_Y is the uniaxial yield stress σ_Y . Otherwise, from von Mises

$$\sigma_Y'^2 = \sigma_Y^2 - \sigma_x^2 + \sigma_x\sigma_y - 3\tau_{xy}^2 = \sigma_Y^2 + \sigma_y^2 - (\sigma_x^2 - \sigma_x\sigma_y + \sigma_y^2 + 3\tau_{xy}^2)$$

Clearly, this expression will take a different value for each element, but for the sake of simplicity we consider mean values. Thus the term in parentheses becomes $\bar{\sigma}^2$, while the mean of σ_y is F_y . Hence

$$\begin{aligned}
\sigma'_Y &\doteq \sqrt{\sigma_Y^2 + F_y^2 - \bar{\sigma}^2} \\
\text{and } M_p &\doteq \frac{1}{4}t^2 \left[\frac{\sigma_Y^2 - \bar{\sigma}^2}{\sqrt{\sigma_Y^2 + F_y^2 - \bar{\sigma}^2}} \right]
\end{aligned}$$

Similar expressions for the x -direction can be obtained by replacing F_y by F_x .

Appendix C: Examples of Plate Analysis

1. What load can be carried by a 4 mm thick mild steel plate 1 m x 0.8 m, near the middle of a lightly framed grillage? Take $\sigma_Y = 24 \text{ kgf/mm}^2$ and $E = 20,000 \text{ kgf/mm}^2$. Aspect ratio is 0.8 and all edges are straight so that from Fig. 4c

$$\bar{\sigma} = 6E \left(\frac{\bar{\delta}}{b} \right)^2$$

With a limit of 0.01 on $\bar{\delta}/b$, $\bar{\sigma} = 12 \text{ kgf/mm}^2$

Since $\bar{\sigma} < \sigma_Y$ the membrane remains elastic.

$$p_2 = 80E \left(\frac{t}{b} \right) \left(\frac{\bar{\delta}}{b} \right)^3 = 8 \text{ tonnes/m}^2$$

The effective yield stress for the plastic moment

$$\sigma'_Y = \sqrt{\sigma_Y^2 - \bar{\sigma}^2} = 12\sqrt{3} \text{ kgf/mm}^2$$

Since all edges are clamped the yield-line load is given by Fig. 3a.

$$p_1 = 9.8 \sigma'_Y \left(\frac{t}{b} \right)^2 = 5.1 \text{ tonnes/m}^2$$

$$\therefore p = 13.1 \text{ tonnes/m}^2$$

If a higher limit of 0.02 were placed on $\bar{\delta}/b$, $\bar{\sigma}$ becomes 48 kgf/mm^2 . The plastic moment vanishes and the membrane action becomes plastic. The modulus is reduced to $\frac{24}{48} E$ and hence $p = p_2 = 32 \text{ tonnes/m}^2$.

2. The flange of a box girder is 1 m wide, 10 mm thick and framed transversely at 2.5 m intervals along its length. It is subjected to an in-plane compressive stress $F_x = 20 \text{ kgf/mm}^2$ due to bending and a shear stress $F_{xy} = 15 \text{ kgf/mm}^2$ due to torsion. What lateral load can be sustained if the permanent RMS deflection is not to exceed 10 mm? Take $\sigma_Y = 45 \text{ kgf/mm}^2$ and $E = 20,000 \text{ kgf/mm}^2$.

The boundary conditions are taken as unrestrained and simply supported along the sides and straight and clamped across the width.

$$\frac{\sqrt{F_x^2 + 3F_{xy}^2}}{E(\bar{\delta}/b)^2} = 16.4 \text{ kgf/mm}^2$$

From Fig. 8b and for $b/a = 0.4$, $\bar{\sigma} = 33 \text{ kgf/mm}^2$. Thus the membrane action remains elastic.

$$\frac{F_x}{E(\bar{\delta}/b)^2} = 10$$

$$\text{From Fig. 7a } p_2 = 2.3E \left(\frac{t}{b} \right) \left(\frac{\bar{\delta}}{b} \right)^3 = -4.6 \text{ tonnes/m}^2$$

$$\text{For yield-line action } \sigma'_Y = \sqrt{\sigma_Y^2 - \bar{\sigma}^2} = 30.6 \text{ kgf/mm}^2$$

Coefficient of orthotropy $\mu = \sqrt{\frac{\sigma_Y^2 - \bar{\sigma}^2}{F_x^2 + \sigma_Y^2 - \bar{\sigma}^2}} = 0.836$

Affine aspect ratio = $b\sqrt{\mu}/a = 0.365$

From Fig. 3c $p_1 = 11.1 \text{ tonnes/m}^2$

Thus the net lateral limiting load is $p = 6.5 \text{ tonnes/m}^2$

Since p_2 is negative it is pertinent to ask whether this condition is stable. Repeating the calculation for $\bar{\delta}/b = 0.011$ instead of 0.01 shows that the lateral load increases to 7.0 tonnes/m^2 . Thus the strength is limited by deflection, not by buckling. However, if there were no lateral load a reduced buckling strength would probably result from a different mode of deflection.

Notation

a	plate length in x -direction.
b	beam length, or plate width in y -direction, $b < a$.
t	plate thickness.
δ	central deflection.
$\bar{\delta}$	RMS deflection.
p_1	UDL per unit area due to bending action.
p_2	UDL per unit area due to membrane action.
$F_x F_y$	mean effective stress applied to respectively short and long sides, compressive positive.
$\bar{\sigma}$	effective von Mises stress.
σ_Y	yield stress.
σ'_Y	reduced yield stress in y -direction = $\frac{\sigma_Y^2 - \bar{\sigma}^2}{\sqrt{F_y^2 + \sigma_Y^2 - \bar{\sigma}^2}}$
μ	coefficient of plastic orthotropy = $\sqrt{\frac{F_y^2 + \sigma_Y^2 - \bar{\sigma}^2}{F_x^2 + \sigma_Y^2 - \bar{\sigma}^2}}$
E	Young's modulus.
E'	reduced modulus = $\frac{\sigma_Y}{\bar{\sigma}} E$ if $\bar{\sigma} > \sigma_Y$.

Definition of boundary conditions:

a) Bending action.

- (i) simply-supported.
- (ii) clamped (i.e. moments developed).

b) Membrane action.

- (i) restrained (in-plane movement suppressed).
- (ii) straight (pull-in allowed, but edges kept straight).
- (iii) unrestrained (edges warp under uniform edge stress).

Practical Relevance

The practical value of the proposed method is that it provides a means of analysing the strength of steel plating which is almost as simple as conventional plastic yield line analysis, but by allowing for membrane stresses is not so wasteful of material. At the same time the complexities of general loading and boundary conditions are simplified so that a more rational and hence reliable design can be made. Appendix C considers two examples.

References

1. J. CLARKSON: A New Approach to the Design of Plates to Withstand Lateral Pressure. Trans. I.N.A., Vol. 98., 1956, pp. 443-463.
2. A.G. YOUNG: Ship Plating Loaded Beyond the Elastic Limit. Trans. I.N.A., Vol. 101, 1959, pp. 143-165.
3. D. FAULKNER *et al.*: Synthesis of Welded Grillages to Withstand Compression and Normal Loads. Computers and Structures, Vol. 3, 1973, pp. 221-246.
4. L.G. JAEGER: An Approximate Analysis for Plating Panels under Uniformly Distributed Load. Proc. I.C.E., Vol. 10, 1958, pp. 137-144.
5. R. HOOKE: Post-elastic Deflection Prediction of Plates. Journ. Struct. Div. A.S.C.E., Vol. 96, 1970, pp. 757-771.
6. R.H. WOOD: Plastic and Elastic Design of Slabs and Plates. Thames and Hudson, London, 1961.
7. B.W. YOUNG and J.B. DWIGHT: Residual Stresses due to Longitudinal Welds and Flame-cutting. Camb. Univ. Dept. Eng. Tech. Rep. C-Struct/TR. 9, 1971.
8. N. JONES and R.M. WALTERS: Large Deflections of Rectangular Plates. Jour. Ship Res., Vol. 15, 1971, pp. 164-171.

Summary

The principal objection to Johansen yield-line analysis of steel plating is that significant membrane action is neglected. A simple technique of analysing this effect in isolation is described. Curves are obtained which can be used directly in the design of rectangular plates under uniform lateral load with various combinations of in-plane loading and boundary conditions, on the basis of a limiting lateral deflection.

Résumé

L'objection principale contre l'analyse de la ligne de rupture pour plaques en acier est due au fait que l'effet caractéristique de membrane y est négligé. Ici on présente une méthode simple pour calculer cet effet comme facteur isolé. On obtient des courbes pouvant être utilisées à projeter des plaques rectangulaires sous charge uniforme latérale, avec différentes combinaisons de charges dans le plan et conditions limites, sur la base d'une déflexion limite latérale.

Zusammenfassung

Der hauptsächliche Einwand gegen die Bruchlinien-Analyse für Stahlplatten besteht darin, dass die charakteristische Membranwirkung vernachlässigt wird. Hier wird ein einfaches Verfahren zur Berechnung dieser isoliert auftretenden Wirkung beschrieben. Man erhält Kurven, die sich direkt zum Entwurf rechteckiger Platten unter gleichförmiger seitlicher Belastung mit verschiedenen Kombinationen von Randlast und Grenzbedingungen auf Basis einer begrenzenden seitlichen Krümmung verwerten lassen.

Leere Seite
Blank page
Page vide

The Nodal Section Method for the Analysis of Box Girders

La méthode de section nodale pour l'analyse de poutres en caisson

Die nodale Querschnitts-Methode zur Berechnung von Kastenträgern.

K.C. ROCKEY

Professor and Head of Department, Department
of Civil and Structural Engineering, University
College, Cardiff.

H.R. EVANS

Lecturer, Department of Civil and Structural
Engineering, University College, Cardiff.

1. Introduction

The Nodal Section Method has been developed to provide a relatively simple method of analysis for both single-span and continuous box girders in which the geometry of the cross-section varies along the length of the girder. Although the method assumes a simplified structural behaviour in order to reduce the amount of computation required, it does in fact provide results of a high degree of accuracy. It is anticipated that, since the amount of computation involved is relatively small, the method will prove to be useful during the design of a box girder, when several analyses may be necessary in order to investigate the effect of changing various dimensions. In such a situation, the use of the Finite Element Method which involves extensive calculations proves to be prohibitively expensive.

The Nodal Section Method is based on a method of analysis previously applied to folded plate structures. Indeed, a box girder is only a particular type of folded plate structure, in which the plates have been arranged so as to form a closed section, as shown in Fig. 1. In recent years much research has been devoted to the analysis of folded plates and two main methods have been established, these being the "Elasticity Method" [1, 2] and the "Ordinary Method" [3, 4].

Of these two methods, the Elasticity Method is the more accurate and this method has, in fact, already been adapted to box girder analysis by SCORDELIS [5, 6], this method being termed the "Folded Plate Method". In this method, each component plate of the box girder is considered as an individual element and a stiffness matrix derived for it, the individual stiffness matrices for the plates then being assembled together as in a matrix stiffness method of analysis. The bending of each plate element normal to its plane is analysed by plate flexure theory, and its in-plane bending is analysed by plane stress theory.

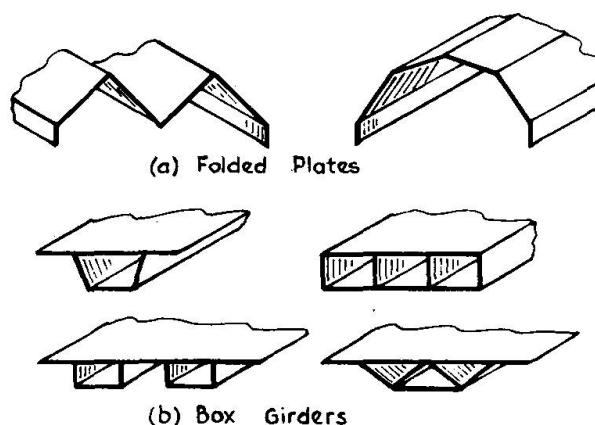


Fig.1. Typical folded plate and box girder cross-sections.

These classical theories necessitate the representation of the applied loading by a Fourier Series, with the result that the computational effort required is still considerable, although very much less than that required in a full Finite Element solution. The Folded Plate Method is, however, very much more restricted in its range of application than the Finite Element Method and can only be applied to box girders in which the geometry of the cross-section remains constant all along the length. Also, in its basic form, the method can only deal with simply supported girders, but it has been extended by Scordelis to deal with girders spanning over intermediate supports, provided that the extreme ends of such girders still remain simply supported. However, since this extension of the method is based on a superposition technique this significantly increases the solution time required.

The Ordinary Method of folded plate analysis is an approximate method in which a simplified structural behaviour is assumed in order to reduce the amount of computation required in obtaining a solution. The present authors have previously shown [7], that, provided no concentrated loads are applied perpendicular to the planes of any of the plates, the errors introduced by these simplifying assumptions become very small provided that the length/width ratio of each component plate in the structure exceeds 3. Now, for the majority of box girder bridges, the dimensions of the component plates will be in accordance with this requirement.

SCORDELIS [6], has already proposed a method, known as the "Finite Segment Method", based on the assumptions of the Ordinary Method. In the Finite Segment Method, a process basically similar to that of the Finite Element Method is followed, each plate being divided initially into a number of rectangular elements which are subsequently assembled together. However, the simplifying assumptions of the Ordinary Method lead to much simpler element stiffness matrices and to many fewer nodal degrees of freedom and consequently to a much more economical solution process than the Finite Element Method. The solution time required by SCORDELIS' Finite Segment Method is of the same order as that required by his Folded Plate Method, but has the advantage of being able to deal with any support conditions. However, in the formulation as presented by SCORDELIS, the Finite Segment Method is restricted to the analysis of box girders in which the geometry

of the girder cross-section remains constant all along its span, the girders being loaded by longitudinal line loads only. Furthermore, no provision is made in the method for dealing with concentrated loads applied normal to the planes of the plates.

The Nodal Section Method is similar to the Finite Segment Method in that it is based on the Ordinary Method of folded plate analysis but its formulation is completely different and leads to further substantial savings of computer storage and time. The Nodal Section Method is not based on a conventional matrix stiffness approach but, instead, involves analysing the girder in a number of simple steps, similar to the steps that would be followed if the analysis was being carried out by hand. In fact, a hand analysis by the Nodal Section Method is a feasible proposition for many simple girders [8]. The advantages of the Nodal Section Method are that it can deal with various support conditions, makes use of a Finite Element plate bending solution to enable concentrated loads normal to the planes of the plates to be considered and, by employing an adaptation of a procedure suggested by JOHNSON and LEE [9] for folded plates, can be applied to the analysis of girders in which the geometry of the cross-section varies along the span. It thus combines a simple solution procedure with a wide field of application.

In the present paper, the basic theory of the Nodal Section Method is presented and results calculated by the method compared to theoretical solutions obtained using the Finite Element Method and other existing methods of analysis.

2. Basic Theory

The Nodal Section theory is based on the Ordinary Folded Plate Theory in which the only assumptions additional to those employed in a conventional elastic analysis are the following:

1. The bending action of an individual plate normal to its plane may be represented by considering a transverse one-way slab strip.
2. The in-plane longitudinal bending action of an individual plate is similar to that of a beam spanning between the end diaphragms.

On the basis of these assumptions, the behaviour of a box girder may be considered to consist of the action of a series of transverse one-way frames elastically supported by a system of interconnected plate beams spanning longitudinally between the supporting diaphragms. These frames only transmit shears and moments in the transverse direction, this action being termed the "transverse frame action", while the plate "beams" only transmit forces in their planes, this action being termed the "longitudinal plate action" of the structure. This idealised behaviour is illustrated in Fig. 2.

2.1. General Outline of Method

The transverse frame action is analysed by assuming each transverse frame to be supported at its joints, as shown in Fig. 2. By applying the slope-deflection equations it is possible to obtain the transverse moments acting within the frame, together with the joint reactions $R_B \dots R_F$. The longitudinal plate action is then

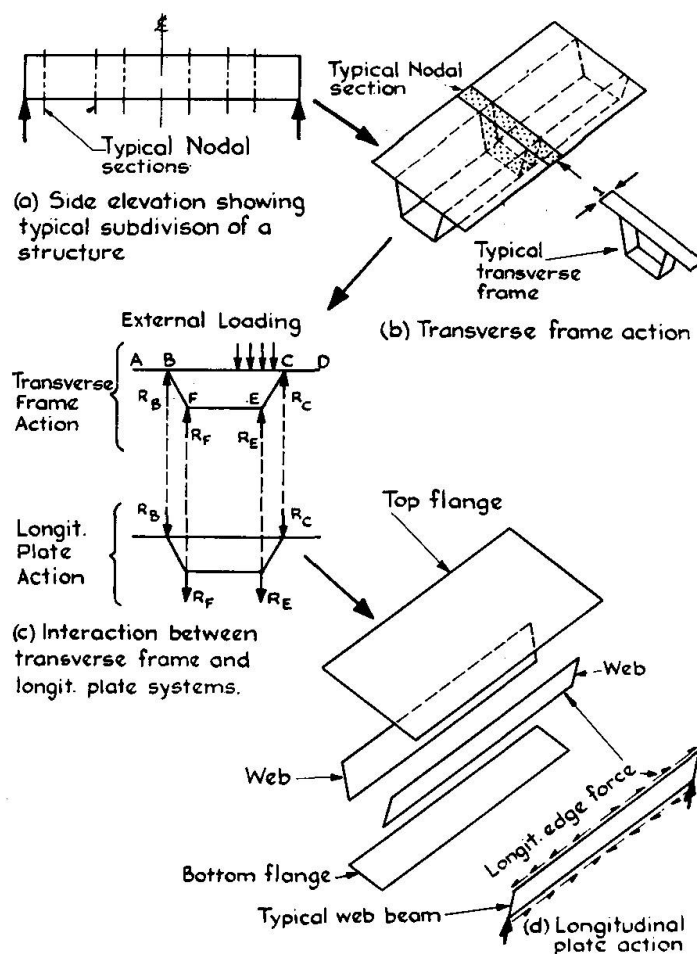


Fig. 2. Idealization of structural behaviour.

analysed by considering each plate to act as a beam spanning between the supporting diaphragms, the analysis ensuring that the longitudinal strain developed at the edge of each plate is compatible with the edge strain developed in adjacent plates and that the corresponding longitudinal edge forces in adjacent plates are in equilibrium as shown in Fig. 2. Furthermore, since the frame and plate systems are considered to be interconnected at the joints, as shown in Fig. 2, then the reactions of the frame system and the joint loads of the plate system must be equal and opposite, and the joint deflections of the two systems must be identical.

Since the Nodal Section Method is to be applied to box girders in which the geometry of the cross-section varies along the span, a transverse frame analysis is carried out at a number of sections taken on the structure, as shown in Fig. 2 the transverse frames being assigned a unit width in the longitudinal direction for convenience. The transverse sections are termed "nodal sections" and for a tapered girder, the frame taken at each nodal section will be of different dimensions and each frame is analysed under the action of the external loading pertaining to that particular nodal section. The reactions thus determined at each nodal section are then applied in the negative direction as joint loads on to the plate system and the longitudinal edge shear forces and strains set up in the plates at each nodal section are calculated and made to satisfy equilibrium and compatibility.

From the Nodal Section analysis, values of transverse bending moments, longitudinal stresses and vertical and horizontal joint displacements are determined at each nodal section. The basic method gives the values of these quantities at the joints only, but values at positions across the width of the various plates can also be determined by carrying out some additional simple steps.

Because equilibrium and compatibility conditions at the joints are only satisfied explicitly at the centre line of each of the nodal sections, the accuracy of the solution will vary with the number of nodal sections employed. It will be shown in Section 5 that the rate of convergence to an exact solution is rapid and that accurate results can be obtained with only a few nodal sections.

2.2. Special Consideration for Concentrated Loads

Further consideration must be given to the analysis of the transverse frame system under the action of the external loading. A one-way slab strip is only a good representation of the actual behaviour of a plate when the plate bends into an approximately cylindrical surface so that the proportion of the external load carried by longitudinal bending and twisting is negligible. This is so when the plate has a length/width ratio greater than 3, provided that the lateral loading has a reasonably uniform distribution in the longitudinal direction [7].

To deal with localised loading effects such as a wheel load on a top flange, the out-of-plane bending of each plate subjected to concentrated loading must first be analysed by the Finite Element Method. In this Finite Element analysis, the longitudinal edges of the plate are assumed to be fully clamped and the edge holding forces and moments are calculated. These fictitious holding forces are then applied in the negative direction to the box girder as joint "loads" and the box girder analysed by the Nodal Section Method.

Once the Nodal Section analysis has been completed, the results are then superimposed on to the initial Finite Element solution so that the fictitious edge holding forces and moments are eliminated.

In bridge design, it is often necessary to calculate the bending moments set up in the top flange in the locality of the applied concentrated loading. The initial Finite Element solution gives these moments, on the assumption that the longitudinal edges of the flange plate are clamped. To obtain the true values of these moments, another Finite Element plate bending solution of the loaded plate must be carried out after the Nodal Section analysis has been completed. In this final step, the deflections of the longitudinal edges of the plate, as predicted by the Nodal Section Method, are imposed on the plate, which is otherwise unloaded. By superimposing the results of the two Finite Element analyses, a complete picture of the moments set up in the loaded flange is obtained. The steps in a complete solution of this type are illustrated in Fig. 3.

The introduction of the Finite Element solution of the deck plates does, of course, increase the overall solution time. However, it must be appreciated that in the proposed procedure, a Finite Element solution is only required for those plates that are subjected to localised loading, and the number of plates loaded in this way is usually small compared to the total number of plates in the cross-section.

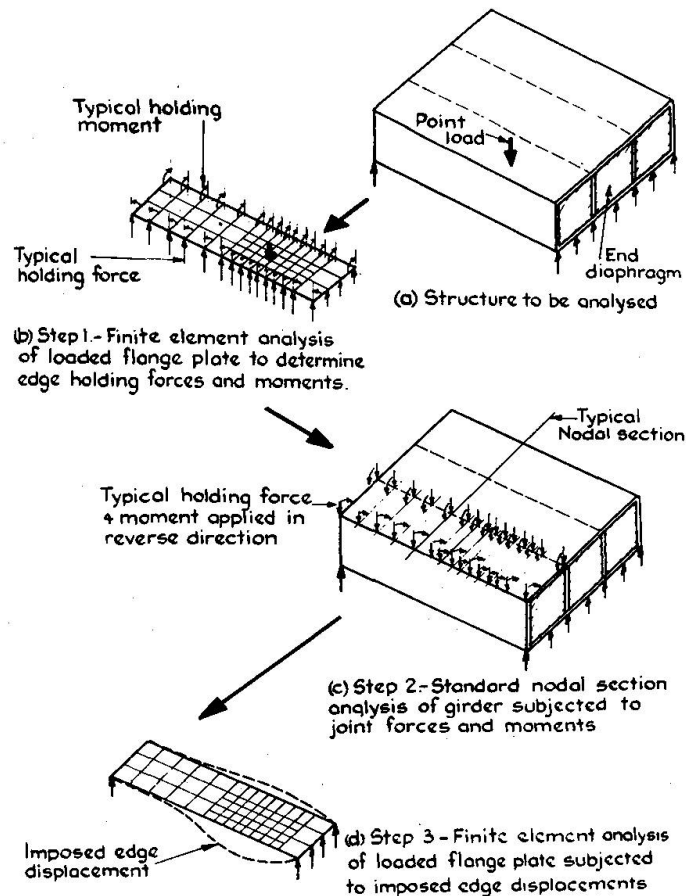


Fig. 3. Solution procedure for box girder subjected to point loading.

Furthermore, these plates are only analysed for bending normal to their planes so that only 3 degrees of freedom have to be considered at each nodal point instead of the 6 degrees of freedom that would have to be considered at each node in a full Finite Element analysis of the complete girder.

As an alternative to using the Finite Element Method, the edge holding forces of the plates subjected to concentrated loads may also be obtained from design tables [10]. The fictitious joint loads to be considered in the Nodal Section analysis may thus be determined directly without any additional solution time being required.

2.3 Sway Correction

Since, as discussed earlier, it is assumed that the frame system is *elastically* supported at the joints by the plate system, a situation is created in which the displacements of the plate system are produced by the frame reactions, whilst these reactions themselves depend partly on the plate displacements.

To overcome this problem, the Nodal Section analysis is divided into two parts. In the first part, which will be called the "No-Sway Solution", the box girder is analysed assuming the joints of the frame system to be *rigidly* supported by the plate system, whilst, at the same time, allowing the joints of the plate system to deflect.

The resulting incompatibilities between the deflections of the slab and plate systems are then removed by a subsequent "Sway Correction".

2.4. Continuous Box Girders

During the longitudinal plate analysis, each plate is analysed as a beam of variable cross-section spanning between the supporting diaphragms. If these beams are statically indeterminate, as in the case of a continuous girder, then a matrix approach is employed.

3. No-Sway Analysis

In this Section, the matrix formulation of the No-Sway analysis will be described. The analysis will be presented in general terms, but in some cases the equations will be written for the specific case of the typical structure shown in Fig. 4 to clarify their form. Only an outline of the various stages in the analysis can be given in the present paper, but greater detail of some of the steps has been included in earlier reports by the authors [11].

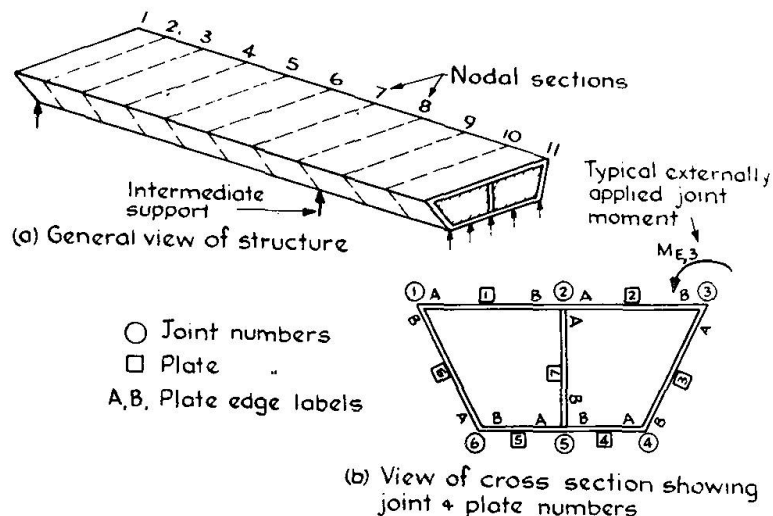


Fig. 4. Typical structure considered in the analysis.

3.1. Idealisation of Structure

Before the analysis can be started, the structural idealisation has to be carried out. First a number of nodal sections must be taken across the structure. These need not be equally spaced and should be distributed efficiently, i.e. more should be positioned in regions of anticipated high stress gradients as in a graded Finite Element mesh. In the general case, the nodal sections are numbered sequentially from 1 to n , a typical nodal section being denoted by n .

The next step is to define the cross-section of the structure. The plates are numbered from 1 to p_o , a typical plate being denoted by p and the joints are numbered from 1 to j_o , a typical joint being denoted by j . In addition, each longitudinal edge of each plate must be identified by the letter A or B , to assist the assembly procedure employed in the solution.

The following rules must be observed in carrying out the structural idealisation:

1. As will be discussed in Section 3.3, the method is only capable of dealing with structures in which no more than 3 plates meet at any joint, and 2 of these 3 plates must be co-planar. Consequently, a structure containing a joint such as that shown in Fig. 5 cannot be analysed, unless the joint is idealised as shown.

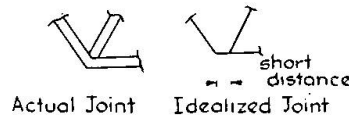


Fig. 5. Idealization of a typical 3 plate joint.

2. When a joint connects two plates only, then edge A of one plate and edge B of the other plate must be located at the joint, as at joints 1, 3, 4 and 6 of the structure illustrated in Fig. 4.
3. When a joint connects three plates, then edge A of one of the co-planar plates and edge B of the other co-planar plate must intersect at the joint. Either edge A or edge B of the third plate can be located at the joint, see joints 2 and 5 in Fig. 4.
4. In a structure containing adjacent co-planar plates, these plates must be numbered sequentially, see plates 1 and 2, and 4 and 5 in Fig. 4.

Having numbered and labelled the cross-section, a "connectivity" matrix $[AD]$ is set up, which specifies which edges of which plates meet at each joint. Each column of the matrix corresponds to a plate edge and each row corresponds to a joint, the plate edges meeting at a particular joint being indicated by inserting the figure "1" in the appropriate place in the matrix. The construction of the $[AD]$ matrix for the cross-section shown in Fig. 4 is as follows:

Edge	Plate 1		Plate 2		Plate 3		Plate 4		Plate 5		Plate 6		Plate 7		
	A	B	A	B	A	B	A	B	A	B	A	B	A	B	
$[AD] =$	1	0	0	0	0	0	0	0	0	0	0	1	0	0	Joint 1
	0	1	1	0	0	0	0	0	0	0	0	0	1	0	» 2
	0	0	0	1	1	0	0	0	0	0	0	0	0	0	» 3
	0	0	0	0	0	1	1	0	0	0	0	0	0	0	» 4
	0	0	0	0	0	0	0	1	1	0	0	0	0	1	» 5
	0	0	0	0	0	0	0	0	0	1	1	0	0	0	» 6

3.2 Transverse Frame Analysis

As discussed in Section 2.1, a transverse frame, such as that shown in Fig. 2, is analysed for transverse bending at each nodal section during the transverse frame analysis. This analysis is the same for each nodal section unless the nodal

section coincides with a diaphragm, which, by preserving the cross-sectional shape, prevents transverse bending occurring. Thus, for the typical structure shown in Fig. 4, nodal sections 1, 8 and 11 are supported by diaphragms, and a transverse frame analysis is not required at these sections.

The transverse frame analysis at a typical nodal section n will now be considered. It should be remembered that, in the No-Sway Solution now being discussed, those joints of the frame system which are *not* located at free edges are assumed to be rigidly supported by the plate system, so that no vertical or horizontal movements of these joints can occur, only transverse joint rotations being permitted. Joints located at cantilever free edges are considered to be unsupported.

Consider a typical plate p at a typical nodal section n , as shown in Fig. 6. The transverse span of the plate at this section is termed $s_{p,n}$, the thickness is termed $t_{p,n}$, the inclination to the horizontal $\phi_{p,n}$ and the modulus of elasticity $E_{p,n}$. The notation and the positive directions for the moments and rotations at the edges of the plate are as illustrated in Fig. 6, anticlockwise moments and rotations being considered positive.

In order to reduce the number of subscripts, the subscript n will be deleted whenever possible, because all expressions relate to the general nodal section n .

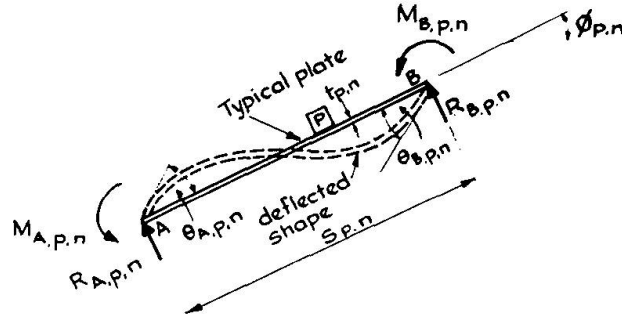


Fig. 6. Section through a typical plate p at nodal section n .

The *Slope Deflection Equations* for the typical plate p , see Fig. 6, may be written as:

$$\begin{aligned} M_{A,p} &= 2\lambda_p \theta_{A,p} + \lambda_p \theta_{B,p} + MF_{A,p} \\ M_{B,p} &= \lambda_p \theta_{A,p} + 2\lambda_p \theta_{B,p} + MF_{B,p} \end{aligned} \quad (1)$$

where $\lambda_p = \left(\frac{t^3 E}{6} \right)_p$

An equation similar to (1) may be written for each plate in the cross-section from 1 to p_o , provided that the plate does not have a free edge. In the case of a plate, such as an edge cantilever, which does have a free edge, then, in equation (1), $\theta_{A,p} = \theta_{B,p} = 0$.

When equations similar to (1) have been written for *all* plates from $p = 1$ to p_o at the given nodal section they may be summarised as:

$$\{M\} = [A\theta] \{\theta\} + \{MF\} \quad (2)$$

In this equation the vector $\{M\}$ represents all the plate edge moments, $\{\theta\}$ represents the vector for the plate edge rotations and $\{MF\}$ represents the vector

for the fixed end moments, thus for the typical structure shown in Fig. 4, each of these vectors contains 14 terms.

Clearly, the plate edge moments at any joint must be in equilibrium with any moment applied externally to that joint. For the particular case of the structure shown in Fig. 4, the equilibrium equation for joint 3 for example is:

$$M_{B,2} + M_{A,3} = M_{E,3}$$

Similar equilibrium equations may be written for each joint in the cross-section and the equations for the complete cross-section may be written in a general matrix form as:

$$\{\Sigma M\} = \{M_E\} \quad (3)$$

It will be seen that the required addition of the plate edge moments may be accomplished directly by using the $[AD]$ matrix defined in Section 3.1, as follows:

$$\{\Sigma M\} = [AD] \{M\} \quad (4)$$

Then, from equations (2), (3) and (4)

$$[AD] [A\theta] \{\theta\} + [AD] \{MF\} = \{M_E\} \quad (5)$$

Having satisfied equilibrium, the compatibility of the rotations at the joints must next be considered. This compatibility condition simply requires that the edge rotations of each plate meeting at a joint are identical.

For example, for the particular case of the structure shown in Fig. 4, using β_j to denote the joint rotation, the compatibility equation for joint 3 is:

$$\theta_{B,2} = \theta_{A,3} = \beta_3$$

It will be seen that the compatibility equations for the complete cross-section may again be established by using the $[AD]$ matrix as follows:

$$\{\theta\} = [AD]^T \{\beta\} \quad (6)$$

Substituting in equation (5)

$$[AD] [A\theta] [AD]^T \{\beta\} + [AD] \{MF\} = \{M_E\}$$

Defining, for convenience, a new matrix $[A\beta] = [AD] [A\theta] [AD]^T$, then:

$$[A\beta] \{\beta\} + [AD] \{MF\} = \{M_E\}$$

The only unknown in this equation is the vector $\{\beta\}$ representing the joint rotations and this may now be determined as:

$$\{\beta\} = -[A\beta]^{-1} ([AD] \{MF\} - \{M_E\}) \quad (7)$$

Knowing the joint rotations $\{\beta\}$, the plate edge rotations $\{\theta\}$ may then be determined from equation (6) and a further substitution back into the matrix form of the slope deflection equations, i.e. equation (2), yields the required values of the *Transverse Moments* $\{M\}$ acting at the plate edges at the typical nodal section n . From a consideration of these edge moments and the external load acting perpendicular to the plane of each plate, the transverse moments and the lateral displacements at positions across the width of each plate can be determined.

Once the transverse moments at the plate edges are known, the edge support reactions normal to the plane of each plate may be found. These are shown as $R_{A,p}$ and $R_{B,p}$ in Fig. 6 and for the typical plate they are given by:

$$\begin{aligned} R_{A,p} &= \frac{(M_A + M_B)}{S} + RF_{A,p} \\ R_{B,p} &= \frac{-(M_A + M_B)}{S} + RF_{B,p} \end{aligned} \quad (8)$$

Where the terms $RF_{A,p}$ and $RF_{B,p}$ represent the reactions due to the external loading acting on the span.

An equation similar to (8) may be written for all plates in the cross-section, other than edge cantilever plates, from 1 to p_o . These equations may be summarised as:

$$\{R\} = [AH] \{M\} + \{RF\} \quad (9)$$

so that the vector representing the edge reactions normal to the plane of each plate $\{R\}$ at the typical nodal section n may be determined. The vertical and horizontal components of these normal reactions may then be obtained by simple resolutions, and a vector $\{R_z^e\}$ containing the vertical components of the plate edge reactions and another vector $\{R_y^e\}$ containing the horizontal components of these reactions may be established. By using the $[AD]$ matrix once again, the total vertical and horizontal reactions at each joint may be obtained as:

$$\begin{aligned} \text{vertical joint reactions } \{RZ\} &= [AD] \{R_z^e\} \\ \text{horizontal joint reactions } \{RY\} &= [AD] \{R_y^e\} \end{aligned} \quad (10)$$

The transverse frame analysis is now complete for the typical nodal section n . The analysis is repeated for every nodal section, giving the transverse bending moments $\{M_n\}$ at each of these sections, together with the intensities of the vertical and horizontal reactions at the joints $\{Rz_n\}$ and $\{Ry_n\}$.

3.3. Linking Analysis

In this stage of the analysis, the joint reactions obtained from the transverse slab analysis are reversed in direction and then applied as joint loads on to the plate system. Since it is assumed that the plate system can only transmit forces in the planes of the various plates, the joint loads are resolved into their components in the planes of the plates to give the plate loads.

In the case of a joint at which more than 2 plates meet, the transverse frame reactions cannot be resolved into components in the direction of the intersecting plates, since only two equilibrium equations are available, i.e. the vertical and horizontal resolution of forces at the joint. However, if two of the three plates meeting at the joint are co-planar, then the total in-plane force component acting on these two plates can be determined and the analysis can be continued. The type of joint idealisation required to enable this restriction to be met has already been shown in Fig. 5.

3.4. Longitudinal Plate Analysis

In the longitudinal plate analysis, the plates are analysed as beams spanning between the supports and since the linking analysis is only able to provide the total plate load acting on any series of adjacent co-planar plates, such a system of co-planar plates is considered as one wide beam unit during the plate analysis. For the typical structure of Fig. 4, the beam units considered are as shown in Fig. 7, plates 1 and 2 being considered to act as a single beam, plates 4 and 5 being considered to act together as another single beam, and plates 3, 6 and 7 each being considered as an individual beam.

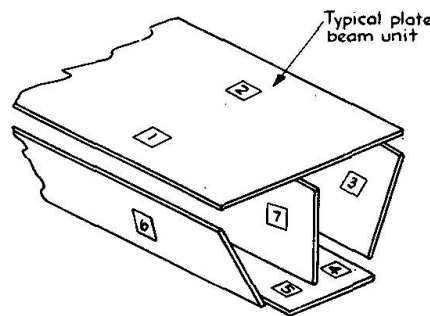


Fig. 7. Beam units considered during analysis of typical structure.

Thus, in the general case, a single plate beam unit considered during the longitudinal plate analysis may consist of several plates and may be connected to other units at its edges and also along several other lines within its width. A typical beam unit is shown in Fig. 8 this unit containing plates 1, 2... r ... v . It is assumed that all the co-planar plates within the beam unit are numbered consecutively (in accordance with restriction 4 in Section 3.1), and that at the typical nodal section n , each co-planar plate has the same thickness ($t_{1,n} = t_{2,n} \dots = t_{r,n} \dots = t_{v,n}$) and the same elastic modulus ($E_{1,n} = E_{2,n} \dots = E_{r,n} \dots = E_{v,n}$). However, the theory can be adapted to accommodate different thicknesses, etc.

During the longitudinal bending, the forces shown in Fig. 8 will be set up at the typical nodal section n of the beam unit, this nodal section being assumed to

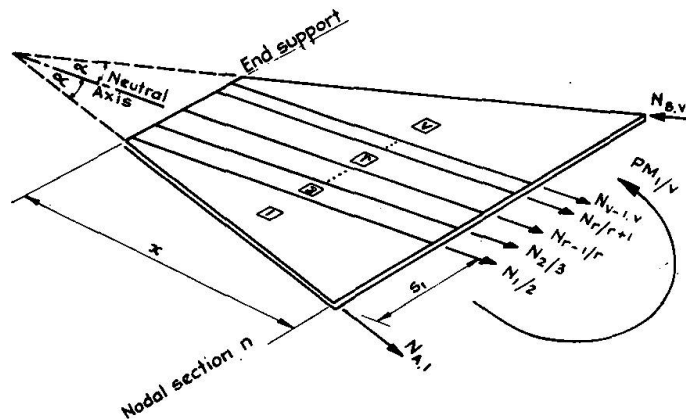


Fig. 8. Forces set up in a typical plate beam unit containing several co-planar plates.

be at a distance x from the end of the beam. For clarity, the suffix n relating to the nodal section will be omitted from the following equations, but it should be remembered that these equations relate to nodal section n . The forces set up are:

1. Longitudinal forces $N_{A1}, N_{1/2} \dots N_{r/r+1} \dots N_{Bv}$ set up along the lines at which the beam unit is connected to adjacent web units. These forces are set up by virtue of the longitudinal shear developed between the adjacent units, this shear being assumed to have an intensity $U_{A1}, U_{1/2} \dots U_{r/r+1} \dots U_{Bv}$ at the various joints. The positive directions of these forces are shown in Fig. 8, all the forces, apart from N_{Bv} being positive when tensile.
2. A bending moment $PM_{1/v}$ set up by the total in-plane plate load acting on the beam unit as obtained from a resolution of the transverse frame reactions. This moment is calculated assuming the beam unit to be completely disconnected from all other beam units, and is defined as positive when it is a sagging moment, as shown in Fig. 8.

Having defined the forces acting on the section, the longitudinal bending stresses set up by these forces at nodal section n can now be calculated from beam theory. In the first instance, the bending stresses parallel to the neutral axis of the beam unit will be calculated. It will be appreciated that with a tapered web beam the neutral axis of the beam will be inclined to the horizontal at an angle α as defined in Fig. 8. For convenience, define $H = s_1 + s_2 \dots s_r \dots + s_v$ and let $t = t_1 = t_2 \dots = t_r \dots = t_v$.

Total moment (sagging positive) on cross-section

$$M = PM_{1/v} + N_{A,1} \frac{H}{2} \cos \alpha + N_{1/2} \left(\frac{H}{2} - s_1 \right) \dots + N_{r/r+1} \left(\frac{H}{2} - (s_1 + s_2 \dots + s_r) \right) \dots + N_{B,v} \frac{H}{2} \cos \alpha \quad (11)$$

Total axial force (tension positive) on cross-section =

$$= N_{A,1} \cos \alpha + N_{1/2} \dots + N_{r/r+1} \dots - N_{B,v} \cos \alpha$$

Thus knowing the bending moment and axial forces acting on the section from equation (11) the total longitudinal stresses set up at all points across the section can now be determined from standard beam theory. For example, for the typical case of a single plate " p ", which does not form part of a co-planar plate unit, the stress acting at edge " A " is as given in equation (12).

$$\bar{\sigma}_{A,p} = \frac{6}{t_p s_p^2} PM_p + \frac{4}{t_p s_p} N_{A,p} \cos \alpha_p + \frac{2}{t_p s_p} N_{B,p} \cos \alpha_p \quad (12)$$

The stresses at the edge of the typical plate, i.e. $\bar{\sigma}_{A,p}$ and $\bar{\sigma}_{B,p}$ calculated according to equation (12), act parallel to the neutral axis of the plate. Before equilibrium and compatibility between this and adjacent plates can be considered these stresses must be converted into stresses along the edges of the plate unit. The resolution at edge A of plate p is illustrated in Fig. 9 and the stress along this edge at section n may be written as:

$$\sigma_{A,p} = \frac{\bar{\sigma}_{A,p}}{\cos^2 \alpha_p} - \frac{2U_{A,p} \tan \alpha_p}{t_p} \quad (13)$$

and a similar equation may be written for edge B of the plate.

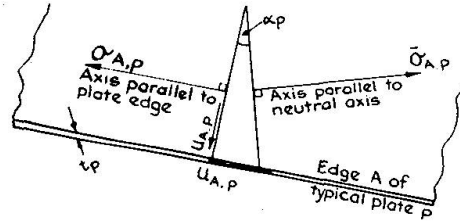


Fig. 9. Resolution of stresses at typical plate edge.

Thus, for the typical plate beam unit at nodal section n , by using equations (12) and (13) a relationship can be established between stresses (σ) and hence the strains (ϵ) set up along all the lines at which the unit is connected to adjacent beam units and the longitudinal shear forces (N) and the distributed shear forces (U) acting along these lines, together with the bending moment (PM) that would be set up in the unit assuming it to be completely disconnected from adjacent units.

Similar relationships may be established for all other plate beam units within the cross-section. If the beam unit has a free edge, as in the case of an edge cantilever, then the expressions must be modified to allow for the fact that no shear forces exist along this edge.

When the expressions have been established for all units at nodal section n , they may be written in a matrix form as follows:

$$\{\epsilon\} = [SN] \{N^e\} + \{MO\} - [SU] \{U^e\} \quad (14)$$

For the typical cross-section shown in Fig. 4, the strain vector $\{\epsilon\}$ for nodal section n will contain terms in the following order:

$$\epsilon_{A,1}; \epsilon_{1/2}; \epsilon_{B,2}; \epsilon_{A,3}; \epsilon_{B,3}; \epsilon_{A,4}; \epsilon_{4/5}; \epsilon_{B,5}; \epsilon_{A,6}; \epsilon_{B,6}; \epsilon_{A,7} \text{ and } \epsilon_{B,7}.$$

At a joint between adjacent beam units, the strains along the joint must satisfy compatibility. For example, for the typical cross-sections shown in Fig. 4, the strain compatibility equation for Joint 3 at the typical nodal section n becomes:

$$\epsilon_{B,2} + \epsilon_{A,3} = 0$$

The compatibility equations for the complete cross-section at nodal section n may be written as:

$$\{\Sigma\epsilon\} = 0 \quad (15)$$

It will be seen that the required addition of the plate edge strains can be carried out by setting up a matrix, that will be denoted by $[AD^1]$, which is a modified form of the $[AD]$ matrix defined earlier. For the typical structure shown in Fig. 4, $[AD^1]$ has the following form:

$$[AD^1] = \begin{bmatrix} 1 & 0 & 0 & 0 & 0 & 0 & 0 & 0 & 0 & 1 & 0 & 0 \\ 0 & 1 & 0 & 0 & 0 & 0 & 0 & 0 & 0 & 0 & -1 & 0 \\ 0 & 0 & 1 & 1 & 0 & 0 & 0 & 0 & 0 & 0 & 0 & 0 \\ 0 & 0 & 0 & 0 & 1 & 1 & 0 & 0 & 0 & 0 & 0 & 0 \\ 0 & 0 & 0 & 0 & 0 & 0 & 1 & 0 & 0 & 0 & 0 & 1 \\ 0 & 0 & 0 & 0 & 0 & 0 & 0 & 1 & 1 & 0 & 0 & 0 \end{bmatrix}$$

and the required addition may be obtained as:

$$\{\Sigma \varepsilon\} = [AD^1] \{\varepsilon\} = 0 \quad (16)$$

Then, substituting for $\{\varepsilon\}$ from equation (14):

$$[AD^1] [SN] \{N^e\} + [AD^1] \{MO\} - [AD^1] [SU] \{U^e\} = 0 \quad (17)$$

Also, at a joint between two plate beam units, in addition to the strain compatibility condition the shear forces along the joint must satisfy equilibrium.

For the typical cross-section shown in Fig. 4, the shear force equilibrium for joint 3 for example is as follows:

$$N_{B,2} = N_{A,3} = N_3$$

It will be seen that the shear equilibrium equations for the complete cross-section may again be established by using the $[AD^1]$ matrix as follows:

$$\{N^e\} = [AD^1]^T \{N\} \quad (18)$$

Similar equilibrium equations may be written for the distributed shear forces acting along the edge, i.e.

$$\{U^e\} = [AD^1]^T \{U\} \quad (19)$$

Substituting from equations (18) and (19) in equation (17) yields:

$$[AD^1] [SN] [AD^1]^T \{N\} + [AD^1] \{MO\} - [AD^1] [SU] [AD^1]^T \{U\} = 0 \quad (20)$$

Defining, for convenience, two new matrices and a new vector:

$$\begin{aligned} [DN_n] &= [AD^1] [SN] [AD^1]^T \\ [DU_n] &= [AD^1] [SU] \text{ and } [DO_n] = [AD^1] \{MO\} \end{aligned}$$

Then, reintroducing the suffix n to show that the terms relate to the typical nodal section n , equation 20 may be re-written as:

$$[DN_n] \{N_n\} + \{DO_n\} - [DU_n] \{U_n\} = 0 \quad (21)$$

There are two unknowns in this equation, viz. the vectors $\{N_n\}$ and $\{U_n\}$ which represent, respectively, the total longitudinal shear force and the intensity of the longitudinal shear force at each joint at the nodal section n . Another relationship between these two vectors must be established before the equations can be solved.

Such a relationship will now be obtained by considering nodal section n on a typical joint j . Let a co-ordinate axis z be taken along this joint, as shown in Fig. 10a, the distance along the joint between adjacent nodal sections then being $l_{z,n-1}$, $l_{z,n}$, etc. By considering an elemental length δz of the joint, as in Fig. 10b at a distance z from the end support, it is apparent that, $U(z) = dN(z)/dz$.

A portion of a typical curve representing the longitudinal distribution of the joint shear forces is shown in Fig. 10a. Assume that the curve may be represented by a polynomial function:

$$N(z) = N_n + a_1 z + a_2 z^2$$

the origin of the z co-ordinate axis being assumed to be located at section n .

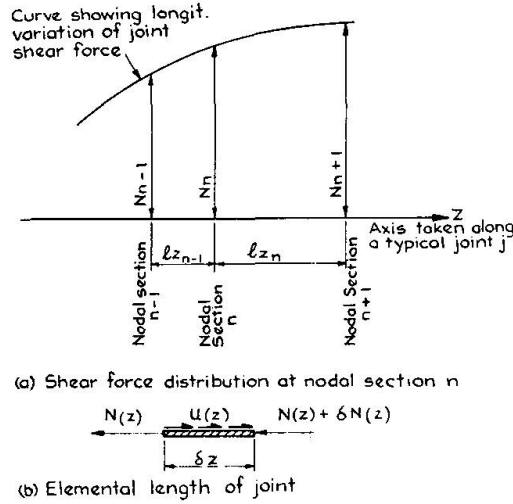


Fig. 10. Distribution of shear forces along typical joint.

$$\text{Then } U(z) = a_1 + 2 a_2 z \quad (22)$$

and by determining the values of the coefficients $a_1 + a_2$ from the values of N at each section, the value of U_n may be determined from equation (22) as:

$$U_n = N_{n-1} \frac{-l_{zn}}{l_{zn-1} (l_{zn-1} + l_{zn})} + N_n \frac{(l_{zn} - l_{zn-1})}{l_{zn} l_{zn-1}} + N_{n+1} \frac{l_{zn-1}}{l_{zn} (l_{zn-1} + l_{zn})} \quad (23)$$

A similar equation may be written for each other joint at nodal section n and these equations may be summarised as:

$$\{U_n\} = [LB_n] \{N_{n-1}\} + [LC_n] \{N_n\} + [LF_n] \{N_{n+1}\} \quad (24)$$

Equation (24) gives the required additional relationship between the $\{U_n\}$ and $\{N_n\}$ vectors,

Substituting for $\{U_n\}$ in equation (21) gives:

$$[DN_n] \{N_n\} + \{DO_n\} - [DU_n] [LB_n] \{N_{n-1}\} - [DU_n] [LC_n] \{N_n\} - [DU_n] [LF_n] \{N_{n+1}\} = 0$$

This equation may be written as:

$$[DB_n] \{N_{n-1}\} + [DC_n] \{N_n\} + [DF_n] \{N_{n+1}\} = -\{DO_n\} \quad (25)$$

Where

$$[DC_n] = [DN_n] - [DU_n] [LC_n];$$

$$[DB_n] = -[DU_n] [LB_n] \text{ and } [DF_n] = -[DU_n] [LF_n]$$

Equation (25) relates to the typical nodal section n only and similar equations may be established for each nodal section and all the equations thus obtained arranged in matrix form. Equation (26) illustrates the form of these equations for 3 typical nodal sections: $n-1$, n and $n+1$.

$$\begin{bmatrix} [DB_{n-1}] & [DC_{n-1}] & [DF_{n-1}] \\ & [DB_n] & [DC_n] & [DF_n] \\ & & [DB_{n+1}] & [DC_{n+1}] & [DF_{n+1}] \end{bmatrix} \begin{Bmatrix} \{N_{n-1}\} \\ \{N_n\} \\ \{N_{n+1}\} \end{Bmatrix} = - \begin{Bmatrix} \{DO_{n-1}\} \\ \{DO_n\} \\ \{DO_{n+1}\} \end{Bmatrix} \quad (26)$$

The equations for the complete structure, i.e. for all nodal sections, can be summarised as shown in equation (27) and by inverting the $[AA]$ matrix, the joint shear forces can be obtained as shown in equation (28).

$$[AA] \{N\} = \{M\} \quad (27)$$

$$\{N\} = [AA]^{-1} \{M\} \quad (28)$$

The terms of the vector $\{N\}$ represent the shear forces at each joint at each nodal section. The joint shear forces relating to any one nodal section, e.g. $\{N_n\}$, can then be extracted from the $\{N\}$ vector and the shear forces at the edges of the individual plates, i.e. $\{N^e\}$, determined, as in equation (18).

Knowing the longitudinal edge shear forces acting on each individual plate, the *Longitudinal Stresses* at the edges of each plate acting parallel to the neutral axis of the plate can then be determined from equation (12). Since in equation (12) these stresses are assumed to be linearly distributed across the width of each plate the stress at any point across the width of the plate can be determined once the edge stresses are known.

Since the stress distribution and therefore the bending moment acting at all sections of each of the plate beam units is now known, the deflection of each individual plate can be determined using normal beam theory. Once all the in-plane plate deflections are known, the *Vertical* and *Horizontal Displacements* of the joints may be obtained from a simple resolution procedure.

The Nodal Section No-Sway Analysis is now complete. During the analysis the following quantities have been calculated at each nodal section:

1. The transverse bending moments at the plate edges and at any required position across the width of each plate.
2. The longitudinal stresses at the plate edges and at any required position across the width of each plate.
3. The deflection normal to the plane and the deflection in the plane of each plate at any required position across the width of the plate.
4. The vertical and horizontal displacement of each joint.

These quantities present a comprehensive picture of the behaviour of the box girder.

4.0. Sway Correction

During the No-Sway analysis described in Section 3, the transverse frame action was analysed assuming the one-way slab strips to be rigidly supported at the longitudinal joints of the girder, whereas, in the longitudinal plate analysis, these joints were allowed to deflect and their deflections were calculated. Consequently, incompatibilities exist between the joint displacements of the plate and frame systems and the object of the Sway Correction is to remove these incompatibilities.

There are two methods by which the Sway Correction may be accomplished. The first of these methods is based on the "Method of Particular Loadings"

developed by YITZHAKI [4] for folded plate structures and this provides a closed-form solution, which is applicable to all girders, but which considerably increases demands on computer time and storage space. The second method employs an iterative technique and does not lead to any increased demands on computer storage space and converges in all cases, the rate of convergence depending on the form of the girder cross-section.

The authors have investigated the use of both methods and have found that the iterative technique is the most suitable for a method of analysis that is to be used in a design office. An adaptation of the Standard Iterative Technique used in folded plate structures was first tried but was found to be unsatisfactory since, in some instances, the rate of convergence was very slow and, in some particular cases, the solution was found to be divergent. As a result of this an improved "Accelerated Iterative Technique" based upon a method established by MAST [12] for folded plates has been developed and Fig. 11 shows how, for a typical girder, the accelerated iterative process rapidly converges to the correct solution where as the normal iterative procedure does not.

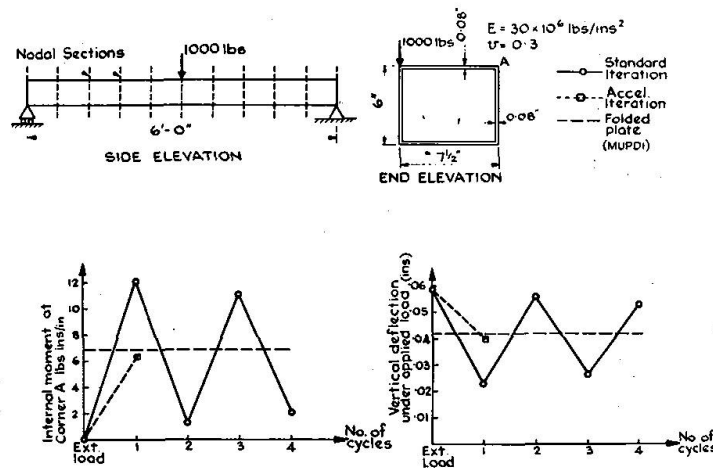


Fig. 11. Comparison of rates of convergence of standard iteration and accelerated iteration sway correction procedures.

The first step in the Sway Correction is to quantify the incompatibilities between plate and frame displacements, arising from the No-Sway Analysis. A convenient way of doing this is to express the incompatibilities in terms of the "relative joint displacements" or "sway displacements" of each component plate. The sway displacement for a typical plate p at nodal section n , i.e. $\Delta_{p,n}$ is defined in Fig. 12a.

Hence, the in-plane plate displacements $v_{p,n}$ and the vertical and horizontal joint displacements $\delta v_{j,n}$ and $\delta h_{j,n}$ obtained from the No-Sway Analysis, must now be converted, by means of simple geometry, into equivalent sway displacements $\Delta_{p,n}$ for the various plates and these sway displacements must be determined at each nodal section that does not coincide with the position of a supporting diaphragm. At a diaphragm position, all such sway displacements are prevented. Clearly should any plate have a free edge, such as an edge cantilever plate, then a sway displacement will not be set up within the plate.

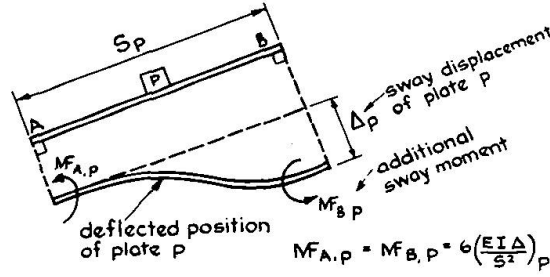


Fig. 12a. Definition of sway displacement of typical plate p at nodal section.

4.1. The Accelerated Iteration Method

It must be remembered that the object of the Sway Correction is to remove the incompatibilities existing between the displacement of the frame and plate systems at the end of the No-Sway Analysis for the external load condition. Defining the incompatibility for a typical plate as:

$$\text{incompatibility} = \text{sway displacement of plate in plate system} - \text{the sway displacement of plate in frame system} \quad (29)$$

then, since in the No-Sway analysis for the girder under external loading, the joints of the frame system are assumed to be non-deflecting, the incompatibility (β) for a typical plate p at nodal section n arising from the No-Sway analysis is:

$$\beta_{p,n}^{Ext} = \Delta_{p,n}^{Ext} - 0 \quad (30)$$

where the superscript *Ext* denotes that the incompatibilities relate to the No-Sway Analysis.

The first cycle of the Accelerated Iteration Method is now commenced. Sway deformations equal to the incompatibilities ($\Delta_{p,n}^{Ext}$) which exist at the end of the external load analysis are imposed on each member of the frame system at each nodal section. These imposed deformations set up additional transverse moments within the members and another No-Sway Analysis is now carried out as described in Section 3. From this analysis, additional sway displacements ($\Delta_{p,n}^I$) are calculated for the plate system. Then, according to equation (29), the incompatibilities arising from the first cycle may be defined as:

$$\beta_{p,n}^I = \Delta_{p,n}^I - \Delta_{p,n}^{Ext} \quad (31)$$

One of the unwanted incompatibilities corresponding to the external loading, as determined from equation (30), may now be removed by superimposing the incompatibilities obtained from the first cycle, as listed in equation (31), in the correct proportion. Any incompatibility may be chosen for removal; for example, to remove the incompatibility in plate 4 at nodal section 6, then:

$$\beta_{4,6}^{Ext} + \mu_I^I (\beta_{4,6}^I) = 0 \text{ therefore } \mu_I^I = - \frac{\beta_{4,6}^{Ext}}{\beta_{4,6}^I} \quad (32)$$

μ_I^I defining the proportion of the values from the first cycle that must be superimposed on to the external load values.

The complete solution at the end of the first cycle may now be obtained as:

$$\text{Complete solution} = \text{external load solution} + \mu_I^I (\text{first cycle solution}) \quad (33)$$

Also, the incompatibilities remaining at the end of the first cycle may be determined as:

$$\beta_{p,n}^{I'} = \beta_{p,n}^{Ext} + \mu_I^I (\beta_{p,n}^I) \quad (34)$$

the remaining incompatibility for plate 4 at nodal section 6 now being zero.

In the *second cycle* of the Accelerated Iteration Method, sway deformations equal to the incompatibilities that exist at the end of the first cycle, as in equation (34), are imposed on the slab system. Another No-Sway Analysis is carried out and additional sway displacements ($\Delta_{p,n}^{II}$) are calculated. Then, from equation (29), the incompatibilities arising from the second cycle are:

$$\beta_{p,n}^{II} = \Delta_{p,n}^{II} - \beta_{p,n}^{I'} \quad (35)$$

A superposition of a certain proportion (μ_{II}^{II}) of these incompatibilities, together with a certain proportion (μ_I^{II}) of the first cycle incompatibilities, from equation (31), will enable any two of the unwanted incompatibilities corresponding to the external loading listed in equation (30), to be removed.

For example, if the incompatibilities of plates 4 and 9 at nodal section 6 are chosen for removal, then:

$$\begin{aligned} \text{for plate 4} \quad & \beta_{4,6}^{Ext} + \mu_I^{II} (\beta_{4,6}^I) + \mu_{II}^{II} (\beta_{4,6}^{II}) = 0 \\ \text{for plate 9} \quad & \beta_{9,6}^{Ext} + \mu_I^{II} (\beta_{9,6}^I) + \mu_{II}^{II} (\beta_{9,6}^{II}) = 0 \end{aligned} \quad (36)$$

From these equations, the values of the proportions μ_I^{II} and μ_{II}^{II} may be determined and then the complete solution at the end of the second cycle may be obtained as:

$$\begin{aligned} \text{Complete solution} = & \text{external load} + \mu_I^{II} (\text{1st cycle} + \mu_{II}^{II} (\text{2nd cycle} \\ & \text{solution} \quad \text{solution}) \quad \text{solution}) \end{aligned} \quad (37)$$

Also, the incompatibilities remaining at the end of the second cycle may be determined as:

$$\beta_{p,n}^{II'} = \beta_{p,n}^{Ext} + \mu_I^{II} (\beta_{p,n}^I) + \mu_{II}^{II} (\beta_{p,n}^{II}) \quad (38)$$

the remaining incompatibilities on both plates 4 and 9 at nodal section 6 now being zero.

A *third cycle* of the Accelerated Iteration Method may now be carried out, in which sway deformations equal to the incompatibilities that exist at the end of the second cycle are applied to the frame system and another No-Sway Analysis of the girder carried out. This third cycle will provide a further set of incompatibilities which, when taken in conjunction, with those obtained from the first and second cycles, will enable any three of the initial incompatibilities corresponding to the external loading to be removed. Thus, a solution of greater accuracy may be obtained after the third cycle.

Further iterative cycles may be carried out, each successive cycle commencing with the application to the frame system of sway deformations equal to the incompatibilities remaining at the end of the previous cycle. In each cycle, a

No-Sway Analysis of the girder has to be carried out, and each cycle provides a new set of incompatibilities which enables one more of the original incompatibilities, arising from the external load analysis, to be eliminated. In order to remove all these original incompatibilities and thus provide an exact solution, the total number of iterative cycles required is theoretically equal to the product of the number of plates in the cross-section and the number of nodal sections taken, i.e. $p_o \times n_o$, and the last of these cycles would involve the solution of $p_o \times n_o$ simultaneous equations.

However, in practice it is found that, by virtue of the nature of the deformations set up in the box girder, the elimination of one particular incompatibility leads to the simultaneous elimination of several others, so that an accurate solution can be obtained by taking very many fewer cycles than are theoretically necessary for an exact solution. The reasons for this are two-fold:

In the first place, any set of sway displacements set up will have a variation over the length of the girder which is a function of the elastic properties of the girder. Thus, any set of sway displacements such as Δ^I , set up by another set of sway displacements, such as Δ^{Ext} will have a longitudinal distribution similar to the original set and the ratio of Δ^I to Δ^{Ext} will be almost the same at each nodal section. Consequently, when the incompatibilities are eliminated from a particular plate at a particular nodal section, they are also made extremely small at all the other nodal sections on that plate. Thus, accurate results may be obtained by considering the removal of incompatibilities at a few nodal sections only; in many cases it has been found sufficient to remove the incompatibilities at only one nodal section and in no case has the removal of the incompatibilities at more than two nodal sections been found necessary in order to provide a convergent solution.

Secondly, within any closed cell of the cross-section, the relationship between the sway displacement of any one plate and the sway displacements of the other plates within the cell is dependent on the resistance of the girder cross-section to distortion. For any set of sway displacements, such as Δ^I , set up by another set of sway displacements, such as Δ^{Ext} , the ratio of Δ^I to Δ^{Ext} will be similar for each plate within the closed region. Consequently, when the incompatibilities are removed from any one plate within the closed cell, they are also greatly reduced for all the other plates within the cell.

Satisfactory convergence of the Accelerated Iteration Method can thus be achieved by removing the incompatibilities at one or two nodal sections only and carrying out one iterative cycle for each closed cell within the cross-section, together with one cycle for any other plates that may exist in the cross-section. Thus, for a multi-cell girder, where the cross-section effectively forms only one closed region, one iterative cycle only is required. For a girder containing discreet cells, such as that shown in Fig. 12b, one iterative cycle is required for each box, together with an additional cycle for each connecting flange, so that three iterative cycles are required in this particular case. The order in which the 3 cycles are carried out is immaterial as illustrated in the convergence plot shown in Fig. 12b.

When all the required iterative cycles have been completed for a given section, the final results for the complete girder are obtained by superimposing the appropriate proportion of the values calculated in each cycle on to the original values obtained from the external load analysis.

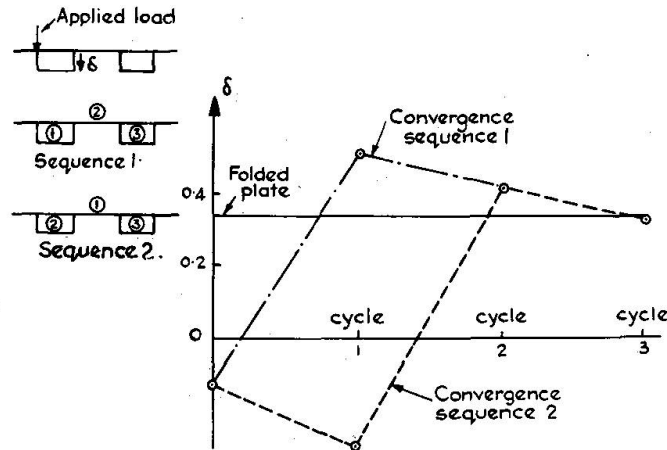


Fig. 12b. Illustration of convergence of solution for discrete cell girder.

5. Discussion of Results

In this section, the accuracy of the Nodal Section Method will be assessed by analysing several different types of girders subjected to different loading and support conditions and comparing the results obtained from the Nodal Section Method with those results obtained from a full three-dimensional Finite Element analysis and also to results obtained from the Folded Plate Method (MUPDI) developed by Scordelis. Both these methods are currently widely used in box girder analysis and their accuracy, within their particular fields of application, has been firmly established.

The first type of girder considered will be the simply-supported, single-cell girder shown in Fig. 13. A full parametric study of such girders has been carried out by the authors [14] in which 20 girders of differing dimensions were analysed, the girder dimensions and proportions being chosen on the basis of a statistical survey of the girders currently in service. All these girders were subjected to a line

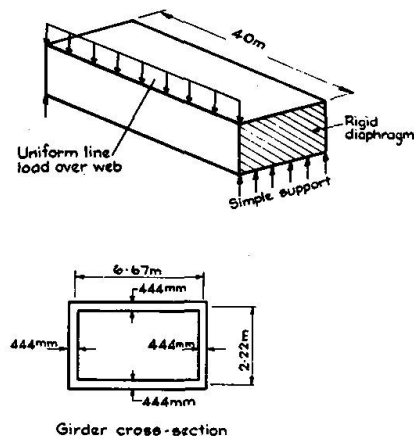


Fig. 13. Details of typical single-cell girder.

loading applied over one web, as shown in Fig. 13, since such a loading would tend to set up gross cross-sectional deformations and would thus provide a good test of the accuracy of the Nodal Section Method.

The extensive results obtained from this parametric study have been presented in detail in a separate report [14] and cannot be repeated here. However, a sample of the results will be presented for the girder having the dimensions shown in Fig. 13 and this girder may be regarded as a typical single-cell girder, since its proportions closely represent the most frequently occurring proportions observed during the statistical survey of practical girders.

Since both the Finite Element and Nodal Section methods require an idealisation of the structure, convergence tests were carried out first of all for the typical girder to determine the accuracy obtainable from various idealisations. The finite element meshes and nodal section positions considered are shown in Fig. 14 and the results of the convergence tests are summarised in Fig. 15 where the predicted transverse moments and longitudinal stresses at the loaded joint at the mid-span cross-section are compared to values given by the folded plate method. The results show clearly that both methods converge rapidly and that for the particular loading case considered, reasonably accurate results can be obtained by taking 5 nodal sections only.

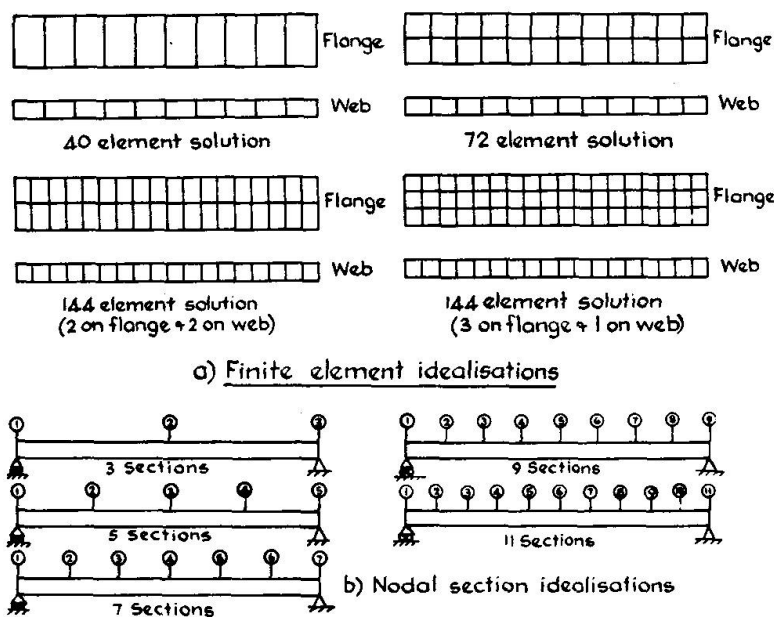


Fig. 14. Idealisations considered in convergence tests.

In each Nodal Section Analysis, two cycles of the sway correction procedure were carried out since it has been found that two cycles are necessary in order to obtain accurate values of the transverse moments for concrete girders in which the resistance to cross-sectional deformations is high. The longitudinal stresses and deflections of both concrete and steel girders and also the transverse moments of steel girders are obtained accurately after 1 sway correction. In no case during the parametric study of single-cell girders was it found necessary to employ more than 2 cycles of the sway correction procedure.

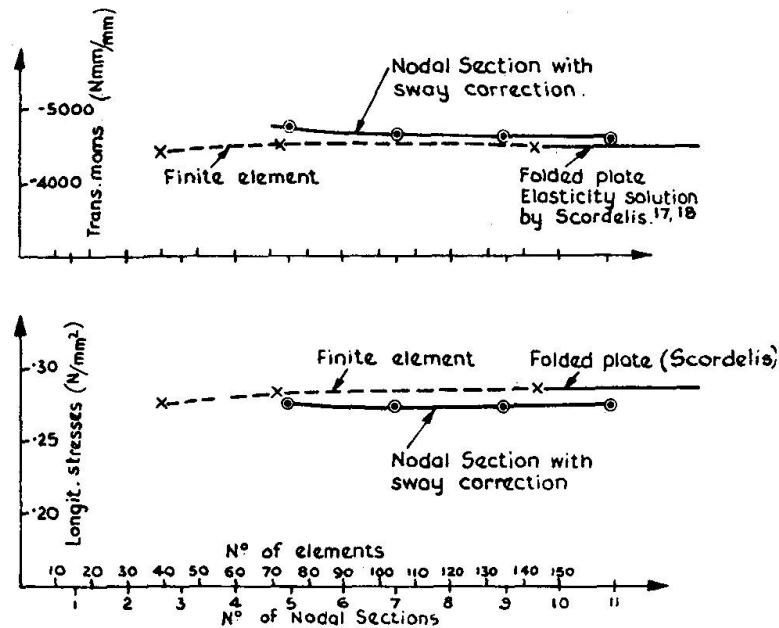


Fig. 15. Convergence of transverse moments and longitudinal stress values for a typical single-cell girder.

In Fig. 16 the Finite Element and Nodal Section solution times for the parametric study are plotted, and this diagram illustrates clearly the main disadvantage of the finite element method in a design context. For the finest mesh considered in the analysis, i.e. the mesh containing 144 elements, a solution time of 20 minutes was required on an I.C.L. System 470 computer, whereas the comparable time for the Nodal Section solution employing 11 sections and 2 sway corrections, was of the order of 1 minute. The finite element mesh containing 144 elements, whilst being more than adequate to provide accurate results for the simply supported single-cell girder of Fig. 13, would certainly not be sufficient for the analysis of multi-cell, multi-span girders and the use of larger meshes for such structures would make the Finite Element Solution time prohibitive in any design study.

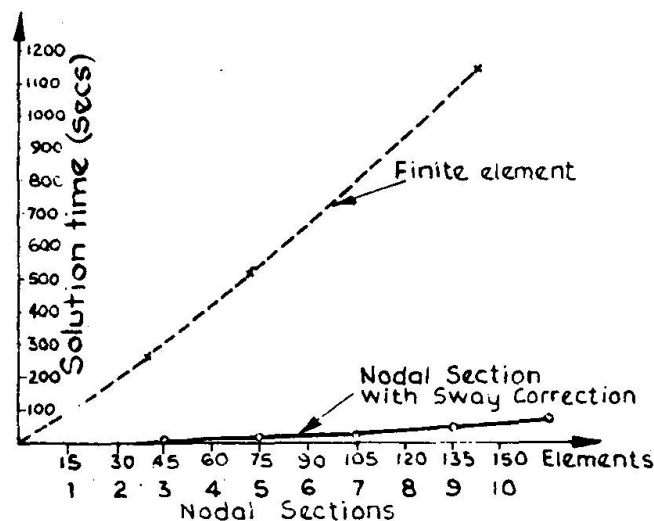


Fig. 16. Comparison of solution times for a typical single-cell girder.

In addition to the actual computer time used, the Finite Element Solution also requires a great deal of data preparation time. The 144 element mesh used in the present investigation required the preparation of some 300 computer cards, compared to the preparation of some 25 cards for the comparable Nodal Section Solution, and this is another serious disadvantage of the Finite Element Method in any design application.

Since the values given in Fig. 15 relate to the loaded corner of the girder only, the transverse moments, longitudinal stresses and vertical deflections for the complete central cross-section are shown in Fig. 17 and it is seen that the distributions predicted by the Nodal Section and Folded Plate methods agree closely.

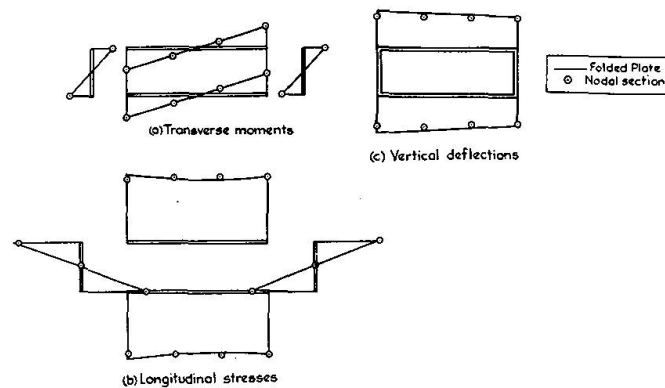


Fig. 17. Distribution around mid-span cross-section of typical girder.

Figures 15 and 17 shown the accuracy obtainable with the Nodal Section Method for one typical girder only. Obviously, as the girder proportions were varied during the parametric study, significant changes occurred in the structural behaviour, but, in all cases, the accuracy of the Nodal Section solution was maintained. An example of this is given in Fig. 18 where the effects of varying the

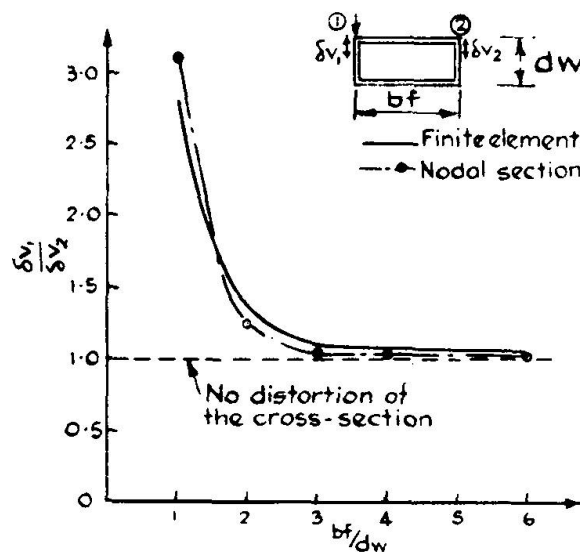


Fig. 18. Variation in ratio of vertical web deflections with variation in flange width/web depth ratio (bf/dw).

flange width/web depth parameter are illustrated. The amount of cross-sectional deformation under load is seen to vary rapidly with a change of this parameter, but the curves obtained from the nodal section and finite element solutions are seen to agree closely throughout the complete range considered.

In addition to single-cell girders, the two types of girder shown in Fig. 19 were also analysed. Since, as discussed earlier, the finite element solution times for such girders would be prohibitive, the Nodal Section values will in both cases be compared to results obtained from the Folded Plate Method.

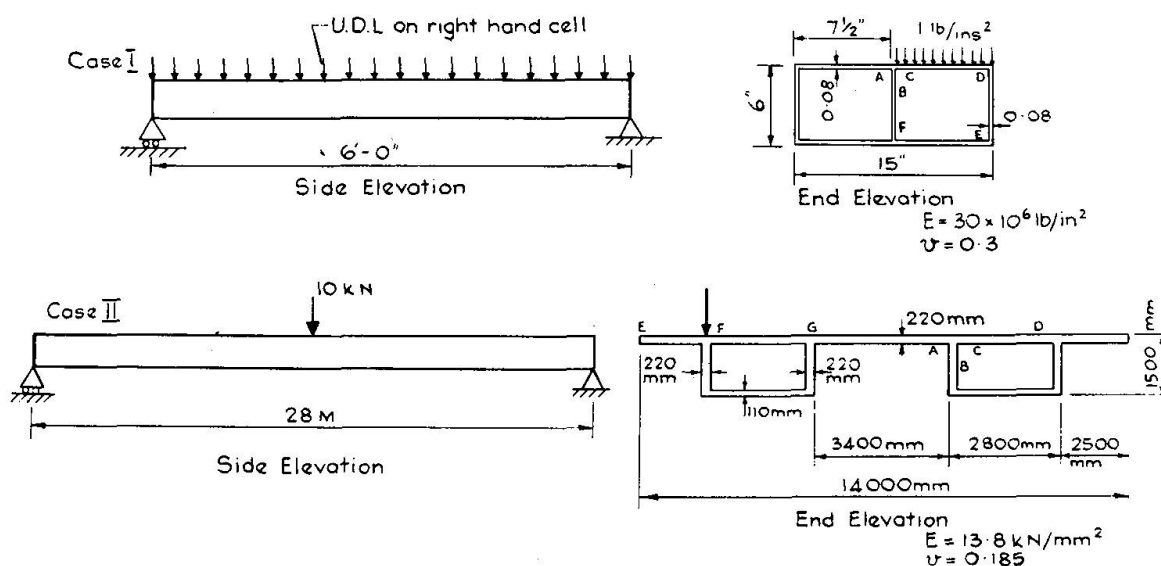


Fig. 19. Typical sections considered.

In Fig. 19, Case I shows a simply supported double-cell steel box, the girder being subjected to a transversely unsymmetrical loading consisting of a uniformly distributed load applied over one of the cells. Certain, typical results for this girder are listed in Table 1 – Case I and it is seen that the values of transverse moments, longitudinal stresses and deflections given by the Nodal Section Method agree closely with those given by the Folded Plate Method.

Similarly, close agreement of the values given in Table 1 – Case II is observed, these values having been obtained for the typical discrete-cell, concrete girder illustrated in Fig. 19 Case II. The convergence characteristics of the Nodal Section solution for this girder have been discussed earlier and shown in Fig. 12b and the results given in Table 1 – Case II were obtained after the third iterative cycle. For a point loading applied over a web, such as that shown in Fig. 19 – Case II, the Nodal Section Method, in common with most other methods, is not capable of predicting accurate values of the extremely high stresses set up in the immediate vicinity of the point loads. However, at positions away from the point load, satisfactory values are given by the method, as shown in the table.

Table 1. Case I - Double-cell girder

Solution	Transverse Moms (lbs ins/inch) at $\frac{1}{2}$ - span						Longit. stresses (lbs/ins ²) at $\frac{2}{5}$ - span						Deflections (ins $\times 10^{-5}$) at $\frac{1}{2}$ - span					
	Pt. A		Pt. B		Pt. C		Pt. D		Pt. B		Pt. D		Pt. E		Pt. F		Vert.	
	Pt. A		Pt. B		Pt. C		Pt. D		Pt. B		Pt. D		Pt. E		Pt. F		Pt. B	
Folded Plate	1.27		-3.17		4.44		2.39		558		1129		-1130		-556		39.5	
Nodal Section	1.37		-3.08		4.44		2.41		534		1135		-1135		-534		33.1	

Case II - Discreet-cell girder

Solution	Transverse Moms (Nmm/mm) at $\frac{1}{2}$ - span						Longit. stresses (N/mm ² $\times 10^4$) at $\frac{2}{5}$ - span						Vert. deflection (mm $\times 10^3$) at $\frac{1}{2}$ - span					
	Pt. A		Pt. B		Pt. C		Pt. D		Pt. E		Pt. F		Pt. G		Pt. A		Pt. F	
	Pt. A		Pt. B		Pt. C		Pt. D		Pt. E		Pt. F		Pt. G		Pt. A		Pt. F	
Folded Plate	403		304		99		6.2		206		200		167		130		432	
Nodal Section	474		361		113		7.5		206		186		161		130		352	

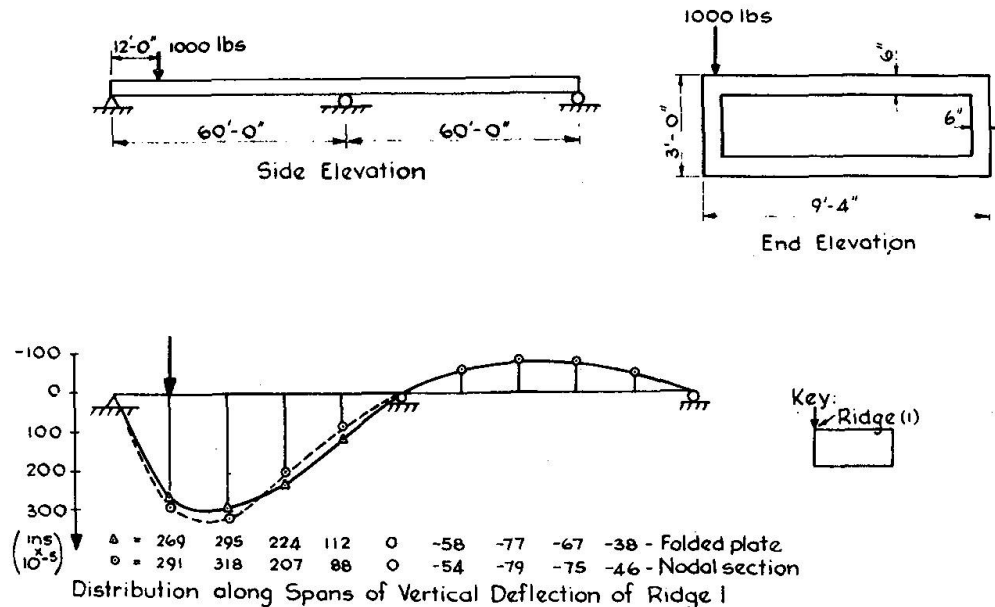


Fig. 20. Results for unsymmetrically loaded continuous girder.

All the girders considered in the comparison so far have been simply supported, but in Fig. 20 a continuous single-cell girder subjected to an unsymmetrical point loading over one web is illustrated, the loading being applied to one span only at a position close to the end support. In the figure, the variation along both spans of the vertical deflection of the loaded joint is plotted, and the unsymmetrical nature of the behaviour about the mid-span support position is clearly illustrated. The curves predicted by both the Nodal Section and Folded Plate methods are seen to correspond closely in both the loaded and unloaded spans.

Finally, the tapered girder shown in Fig. 21 was analysed, the girder once again being subjected to an unsymmetrical line loading applied over one of the webs. In this case, the Folded Plate method could not be used in the analysis since it is not capable of dealing with girders of non-uniform cross-section, consequently, the Nodal Section results are compared to values obtained by the Finite Element Method. In the figure, the variation along the span of the vertical deflection of a typical joint is plotted together with the distribution of the transverse moments and longitudinal stresses around the mid-span cross-section, and the Nodal Section and Finite Element values are once again seen to agree closely in all cases.

6. Advantages of the Nodal Section Method

The nodal section method provides a simple and accurate method of analysis for box girders. The computer programme (BOXGDR) based on the method requires relatively little computer time and storage space and is thus an economical means of analysing girders at the design stage, when many analyses may be necessary in order to achieve the optimum dimensions. The programme has the further advantage that both the preparation of data and the interpretation of results is relatively simple thus leading to additional significant economies.

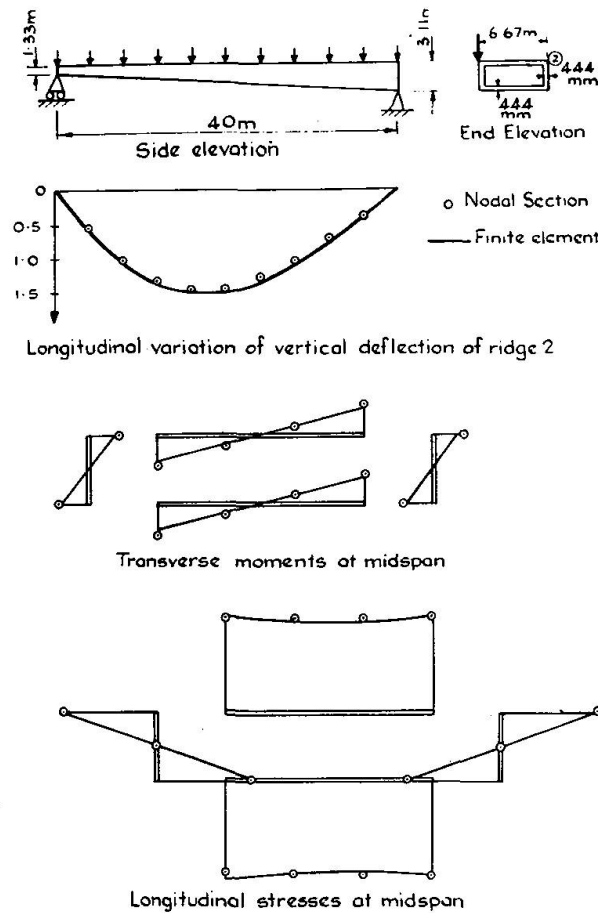


Fig. 21. Results for tapered girder.

Furthermore, the sequential nature of the calculations enables solutions to be obtained by hand, in many cases, without requiring the use of digital computers. In addition to the obvious economic advantages, such a hand solution enables the engineer to retain a better appreciation of the structural behaviour, particularly since each step within the analysis is related to a certain aspect of the physical behaviour.

Finally, the nodal section method is extremely adaptable and may be applied to the analysis of box girders of any cross-sectional shape under any loading conditions. It is also the only method, other than the very expensive finite element method, that is capable of dealing with the analysis of box girders in which the geometry of the cross-section varies along the span. Such girders are, of course, frequently encountered in practice, as, for example, in the case of motorway bridges having web plates of varying depths.

7. Conclusions

In this paper, the basic theory of the Nodal Section Method has been presented and the accuracy of the method in the analysis of a number of different girders has been illustrated. It is anticipated that this accuracy, coupled with the simplicity of the solution procedure, which enables solutions to be obtained either by

hand or from a computer programme that is very economical of computer time and storage space, will make the method a valuable analytical tool for use during the design of box girders.

Several developments of the method are in hand at the present time. In the first place, the method is being extended to consider the effects of shear lag on the distribution of the longitudinal stresses set up in the flanges of a girder, and the proposed approach (13), which is based on the use of empirical factors, has yielded results of good accuracy. The method is also being developed for the analysis of box girders curved in plan, and results obtained to date show excellent agreement between the Nodal Section values and values obtained both experimentally and from a Finite Element study. Finally, the analysis of girders on skew supports and girders containing deflecting internal diaphragms is being considered together with the behaviour of girders of non-uniform cross-section. All these developments will greatly extend the field of application of the method without, in any way, affecting the simplicity and economy of the solution procedure.

The integration of the Nodal Section Method with a Finite Element solution is also being considered. Such an arrangement has been described in the present paper in the method for dealing with concentrated loadings. It is intended to develop this technique further so that the designer can if he wishes, when dealing with a position of rapidly changing stress, such as at column supports and internal diaphragms, use a Finite Element Solution to provide a more detailed picture of the stress field in the local area. This procedure thus providing an accurate and economical method of analysis with great adaptability and a wide field of application.

List of Symbols

$1 \dots n \dots n_o$	nodal section numbering.
$1 \dots p \dots p_o$	plate numbering.
$1 \dots j \dots j_o$	joint numbering.
A and B	plate edge labels.
AD	connectivity matrix.
S	plate width.
t	plate thickness.
\emptyset	inclination of plate to horizontal.
M	transverse bending moments.
N	longitudinal shear forces at the edges of the plate beams.
σ	longitudinal stresses.
Δ	sway displacement of a plate.

Acknowledgments

The Authors wish to thank the Highways Engineering Computing Branch of the Department of the Environment and R. Travers Morgan & Partners, Consulting Engineers, for sponsoring the development of the Nodal Section Method.

In particular, the Authors gratefully acknowledge the many fruitful discussions that they have had with Dr. R. G. Anderson of R. Travers Morgan & Partners.

The Authors are also indebted to Mr. J.W. Waddell, postgraduate student at the Department of Civil and Structural Engineering, University College, Cardiff, for the assistance that he has given in many stages of the investigation.

References

1. GOLDBERG, J.E., and LEVE, H.L.: Theory of Prismatic Folded Plate Structures. *Publs. int. Ass. Bridge Struct. Engng*, Vol. 17, 1957, pp. 59–86.
2. DE FRIES SKENE, A., and SCORDELIS, A.C.: Direct Stiffness Solution for Folded Plates, *J. Struct. Div. Am. Soc. Civ. Engrs.*, Vol. 90, ST4, August 1964, pp. 15–47.
3. GAAFAAR, I.: Hipped Plate Analysis, Considering Joint Displacements. *Trans. Am. Soc. Civ. Engrs.*, Vol. 119, 1954, pp. 743–784.
4. YITZHAKI, D.: The Design of Prismatic and Cylindrical Shell Roofs. Haifa, Haifa Science Publishers, 1958.
5. SCORDELIS, A.C.: Analysis of Simply Supported Box Girder Bridges. University of California, Berkeley, Report No. SESM 66-17, October 1966.
6. SCORDELIS, A.C.: Analysis of Continuous Box Girder Bridges. University of California, Berkeley, Report No. SESM 67-25, November 1967.
7. EVANS, H.R., and ROCKEY, K.C.: A Critical Review of the Method of Analysis for Folded Plate Structures, *Proc. Instn. Civ. Engrs.*, 1971, 49 (June), pp. 171–192.
8. ROCKEY, K.C., and EVANS, H.R.: A Hand Solution Technique for Box Girders. To be published.
9. JOHNSON, C.D., and LEE, T.: Long Nonprismatic Folded Plate Structures, *J. Struct. Div. Am. Soc. Civ. Engrs.*, Vol. 49, ST6, June 1968, pp. 1457–1484.
10. PUCHER, A.: Influence Surface of Elastic Plates. Springer Verlag, Vienna, New York, 1964.
11. ROCKEY, K.C., and EVANS, H.R.: A Report on the Nodal Section Method. University College, Cardiff, Report No. NS/C/9, November 1972.
12. MAST, P.E.: An Iteration Method for Folded Plate Analysis. *Proc. World Conference on Shell Structures*, 1962, National Academy of Sciences, Washington D.C., 1964, pp. 517–526.
13. ROCKEY, K.C., and EVANS, H.R.: The Development of the Nodal Section Method to Include the Effects of Shear Lag. University College, Cardiff, Report No. NS/C/Extra 2, June 1974.
14. ROCKEY, K.C., and EVANS, H.R.: An Assessment of the Accuracy of the Nodal Section Method. University College, Cardiff, Report No. NS/Par/1, March 1974.

Summary

This paper describes the basic theory of the Nodal Section Method. This method has been developed for the analysis of box girders and, by assuming an idealised structural behaviour, it provides a simplified solution procedure, which it is anticipated will prove to be of use during the design stage, when many analyses of the girder may be required. Results are presented for many different types of box girders, the values given by the Nodal Section Method being compared to those obtained from other established methods, and the accuracy of the Nodal Section values is illustrated.

Résumé

La contribution décrit la théorie de base de la méthode de section nodale. Cette méthode a été développée pour l'analyse de poutres en caisson et, en admettant un comportement structural idéalisé, elle fournit une solution de procédure simplifiée, laquelle s'avère utile durant la phase du projet lorsque beaucoup d'analyses de poutres sont demandées. On présente des résultats pour de nombreux types différents de poutres en caisson; les valeurs fournies par la méthode de section nodale sont comparées à celles obtenues par d'autres méthodes établies. La précision des valeurs de la section nodale est démontrée.

Zusammenfassung

Die vorliegende Arbeit beschreibt die Grundtheorie der nodalen Querschnitts-Methode. Diese wurde zur Berechnung von Brückenträgern entwickelt; unter Annahme eines idealisierten baulichen Verhaltens liefert sie eine vereinfachte Verfahrenslösung, welche sich während des Projektstadiums als nützlich erweist, falls viele Berechnungen für den Träger erforderlich sind. Es werden Resultate für zahlreiche Typen von Kastenträgern mitgeteilt, wobei die aus der nodalen Querschnitts-Methode herrührenden Werte mit jenen von anderen Methoden verglichen werden und die Genauigkeit der nodalen Querschnittswerte veranschaulicht wird.

A Plastic Collapse Mechanism for Compressed Plates

Un mécanisme de rupture plastique pour plaques comprimées

Ein plastischer Bruchmechanismus für gedrückte Platten

A.C. WALKER

N.W. MURRAY

Monash University, Department of Civil Engineering, Clayton, Victoria, 3168

1. Introduction

The analysis developed in this paper sets out to explain and predict the manner in which rectangular plates, subject to uniform compression along two opposite edges, behave when they are compressed beyond their ultimate load. The classical elastic theory for the instability of a flat plate [1] and the analysis for the subsequent large deflection behaviour [2] are now well-known. For individual thin plates ($\sigma_y/\sigma_{cr} > 1.5$) the maximum load can be predicted with sufficient accuracy by assuming that when the mid-plane direct stress at some location along an unloaded edge reaches a yield condition the plate will no longer be able to sustain a further increase in loading. The same criterion may be applied to thicker plates, although there is less justification for it, and a semi-empirical design curve has been formulated [3, 4] in which the effects of initial imperfections have been included by using a generalised imperfection parameter.

But, of course, plates in engineering practice are not used in isolation; they form elements in thin-walled structures. If these structures are sufficiently redundant in topology, the failure of a single plate need not mean that the structures as a whole will fail. It is necessary in such a situation, however, to know the load-deformation characteristics of the buckled plates in order that the stiffness and remaining strength of the structure can be determined. Furthermore, a study of the load deflection characteristics during and after buckling not only indicates how suddenly a structure will fail (i.e. how "brittle" or "tough" it is) but also how sensitive it is to initial imperfections. A few analytical attempts to obtain the post-buckling characteristics of plates have been made. GRAVES-SMITH [5] and others at Cambridge used numerical methods to obtain an elasto-plastic solution. They obtained theoretical load-deflection curves for a few plates but the method employed required large amounts of computer time and it appears that for this reason more general studies have not been made. More recently SHERBOURNE *et al.* [6, 7] have used a plastic mechanism method to study the post-buckling behaviour of flat and corrugated plates. Although good agreement between theory and experi-

mental results was obtained in some cases this was not true in others for which the agreement was poor. Sherbourne's analysis assumed a particular shape of mechanism and the plastic unloading line was obtained by allowing the geometric proportions of the shape to vary and determining, by means of a computer, the minimum load corresponding to a specified deflection amplitude.

MURRAY [8, 9] has tested thirteen plates stiffened by bulb flats; these plates were observed to fail either by lateral buckling of the stiffener or by a concertina-like buckling of the plate-deck. It is only the latter case which is considered here. To obtain a theoretical estimate of the plastic collapse behaviour, the geometry of the plastic mechanism (as indicated by laboratory observations (see Fig. 1a)) was assumed and a numerical minimisation technique was employed to fix the size of the mechanism. It was found necessary to use a small — and a large — deflection theory in order to explain the behaviour of these plates. Unfortunately, it was not possible in the experimentation to obtain the plastic collapse line because the apparatus could not follow the unloading which occurred. Thus the theory could not be thoroughly checked against experiment. The theory developed by MURRAY does not explain one observed phenomenon in his study of the behaviour of stiffened plates. He observed in the laboratory that for stiffener buckling sudden collapse occurred as predicted by theory. However, for the concertina-like plate buckling cases failure was somewhat more gradual whereas his theory predicted that the suddenness of collapse would be similar to that for the stiffener buckling cases. In other words, the experimental results crossed the theoretical collapse line (Fig. 1b) and penetrated deeply into a region where failure should have occurred already.

In this paper a similar approach is taken, rigid-plastic analysis is used and results are derived that are in good agreement with experiment. But since this analysis, like the others referred to earlier, assumes a mode of plastic deformation, it is useful to consider the mechanics by which such a plastic mechanism may be formed. To obviate the problems involved in solving the non-linear elasto-plastic plate formulation the phenomena are discussed with reference to simple conceptual models.

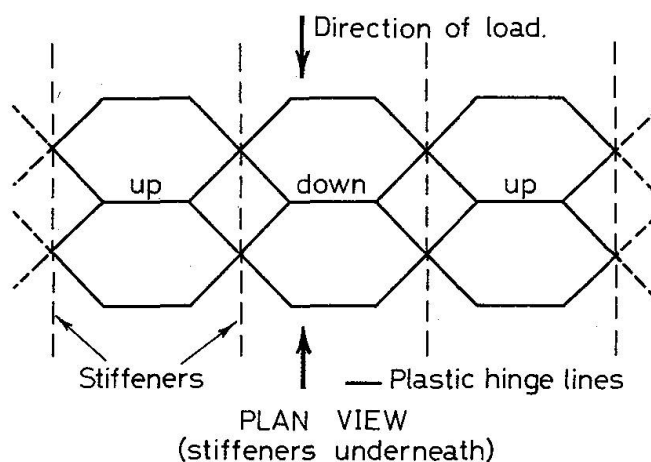


Fig. 1a

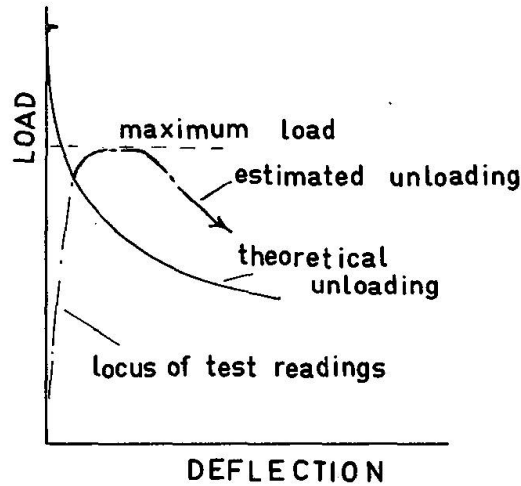


Fig. 1b

2. Concept of Plastic Mechanism

When a structure is wholly elastic the analysis can be performed using the well-established method involving the requirements of compatibility and equilibrium or the equivalent condition of energy extremum. But when the material begins to yield in some region due to the state of stress there, the analytical problems increase by an order of magnitude. Recently, large computers in conjunction with discrete numerical methods, such as finite elements or finite differences, have been used to follow the load-deformation characteristics of simple structural elements as the plasticity spreads due to increased loading. However, even with such machines it is not a simple task and is often costly in machine time. It is therefore not a viable approach for initial design calculations — at least not with today's computers.

An alternative approach has been to assume a state in which the plasticity has spread to such an extent that all the deformations occur in that region and we neglect the deformations that occur in the remaining elastic portion. The behaviour of the plastic portion is itself simplified, without distorting the physics of the region, so that the mathematics become elementary. The type of conceptual model used here is shown in Fig. 2a for elastic behaviour and Fig. 2b for plastic behaviour.

In this, the rotational spring stiffness c models the elastic flexural rigidity of a strut and the curves (i), (ii) and (iii) in Fig. 2c indicate the elastic load-deflection relationship for various values of initial imperfection w_0 . Now turning to plastic behaviour we take the particular example of a strut with rectangular cross-section, breadth b and depth d , that is subjected to a moment M'_p and a longitudinal force P ; if the material everywhere on the cross-section is assumed to be stressed to its yield stress, the maximum moment it can carry is [10]

$$M'_p = M_p \left[1 - \left(\frac{P}{P_y} \right)^2 \right], \quad (1)$$

where M_p is the plastic moment $\frac{bd^2}{4} \sigma_y$. Putting an equivalent hinge in the middle,

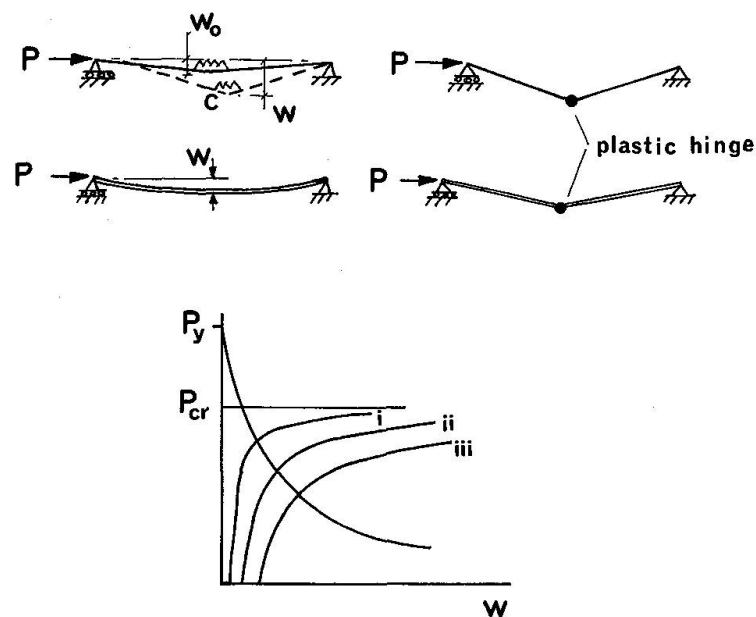


Fig. 2

Fig. 2b, we determine the curve (iv) in Fig. 2c. This method assumes that there is a sudden transition from elastic to plastic mode at the intersection of the curves. Of course in reality there is a gradual spread of plasticity across the section, but because most of the energy in the column in both the elastic and plastic modes is bending strain energy this approach has in the past been a sufficiently accurate and useful aid in describing the behaviour of struts and frameworks [10].

In this paper we are interested primarily in long rectangular plates and it is observed during tests that these will deform into regular wave-like patterns of the type shown in Fig. 3a. Measurements of a typical elastic plate supported at its edges give a load-deflection relationship of the shape indicated in Fig. 3b. If the plate is sufficiently thin it will support axial loads in excess of the critical load

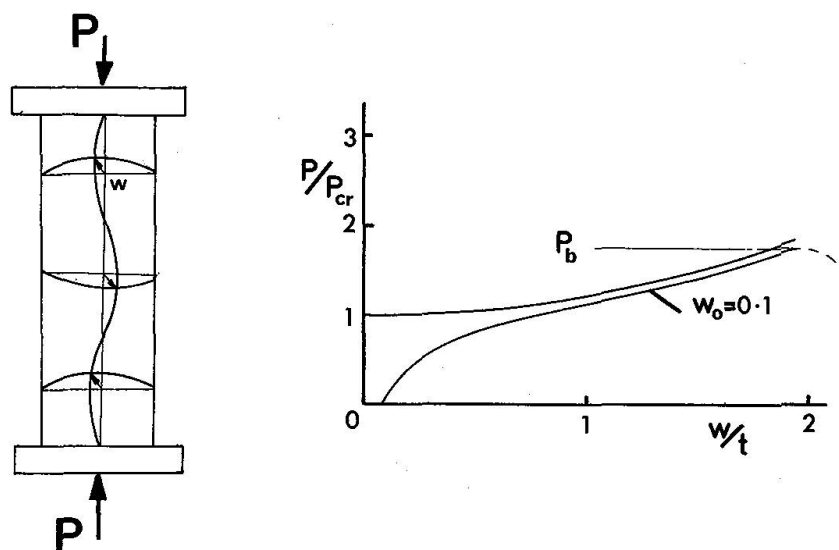


Fig. 3

corresponding to the perfectly flat condition. It is well-known that this increase is due to the restraining effect of the membrane action and that the longitudinal direct stresses become greater at the edges during buckling. As stated earlier, the unloading characteristics of an axially loaded thin plate are difficult to obtain experimentally because collapse occurs very rapidly once a mechanism starts to form. Elastic energy stored as membrane and bending stresses is released during this process and drives the mechanism until its deformations are large. Fig. 4a shows the deformed shape of the mechanism observed for medium-thick steel plates ($\sigma_y/\sigma_{cr} < 1.5$) and Fig. 4b typifies the corresponding shape for thin plates (although the shape shown in Fig. 4a has also been observed).

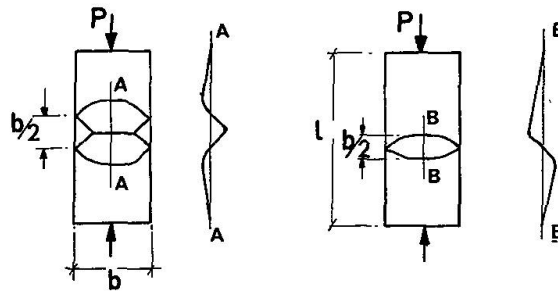


Fig. 4

In the next two parts of this section the simple lumped parameter model introduced in Fig. 2 is extended for the purpose of explaining the physics of elastic and post-elastic plate buckling. This study facilitates the understanding of the phenomena referred to above and, finally, indicates a suitable form of plastic mechanism to be used in the analysis in Section 3. The form of this mechanism is different from that used by MURRAY [9]. Their relationship is discussed in Section 5.

2.1 Square Plate

A simple lumped-parameter model of a square plate that incorporates the stiffening effect of the mid-plane membrane forces is shown in Fig. 5. The longitudinal strip AB is modelled (Fig. 5b) by two longitudinal rigid links and a rotational spring which has a lumped flexural stiffness $c/2$. The lateral strip CD is modelled by two lateral extensional springs of stiffness k and a rotational spring

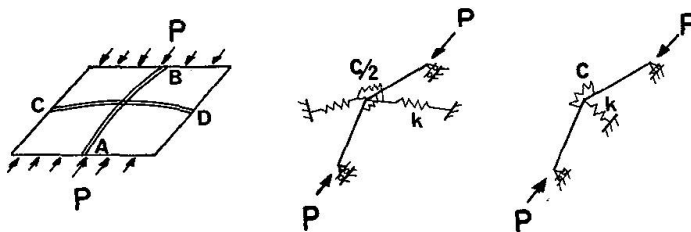


Fig. 5

of stiffness $c/2$. As this model deflects upwards by an amount w the lateral springs each extend, to a first order approximation, by an amount $\frac{w^2}{l}$. Thus the two lateral springs can be replaced by a non-linear transverse spring (Fig. 5c) which carries a load equal to $\frac{4kw^3}{l^2}$. The equilibrium equation for small deflections of this model with no initial imperfections is

$$(4 - p)w = k^*w^3, \text{ where } p = \frac{Pl}{c}, k^* \equiv \frac{k}{c} \quad (2)$$

and its load-deflection characteristics are shown in Fig. 6. The other graphs in this figure are load-deflection curves when there are initial imperfections. Thus this lumped parameter mechanism models the behaviour of a square plate in the elastic range.

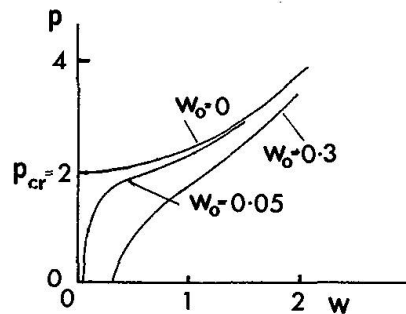


Fig. 6

Up to the initiation of yielding both the extensional and rotational springs maintain their stiffness values, but afterwards the moment at the centre pin may be considered to reach a maximum value of M_p' which is a function of the axial load (see eqn. (1)). The rotational spring must then be replaced by one with zero stiffness because at a full plastic hinge $\frac{dM}{d\theta} = 0$. During the development of the plastic mechanism and as yielding penetrates deeper into the plate the stiffness of the transverse springs (Fig. 5b) is reduced. Eventually when the deflections are large the mechanism yields across the full section and k is then zero. If we assume a value of k that is small relative to its initial value and constant throughout the deformation, the curve *II* (Fig. 7b) is obtained for the mechanism shown in Fig. 7a.

Suppose the model were to be tested in a laboratory. As the load was applied we would expect the experimental points to follow curve *I* until the onset of yielding. Eventually, when the deflections are large the experimental points should become asymptotic to curve *II*. But we should not expect that the points would transfer from curve *I* to curve *II* at point *A*. This is what happens in the case of a simple strut in which nearly all of the energy is flexural, but is cannot happen in the case of the plate model because the stiffness k of the lateral spring (which represents the membrane stiffness) still has its elastic value at point *A*. Thus the rotational spring is restrained from developing its full plastic moment until point *B*. The experimental points will therefore proceed beyond point *A* to near *B* and then droop down asymptotically along curve *III* towards curve *II* but from

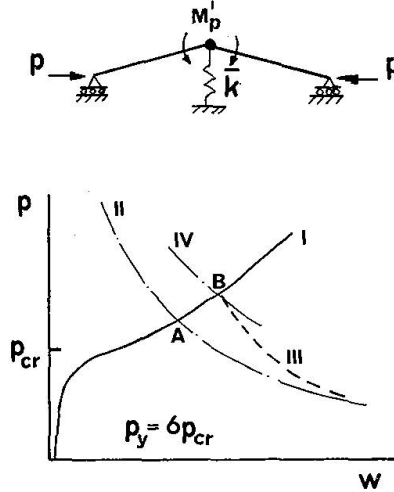


Fig. 7

above. During this stage the value of k is decreasing towards zero. Point B and the actual failure load may or may not be well above A depending on the values of the parameters defining the plate geometry. We can surmise that if the intersection of Curves I and II (Fig. 7b) is used as an estimate of the failure load it will probably, but not necessarily, be conservative.

The position of B (Fig. 7b) for the model shown in Fig. 7a can be found by considering its equilibrium in the same way for the model shown in Fig. 5c. Moments about the left hand end give

$$Pw - M_p' - \frac{k w^3}{l} = 0$$

By using eqn. (1) and after re-arranging we obtain

$$P = \frac{-w + \sqrt{w^2 + \frac{4M_p}{P_y^2} \left[\frac{k w^3}{l} + M_p \right]}}{2(M_p/P_y)^2} \quad (3)$$

This equation is plotted as Curve IV in Fig. 7b and its intersection with curve I defines the point B . As the mechanism develops the value of k decreases (as stated above) and when k becomes zero eqn. (3) gives curve II .

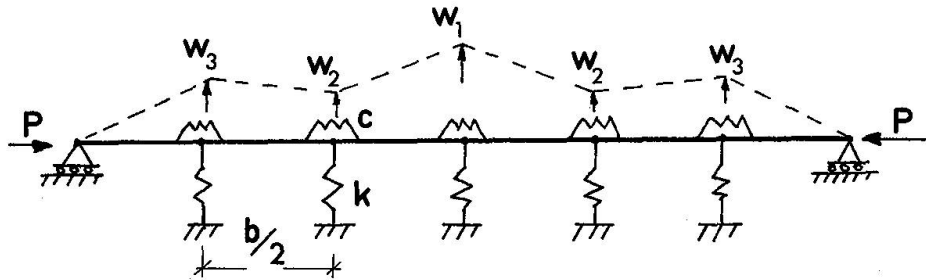
2.2 Rectangular Plate

The model of the previous section can be extended to enable us to study the mechanics of a rectangular plate.

Figure 3a shows a plate with an aspect ratio 3:1 and Fig. 8 its model. We can compute the model's elastic behaviour with a wide variety of initial imperfections. The spacing of the springs and hinges is equal to the half width of the plate and the equilibrium condition is:

$$\text{Section 1-2: } (6-p)w_1 + (-8+p)w_2 + 2w_3 = -k^*(w_1^2 - w_{01}^2)w_1 + 6w_{01} - 8w_{02} + 2w_{03}$$

Section 2-3: $(-8+p)w_1 + (14-p)w_2 + (-8+p)w_3 = 2k^*(w_2^2 - w_{02}^2)w_2 + 8w_{01} + 14w_{02} - 8w_{03}$
 Section 3-end: $2w_1 + (-8+p)w_2 + (10-2p)w_3 = -2k^*(w_3^2 - w_{03}^2)w_3 + 2w_{01} - 8w_{02} + 10w_{03}$
 where w_{01} is the initial value of w_1 , etc., $p \equiv \frac{Pb}{c}$ and $k^* \equiv \frac{k}{c}$ (4)



$$(3-p)w_1 + (-4+p)w_2 + w_3 = -k^*(w_1^2 - w_{01}^2)w_1 + 3w_{01} - 4w_{02} + w_{03}$$

$$(-4+p)w_1 + (7-p)w_2 + (-4+p)w_3 = -2k^*(w_2^2 - w_{02}^2)w_2 + 4w_{01} + 7w_{02} - 4w_{03}$$

$$w_1 + (-4+p)w_2 + (5-2p)w_3 = -2k^*(w_3^2 - w_{03}^2)w_3 + w_{01} - 4w_{02} + 5w_{03}$$

where w_{01} is the initial value of w_1 , $p \equiv \frac{Pb}{c}$, $k^* \equiv \frac{k}{c}$

Fig. 8

In Fig. 9a the initial imperfections indicated cause the model to deform in a uniform waveform. But such regularity in the initial imperfections would be unusual in practice and Fig. 9b indicates the gradual change of waveform as the load is applied to a model with irregular deformations.

For this latter model, the onset of plasticity will occur at the central hinge and, as shown in Fig. 10a for a moderately thick plate ($\sigma_y/\sigma_{cr} \simeq 2$), there is unloading accompanied by reduction of the deflection in the elastic portion until the plastic condition is reached at the adjacent hinges after which a completely local mechanism forms. For a much thinner plate ($\sigma_y/\sigma_{cr} \simeq 6$) the hinges form at both positions almost simultaneously as shown in Fig. 10b.

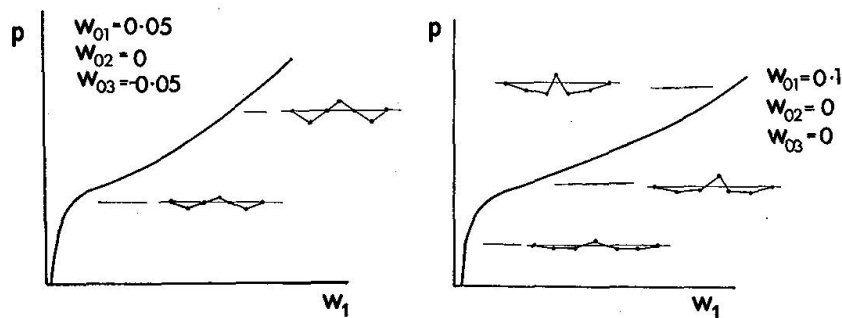


Fig. 9

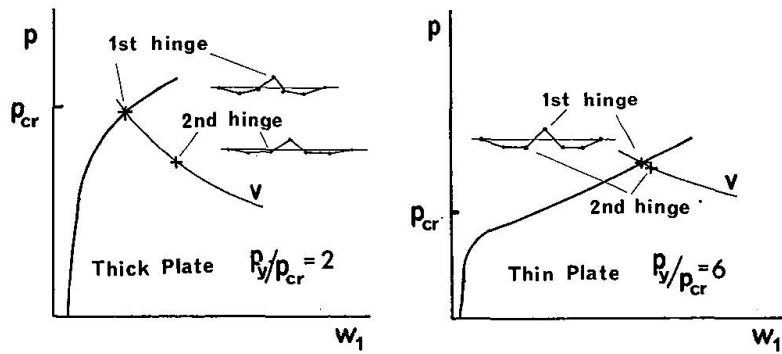


Fig. 10

It is now possible to infer the probable causes for the deformed shapes in Fig. 4. Taking the thinner plate first; as the load is increased, the out-of-plane deformations will grow and their shape will largely be determined by initial geometry. In our model there was symmetry about the central hinge but of course this will probably not occur in the analogous imperfection in a practical plate. When the maximum load is reached, that is after the edge stresses have attained a yield condition, the plate begins to unload. The deflections at the position of yielding increase rapidly and, as indicated by the model, the remaining elastic portion becomes flatter. The plastic moment will be reached at the positions of maximum deflection and a mechanism will start to form. This will have a curved form in plan because the out-of-plane deflections vary across the plate from a maximum at the centre to zero at the edge. This variation is approximately sinusoidal in form so the curve of the yield line is the intersection of an inclined flat plane with a sinusoidal cylinder. Because the plastic hinges form over such a small range of deflection it is easy for one of the outer hinges to form completely before the formation of the other outer hinge is at all started. When this happens it is sufficient that only one side of the mechanism forms for deflection to proceed and the other side flattens out. Because of the asymmetry of the deflections in practice this will occur in most cases.

In the thicker plate there is usually a symmetrical buckled plastic shape and this is in fact the amalgamation of two mechanisms as shown in the thin plate. The reason is that the asymmetry of deflected shape is not so well developed and the separation of the deflections at which the first and second hinges form means that the two outer hinges are forced to form almost simultaneously.

It is interesting to compare this model behaviour to that observed in the laboratory during tests on long rectangular plates ($40 \lesssim b/t \lesssim 60$). As the axial load is increased initial imperfections grow in magnitude and gradually form a regular pattern of elastic waves whose wavelength is approximately equal to their width. At this stage the longitudinal stresses are greater at the edges (where the plate is straight) than at the centreline. Finally the plate yields at the edges triggering the development of a plastic mechanism which initially, for a very uniform elastic deflection pattern, spreads over a large portion of the plate (Fig. 11). But of course some region has a slightly greater deflection and it is noticed that this now begins to deflect at a much faster rate and the other regions begin to flatten out. The result is the local plastic deformed shape indicated in Fig. 4a.

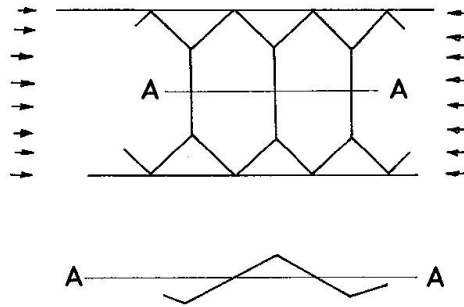


Fig. 11

The model analysis in this section has indicated that the buckled shape of a plate is governed not only by plasticity in the material but also by the initial deformations and the rate of growth of the elastic buckles in that part of the plate that is adjacent to the plastic zone. This, of course, is a very complex problem to analyse mathematically and it is useful to consider approximate, but much simpler, approaches in an attempt to afford some insight to the plate plastic unloading characteristics. One approach would be to assume that the initial deformations were so regular that the buckling mechanism formed simultaneously everywhere in the plate as in Fig. 11. The link and spring analogue of this mechanism is shown in Fig. 9a with the resulting plastic unloading line shown as curve *II* in Fig. 12. This is similar to the model in Section 2.1, it underestimates the collapse load and lies below the actual unloading curve *V*.

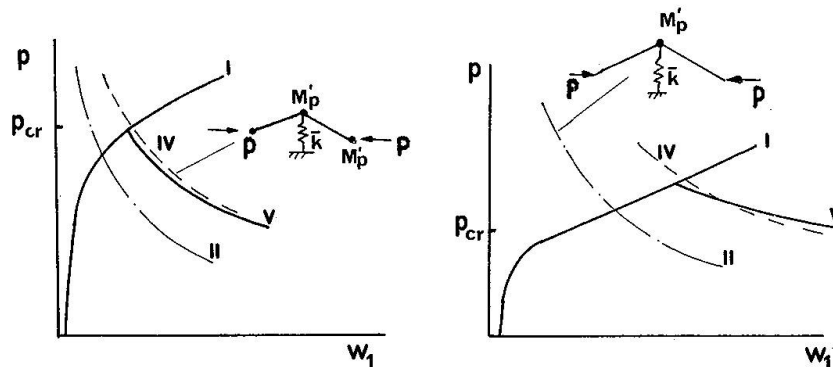


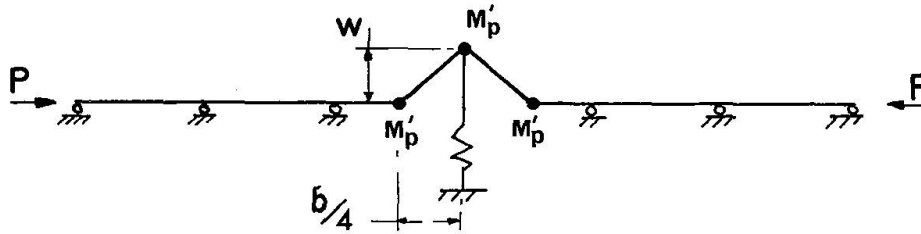
Fig. 12

An alternative approach is to assume that the elastic deflections are zero and that the deformations occur only as a plastic mechanism. A study of Figs 9, 1a and 11 suggest that the mechanism as shown in Fig. 13 will be the one which the plate eventually tries to develop because the hexagonal plates (Figs. 1 and 11) are pivotted along their long diagonal. The length of the link (Fig. 13) is an estimated value.

This model can be analysed simply to give the equilibrium equation:

$$Pw = 2M_p \left[1 - \left(\frac{P}{P_y} \right)^2 \right] + \bar{k} w^3 \quad (5)$$

where $\bar{k} = \frac{bk}{2l^2}$ and the corresponding unloading line is shown as curves *VI* in Fig. 12.



$$P_W = 2M'_p \left[1 - \left(\frac{P}{P_y} \right)^2 \right] - 2k w^3$$

Fig. 13

In this mechanism we are eliminating the contribution of the elastic portion of the plate but at the same time increasing the amount of plastic energy dissipated by increasing the rotation of the outer plastic hinges. Although this mechanism is not that which corresponds to the exact solution of the problem it serves the purpose of simplifying the analysis and provides a good approximation of the maximum load and the unloading line. In the next section we make a similar simplification for an axially loaded plate and henceforth in this paper we consider only the symmetric buckle pattern.

3. Continuum Analysis

As we have seen the actual buckled shape of a compressed plate is affected by the elasticity of the deflected regions adjacent to the region of plasticity. But the model analysis in the previous section suggests that a modified mechanism in which this elastic energy is eliminated may predict the plate buckling behaviour with adequate accuracy. This modified mechanism is shown in Fig. 14 and in the first instance it is analysed using bending action only. In Section 3.2 membrane deformation is considered.

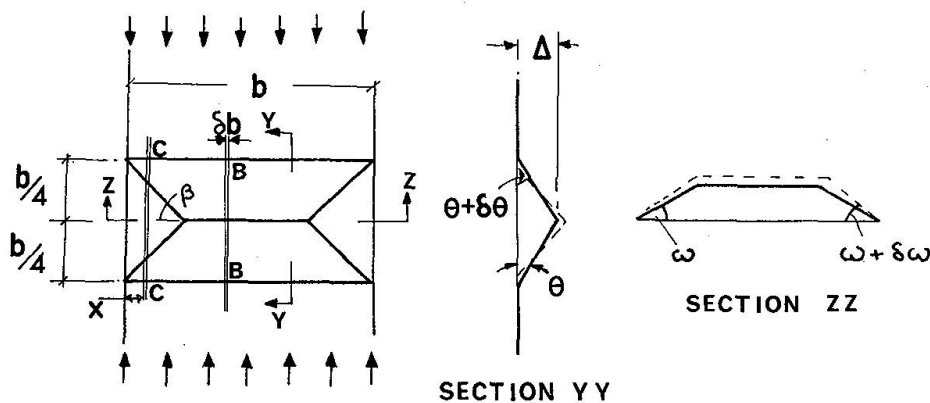


Fig. 14

3.1 Plastic Bending

The theory developed by MURRAY [8] is used here. The plate is considered as being composed of longitudinal strips. There are two typical regions; one containing strips typified by *BB* and another region comprising strips like *CC*. For strip *BB* of width δb (see Fig. 14a and Fig. 15a) the equilibrium equation is

$$P\Delta = 2M'_p \quad (6)$$

that is

$$P = \sigma_y t \delta b \left[\sqrt{\left(\frac{\Delta}{t}\right)^2 + 1} - \frac{\Delta}{t} \right] \quad (7)$$

The width of the region is $b(1 - \frac{1}{2} \cot \beta)$ so that the load P_1 that this portion of the plate can support is

$$P_1 = \sigma_y t b (1 - \frac{1}{2} \cot \beta) \left[\sqrt{\left(\frac{\Delta}{t}\right)^2 + 1} - \frac{\Delta}{t} \right] \quad (8)$$

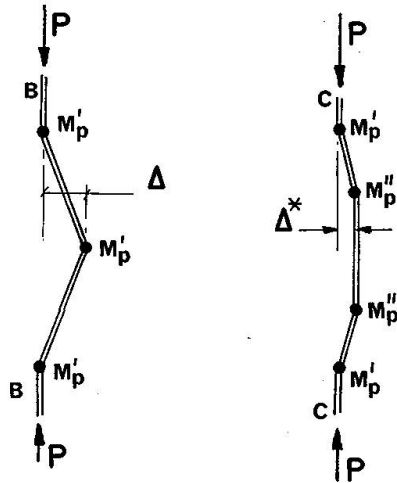


Fig. 15

For strip *CC*, the geometry is shown in Fig. 15b; the inner hinge is inclined in plan at an angle β and MURRAY [11] has shown that for such a situation the effective plastic moment M_p'' is

$$M_p'' = M_p' \sec^2 \beta = M_p' \left[1 - \left(\frac{P}{P_y} \right)^2 \right] \sec^2 \beta \quad (9)$$

The equilibrium equation for this strip is

$$M_p' (1 + \sec^2 \beta) = P\Delta^* \quad (10)$$

where $\Delta^* \equiv \Delta \frac{x}{\frac{b}{4} \cot \beta}$

and x is the distance of the strip from the plate edge. The load P_2 carried by these outer regions is

$$P_2 = 2 \int_0^{\frac{b}{4} \cot \beta} \frac{\sigma_y t^2}{4 \Delta^*} (1 + \sec^2 \beta) db$$

$$= \sigma_y \frac{tb}{4} \cot \beta \left\{ \sqrt{\left(\frac{2\Delta}{Kt}\right)^2 + 1} - \frac{2\Delta}{Kt} + \frac{1}{2\Delta/Kt} \log_n \left[\sqrt{\left(\frac{2\Delta}{Kt}\right)^2 + 1} + \frac{2\Delta}{Kt} \right] \right\} \quad (11)$$

where $K \equiv 1 + \sec^2 \beta$.

The average stress σ for the whole plate width is therefore

$$\frac{\sigma}{\sigma_y} = [\sqrt{(\varepsilon)^2 + 1} - \varepsilon] + \frac{1}{4} \left\{ -2 \cot \beta [\sqrt{(\varepsilon)^2 + 1} - \varepsilon] \right.$$

$$\left. + \cot \beta \left[\sqrt{\left(\frac{2\varepsilon}{K}\right)^2 + 1} - \frac{2\varepsilon}{K} \right] + \frac{\cot}{2\varepsilon/K} \log_n \left[\sqrt{\left(\frac{2\varepsilon}{K}\right)^2 + 1} + \frac{2\varepsilon}{K} \right] \right\} \quad (12)$$

where $\varepsilon \equiv \Delta/t$.

The variation of σ/σ_y for a fixed value of ε and with different values of β is not great and the minimum value for $\varepsilon \gtrsim 2$ is always given by $\beta = 45^\circ$. Putting this value in eqn. (12),

$$\frac{\sigma}{\sigma_y} = \frac{1}{2} \left[\sqrt{(\varepsilon)^2 + 1} - \varepsilon \right] + \frac{1}{4} \left[\sqrt{\left(\frac{2\varepsilon}{3}\right)^2 + 1} - \frac{2\varepsilon}{3} \right]$$

$$+ \frac{3}{8\varepsilon} \log_n \left[\sqrt{\left(\frac{2\varepsilon}{3}\right)^2 + 1} + \frac{2\varepsilon}{3} \right] \quad (13)$$

As $\varepsilon \rightarrow 0$ the average stress $\sigma \rightarrow \sigma_y$. Equation (13) gives the loaddeflection curve for small ε ; in the next section a correction for membrane effects is derived. However, it is found that the expression (13) dominates especially in the important region of interest, *viz.* near the plate failure load.

3.2 Membrane Action

In this analysis a very simplistic approach is followed and essentially is based on the premise that during a virtual displacement of the ends the mechanism will deform such that the surface area must increase to maintain integrity of the plate. We shall assume that all the required membrane deformation takes place at the hinge lines and at a constant stress equal to the yield stress. Thus, during a virtual change, the angle $\theta \rightarrow (\theta + d\theta)$, see Fig. 14b, and the edges of the mechanism approach each other by $\frac{1}{2} b \theta d\theta$. Also, the ridge extends by $\frac{b}{2} \cot \beta \sin \omega d\omega$ where β is the true angle (Fig. 14b). Using the approximation

$$\cot \beta \sin \omega \simeq \tan \theta$$

the change in perimeter ε_p of the mechanism at some height y is therefore

$$\varepsilon_p = 2b \theta d \theta [(1 + \tan \beta)y - 1] \quad (14)$$

and the plastic energy dissipated during the virtual change of state is

$$2\sigma_y b \theta d \theta \int_0^{\frac{b\theta}{2}} [(1 + \tan \beta)y - 1] dy = \frac{\sigma_y t}{2} b^2 \theta^2 d\theta \left[\frac{1 + \tan^2 \beta}{1 + \tan \beta} \right] \quad (15)$$

The work done during the virtual change is

$$\sigma_m b t \frac{b}{2} \theta d\theta \quad (16)$$

where σ_m is the contribution to the average stress due to membrane action. Equating (15) and (16), we have

$$\frac{\sigma_m}{\sigma_y} = \frac{\varepsilon}{b/t} \left[\frac{1 + \tan^2 \beta}{1 + \tan \beta} \right] \quad (17)$$

and for moderate deflections, with $\beta = 45^\circ$

$$\frac{\sigma_m}{\sigma_y} = \frac{\varepsilon}{b/t} \quad (18)$$

The total average stress applied to the mechanism is the sum of the bending and membrane actions. Fig. 16 and 17 show the comparison of predictions of the theory developed above and experimental values obtained by SHERBOURNE and KOROL [6]. The tests were on square thin-walled tubes loaded axially and the elastic line, which was for simply-supported plates with stress-free unloaded edges [3], assumes no initial deformations. The plastic mechanism unloading line is seen to provide reasonable agreement for the maximum load and for the rate of collapse of the plates.

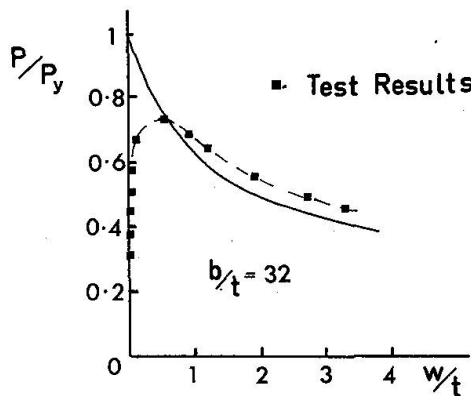


Fig. 16

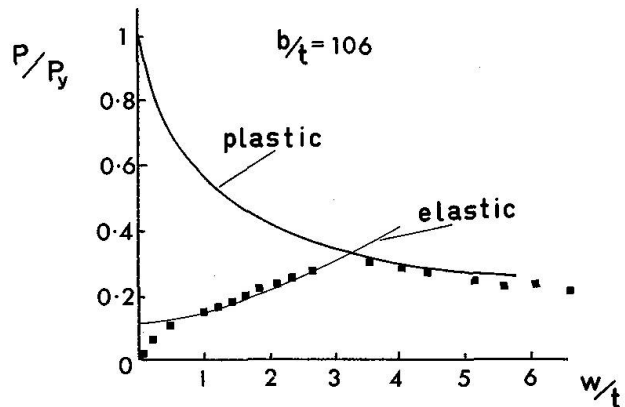


Fig. 17

4. Stiffened Plates

The results of the above plate analysis can be applied to stiffened plates loaded axially and which fail by yielding at the intersection of the plate and stiffener. Two examples are considered in detail here; they are from tests described in Reference (9) and have the geometries shown in Fig. 18 and an average yield stress of 377 MN/m^2 . The longitudinal deformed shape is assumed to be as shown in Fig. 18 and the stiffener is considered to be yielding across to depth. The analysis is similar to that in Reference (9) and requires the satisfaction of the compatibility condition,

$$\alpha = \frac{\Delta^2}{b \left[\frac{t_1}{2} + h_2 - c \right]} \quad (19)$$

from which the central deflection is obtained as

$$\delta = \frac{t_1^2 l \left(\frac{\Delta}{t_1} \right)^2}{b \left[\frac{t_1}{2} + h_2 - c \right]} \quad (20)$$

Also, equilibrium must be satisfied for the deformed position, i.e. for total axial force P ,

$$P = P_{pl} + F_{sc} - F_{st} \quad (21)$$

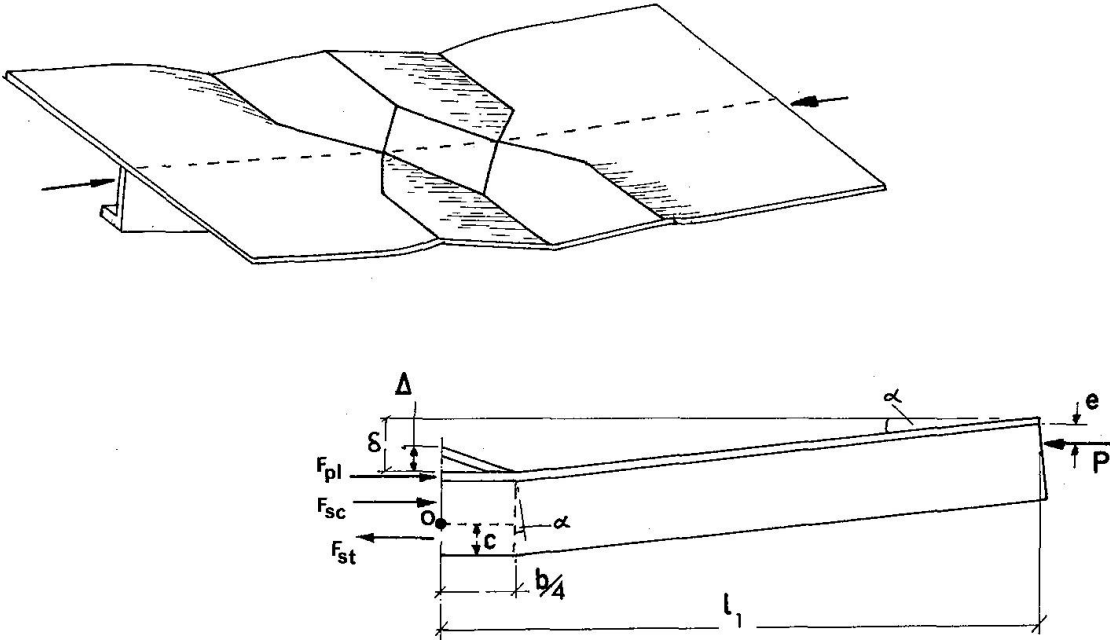
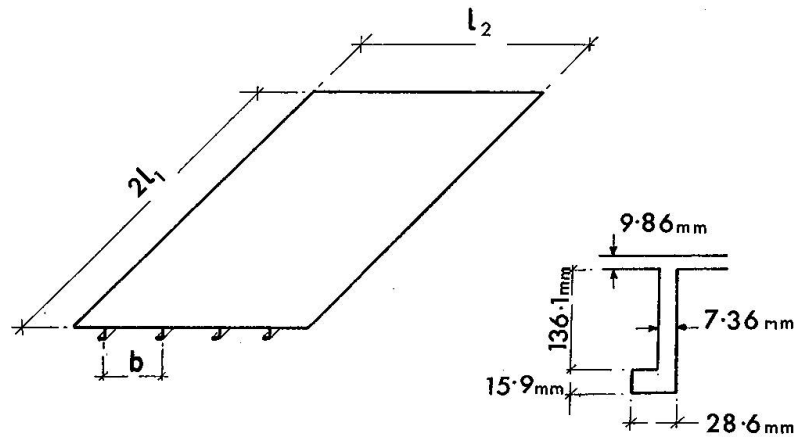


Fig. 18

and for moment equilibrium about 0,

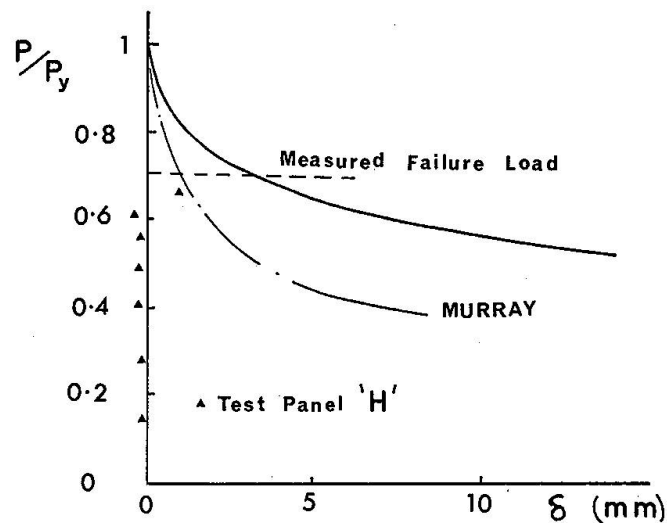
$$F_{pl} \left[\frac{t_1}{2} + h_2 - c \right] + F_{sc} \frac{h_2 - c}{2} + F_{st} \frac{c}{2} = P (\delta + h_2 - e - c) \quad (22)$$

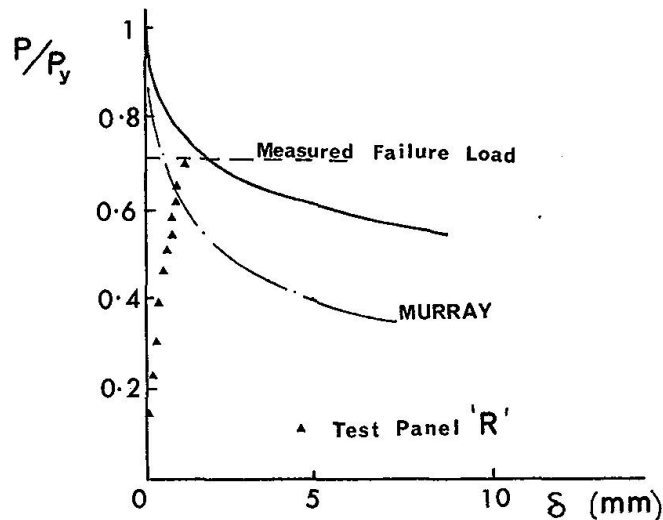
in which the plate force F_{pl} is obtained using equations (13) and (18). For the two stiffened plate geometries tabulated in Fig. 19 the unloading line obtained by satisfying the above condition is shown in Figs. 20 and 21. Also shown there are cocorresponding theoretical results obtained by MURRAY using a mechanism indicated by Fig. 1a for plate collapse.



Panel 'H'	$l_1 = 1.6 \text{ m}$	$l_2 = 2.44 \text{ m}$	$b = 533 \text{ mm}$
Panel 'R'	$l_1 = 0.8 \text{ m}$	$l_2 = 1.22 \text{ m}$	$b = 457 \text{ mm}$

Fig. 19





5. Discussion and Conclusions

1. Previously the behaviour of isolated struts and frameworks have been studied by superimposing two theoretical curves, one derived from elastic theory and the other from rigid-plastic theory. Adequate descriptions of strut and framework buckling phenomena have been obtained because nearly all of the energy of both the elastic and plastic modes is bending strain energy. In considering the behaviour of axially loaded plates significant amounts of energy are also stored in the form of membrane stresses. In this paper the effect of membrane (elastic) stresses on the buckling behaviour of axially loaded plates is considered. It is shown that the elastic strain energy available in this form can affect the failure load, the shape of the plastic mechanism developed during failure and the suddenness of collapse. The understanding of the failure process has been facilitated by studying the behaviour of analogous spring and link mechanisms. From these studies and laboratory observations it appears that the process of failure is as follows.

With increasing axial load eventually the plate develops a regular pattern of buckles in roughly square panels. One might expect that the plastic mechanism would also follow a similar regular pattern throughout the plate. From the studies of the spring and link analogues (Fig. 9) it is shown that the irregularity of initial imperfections plays a dominant role and instead of developing a plastic mechanism which extends right throughout the plate only one section becomes fully developed. While this is happening the buckles throughout the remainder of the plate decrease in amplitude and finally disappear after failure.

2. This analysis has been applied to published results for thin-walled square tubes and agreement between theoretical and experimental results is found to be good.

3. For the case of stiffened plates failing by plate buckling (i.e. not by stiffener buckling) (Figs. 20 and 21) the previously published analysis of MURRAY [9] predicts sudden collapse in contrast to laboratory observations. The mechanism used by

him is shown in Fig. 1a, and it is seen that it is equivalent to a plastic mechanism which extends throughout the plate. The only significant difference between his mechanism and the one derived here is that the outer hinge line is moved inwards (c.p. Figs. 1a and 14a). As seen in Figs. 20 and 21 this raises the plastic mechanism line, thereby allowing more gradual collapse. It is now apparent that Murray's mechanism (Fig. 1a) has the maximum separation of the outer hinges while the present mechanism (Fig. 14a) has these hinges as close together as they can be. Thus the two curves in each of Figs. 20 and 21 are bounds and the actual collapse curve (as suggested for example by Fig. 1b) will lay somewhere between them. The location of these outer hinge lines although initially near to those of Fig. 1a must approach closer to those of Fig. 14a during the failure process.

6. Acknowledgments

This work was carried out while the first author was visiting Monash University, Melbourne. He would like to record his gratitude to the Australian Road Research Board and the Lower Yarra Crossing Authority for their financial support during that period of time.

Practical hints for the Engineer and Designer

There is a continuing desire on the part of engineers to develop structural forms to give ever increasing efficiency. In many circumstances this means that structures are becoming thinner and more slender. The exact analysis of such structures, for example box girders, is extremely difficult when the non-linear effects of plasticity and buckling are included.

Nevertheless, these characteristics do in fact govern the maximum load which the structure can carry and must be included in design calculations.

As a means of circumventing the analytical problems, there is growing trend to separate the influences of buckling and plasticity. This paper is concerned with the latter and proposes a simple analysis whereby the post-buckled behaviour of stiffened plates and plate elements can be simply calculated from a plastic mechanism. Also, the paper discusses, by means of a simple model, the influence of large elastic deflections and membrane stresses on the magnitude of the collapse load.

Due to the complexity of the analysis of thin structures, it is essential that engineers and designers have a clear picture of the mechanics of the behaviour of such structures. The aim of this paper is the simple presentation of an approach to developing such a picture. With the increasing complexity of structural forms, these simple approaches will have wide application and provide an approach complementary to the more cumbersome and involved methods of computer based numerical analysis.

References

1. S. P. TIMOSHENKO and J. M. GERE: Theory of Elastic Stability, McGraw-Hill, 1961.
2. J. M. COAN: Large Deflection Theory for Plates with Small Initial Curvature Loaded in Edge Compression. Journal of App. Mech., Vol. 18, A.S.M.E., Vol. 73, 1951.
3. A. C. WALKER: The Post-Buckling Behaviour of Simply-Supported Square Plates. Aero Quart., Vol. 20, 1969.
4. R. G. DAWSON and A. C. WALKER: Post-Buckling of Geometrically Imperfect Plates. Journal of Struct. Div., A.S.C.E., Vol. 98, 1972.
5. T. R. GRAVES-SMITH: A Variational Method for Large Elasto-Plastic Theory in its Application to Arbitrary Flat Plates. Proc. Int. Confer. Solid Mech., 1969.
6. A. N. SHERBOURNE and R. M. KOROL: Ultimate Strength of Plates in Uniaxial Compression. A.S.C.E. Nat. Struct. Eng. Meeting, 1971.
7. A. N. SHERBOURNE, C. Y. LIAN and C. MARSH: Stiffened Plates in Uniaxial Compression. Pub. I.A.B.S.E., Vol. 31, 1971.
8. N. W. MURRAY: The Behaviour of Thin Stiffened Steel Plates. I.A.B.S.E., Vol. 33-I, 1973.
9. N. W. MURRAY: Buckling of Stiffened Panels Loaded Axially and in Bending. To be published in The Structural Engineer.
10. J. A. L. MATHESON: Hyperstatic Structures. Vol. 1, Chapt. 8, Butterworth 2nd Ed.
11. N. W. MURRAY: Das aufnehmbare Moment in einem zur Richtung der Normalkraft schräg liegenden plastischen Gelenk. Die Bautechnik, Heft 2, 1973, Seite 57.

Summary

This paper examines the behaviour of uniformly compressed rectangular thin plates when they are loaded beyond their ultimate load. The manner in which plates buckle is described, the behaviour of analogous mechanisms consisting of rigid links and springs are studied and from these studies a plate mechanism is derived. It is shown that the membrane elastic energy plays a significant role in determining the post-buckling behaviour of a thin plate.

Résumé

Dans cette contribution, on étudie le comportement de plaques minces rectangulaires sous l'influence de compressions uniformes et qui sont chargées au-dessus de leur charge ultime. On dérive le genre du voilement des plaques et on étudie le comportement de mécanismes analogues comprenant des membres rigides et des ressorts. On montre que l'énergie élastique de la membrane joue un rôle significatif dans la fixation du comportement du voilement postcritique d'une plaque mince.

Zusammenfassung

Der Beitrag untersucht das Verhalten gleichmässig gedrückter dünner rechteckiger Platten, die über ihre zulässige Last hinaus belastet werden. Die Art der Plattenbeulung wird beschrieben und das Verhalten analoger Mechanismen, bestehend aus

starren Gliedern und Federn wird studiert und aus diesen Untersuchungen ein Plattenmechanismus abgeleitet. Es wird gezeigt, dass die elastische Membranenergie eine wichtige Rolle bei der Bestimmung des Nachbeulverhaltens einer dünnen Platte spielt.

Minimum Wall Thickness of Circular Concrete Tanks

Epaisseur minimale de réservoirs en béton armé de section circulaire

Mindestwandstärke kreisförmiger Stahlbetontanks

V.A. YERLICI

Professor and Dean of Engineering, Boğaziçi University (formerly Robert College), Istanbul, Turkey.

Introduction

“Primary tensile cracking”, cracks transversing the entire thickness [2] in the walls of reinforced concrete, liquid carrying tanks, creates an undesirable situation [4]. Appreciable circumferential tensile stresses develop in the concrete of the walls of circular tanks due to (a) the shrinkage tendency of concrete, (b) drop in ambient temperature and temperature gradient in the concrete, and (c) the ring tension induced by the hydrostatic pressure. “Primary tensile cracks” form, vertically, when the average of these stresses exceeds the tensile capacity of concrete, necessitating expensive repairs.

This study is an attempt to develop a formula to determine the minimum wall thickness of circular reinforced concrete tanks, sufficient to prevent “primary tensile cracking” of concrete. It takes into account the time-dependent nature of shrinkage, relaxation of the stresses due to tensile creep of concrete, frictional restraint at the base of the tank, and thermal effects. Thermal coefficients of steel and concrete are assumed to be equal and effects of any temperature gradient along the height of the tank are ignored. Furthermore, instantaneous modulus of elasticity of concrete under tension is considered to be independent of time, since it tends to approach a constant value, much faster than the modulus of elasticity of concrete under compression, following a relatively short curing period [9].

Shrinkage and Tensile Creep Strains in Concrete

The average time-dependent shrinkage strain of unrestrained concrete, $(\varepsilon_{sh})_t$, may be expressed as [7]

$$(\varepsilon_{sh})_t = (\varepsilon_{sh})_{\infty} (1 - e^{-\xi(t-t_o)}) \quad (1)$$

where t is the age of concrete at the time of strain measurement, t_o is the age of concrete at the start of shrinkage, $(\varepsilon_{sh})_{\infty} = (\varepsilon_{sh})_{t=\infty}$, and ξ is the coefficient determining the change of slope of the shrinkage curve [6].

The total, initial and time-dependent linear strain of concrete per unit of tensile stress, $1/(E_c)_t$, may be expressed as [1, 10]

$$1/(E_c)_t = 1/E_{ci} + \kappa(\varepsilon_\infty + \eta/t_i)(1 - e^{-\zeta(t-t_i)}) \quad (2)$$

where t_i is the age of concrete at the loading time, E_{ci} is the instantaneous tensile modulus of elasticity of concrete, ε_∞ is the maximum strain in concrete loaded at a very old age, η is the coefficient determining the relation between maximum creep strain and ε_∞ , ζ is the coefficient determining the change of slope of the creep curve, and κ is a coefficient introducing the influences of the climatic conditions, geometric dimensions of the member, composition of the concrete, etc., on the creep of concrete [3].

Shrinkage Stresses in Concrete Restrained by Reinforcement

Using relations (1) and (2) stated above, it is shown in Reference [11] that the average concrete stress in the sections of concentrically reinforced concrete bars under pure shrinkage for any specific age of concrete, t_1 , can be expressed as $-\rho\chi(t_1)$. Here, ρ is the percentage of steel and

$$\chi(t_1) = (\xi(\varepsilon_{sh})_\infty/\Phi) \int_{t_0}^{t_1} [(\xi - \zeta)e^{\xi t_0} \int_{t_0}^{\bar{t}} t \Lambda e^{t(\Omega - \xi)} dt - t_0 \Lambda e^{\Omega t_0}] \bar{t} - \Lambda e^{-\Omega \bar{t}} d\bar{t} \quad (3)$$

where $\Phi = (\rho/E_{ci}) + (1/E_s)$, E_s is the modulus of elasticity of steel, $\Lambda = \zeta\rho\kappa\eta/\Phi$, and $\Omega = (\zeta\rho\kappa\varepsilon_\infty/\Phi) + \zeta$.

The value of $\chi(t_1)$ as given by Eq. (3) can easily be computed with the help of a digital computer for any ρ , t_0 , t_1 combination in terms of the material constants E_s , E_{ci} , $(\varepsilon_{sh})_\infty$, ξ , κ , η , ε_∞ , and ζ , which can all be determined from test data. χ values for a particular set of these constants are given in Fig. 1 for various ages of concrete, t_1 , various percentages of reinforcement, ρ , and for various maximum unrestrained shrinkage strains of concrete, $(\varepsilon_{sh})_\infty$. Effort has been made to choose realistic values for constants in the preparation of Fig. 1; the following were assumed: $t_0 = 7$ days, $E_s = 29 \times 10^6$ psi (2.04×10^6 kg per sq cm), $E_{ci} = 5 \times 10^6$ psi (0.352×10^6 kg per sq cm), $\xi = 0.037$, $\kappa = 1.0$. Also, based on tensile creep data of Rose Dam concrete [9], constants η , ε_∞ , and ζ were taken as 3.2×10^{-6} /psi (45.4×10^{-6} /kg per sq cm), 0.04×10^{-6} /psi (0.568×10^{-6} /kg per sq cm), and 0.06 respectively.

Stresses in Concrete Wall Due to Base Restraint

Uniform circumferential tensile stresses develop in the concrete of tank walls, due to environmental temperature drop and to shrinkage of concrete, whenever free contraction of the tank is restrained by the frictional resistance of its subbase. These stresses quickly vanish with height [8]. Deflected wall shape for such a tank is shown in Fig. 2. A free tank contracts from the center of its base and, unless the tank dimensions are unusually large, the frictional force developed can

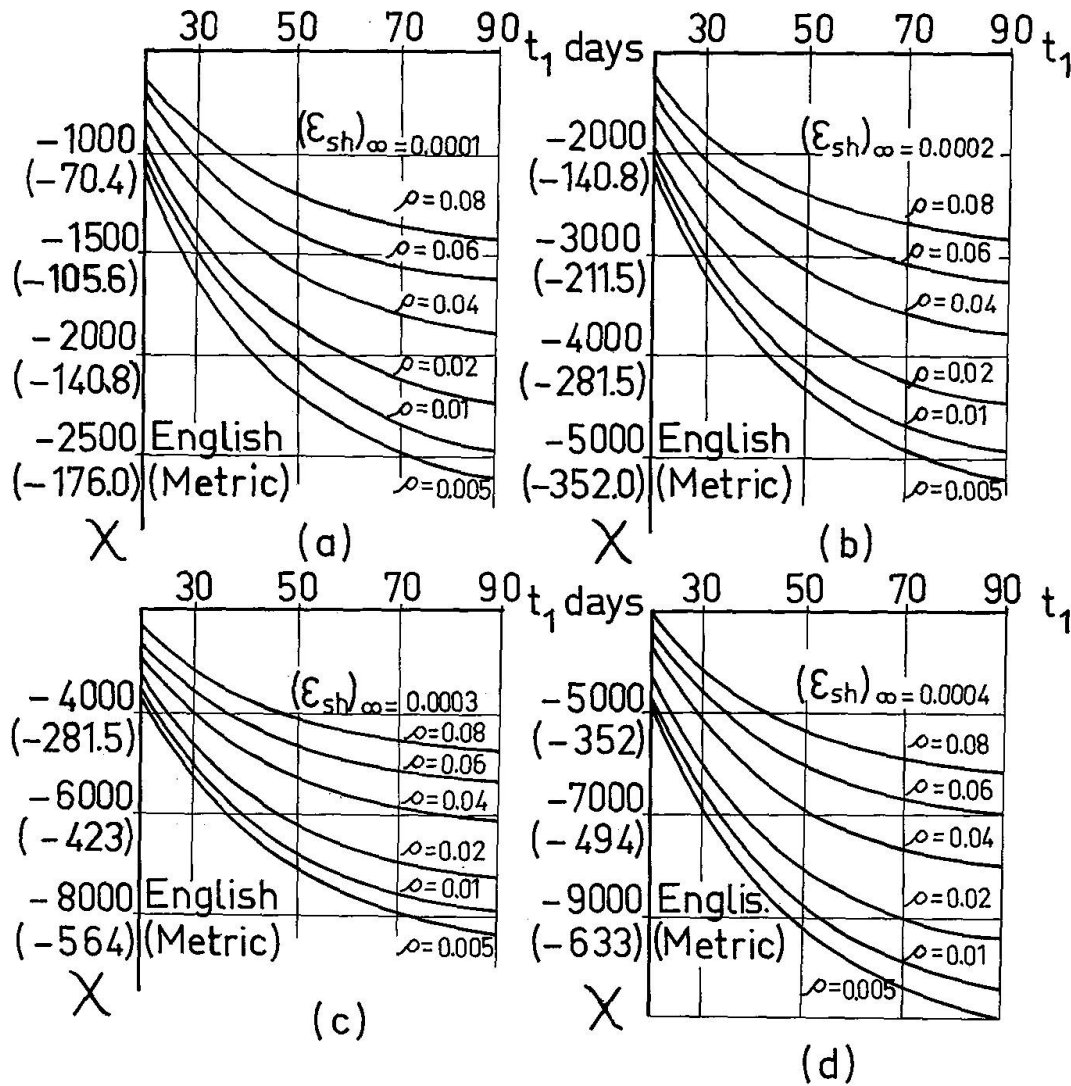
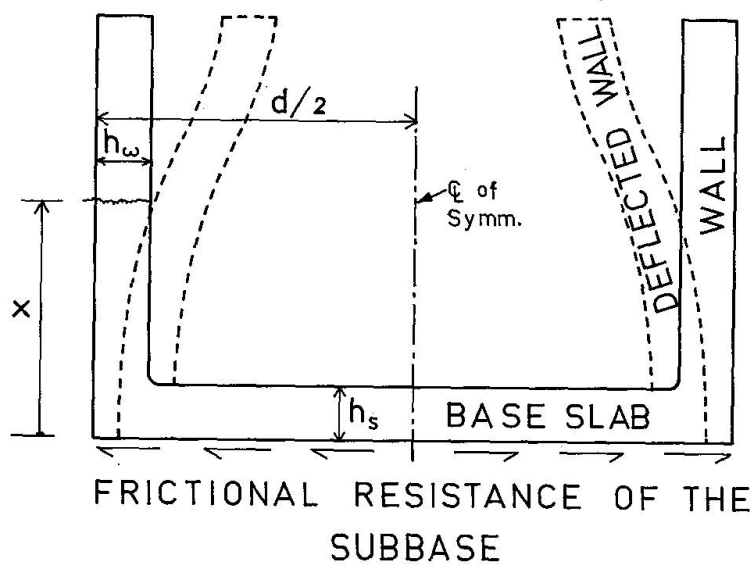

 Fig. 1. $\chi - t_1$ relationship.


Fig. 2. Cross section of the tank.

nowhere reach a magnitude high enough to arrest the movement of the tank's base completely [5]. If the subgrade resistance is assumed to be a linear function of the tank diameter, d , and if the average friction coefficient, μ , between the tank base and the ground is taken as constant, then, these stresses can be expressed as $\delta Z \mu / 2 d h_s$ [5]. Here, Z is the total ground reaction and is equal to the weight of the tank and the enclosed liquid, h_s is the thickness of the base slab of the tank, and δ is restraint reduction factor, introducing the height effect. Assuming rotational fixity at the base and uniform wall thickness, δ varies with the distance from the wall base, x , the wall thickness, h_w , and the tank diameter as shown in Fig. 3 [8]. δ should be taken as equal to zero for elevated tanks.

The average friction coefficient varies with the displacement of the base slab and, in the absence of accurate pertinent data, it can be determined with the help of Fig. 4 [5], where α is the thermal coefficient of expansion of concrete and T is the maximum expected drop in ambient temperature.

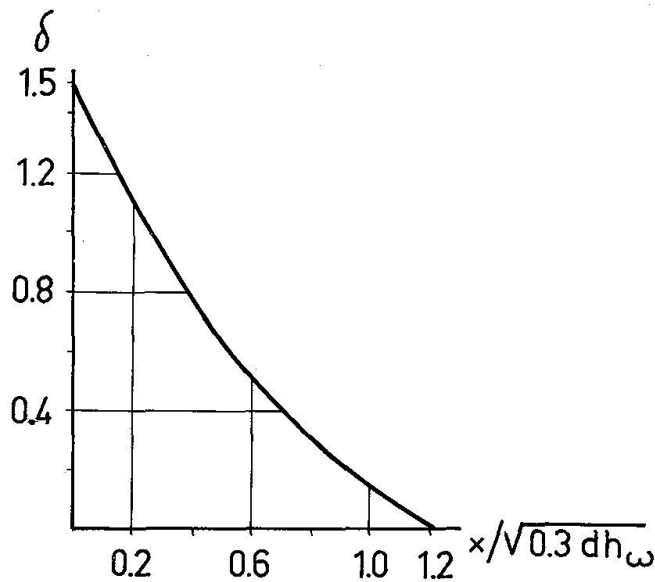
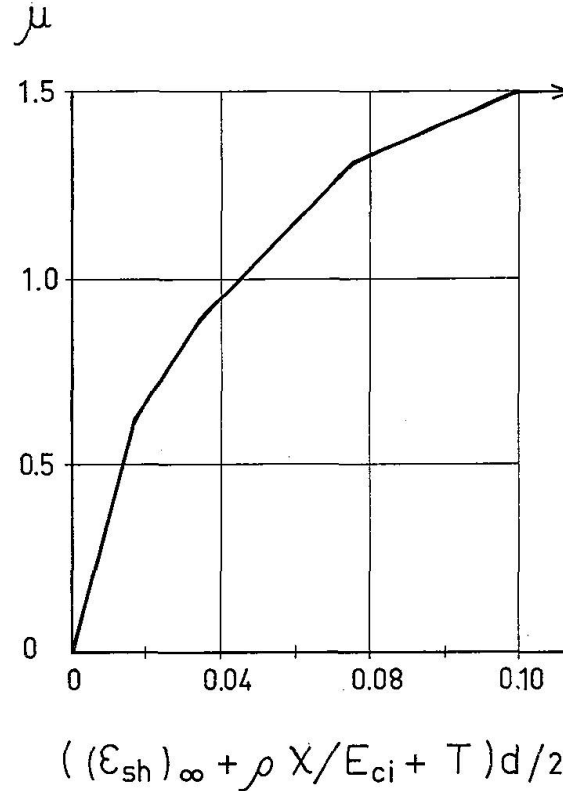


Fig. 3. $\delta - x / \sqrt{0.3 d h_w}$ relationship.

Stresses in Concrete Wall Due to Temperature Gradient

Circumferential thermal stresses develop in the concrete of the tank walls under a temperature gradient in radial direction. It can be shown that (8) when linear variation of temperature through the wall thickness is assumed and the effect of Poisson's ratio is ignored, these stresses vary uniformly and reach $\pm 0.8 E_{ct} \alpha |T_1 - T_2|$ values at the exterior and interior surfaces. Here, T_1 and T_2 are the temperatures of the tank wall at the interior and exterior surfaces, respectively. Although these stresses do not alter the average concrete stresses, they may force flexural type of cracking from one face, reducing the cross-sectional area of concrete resisting tensile cracking.

A temperature gradient along the height of the tank will increase the average circumferential concrete stresses (8). However, this effect is assumed to be relatively unimportant for normal tank conditions and is ignored.


 Fig. 4. μ – maximum displacement relationship (5).

Minimum Wall Thickness

The average circumferential tensile stress in the concrete of the tank walls for any age t_1 can be found by summing up the stresses developed due to the shrinkage tendency of concrete, environmental temperature drop, and ring tension, F , caused by hydrostatic pressure as

$$f_{ct} = \{ -\rho\chi(t_1) + \delta Z\mu/(2dh_s) + F/[A_c(1 + \rho E_s/E_{ci})] \} \quad (4)$$

Here, A_c is the cross-sectional area of concrete. If h_w is the wall thickness in inches, and the tensile force, F , is computed for a ring depth of 12 in., then, $A_c = 12 h_w$. On the other hand, the usual procedure in tank design is to provide sufficient circumferential steel reinforcement to carry all the ring tension, at a certain allowable stress, f_s , as though designing for a cracked section (4). Accordingly, $\rho = F/(A_c f_s)$. Substituting these values of A_c and ρ into Eq. (4) and introducing the tensile stresses caused by temperature gradient, and assuming a linear interaction between tension and flexural types of cracking, one obtains:

$$\begin{aligned} & \{ F[-\chi/(12h_w f_s) + (f_s E_{ci})/(12h_w f_s E_{ci} + F E_s)] \\ & + (\delta Z\mu)/(2dh_s) \} \gamma/f_t + \{ 0.8 E_{ci} \alpha |T_1 - T_2| \} \gamma/f_r = 1 \end{aligned} \quad (5)$$

Here, f_t is the average tensile strength of concrete per unit area, f_r is the modulus of rupture of concrete, and γ is the appropriate safety factor against “primary tensile cracking” of concrete in tank walls.

χ values, given by Eq. (3), decrease in time as can be seen in Fig. 1 and approach an asymptotic value for all intensities of shrinkage and percentages of reinforcement. In designing for wall thickness, the minimum χ value should be used with Eq. (5) in order to cover all the significant effects of the shrinkage of concrete. For practical purposes, it would be accurate enough to take minimum χ value = χ ($t_1 = 90$ days). Such minimum values of χ , based on the same set of material constants used in the preparation of Fig. 1, are given in Fig. 5 for various maximum unrestrained shrinkage strains of concrete and for varying percentages of reinforcement.

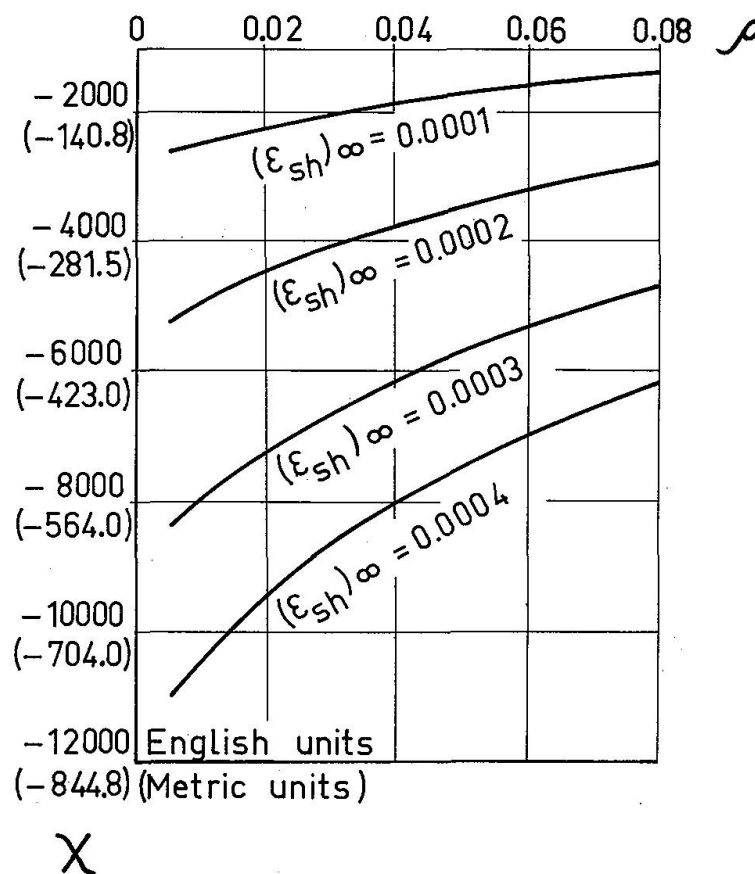


Fig. 5. $\chi(t_1 = 90 \text{ days}) - \rho$ relationship.

Fig. 6 shows the variation in the minimum χ values given in Fig. 5 with change in E_{ci} and κ . The minimum χ values of Fig. 5 can be adjusted for use with different E_{ci} and κ values when multiplied by the corresponding adjustment factors β_1 and β_2 given in Fig. 6, respectively.

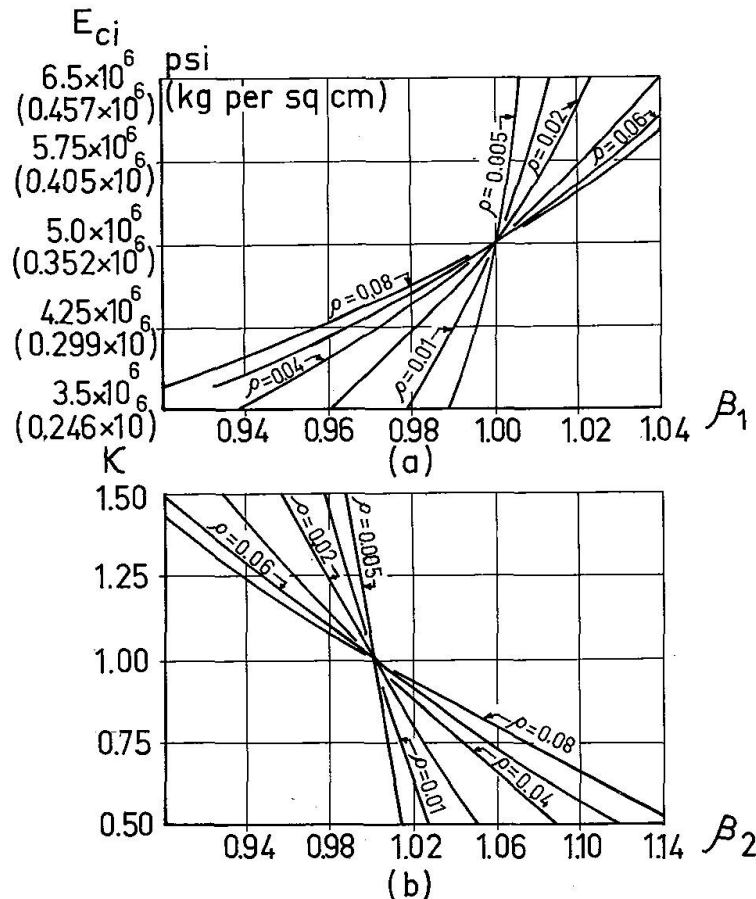


Fig. 6. Adjustment factors, β_1 and β_2 for corresponding E_{ci} and κ values, respectively.

Example

Determine the minimum wall thickness, h_w , for the given circular water tank, sufficient to prevent "primary tensile cracking" at the specified depth. Given: $d = 300$ in., $x = 24$ in., $F = 10,000$ lb per ft of wall depth, $f_t = 280$ psi, $f_r = 560$ psi, $f_s = 20,000$ psi, $E_{ci} = 4.0 \times 10^6$ psi, $E_s = 29 \times 10^6$ psi, $(\epsilon_{sh})_\infty = 0.0003$, $\kappa = 1.25$, $Z = 0.7 \times 10^6$ lb, $h_s = 12$ in., $T = 30$ deg F, $|T_1 - T_2| = 6$ deg F, $\alpha = 6.0 \times 10^{-6}$ per deg F, and $\gamma = 1.4$.

Area of circumferential reinforcement, $A_s = F/f_s = 10,000/20,000 = 0.5$ sq. in. Assume $h_w = 14$ in. For the given d , x , and assumed h_w , Fig. 3 gives $\delta = 0.43$. Assume $\rho = 0.005$. For the given $(\epsilon_{sh})_\infty$ and assumed ρ , Fig. 5 gives $\chi(t_1 = 90 \text{ days}) = -8333$. For the given E_{ci} and κ , Fig. 6 gives $\beta_1 = 0.994$ and $\beta_2 = 0.994$. Therefore, adjusted $\chi(t_1 = 90) = \beta_1 \beta_2 \chi = 0.994 \times 0.994 (-8333) = -8230$. Then, $((\epsilon_{sh})_\infty + \rho \chi / E_{ci} + \alpha T) d / 2 = 0.0705$ and Fig. 4 gives $\mu = 1.18$. Substituting the values given and found above into Eq. (5) and solving it for h_w one finds $h_w = 12.4$ in.

Therefore, use 12.5 in. thickness.

Actual $\rho = A_s / A_c = 0.5 / 12 \times 12.5 = 0.0033$, less than assumed ρ , therefore, O.K.

In the above example, about 25% of the concrete strength is used up by the frictional restraint at the base of the tank and 29% by the temperature gradient.

For the given tank, effect of base restraint vanishes 36 in. above ground, Fig. 3. Disregarding the base restraint and the temperature gradient, and then using the rest of the previously given data, minimum wall thickness is found to be, $h_w = 5.7$ in. from Eq. (5). This value is only 1.7 in. larger than the wall thickness found by feeding the same data into the thickness formula given in Reference (4).

Conclusion

Minimum wall thickness of circular reinforced concrete tanks, sufficient to prevent "primary tensile racking", can directly be determined from Eq. (5). The solution takes into consideration the effects of hydrostatic pressure, shrinkage and tensile creep of concrete, ground restraint, thermal stresses and the interaction between the tensile and flexural type of cracking forces in concrete. For usual design purposes, values of δ , μ , and χ used in Eq. (5) can readily be obtained from Fig. 3, 4, and 5 and 6 respectively.

Notation

The following symbols are used in this paper:

A_c	cross-sectional area of concrete.
A_s	area of circumferential reinforcement.
d	diameter of the tank.
E_{ci}	instantaneous tensile modulus of elasticity of concrete.
$(E_c)_t$	time-dependent tensile strain modulus of concrete.
E_s	modulus of elasticity of steel.
F	ring tension per unit depth of tank wall due to hydrostatic pressure.
f_{ct}	average circumferential tensile stress in concrete.
f_t	average tensile strength of concrete per unit area.
f_r	modulus of rupture of concrete.
f_s	allowable stress in steel.
h_s	thickness of the base slab of the tank.
h_w	thickness of the tank wall.
T_1 and T_2	temperature of the tank wall at the interior and exterior surfaces, respectively.
T	maximum expected drop in ambient temperature.
t	age of concrete at the time of strain measurement.
t_o	age of concrete at the start of shrinkage.
t_1	a specific age for concrete.
t_i	age of concrete at the time of loading.
x	distance from ground to the tank wall slice under consideration.
Z	total ground reaction under the tank.
α	thermal coefficient of expansion of concrete.
β_1 and β_2	adjustment factors.
γ	appropriate factor of safety against "primary tensile cracking of concrete" in tank walls.

δ	restraint reduction factor.
ε_{∞}	maximum strain of concrete loaded at a very old age.
$(\varepsilon_{sh})_t$	average time-dependent shrinkage strain of unrestrained concrete.
$(\varepsilon_{sh})_{\infty}$	$(\varepsilon_{sh})_{(t=\infty)}$.
ζ	coefficient determining the change of slope of the creep curve.
η	coefficient determining the relation between maximum creep strain loaded at a very young age and ε_{∞} .
κ	a coefficient introducing the influences of the climatic conditions, geometric dimensions of the member, composition of the concrete, etc., on the creep of concrete.
Λ	$\zeta\rho\kappa\eta/\Phi$.
μ	average friction coefficient between the tank base and the ground.
ξ	coefficient determining the change of slope of the shrinkage curve.
ρ	percentage of reinforcement.
Φ	$(\rho/E_{ci}) + (1/E_s)$.
$\chi(t_1)$	a function given by Eq. (3).
Ω	$(\zeta\rho\kappa\varepsilon_{\infty}/\Phi) + \zeta$.

Practical Consequences

The environmental conditions around the building site, the method of construction, the properties of materials used in the construction, the existing foundation conditions, the time of initial loading, and utilization greatly vary from one reinforced concrete tank to the other. Different minimum tank wall thicknesses are needed to prevent "primary tensile cracking" in different tanks because the above stated factors significantly influence the ultimate tensile strength, the shrinkage, and the tensile creep properties of concrete, the amount of base friction restraining the displacement tendencies of the tank, and the amount of the maximum temperature gradient which may develop in the tank walls. Eq. (5), which accounts separately for all these effects, enables the designer to determine the required minimum wall thickness for a circular reinforced concrete tank under any given set of conditions. Use of tank wall thicknesses greater than those thus found not only leads to waste in material and labor, but, in extreme cases, may force cracking because of the adverse effect of wall thickness on the base restraint of the tank. Therefore, the minimum wall thickness found with the help of Eq. (5) is the most economical solution to the problem ensuring safety against cracking under all conditions.

References

1. AROUTIOUNIAN, N.Kh.: Some Problems in the Theory of Creep. Pergamon Press, London, 1966.
2. BIANCHINI, A.C., KESLER, C.E., and LOTT, J.L.: Cracking of Reinforced Concrete Under External Load. Causes, Mechanism and Control of Cracking in Concrete, SP-20, American Concrete Institute, Detroit, 1968, pp. 73-85.
3. BRANSON, D.E., and CHRISTIASON, M.L.: Time Dependent Concrete Properties Related to Design-Strength and Elastic Properties, Creep and Shrinkage. Designing for Effects of Creep, Shrinkage, and Temperature in Concrete Structures. SP-27, American Concrete Institute, Detroit, 1971, pp. 257-277.

4. Circular Concrete Tanks Without Prestressing. Concrete Information, Portland Cement Association, Chicago.
5. FRIBERG, B.F.: Frictional Resistance Under Concrete Pavements and Restraint Stresses in Long Reinforced Slabs. Proceedings, Thirty-third Annual Meeting of the Highway Research Board, Washington D.C., Jan. 1954, pp. 167-184.
6. L'HERMITE, R.G.: Volume Changes of Concrete. Proceedings, Fourth International Symposium on Chemistry of Cement, National Bureau of Standards, Monograph 43, Vol. II, Washington D.C., 1962.
7. LYSE, I.: The Shrinkage and Creep of Concrete. Magazine of Concrete Research, Vol. II, No. 33, London, Nov. 1959, pp. 143-150.
8. TIMOSHENKO, S., and WOINOWSKY-KRIEGER, S.: Theory of Plates and Shells. Mc Graw-Hill Book Company, Inc., New York, 1959.
9. YERLICI, V.A.: Stresses and Strains Developed in Long, Continuously Reinforced Concrete Pavements Due to Shrinkage and Temperature Drop. (In Turkish), Bulletin Series 301, Robert College Research Center, Boğaziçi University, Istanbul, 1963.
10. YERLICI, V.A.: Behavior of Plain Concrete Under Axial Tension. ACI Journal, Proceedings V. 63, No. 8, August 1965, pp. 987-992.
11. YERLICI, V.A.: Stresses and Cracking in Reinforced Concrete Members Under Axial Tension. Materials and Structures, No. 23, Vol. 4, Paris, Sept-Oct. 1971, pp. 313-322.

Summary

A formula is developed for determining the minimum wall thickness of circular reinforced concrete tanks, sufficient to prevent "primary tensile cracking" of concrete. It accounts for the effects of hydrostatic pressure, time-dependent shrinkage and tensile creep of concrete, ground restraint, thermal stresses and the interaction between the tensile and flexural type of cracking forces in concrete and easily lends itself to solution with the help of accompanying charts.

Résumé

On développe une formule pour la détermination de l'épaisseur minimale de réservoirs en béton armé, à section circulaire, suffisante à prévenir la rupture intégrale du béton. Elle s'explique par l'effet de la pression hydrostatique, par le retrait dépendant du temps et l'effet du fluage du béton ainsi que par le serrage au fond du réservoir; en plus par les contraintes thermiques et l'interaction entre l'effet de dilatation et de flexion des forces de rupture dans le béton. On arrive facilement à la solution du problème à la main des diagrammes accompagnants.

Zusammenfassung

Es wird eine Formel zur Bestimmung der Mindestwandstärke kreisförmiger Stahlbetontanks entwickelt, die das durchgehende Reißen des Betons verhindert. Dieses erklärt sich aus der Wirkung des hydrostatischen Druckes, des zeitabhängigen Schrumpfung und Kriechens des Beton, der Einspannung am Boden des Tanks, aus Wärmebeanspruchungen und der Wechselwirkung zwischen der durch Dehnung und Biegung veranlassenen Risskräfte im Beton. Die angegebene Formel verhilft unschwer zur Lösung mit Hilfe der beigefügten Diagramme.

Erratum

Band 34-II der «Abhandlungen».
Vol. 34-II des «Mémoires».
Vol. 34-II of “Publications”.

Aufsatz **G. Eisenbiegler**:

Dreiseitig gelagerte isotrope Rechteckplatten mit linear veränderlicher Dicke

*Isotropic Rectangular Plates of Linearly Variable Thickness Supported
on Three Sides*

*Dalles rectangulaires isotropes à épaisseur linéairement variable
appuyées sur trois côtés*

Die Tabelle I.10 (Seite 63) und die Tabelle II.8 (Seite 66) sind irrtümlicherweise vertauscht worden.

Par erreur le tableau I.10 (page 63) et le tableau II.8 (page 66) ont été confondus.

Table I.10 (page 63) and table II.8 (page 66) have been taken by mistake.

Leere Seite
Blank page
Page vide